# Forschungszentrum Karlsruhe

Technik und Umwelt

Wissenschaftliche Berichte

FZKA 6650
EUR 20162 EN

Nuclear Fusion Programme
Annual Report of the
Association Forschungszentrum Karlsruhe/
EURATOM
October 2000 - September 2001

compiled by W. Bahm
Programm Kernfusion

Forschungszentrum Karlsruhe GmbH, Karlsruhe
2002

Forschungszentrum Karlsruhe GmbH
Postfach 3640, 76021 Karlsruhe

**Preface**

**The need for fusion energy**

Nuclear Fusion is a promising option to replace fossil fuels for energy production. The worldwide energy demand with an estimated increase of electricity production by at least a factor of two in the second half of this century, fading resources of raw materials and a growing concern about global warming require innovative solutions.

While renewable energy sources such as photovoltaic, wind, biomass etc. may become attractive for wide spread settlements, the growing number of megacities will require large power units. This is the market share where nuclear fusion energy may play an substantial role. Practically inexhaustible fuel resources, attractive safety features and no emissions of greenhouse gases are the advantageous features of fusion energy.

**Fusion research in the European Union**

Considering the importance of a secure, environmentally acceptable and affordable supply of energy for the welfare and prosperity of their citizens the European Union supports the development of new energy sources. The fusion research programme, integrating the total research work of the member states and Switzerland, represents the worlds largest effort in this field and has gained a leading position worldwide. Furthermore the European fusion research programme represents a successful example of an integrated European research network.

**The role of Forschungszentrum Karlsruhe**

While the German research laboratories Forschungszentrum Jülich and Max-Planck-Institute for Plasma Physics Garching/Greifswald concentrate on plasma physics and plasma wall interaction, the Forschungszentrum Karlsruhe is engaged in different key issues of design and technologies required for ITER and future fusion reactors.

**The main work areas**

For the ITER project, Forschungszentrum Karlsruhe developed superconducting magnets to confine the plasma, gyrotron type microwave generators to start the nuclear burn, and exhaust gas pumping and fuel clean-up systems. ITER will demonstrate the physics of a reactor grade plasma implementing already these essential reactor technologies. Furthermore four HCPB test blanket modules, each devoted to specific issues, are being developed to be tested in the first ITER operation phase.

One of the highlights of the Associations research programme constitutes the test programme of the ITER toroïdal field model coil in the TOSKA facility. The experiments performed so far were very successful, the worldwide highest maximal current of 80 kA was attained without any problems.

Tritium, one of the fuel components of a nuclear fusion reactor will be produced by reactions of fusion neutrons with lithium contained in the breeding blanket. Development of an energy convertor that delivers high grade heat and supplies enough tritium to maintain the operation is one of the most challenging engineering tasks undertaken by the Association whereby emphasis is laid on the development of a helium cooled pebble bed blanket.

Experimental work related to fuel cycle issues of ITER is directed to the development of the cryopump for exhaust gas pumping from the torus and the development of tritium processes and the design of tritium involving components and systems. Main experimental facilities are the testbed TIMO for the ITER model cryopump and the Tritium Laboratory TLK processing considerable amounts of tritium for testing components on a technical level.

Contributions by the TLK to the preparation of the technical basis for the proposal of Cadarache as European ITER site aim at the management of effluents and releases and at the tritium storage and inventory.

Cost and environmental characteristics of future fusion reactors will crucially depend on solutions to the structural materials issue. Radiation damage from fusion neutrons and high loads of heat and mechanical stresses are expected to limit the lifetime of plasma near components and to determine the amount and radioactivity of waste. The development of low activation radiation resistant steels requires a long term programme proceeding stepwise to final qualification in a large dedicated fusion neutron source. The Association devotes a major activity in this field of work.

Reactor studies will gain importance in the programme. Contributions of the Associations relate to technical issues and studies of safety/environmental impact.

Contributions to the JET exploitation are being performed in the frame of the JET task force "fusion technology" covering tritium profiling in plasma

facing materials, using the Active Gas Handling System of JET as a test bed for the development of components, and providing methods and procedures for the handling of tritium contaminated materials.

The work for fusion technology, as briefly outlined above, is carried out in the frame of the European Fusion Development Agreement (EFDA). It is targeted to foster cooperative efforts of the laboratories associated to the EU Fusion Programme, in particular in view of construction and exploitation of larger experimental facilities such as JET and ITER.

## Support to the Physics Programme

The tokamak represents the main development line of the common programme. In parallel, the stellarator concept is under development to potentially improve the confinement for reactor operation. The Association, assisted by the University of Stuttgart, contributes the complete 10 megawatt microwave heating installation to the Wendelstein-7X stellarator, being built by the IPP-EURATOM Association in Greifswald, Germany.

## Organisation of the work

Forschungszentrum Karlsruhe is engaged at present in 12 research programmes of different scopes and sizes. Programmes are organized in a matrix form were small management groups coordinate the work that is executed in a variety of scientific and technical departments. Competition of the programmes lead to frequent fluctuations of contributions from the departments depending on the attractiveness of the task and the provision of resources. A continuous support from the European Commission together with the longer term perspective of the programme are important, therefore, to maintain the competence available for the fusion programme.

About 170 professionals and technicians are involved in the fusion programme of the Association FZK-EURATOM with additional support of the central technical departments.

## This report

Progress from October 2000 to September 2001 is reported. For more information please contact the programme management or the responsible scientists.

Our website www.fzk.de/fusion may help to give further access to our work.


J.E. Vetter

# Contents                                                                    Page

**Preface**

**EFDA Technology Programme**

# EFDA Technology Programme

# Heating and Current Drive

**G 55 TT 07**
**Ceramics for Heating and Current Drive, and Diagnostics Systems: Irradiation Effects**

**1. Introduction**

In electron cyclotron wave systems for heating and current drive (ECH-CD) and for plasma diagnostics, special window structures have to fulfil vacuum operation and tritium retention requirements with ideally broadband transmission and low power absorption. Actual window materials, which are CVD diamond for high power transmission and fused silica for broadband transmission, imply a potential use over a wider spectral range reaching from DC/RF applications to optical systems.

For material performance analysis, the physical data base is well established for CVD diamond by previous work in this task. This is especially true for dielectric loss at EC wave frequencies as well as for thermal conductivity [1]. Accordingly a torus window demonstrator is now under high power evaluation ( see Task G55 TT 19). For silica materials, there is special focus on KU1 quartz glass which is provided by the Russian Federation within the ITER agreement as it has been shown to be highly radiation resistant with respect to its optical properties. Broadband electrical characterisation (DC to 145 GHz) is shared between CIEMAT and the Forschungszentrum to assess the possible use of the material for different diagnostic applications. Even though mechanical strength is a key performance parameter, the data base has still to be fixed. So while mechanical strength in fusion ceramics like alumina and SiC was investigated in experiments reaching dpa levels, for CVD diamond and fused silica, potential effects of neutron irradiation have to be quantified even at the $10^{-4}$ dpa level which is considered as a conservative testing condition for window materials.

**2. Dielectric properties of KU1 glass**

In the microwave range, the temperature dependence of the as-received material was investigated in cooperation with CIEMAT at 15 and 145 GHz [2] to evaluate possible risks for operation under thermal loads. Quite different behaviour was found. At 15 GHz a very strong decrease in loss by more than one order of magnitude was observed on increasing temperature from -180°C to 220°C which helps to prevent thermal runaway. But at 145 GHz only a slight decrease (1.7 to $1.2 \cdot 10^{-3}$) was measured from RT to 100°C. There is evidence that at 145 GHz the loss reaches a broad local maximum between 200 and 250K suggesting that a dielectric loss peak may be present near this frequency. The weak negative slope in the temperature dependence of tan$\delta$ was also observed for RT-450°C in the reference silica grade Infrasil 301 even though at considerably low loss level ( factor of 4) [3].

Two KU1 discs were irradiated up to $10^{21}$ n/m$^2$ (E>0.1MeV) at 50°C. The results achieved with the combined dielectric test facilities are given in Fig.1 in comparison to a control specimen. In the region of lowest loss, 100 kHz to 100 MHz, a slight increase is observed, but the loss remains below $10^{-4}$. Above about 60 MHz the loss tangent values obtained indicate no permanent effect from the neutron irradiation.

**3. Mechanical strength of CVD diamond and quartz glass**

The mechanical strength studies were focused on the aspect of spontaneous crack growth and targeted at clarifying a potential permanent radiation effect induced by structural damage at $10^{21}$ n/m$^2$ (E>0.1MeV). Applying a biaxial

mechanical test method (ball-on-ring test), the influence of specimen machining could be kept under close control. Special considerations were given to the push speeds, which were set to 25 µm/s, which could be considered to be fast enough to avoid possible systematic strength reductions by subcritical crack growth phenomena.
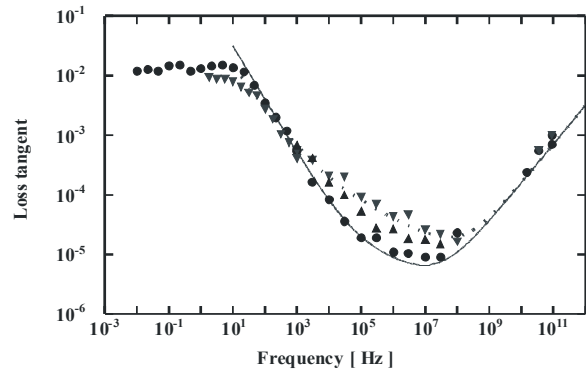


Fig. 1: The loss tangent of unirradiated (circles) and neutron-irradiated (to $10^{21}$ n/m$^2$) KU1 (up and down triangles). [2]

For the destructive strength studies, CVD diamond specimens were acquired which were laser-cut at FhG-IAF (Freiburg, D) as 11 mm disks out of typical window sized disks grown by the 'Ellipsoidal Reactor' approach. The median strength values of the neutron-irradiated specimens from all three windows group between 400 MPa and 440 MPa. Even though the various model windows covered a significantly wide thickness range (0.9 – 1.5 mm), no systematic thickness dependence was found. The values obtained agree well with values extrapolated into this range using the results for unirradiated thinner discs which imply a range of 370 – 450 MPa. This assessment is clearly corroborated by the mean strength values obtained with the control specimens from the 2.5" windows which group at 380 MPa. There is a startling difference observed for the control specimens from the 4" window which show a larger average strength (475 MPa). This set produced also a much larger scatter than described by a Weibull modulus m ranging around 20, which holds for all other specimen sets. These inconsistent results can be interpreted as an indirect evidence for particularly grown-in stresses during the growth of this special large window.

Strength studies with KU1 specimens were persued together with sets from another typical high purity grade (Infrasil 301). The tests reported last year for unirradiated Infrasil document a pronounced variation of the strength properties with the surface quality. This is important as KU1 specimens with a sufficient parallelism were only achieved with machining tools standardly used for ceramics, as they had to be cut from rods.

Therefore the high levels of the median strength (300 MPa) found for Infrasil with the as-received optical quality and the strength reduction after irradiation to $10^{21}$ n/m$^2$ (250 MPa) - which is likely to fall within the variability inherent to external handling - was not suited to compare with the KU1 results. Rather the results obtained (cf. Fig. 2) group perfectly around the median strength values of the abraded surfaces in Infrasil (124 MPa). The neutron-irradiated specimens show some smaller strength (111 MPa) and larger scatter which, however, in the light of the observations made with the Infrasil specimens only hint at a less homogeneous surface quality. This also implies that the slightly larger mean values obtained for the few control specimens fall within the uncertainties of the sampling. From the typical Weibull modulus around 10, a safety factor for surface

scaling and tolerable failure probability can be estimated [4]. For a factor of 2.5, the critical stress value reaches the typical strength specifications (60-65 MPa) given by commercial producers of high purity silica grades.
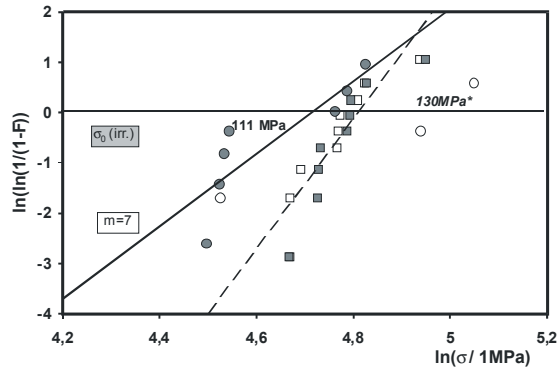


Fig. 2:    Weibull analysis of the critical strength measured for disks of KU1 with machined surfaces. The data are given for neutron-irradiated specimens ( full circles ), unirradiated control specimens ( open circles ) and for comparison for irradiated / unirradiated Infrasil 301 with abraded surface (full / open squares) [4]

Staff:

M. Blumhofer
R. Heidinger
A. Meier
M. Rohde
P. Severloh

Literature:

[1] R. Heidinger, M. Rohde, R. Spörl, Neutron irradiation studies on window materials for EC wave systems, Fusion Engineering and Design, in press

[2] R. Vila, J. Molla, R. Heidinger, A. Moroño, and E.R. Hodgson, Electrical and dielectric properties of irradiated KU1 quartz glass from DC to 145 GHz, Proc. ICFRM-10, Baden-Baden (D), October 2001

[3] R. Heidinger, A. Meier, J. Burbach, R. Schwab, R. Spörl, Dielectric property measurements at elevated temperatures based on open resonators, Proc. 11th Conf. + Exh. on Microwaves, Radio Communication, and Electromagnetic Compatibility (MIOP), Stuttgart (D), 8-10/5/2001,
ISBN 3-924651-4,pp .186-190

[4] R. Heidinger, Mechanical strength of neutron irradiated window materials, Proc. ICFRM-10, Baden-Baden (D), October 2001

# G 55 TT 19 EU
# ITER ECRF Window Development

## 1. Introduction

To satisfy the electrical, thermomechanical and nuclear requirements in continuous wave (CW) operation millimeter wave vacuum windows for electron cyclotron heating in thermonuclear plasma fusion energy research, water-edge-cooled window assemblies using large synthesized diamond disks have been developed in Europe, Japan, Russia and the USA. The diamond employed in these studies has been manufactured predominantly at DeBeers Industrial Diamond Division (UK) Ltd. by microwave plasma assisted chemical vapor deposition (MPACVD) and consists of polycrystalline diamond disks with diameter and thickness up to 119 mm and 2.23 mm, respectively. Due to low mm-wave losses (tan δ = 2-3x$10^{-5}$), outstanding thermal conductivity ($\approx$ 1800 W/mK), good ultimate bending strength (400 MPa) and radiation tolerance up to a neutron fluence of $10^{20}$ n/m$^2$ ($10^{-5}$ dpa), water-edge-cooled MPACVD-diamond windows promise to provide a practical technical solution for the transmission of CW millimeter waves at power levels in excess of 1 MW [1-4].

## 2. 1 MW, 170 GHz, CW CVD-Díamond Gyrotron Window

A new CVD-diamond disk has been purchased by the EU-Home Team and a new window unit (disk diameter 106 mm, thickness 1.852 mm, aperture 88 mm) has been manufactured in collaboration with the RF-Home Team and has been characterized at low power levels. During these measurements a sag of the window disk (120-140 μm) has been observed which corresponds to a static stress of approximately 0.7 MPa. Nevertheless, in order to fulfil this ITER task in time, high power tests have been performed. The gyrotron was operated at 1 MW output power and 1.5 s pulse length with 50% efficiency. On 26.05.2001 the window was broken after a pulse length of 0.2 s. The crack pattern is characteristic of failure induced by homogeneous and biaxial stress and thus reveals that the static stress due to the bow of the window was too large. The fact that the sag after the crack is even larger (200 μm), indicates that it was introduced during the brazing to the waveguide cuffs.

A third CVD-diamond disk window unit does not show any sag (within the thickness and paralleslism tolerances). The high power tests are scheduled for late fall of this year.

## 3. 1 MW, 170 GHz, CW CVD-Diamond Torus Window

High power tests of the torus window unit with irradiated CVD-diamond disk were performed at JAERI, Japan. Though the diamond window housing was originally designed for use in a closed system with evacuated waveguides on both sides, this setup was first used with the waveguide on the load side removed. This made it possible to monitor visible effects and the temperature distribution on the window by a video-camera and an infrared-camera, respectively. The infrared-camera measurements indicated a temperature increase of the uncooled window center temperature of 19°C at a pulse length of 350 ms and a power level of 500 kW and a temperature increase of 33°C at a pulse length of 2 s and 300 kW microwave power, respectively. In addition, luminous light spots were found during the pulses, both visible with the IR- and video camera. The pulse length and beam power were limited due to arcing in the non-evacuated dummy load.

Measurements in the closed, evacuated setup allowed transmission of 0.58 MW beam power at a pulse length of 15 s. In this case the temperature of the cooling water was saturated at a temperature increase of 0.9°C, the measured temperature difference at the inconel cuffs was 27°C. In addition, transmission of 0.2 MW beam power at 132 s pulse length was demonstrated, resulting in a temperature increase of the cooling water of 0.29°C.

Using the above results, the loss tangent could be estimated to be 4.7·$10^{-5}$ which is in agreement with the low power characterization measurements [5].

The thermal conductivity - which was reduced to 850 W / mK by irradiation with neutron - must have been recovered during the brazing process (annealing effects) to about 1500 W / mK.

## 4. Window Unit for JET

As part of the JET-EP program conceptual designs of single and double disk window units have been performed both for quasi-optical transmission and for waveguide transmission. It was decided to use a double disk window mainly in order to fulfil the safety rules for tritium operation. A disk with a thickness of 2.22 mm allows both transmission without reflections at 113.3 GHz (4λ/2) and at 170 GHz (6λ/2). The distance between the disks is 95.24 mm which results in a transmission bandwidth (1% reflection) of 1.9 GHz. For a loss tangent of 2 · $10^{-5}$ the absorbed power per disk is 340 W. According to numerical simulations steady state conditions are achieved in about 4 s. For the nominal RF-power of 1 MW the peak temperature at the center of the disk is estimated to rise by about 32°C above the temperature of the cooling water. For cooling a water flow rate of about 13 l/min is needed. The moderate value of the absorbed power in a disk allows cooling of all six window units (needed for 5 MW RF power) in series by one cooling circuit.

On each side of the window unit (gyrotron and torus side) arc detectors are foreseen. Since the CVD-diamond disks are sufficiently transparent arcs between the disks are also detectable. However, in the space between the disks microwave induced arcs are very improbable because of the clean and ultra high vacuum conditions.

Good vacuum conditions with p $\cong$ $10^{-6}$ Pa are expected to be achievable within the interspace since the total volume between the two window disks is small and the window units can be baked out. For the pumping of the whole window block (6 units) a single ion getter pump with a pumping efficiency of about 50 liters/s has been estimated to be sufficient. Radiation of some microwave power through the pumping tubes into the ion getter pump is suppressed (by about 20 dB) due to a slit arrangement at the wall of the transmission waveguide inside the window unit. This slit arrangement has a sufficiently large pumping impedance of about 4 liters/s. Any failure of a window should be detectable as a pressure rise at the ion pump even if a vacuum of about $10^{-3}$ Pa is present on opposing surfaces.

Staff:

A. Arnold (Uni Karlsruhe)
H.J. Burbach
G. Dammertz
R. Heidinger
S. Illy
A. Meier
B. Piosczyk
M. Rohde
P. Severloh
M. Thumm

Literature:

[1] R. Heidinger, A. Meier, M. Thumm, A. Arnold, "MPACVD diamond disks characterised as window components for megawatt gyrotrons", Proc. 9th Int. Conf. Displays and Vakuum Electronics, Garmisch-Partenkirchen, 2001, pp. 357-362.

[2] M. Thumm, "MPACVD-diamond windows for high-power on long-pulse millimeter wave transmission", Diamonds and Related Materials 10, 2001, pp. 1692-1699.

[3] M. Thumm, A. Arnold, R. Heidinger, M. Rohde, R. Schwab, R. Spoerl, "Status report on CVD-diamond window development for high power ECRH", Fus. Eng. Design, 53, 2001, pp. 517-524.

[4] R. Heidinger, M. Rohde, R. Spörl, "Neutron irradiation studies on window materials for EC wave systems", Fusion Engineering and Design, in press.

[5] R. Heidinger, A. Meier, M. Thumm, "Dielectric loss studies in diamond window components for Megawatt gyrotrons", Proc. 2nd IEEE Int. Vacuum Electronics Conf. ( IVEC 2001), ESA-Report WPP-189, Noordwijk (NL), pp. 227-230.

# G 55 TT 22 EU
## ITER ECRF Advanced Source Development

Millimeter waves in the frequency range between 90 and 170 GHz can be used with great advantage for heating and controlling of instabilities in magnetically confined plasmas of thermonuclear fusion devices. At present gyrotrons with an output power of 1 MW and a frequency of about 140 GHz are close to become state of the art even for long pulse operation up to CW [1].

For fusion experiments of the next generation such as the International Thermonuclear Experimental Reactor (ITER), it is estimated that a microwave power up to 40 MW at 170 GHz operated almost in CW will be needed. To reduce the costs of the installations of the electron cyclotron wave (ECW) system an increase of the output power per unit to about 2 MW is desired. Coaxial cavity gyrotrons have the potential to fulfill this requirement. The experimental results achieved at FZK recently on coaxial cavity gyrotrons, have demonstrated the feasibility for a technical realization of a 2 MW, CW, 170 GHz coaxial cavity gyrotron [2-10].

In particular the following results have been achieved:

- A microwave output power up to 2.2 MW at 165 GHz has been generated stably in short pulse (ms) operation with an efficiency of 28%. In operation with a single-stage depressed collector the efficiency of 30% has been increased up to 48% at 1.5 MW (nominal output power). In single pulses the pulse duration has been extended up to 9 ms at $I_b$ = 50 A. A further extension of the pulse length toward 100 ms is foreseen.
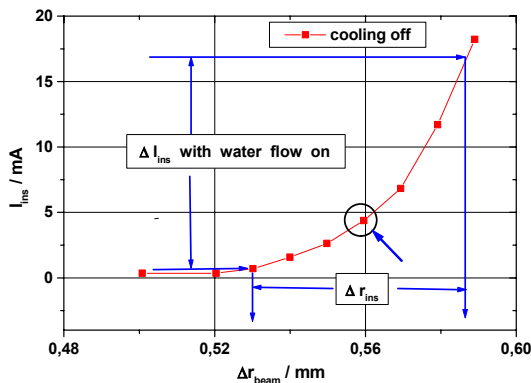


Fig. 1: Mechanical vibration of the coaxial insert under operating conditions. The marked point indicates the position before turning on the water flow

- The mechanical stability of the coaxial insert is a crucial issue for stable long pulse and CW operation of coaxial gyrotrons. Therefore , the effect of mechanical vibrations of the insert have been simulated under operating conditions. The electron beam was radially displaced inside the cavity with the help of the magnetic dipole coils until the beam touched the coaxial insert. The current to the insert $I_{ins}$ depends on the amount of the radial displacement $\Delta r_{beam}$. The results are shown in Fig. 1. The measurements were performed in the following way. First, $I_{ins}$ vs. $\Delta r_{beam}$ was measured when the cooling water was turned off and the level of mechanical vibrations was very low (measured points in Fig. 1). When the water flow was turned on, the current $I_{ins}$ varied within a certain range $\Delta I_{ins}$ (indicated in the figure) because of the vibration of the insert. From $\Delta I_{ins}$, the maximum amplitude of the mechanical vibration is estimated to be within $\pm$ 0.03 mm. The main source of mechanical vibrations is the flow of

the cooling water. The measured mechanical amplitude is sufficiently low to allow a stable long pulse operation.

- The losses at the coaxial insert have been measured calorimetrically to be 0.1% of the RF output power (Fig. 2). This value which is about twice as large as the calculated RF losses will probably not cause technical problems even in CW operation. The increased losses are expected to be due to heating by diffracted stray radiation inside the gyrotron.
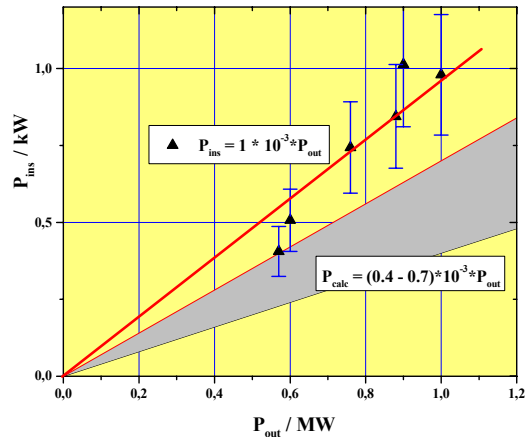


Fig. 2: Measured and calculated losses at the coaxial insert in dependence of the RF output power for the $TE_{31,17}$ mode

- The microwave stray radiation captured inside the gyrotron tube has been found to be distributed uniformly inside the mirror box. The amount of the lost stray microwave power has been found to be as large as ( 11 _+ 3%. In order to reduce this value, further design optimization of the RF output system will be performed. However, the uniform distribution of the captured microwave radiation inside the mirror box keeps the technical problems related to dissipation of $P_{stray}$ inside the tube under control, even for a 2 MW gyrotron. The insulating ceramic ring below the collector acts as an efficient relief window for the stray radiation. About 50 % of $P_{stray}$ are escaping through the ceramic ring and can be dissipated outside the tube.

- Fast (~ 0.1 ms) frequency tuning has been performed by applying a bias voltage to the coaxial insert. Step frequency tuning by $\pm$ 2.2 GHz between the nominal mode and the nearest azimuthal neighbors $TE_{31,16}$ (162.8 GHz) and $TE_{31,18}$ (167.2 GHz) as well as continuous frequency tuning up to 70 MHz within the bandwith has been demonstrated.

Staff:

J. Anderer (Uni Karlsruhe)
A. Arnold (Uni Karlsruhe)
H. Baumgärtner
E. Borie
H. Budig
G. Dammertz
O. Drumm (Uni Karlsruhe)
S. Illy
K. Koppenburg
H.-R. Kunkel
M. Kuntze
B. Piosczyk
J. Szczesny
M. Thumm
R. Vincon

Literature:

[1]  G. Dammertz, V. Erckmann, G. Gantenbein, W. Kasparek, H.P. Laqua, G. Müller, M. Thumm, "Electron Cyclotron Resonance Heating for the Stellarator W7-X, Proc. Jahrestagung Kerntechnik, Dresden, 2001, pp. 575-579.

[2]  B. Piosczyk, "A novel 4.5 MW - electron gun for a coaxial cavity gyrotron", IEEE Trans. Electron Devices, 2001, im Druck.

[3]  B. Piosczyk, A. Arnold, E. Borie, G. Dammertz, O. Drumm, O. Dumbrajs , S. Illy, M. Kuntze, K. Koppenburg and M. Thumm, "Development of Advanced High Power Gyrotrons at Forschungszentrum Karlsruhe", Frequenz 55(2001), pp. 242-246

[4]  O. Dumbrajs, P. Nikkola, B. Piosczyk, "On the negative-mass instability in gyrotrons", Int. Journal Electron, 2001, 88 (2): pp. 215-224

[5]  B. Piosczyk, A. Arnold, E. Borie, G. Dammertz, O. Drumm, O. Dumbrajs, S. Illy, M. Kuntze, K. Koppenburg, M. Schmid, M. Thumm, "Progress in the development of advanced high power gyrotrons", 2nd IEEE Int. Vacuum Electronics Conf., 2001, Noordwijk, Niederlande, pp. 327-330.

[6]  B. Piosczyk, A. Arnold, E. Borie, G. Dammertz, O. Drumm, O. Dumbrajs, S. Illy, M. Kuntze, K. Koppenburg, M. Schmid, M. Thumm, "Advanced high power gyrotrons for Fusion applications", Proc. 9th Int. Conf. Displays and Vacuum Electronics, Garmisch-Partenkirchen, 2001, pp. 149-152.

[7]  B. Piosczyk, "A 2.2 MW, CW collector for a coaxial cavity gyrotron.", 26th Inter. Conf. on Infrared and Millimeter Waves, Toulouse, F, September 10-14, 2001

[8]  B. Piosczyk, B.; A. Arnold, H. Budig, G. Dammertz, O. Drumm, O. Dumbrajs, M. Kuntze, M. Schmid, M. Thumm, "Towards a 170 GHz, 2 MW, CW coaxial cavity gyrotron. Experimental results and design considerations.", 26th Inter. Conf. on Infrared and Millimeter Waves, Toulouse, F, September 10-14, 2001

[9]  C. T. Iatrou, K. Avramides, J.L. Vomvorides and B. Piosczyk, "Design Considerations of Powerful, Second-Cyclotron-Harmonic Coaxial-Cavity Gyrotrons" 26th Inter. Conf. on Infrared and Millimeter Waves, Toulouse, F, September 10-14, 2001

[10]  O. Dumbrajs, B. Piosczyk, C.F. Iatrou, "Mode selection for a 2 MW, CW 170 GHz coaxial cavity gyrotron", 26th Inter. Conf. on Infrared and Millimeter Waves, Toulouse, F, September 10-14, 2001

# Plasma Facing Components

**T 436/01**
**Construction and Testing of Divertor Liner Components**

**Introduction**

In the linear plasma facility PSI-2 erosion of CFC material will be accomplished in deuterium and hydrogen discharges in order to study the migration and deposition of the produced hydrocarbon molecules and radicals ($CH_4$, $CH_3$, $C_2H_2$ etc.). For this purpose a special pumping duct arrangement (called "hot liner"), shown in Fig. 1, has been designed and manufactured. The generation of hydrocarbons is realized by the interaction of the plasma column with a graphite target, thus simulating the actual production process in fusion devices. Si-wafers designated to investigate the thickness of the coatings are located at different positions in the hot liner duct. They are supplemented by a mass spectrometer and cavities (Si-coated at the inner walls) allowing to determine the sticking coefficients. In particular the growth of amorphous hydrocarbon coatings as a function of distance to the source and the influence of the surface temperature (variable between 100 to 1000 °C) on the thickness by changing the sticking coefficient will be investigated.

**Results**

During October 2000 to Spring 2001 the mechanical components were fabricated by two companies. Unfortunately, several retreatments became necessary that had to be done in our workshop at IPP Berlin. Also the hot liner head, containing the quartz heaters as well as a number of components made from tungsten, molybdenum and BN-ceramics, was fabricated in our workshop because of the experience and special technologies required.

First experiments, using a sniffer-probe, have been performed to measure the hydrocarbon angle-distribution at the entrance of the hot liner duct and compared with modelling results. Furthermore, optical spectroscopy and mass spectrometry were used to determine the erosion rate and the total number of molecules in front of the heated graphite target. Part of the visible spectrum containing information on the concentration of CH-molecules is shown in Fig. 2. Extrapolating the additional $CH_4$ flux to zero allows to determine the original target flux. In this way a total flux of approximately $10^{18}$ s$^{-1}$ of C-atoms (in form of a variety of molecules) is inferred. A flux of this magnitude should be sufficient to produce detectable coatings in the hot liner structure within exposure times of less than a day. Monte Carlo calculations were also performed to model the complex situation within the hot liner head and to estimate the probability that amorphous coatings are formed.

**Planned activities**

The hot liner structure is completed and cleaned now; it will be mounted to the plasma generator PSI-2 within the next weeks. Experiments aiming to determine the thickness of coatings, the sticking coefficients, and the influence of the surface temperature will start in November.
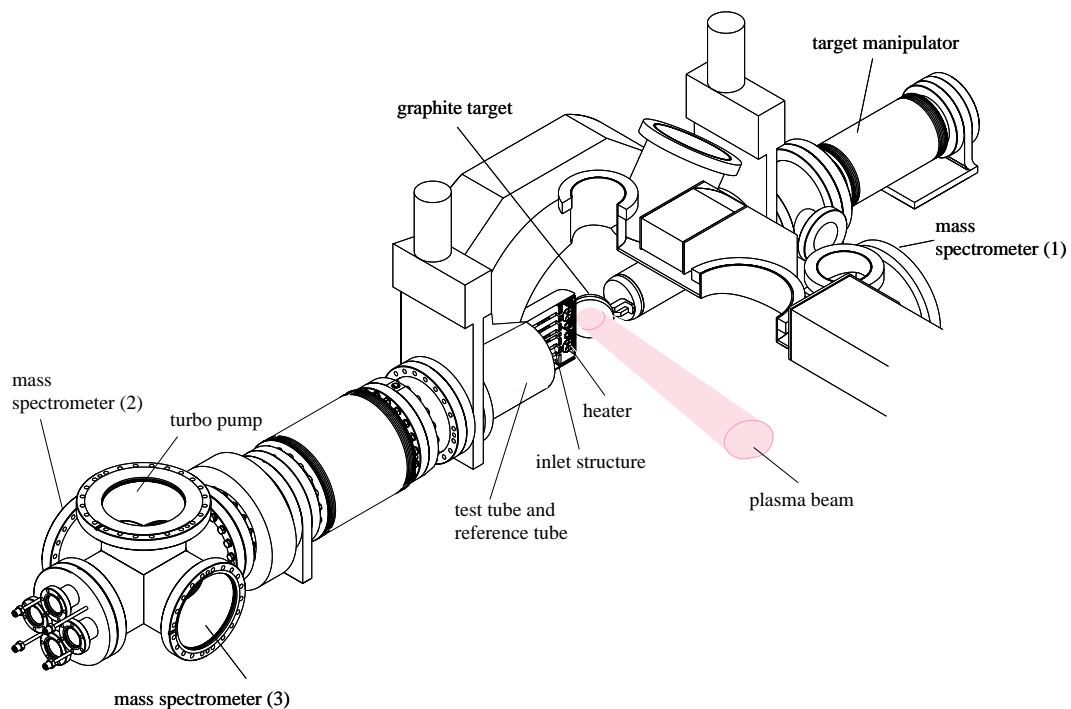


Fig. 1: Arrangement of the "hot liner" experiment. A graphite target acting as a source of hydrocarbons is fixed in the centre plasma region of PSI-2. The molecules escaping from the plasma enter the hot liner duct. The latter consists of two identical channels one with aheated head structure, the other (reference channel) is kept at room temperature
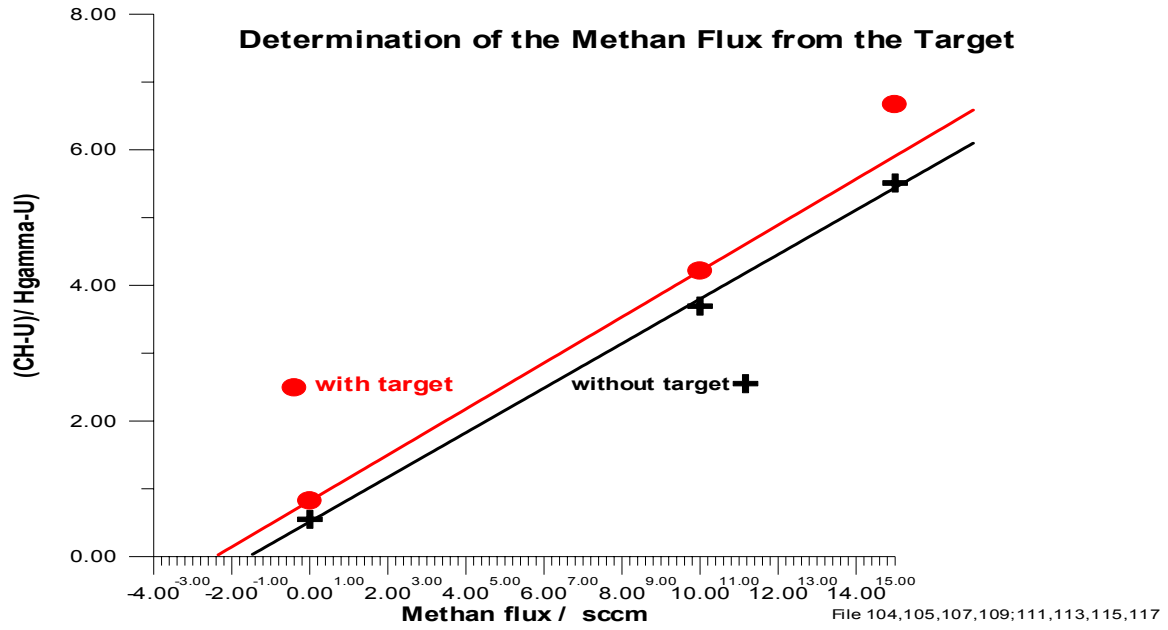
Fig. 2: Intensity of the CH-band at $\lambda$ = 430 nm normalized to $H_\alpha$ with and without the graphite target exposed to the plasma. An additional injection of methane causes a linear increase of the CH photon flux

<u>Staff:</u>

<u>G. Fussmann</u>[1]
D. Naujoks[1]
W. Bohmeyer[1]
Ch.Wu[2]

[1]IPP Berlin
[2]EFDA Garching

First results of modelling and the mentioned pre-experiments were presented at an EFDA meeting in Garching at 22.10.2001

## T 438/01
## Time-resolved Speckle-Diagnostics

The Speckle-Interferometry is a well known technique for measuring contours and deformations of technical surfaces at a high precision. If a surface is irradiated by coherent light, a speckle pattern appears. In an interferometer, this speckle pattern is superposed by an homogeneous reference beam in order to modulate the intensity of the speckles, depending on the relative phase between the reference light and the scattered light reflected from the surface.

One major disadvantage of interferometric measurements in general is the enormous susceptibility of the whole setup to vibrations during and between several exposures. For this reason, we developed an interferometer which is capable of recording all necessary data simultaneously during one laser shot. Thus a measurement of moving or vibrating objects becomes possible.

In most interferometers the measurement object has to be included in the setup itself. Such a kind of setup is not capable to investigate different areas of large and fixed objects like for example the inner wall of a fusion reactor. Therefore the aim was the developement of a dynamic sensor-head which is separated from all bulky parts like powerful laser-sources and PCs.

### Spatial Phase-Shifting

The intensity of a single spot $(x, y)$ in an interferogram is calculated by:

$$I_{(x,y)} = I_{0(x,y)} \cdot \left(1 + \gamma_{(x,y)} \cdot \cos\left(\varphi_{(x,y)}\right)\right) \qquad (1)$$

where $I_{0(x,y)}$ is the visibility, $\gamma_{(x,y)}$ is the modulation and $\varphi_{(x,y)}$ is the phase. These three unknown factors require a set of at least three equations to calculate the interesting factor, the phase $\varphi_{(x,y)}$. For obtaining this set of equations an additional well known phase $\Delta\varphi_{(x,y)}$ is produced at least two times. This is called 'phase-shifting'. It is possible to change the length of one complete optical path in the interferometer between several recordings of the interferogram. Another way of recording several phase data of each speckle is the so called 'spatial phase-shifting' where these data are produced simultaneously at different locations. This is the only possibility to carry out a measurement in vibrating environments. Therefore a new procedure for spatial phase-shifting was developed which does not require any additional components in the setup. This method utilises small phase differences of beams passing a lens adjacently.

### Multiline Interferometer

The contour measurement of a technical surface requires two single interferograms of different wavelengths. The sensitivity of this kind of measurement depends on the so called synthetic wavelength $\lambda_{synth}$ which can be calculated out of the two single wavelengths $\lambda_1$ and $\lambda_2$ and the angle $\Theta$ between surface and direction of observation as can be seen in equation (2):

$$\lambda_{synth} = \frac{\lambda_1 \cdot \lambda_2}{2 \cdot \left|\left(\lambda_1 - \lambda_2\right)\right| \cdot \cos\Theta} \qquad (2)$$

As well as it is necessary to obtain all phase data simultaneously it is also essential to get the two wavelength data at the same time. For these purposes the interferometer is supplied with several wavelengths at the same time. The two superposed interferograms are separated by interference filters situated in front of two cameras recording exactly the same image. (See Fig. 1). A superposition of different wavelengths of a coherent multiline Ar - ion laser is passed to the setup by an optical fiber as can be seen at the bottom left of Fig. 1. This multiline beam is devided in an reference beam and an object beam by beam-splitter 1. These two beams are expanded separately in order to be able to vary the illuminated area on the measurement object without influencing the reference beam. The object beam is passed to the measurement object by two mirrors. The surface of the object is imaged by a system of two lenses which operate as a zoom objective and allow to vary both measurement distance and area. The scattered light from the surface is superposed by the reference beam by beam splitter 2. With beam splitter 3, the emerging interferogram is directed to two separate cameras. An optical bandpass-filter in front of each camera selects one single wavelength in each case. Thus it is possible to record two interferograms of different wavelengths simultaneously.
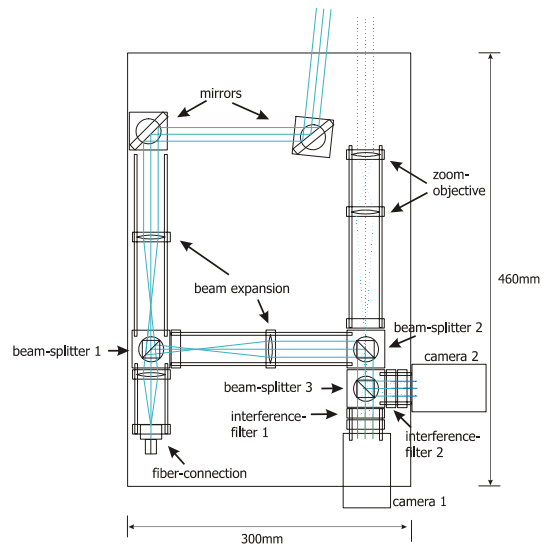


Fig. 1: Sensor-Head

The complete interferometer is integrated in a dynamic sensorhead separated both from the laser-source and from the PC. Fig. 2 shows some results of a measurement with this sensor head.



| (a) | (b) |
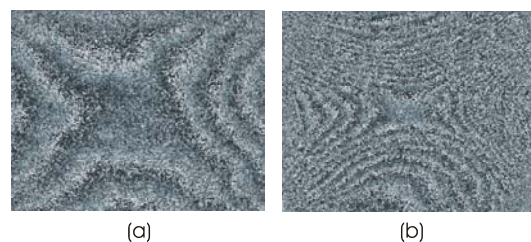
Fig. 2: Two results of measurements of a saddle like contour on an aluminium plate; $\lambda_{synth}$ = 14,25 µm;
(a): measurement area: 4 mm x 3 mm
(b): measurement area: 16 mm x 12 mm

Staff:

A. Koch
P. Evanschitzky
A. Meixner

Technische Universität München
Lehrstuhl für Messsystem- und Sensortechnik

## T 438/03
## Electrical Breakdown and Arcing in ITER

In the framework of ITER task 438 electrical breakdown and arcing in deuterium has been investigated in model experiments to obtain data on the voltage strength of ITER components in dependence on the material and the orientation of the magnetic field. The magnetic flux density amounted to 0.4 T. The following effects have been found:

(i)  At application of the voltage a glow discharge is ignited followed by a transition to an arc. The latter is characterized by the appearance of electrode spots.

(ii) At pressures p<10 mbar and gap distances d<10 mm the inception voltage of the glow discharge increases with decreasing product pd, thus, it obeys the left branch of the Paschen curve [1].

(iii) With transversal magnetic field the voltage needed for the transition from glow to arc (=breakdown voltage) increases with decreasing p but increases with increasing d, thus it deviates from the Paschen law.

(iv) The inception voltages depend strongly on material and conditioning of the electrodes.

(v) Arcing leads to considerable incorporation of deuterium into the electrodes. This has been established by thermodesorption.

Figure 1 shows for graphite electrodes the increase of the breakdown voltage with gap distance in a transverse magnetic field (effect iii).

about $5 \times 10^{21}$ and $10^{21}$ deuterium atoms per mbar and $m^2$ electrode surface for cathode and anode, respectively.

The results lead to the following conclusions:

(1)  At pressures <1 mbar the breakdown voltage is >1 kV.

(2)  For electrically stressed components, it is favorable to use Si-doped CFC or heated molybdenum.

(3)  At locations with $E \perp B$ it is favorable to increase the gap distance.

(4)  If arcing occurs, considerable amounts of gas can be trapped, especially in the cathode.

Staff:

B. Jüttner
J. Rossignol
W. Schneider

Literature:

[1]  Yu. P. Raizer, Gas Discharge Physics, Springer Berlin, 1991.

[2]  M. Akbi, D. Hildebrandt, B. Jüttner, I. Kleberg, and W. Schneider, "Deuterium Trapping in Divertor Tiles at ASDRX-Upgrade", Report IPP 8/15, October 1998.

Fig. 1:   Dependence of the breakdown voltage on the gap distance measured in several runs

Table 1 summarises the voltage for 50% ignition probability at a pressure of 12 mbar and a gap distance of 1 mm, demonstrating the effects (i)-(iv). The electrodes consist of half-spheres with diameter of 10 mm and made of graphite, CFC and CFC doped with Si. Furthermore, a Mo-electrode has been used made from a wire with 0.85 mm diameter in form of a hairpin and heated to 1100 K.. While breakdown was possible at room temperature, the applied voltage did not suffice for breakdown with the hot electrode.

The amount of trapped deuterium during the arcing phase has been found to be proportional to the current-time integral of the arcs [2]. Assuming additionally a proportionality to the working pressure, thermodesorption of the graphite electrodes yielded

Table 1:   Summary of voltage data at 12 mbar

| Material | Configu-ration | Discharge Type | Ignition Voltage (V) | Remarks |
|---|---|---|---|---|
| Graphite (EK 98) | E ⊥ B | GLOW | 600 ±50 | Voltage decreases with increasing p; does not depend on d |
| | | ARC | 750 ±50 | Voltage decreases with increasing p; increases with increasing d |
| | E II B | GLOW | 450 ±50 | Voltage decreases with increasing p; does not depend on d |
| | | ARC | 800 ±200 | Not enough data |
| CFC | E ⊥ B | GLOW | 600 ±50 | Voltage decreases with increasing p; does not depend on d |
| | | ARC | >1000 | Higher voltage needed |
| CFC+Si | E ⊥ B | GLOW | 600 ±50 | Voltage decreases with increasing p; does not depend on d |
| | | ARC | >1200 | Higher voltage needed |
| Mo hot | E ⊥ B | GLOW | 600 ±50 | |
| | | ARC | >1200 | Higher voltage needed |

**T 438/06**
# Chemical Reactivity of Dust and Flakes and D-Mobilisation Experiments from Co-deposited Layers

## 1. Introduction

Evaluation of the safety hazards for advanced tokamaks includes an assessment of the failures of plasma-facing-component (PFC) materials due to accident scenarios, e.g. a loss of coolant accident (LOCA) that injects steam into the torus vacuum vessel. Steam ingress can generate substantial quantities of hydrogen via steam interactions with the proposed PFC materials. Assessment of such LOCAs typically requires experimentally-derived chemical reactivity data for the PFC materials [1]. Measurements for carbon-fiber-composites (CFC) NS31 and NB31 [2], tungsten alloy W-1%La, and DShG-200 beryllium were performed. More comprehensive details concerning this research are found in References [3-5].

## 2. Experimental Details

### 2.1 Sample description and characterization

NS31 and NB31 [2] are advanced 3D carbon fiber composites that have been developed by S.E.P. (Société Européenne de Propulsion) and Dunlop for high thermal conductivity applications. NS31 is produced similarly to NB31 except it includes a final infiltration of liquid silicon resulting in a product with higher density and lower porosity. For our steam oxidation experiments, samples with nominal dimensions (25-mm long by 8-mm wide by 3 to 4-mm thick) were cut from blocks of each CFC. Based on mass and dimensional measurements we computed average densities of 2.13 g/cc(+/- 2%) for NS31 and 1.96 g/cc(+/- 1%) for NB31. Densities of 2.13 g/cc(+/- 0.7%) for NS31 and 1.95 g/cc(+/-0.6%) for NB31 were obtained from water immersion density measurements. Open porosity values of (1.8 +/- 0.4) % for NS31 and (6.2 +/-0.4) % for NB31 were also derived from the immersion density measurements. BET specific surface areas [14] were measured for each CFC test sample using a Kr gas adsorption technique. We obtained BET specific surface areas of 0.15 $m^2$/g (+/-14%) for NS31 and 0.15 $m^2$/g (+/- 7%) for NB31. For each CFC test sample, the BET surface area was ~330 times the geometric surface area. Optical and scanning electron microscopy and energy-dispersive X-ray spectrometry measurements revealed that the microstructures of NS31 and NB31 CFC were similar except for one major difference. Voids and substantial porosity were observed in NB31, whereas, the porosity of NS31 was filled with Si, a fraction of which was converted to SiC during processing at elevated temperatures. However, micro-cracks along material interfaces were still present in the NS31 material.

Tungsten alloy specimens with nominal dimensions (12-mm long by 10-mm wide by 5-mm thick) were cut from a block of W-1%La tungsten alloy (includes 1-wt% $La_2O_3$) fabricated by Plansee for ITER applications. Final sample surface finish was established by mechanical polishing with 600-grit sandpaper. Based on mass and dimensional measurements, we obtained an average density of 18.8 g/cc (+/- 0.7%) for the W-1%La material.

DShG-200 Be samples with nominal dimensions (12-mm long by 12-mm wide by 5-mm thick were tested. Based on mass and dimensional measurements, we computed an average density of 1.84 g/cc (+/- 0.3%) indicating that the Be was essentially fully dense.

### 2.2 Steam oxidation experimental system

Chemical reactivity experiments were conducted with a system comprising a steam generator, a quartz reaction chamber surrounded by a tube furnace, steam condensers, in-line cryotrap, gas analysis instrumentation and an ethylene glycol trap at the terminus of the process line [12,13]. Steam (2500 std-cc/min, 0.84 atm), introduced upstream from the sample furnace, reacted with the hot specimen inside the quartz reaction chamber and was condensed downstream from the sample furnace. Argon carrier gas (100 std-cc/min, 0.84 atm) was used to sweep reaction gases from the hot sample reaction chamber through the process line for on line measurements with a mass spectrometer. In these experiments, oxidation kinetics were tracked by measurements of $H_2$, CO, and $CO_2$ concentrations in the Ar carrier gas. Total quantities of the reaction gases were computed by integrating the mass spectrometer data. Average generation rates for each reaction gas were derived as the total gas quantity generated divided by the steam exposure time and the initial geometric surface area for the sample. A micro-balance with a precision of 0.1 mg was used to measure the specimen mass before and after testing. These weight-change measurements provided a second approach to obtain the total quantities of reaction gases generated in experiments for Be and CFC samples. Weight change measurements could not be used for this purpose in tungsten experiments because of weight loss from mobilization of volatile tungsten oxides.

## 3. Measurements and Results

### 3.1 CFC material

Chemical reactivity experiments were performed for the NS31 and NB31 CFC samples exposed to steam at temperatures from 800 to 1100°C. The weight-loss and mass-spectrometry data provided a good correspondence between the average carbon reaction rates at different test temperatures and the corresponding average generation rates for $H_2$, CO and $CO_2$ [3]. Average hydrogen generation rates are compared in Arrhenius plots in Figure 1 for NS31 and NB31. The results are also compared to previous measurements [6,7] for GraphNOL N3M graphite tested at 1000 to 1700°C and three different CFCs (Dunlop, FMI-HDFG, FMI-4D) tested at 1100 and 1300°C. The Arrhenius expressions were derived from least-squares fits to the data {Rate1 and Rate 2 for N3M, Rate3 for NS31 and Rate4 for NB31}. Units for the pre-exponentials are liters/$m^2$-s and the activation energy is in calories/mole. Activation energies for Rate2, Rate3, and Rate4 are consistent a value of ~70 kcal/mole indicative of chemical reactivity throughout the porous carbon samples [15, 16].

We observe slight differences in the temperature dependence of the average hydrogen generation rates for NS31 and NB31. The higher rate for NS31 at 800°C could be due to oxidation of the Si that was introduced into the porosity during material processing. For test temperatures of 1000 and 1100ºC, the $H_2$ generation rates for NB31 were about a factor of 2 higher than those for NS31. This trend toward reduced oxidation for NS31 at high temperatures could be due to the influence of reduced porosity and $SiO_2$ formation in NS31, factors that could affect mass transport and diffusion of the steam and the gaseous reaction products.

At 1100 °C, $H_2$ generation rates for NS31 and NB31 were much less than data for DUNLOP, FMI HDFG and FMI 4D CFCs. Extrapolation of the NS31 and NB31 data to higher temperature was in reasonable agreement with the previous CFC measurements at 1300 °C. The differences in absolute $H_2$ generation rates for NS31 and NB31compared to the previous data are attributed to material property differences such as density and porosity and to differences in experimental test

conditions such as steam flow velocities and gas measurement techniques.
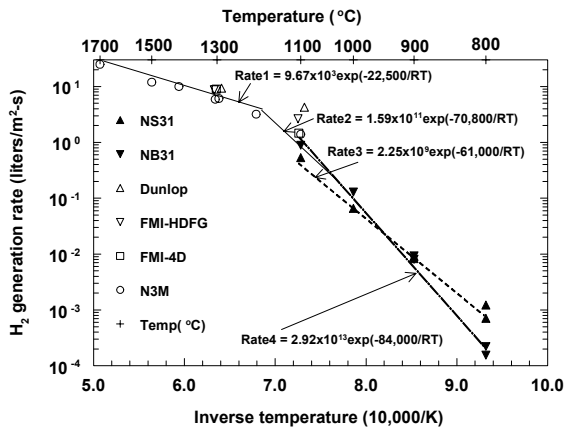


Fig. 1: Hydrogen generation from reaction of graphite with steam

### 3.2 Tungsten material

Chemical reactivity experiments were performed on the W-1%La samples exposed to steam at temperatures ranging from 550°C to 1000°C. Fig. 2 shows Arrhenius plots of the average $H_2$ generation rates for the W-1%La samples and compares these rates to previously published data for a 95% tungsten alloy [8] and tungsten welding rods with 1.5-wt% $La_2O_3$ [9]. The Arrhenius expressions were derived from least-squares fits to the different data sets, with identifications given in the figure legend. The W-1%La alloy data are in reasonable agreement with the 95% W alloy data (W95) and the W weld rod data (W1.5La) for temperatures above 650°C. Below 650°C, both the W-1%La and W-weld rod data are higher than the 95% W alloy data. We suspect that chemical reactivity for these materials at the lowest test temperatures is affected by differences in material composition and surfaces. Differences in experimental test conditions for the present experiments compared to the previous ones (e.g., steam flow rates, orientation and heating method for the test samples, gas measurement technique) could also contribute to the observed differences in the hydrogen generation rates.
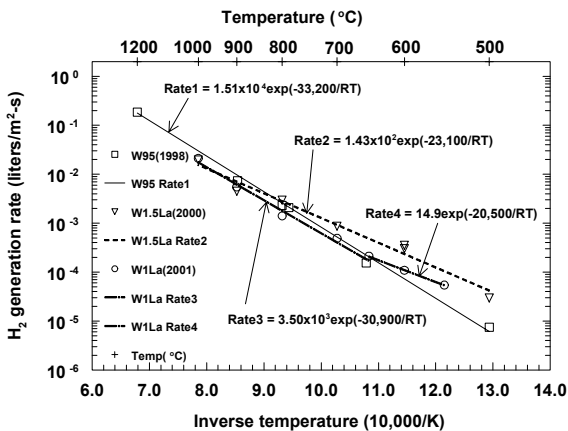


Fig. 2: Hydrogen generation from reaction of tungsten alloy with steam

### 3.3 Beryllium

Chemical reactivity experiments were performed on the DShG-200 Be samples exposed to steam at temperatures ranging from 500oC to 900oC. Essentially no H2 was observed during tests of DShG-200 Be at 500oC and 550oC. Our previous oxidation studies of Be in steam showed parabolic oxidation behavior for temperatures at and below 600°C. This oxidation behavior was very sensitive to the surface conditions of the samples. Therefore, we attribute the absence of a hydrogen signal at test temperatures of 500 and 550°C for DShG-200 Be to a protective, pre-oxidized surface layer that was protective in character. For test temperatures above 550°C, average H2 generation rates were derived from mass-spectrometer measurements and from mass-change measurements.

Fig. 3 shows Arrhenius plots of the average H2 generation rates (INEEL001-WG, -G) that were derived from the weight-gain (-WG) and mass-spectrometer gas (-G) measurements for the DShG-200 Be samples. These rates are compared to previously published data for fully-dense, consolidated powder metallurgy (CPM) Be, {(INEL92-WG, -G) [10], (INEL-96-WG1, -G1) and (INEL-96-WG2, -G2) [12,13], and (TRW65) [11]}. In general the data for DShG-200 Be are in good agreement with the results of the previous studies. Three Arrhenius expressions are given in the figure. These correspond to least-squares fits to the experimental data in three temperature regions: 1200 to 900°C, 830 to 600°C and 600 to 450°C. In the low temperature regime, the experimental data show considerable scatter primarily because the steam-reactivity behavior is parabolic and is very sensitive to the surface conditions of the samples. Because of this, the lowest data points at 600°C were excluded from the least-squares fit and the Rate1 expression provides a general trend for the average hydrogen generation rates below 600°C.
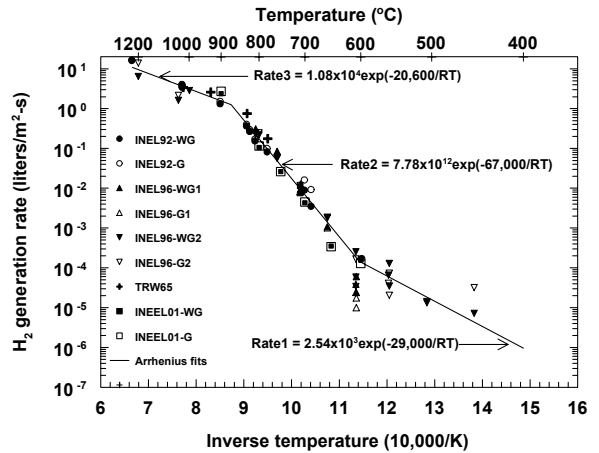


Fig. 3: Hydrogen generation from reaction of beryllium with steam

### 4. Conclusions

Hydrogen generation rate measurement for candidate PFC materials exposed to steam (NS31 and NB31 CFCs, W-1%La and DShG-200 Be) showed that:

Compared to NB31, NS31 was more resistant to steam oxidation at 1000 and 1100°C but was more reactive at 800°. These differences may be related to oxidation of Si in the porosity of NS31. The $H_2$ generation rate data for NS31 and NB31 are consistent with values computed by extrapolation of the measured rates for N3M graphite to 900°C.

$H_2$ generation rates for W-1%La were very consistent with previous steam oxidation measurements for a 95% W alloy at 600°C and higher. Below 600°C, the observed rates for W-1%La were higher than for W95 indicating the possible influence of differences in material composition, surface condition and experiment test conditions.

Measured $H_2$ generation rates for DShG-200 Be at temperatures from 600 and 900°C are in good agreement with many previous studies for CPM Be.

Arrhenius expressions derived from the steam oxidation results presented here are recommended for engineering safety analyses of advanced tokamaks.

Staff:

R. A. Anderl
D. Davydov
R. J. Pawelko
G. Piazza
G. R. Smolik

Literature:

[1]    M. J. Gaeta et al., Fusion Technology 32 (1997) 23.

[2]    J. P. Bonal, D. Moulinier, CEA Technical report DMT/95-495.

[3]    R. J. Pawelko, R. A. Anderl and G. R. Smolik, Physical characterization and steam chemical reactivity of carbon fiber composites, INEEL/EXT-01-00481, May, 2001.

[4]    R. J. Pawelko, R. A. Anderl and G. R. Smolik, Steam chemical reactivity of DSHG-200 Be and W-1%La$_2$O$_3$ Alloy, INEEL/EXT-01-00881, July, 2001.

[5]    R. A. Anderl and R. J. Pawelko, Steam chemical reactivity experiments for Be irradiated to low fluences, INEEL/EXT-2000-01353, October, 2000.

[6]    G. R. Smolik et al., Fusion Technology 19 (1991) 1342.

[7]    G. R. Smolik, B. J. Merrill, S. J. Piet and R. S. Wallace, Evaluation of graphite/steam interactions for ITER, EGG-FSP-9154, Fusion Safety Program, Idaho National Engineering Laboratory, September, 1990.

[8]    G. R. Smolik et al., J. Nucl. Mater. 258-263 (1998) 1979.

[9]    G. R. Smolik et al., Fusion Engineering and Design 54 (2001) 583.

[10]   G. R. Smolik et al., J. Nucl. Mater. 191-194 (1992) 153.

[11]    J. L. Blumenthal and M. J. Santy, An experimental investigation of the behavior of beryllium in simulated launch pad abort experiments, TRW Systems, contract no. 82-6211, Sandia Corporation Rep. SCDC-65-1637 (1965).

[12]   R. A. Anderl et al., Fusion Technology 30 (1996) 1435.

[13]   K. A. McCarthy et al., Fusion Engineering and Design 37 (1997) 543.

[14]   S. Brunauer et al., J. Amer. Chem. Soc. 60 (1938) 309.

[15]   P. L. Walker, Jr., F. Rusinko, Jr., and L. G. Austin, Gas reactions of carbon, Adv. Catal. 11 (1959) 133.

[16]   T. Uda et al., Fusion Engineering and Design 29 (1995) 238.

**T438/08**
**Effect of Plasma Interaction**

**1.   Introduction**

Sputtering, evaporation and macroscopic erosion are determining the lifetime of the "In Vessel" armour materials CFC, tungsten and beryllium presently under discussion for future tokamaks [1]. For CFC armour macroscopic erosion means brittle destruction and dust formation and for metallic armour melt layer erosion by melt motion and droplet splashing. Shielding of divertor armour materials by their own vapour exists during plasma disruptions [2,3]. The evolving plasma shield protects the armour from high heat loads, absorbs the incoming energy and reradiates it volumetrically thus reducing drastically the deposited energy. As a result, vertical target erosion by vaporization turns out to be of the order of a few microns per disruption event and macroscopic erosion becomes the dominating erosion source [4-6].

Dust, melt motion, droplet splashing and redeposited sputtered and evaporated FW and divertor armour material produce complex layers with considerable surface roughness and drastically reduced heat conductivity. ELMs when depositing their energy into such layers might enhance impurity production to unallowable levels because of increased heating of the hot spots. To prevent this the ELM energy in ELMy H-mode operation has to be limited in future tokamaks [7,8].

**2.   Brittle destruction and macroscopic erosion of graphite**

2.1 Experimental evidence for brittle destruction

High pulsed heat load experiments with volumetric heating at e-beam facilities clearly show the existence of brittle destruction of graphite and CFCs [9-10]. High heat load experiments with pulsed surface heat loads at plasma gun facilities and with quasistationary heating in tokamaks give some indications for brittle destruction of CFC [11,12]. A 2-D numerical simulation of brittle destruction and a simple estimation of macroscopic erosion based on a threshold value for the absorbed specific energy of 10 kJ/g for onset of this erosion [9] were performed. The absorbed energy is obtained from a solution of the 2-D heat conductivity equation with the 3 moving boundaries for evaporation, for melt front propagation and for brittle destruction. The velocity of the evaporation front is calculated using a nonsteady state model of surface evaporation based on a kinetic model of the vapour expansion inside of the Knudsen layer as described in [13]. The energy deposition of electrons is calculated by 3-D Monte Carlo [14.]. The 2-D numerical simulation of brittle destruction is based on modelling of the graphite lattice and calculation of cracking of intergranular bonds by thermal shocks [15]. Crack propagation into the depth of the sample produces individual open pits of large depth, when combining large macroscopic erosion might occur which determines the CFC armour lifetime.

Early erosion experiments using volumetric heating were performed for samples from fine grain graphite IG-430U and from CFC CX-2002U at the JEBIS facility [16]. The energy of the electrons impacting perpendicular onto the target was 100 keV, the moderate peak target heat load was .41 GW/m$^2$ and the heat load duration was up to 60 ms. Fig. 1a shows a comparison of measured and calculated peak erosion by evaporation for the CFC sample. In the calculations evaporation of up to 5 atomic carbon clusters are taken into account [17]. According to the calculation the absorbed energy at 60 ms reaches 9.2 kJ/g remains all the time below the threshold for brittle destruction and thus brittle destruction

is not occurring in agreement with the experimental results. For the calculation the realistic power density profile of the impacting electron beam was used. After exposure open pits were observed at the sample. However the pit density is not known. Fig. 1b shows a comparison of measured total erosion and calculated erosion by evaporation for the IG-430U sample with a smaller heat conductivity. The total erosion above 14 MJ/m$^2$ of absorbed energy due to onset of brittle destruction becomes larger than
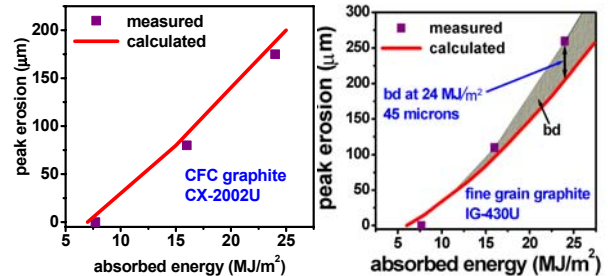


Fig. 1a.                         Fig. 1b

Comparison of measured total and calculated erosion by evaporation only for a CFC (a) and a IG-430U (b) sample at the e-beam facility JEBIS. Sample heating was with 100 keV electrons of peak power density of .41 GW/m$^2$

the calculated value for evaporation only. According to results from surface analysis the surface gets a rather large porosity indicating brittle destruction. The calculated temperature evolution in the bulk fine grain sample is shown in Fig. 2. Because of volumetric heating there is a temperature maximum inside of the sample where intense crack formation starts. The threshold value 10 kJ/g for onset of brittle destruction is reached after about 50 ms and due to crack propagation to the surface the overlaying layer is removed completely. According to the calculation macroscopic erosion contributes at 24 MJ/m$^2$ with 45 microns to the calculated total erosion of 260 microns which is in agreement with the measured value. The surface temperature as seen from Fig. 2 for 50 ms is above the sublimation temperature of 4000 K and even increases with time due to heat flowing from the temperature maximum to the surface. Due to the high surface temperature erosion is dominated by evaporation. With ongoing time the surface due to the moving evaporation front changes its position as can be seen from the temperature profiles.
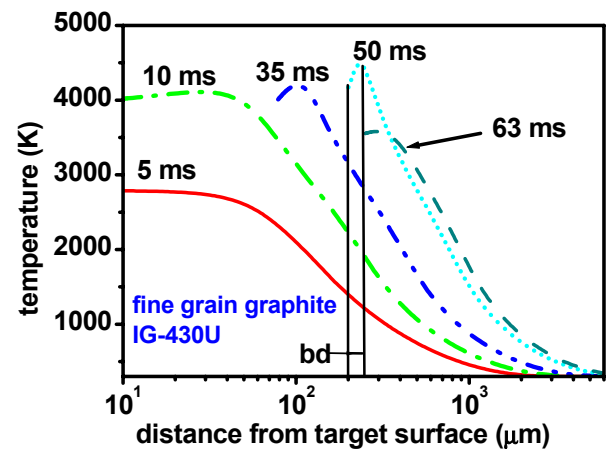


Fig. 2:   Calculated evolution of temperature profiles for the sample IG-430U under the heat load conditions of Fig.1a. At 50 ms macroscopic erosion occurs

Volumetric heating in a tokamak only occurs during run away electron impact. If CFC armour is exposed quite large macroscopic erosion occurs [7]. Hot plasma heating of the

armour is the dominating heating scenario in a tokamak and this is surface heating. In this case macroscopic erosion can only develop if intense crack formation starts at temperatures considerably below the sublimation temperature of 4000 K, because when reaching this value intense evaporation starts and this would dominate the erosion. For pulsed high surface heat loads typical for the thermal quench phase of a disruption the total external pressure from the impacting hot plasma and from the vapour cloud gets at least 5 bars thus shifting the start of the sublimation to temperatures above 4500 K [2]. In this case macroscopic erosion might be able to compete with evaporation. Cracks as the starting mechanism for brittle destruction because of propagation into the depth of the sample might accumulate under the surface for quasistationary and cyclic heat loads. Such a predamaging when occurring in the course of repetitive heating might result in a considerable reduction of the brittle destruction threshold and then macroscopic erosion will dominate erosion also for surface heating. Such a mechanism presently is under investigation for pulsed and quasistationary surface heat loads.

Cyclic surface heat load experiments are performed at the plasma gun facility in Troitsk [18].Fig.3 shows SEM images of a CFC sample before and after 40 exposures. The target was perpendicular to the impacting hot plasma. The deposited energy per exposure was 15 MJ/m2 ,the heat load duration was 30 us. After 40 shots rather large open pits of sizes up to a few hundred microns in width and depth covering about 4 % of the sample surface are to be seen. Extending the exposure up to 100 cycles resulted in an increase of the density of the open pits [18]. This might indicate an arising predamaging effect. However macroscopic erosion was not observed. This indicates that for such pulsed surface heat loads of rather short duration the damage threshold for brittle destruction remains high and evaporation is dominating as long as there is no degradation of material properties.
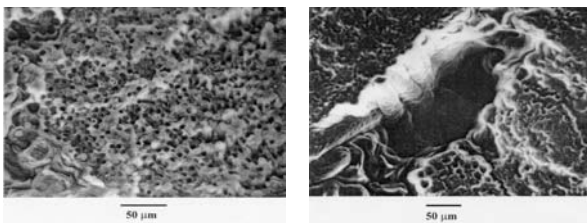


before exposure          after exposure

Fig. 3:  SEM images of the CFC sample SEP NB 31 unexposed and exposed to pulsed cyclic heat loads at the plasma gun facility MK 200 UG

Very few experimental indications of brittle destruction of graphite armour in tokamaks are also available. In D III-D a fine grain graphite sample was exposed to only one heat pulse with 50 MW/m$^2$ during .6 s simulating a leading edge [11] and in TEXTOR-94 a Si doped CFC limiter made from SEP NS31 was exposed to 26 shots with power loads of 12-14 MW/m$^2$ for 3 s [12]. In the DIII-D and the TEXTOR-94 samples rather large open pits with deepness up to 150 microns were observed. After 26 exposures, some of them ending in disruptions the TEXTOR sample showed a factor of 3.5 larger density of pits compared with the initial density [19]. Using the given heat loads the evolution of the surface temperature and of the absorbed energy was calculated. For the TEXTOR sample with a quasistationary heat load the calculated surface temperature reaches about 2600 K corresponding to less than 6 kJ/g of absorbed energy. This rather low threshold value might indicate that single pits are formed at positions where defects are existing in the sample. The observed large depth of the pits clearly demonstrates

crack propagation into the material what finally might result in rather large macroscopic erosion when single pits combine. Unfortunately erosion profiles were not measured and the exposure was not continued till a macroscopic crater was achieved.

2.2 Numerical simulation of brittle destruction

For understanding of open pit formation with crack propagation, for estimating the potential of sample predamaging and for quantification of macroscopic erosion under surface heat loads a 2-D numerical simulation model was developed [15]. Thermal stress in a heated graphite sample due to the anisotropic properties of graphite might result in breaking of intergranular lattice bonds. As a consequence of intense cracking macroscopic layers are destroyed and graphite dust is produced. Important for brittle destruction to occur are the anisotropy of the graphite grains, the failure stress distribution of the bonds connecting adjacent grains and the temperature and its gradient in the bulk material. Cracks preferentially are propagating into the depth of the sample rendering brittle destruction the potential for large macroscopic erosion. Therefore the analysis of brittle destruction is mandatory for a damage evaluation of CFC armour. Pores in the bulk are not considered presently. Annealing effects are modelled in such a way that the heat conductivity gets its original value when grains with broken bonds by thermal expansion are coming in contact again.

Hot plasma heating of the divertor armour during the thermal quench phase of a disruption causes erosion by evaporation. During the time duration of the pulsed heat load of typically 10 ms with heat loads up to a few GW/m$^2$ the vapour shield which is formed drastically reduces the effective target heat load and reduces erosion by evaporation to a few microns [2]. The effective heat load as calculated with FOREV-2 was used for a first numerical simulation of pit formation and crack propagation for surface heating. Because of lack of data the same failure stress values as for volumetric heating were used. To get a handable simulation problem the sample size used in the calculations was limited to a surface length of 2 mm and a thickness of .7 mm thus allowing to simulate a single pit. Fig. 4 shows the calculated evolution of such a pit for an initial peak target heat load of 3 GW/m$^2$. Between the pulses cooling down of the sample to its initial temperature was assumed. Brittle destruction forms an open pit and the sample shows crack propagation into the bulk as indicated by the thin black lines at the bottom of the pit. Due to this predamaging the depth of the open pit increases during the next pulses as is seen from Fig.4. Increasing the time duration of the heat pulse would increase the number of the pits and their depth.
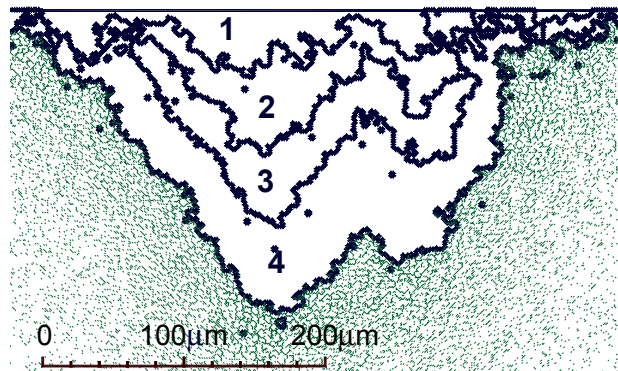


Fig. 4:  Results from numerical simulation of evolution of size and depth of a single pit under pulsed cyclic surface heat loads simulating disruptions with 30 MJ/m$^2$ and duration of 10 ms

The 2-D simulation describes the formation and growth of single pits under surface heating. Actually pits may arise everywhere at the heated surface provided that the heating is intense enough for intense crack formation. If the overall pit density increases with ongoing heating a macroscopic erosion crater of considerable depth finally might arise. To describe this a 3-D simulation model which is presently under testing has to be applied. Moreover validated failure stress values have to be used for estimating macroscopic erosion for surface heat loads. Target shielding by the dust particles from brittle destruction is of no concern for the magnitude of the macroscopic erosion. The target shielding by dust particles only delays the formation process of the open pits and thus some more heat pulses with surface heating are necessary till the pits combine into macroscopic erosion.

3. Melt layer erosion of metals

Experimental results from e-beam and plasma gun facilities and from tokamaks demonstrate the existence of a rather pronounced radial motion in the melt layer from the centre of the melted pool to the periphery [9,20,21]. As a result a considerable part of the melt layer is swept away, mountains of ejected melted material are formed at the crater edge and droplet splashing occurs. During such off-normal events as disruptions, VDEs and RAE impact the energy flux at the armour material reaches values sufficient for melting of metals and a thin melt layer appears at the target surface. Melt motion driven by external forces also produces a considerable surface roughness and destroys any castellation thus increases the fatigue stress of the metallic armour. The numerical simulation of melt motion is based on a 1-D fluid dynamics model [5].

3.1 Tokamak disruptions

A first application of numerical simulation of melt motion was done for hot plasma impact onto a vertical tungsten target. A typical disruption condition with a peak power density of 3 $GW/m^2$ and a time duration of 10 ms and with the separatrix strike point (SSP) downstream was used. Time dependent tungsten armour heat loads and plasma shield pressure profiles were calculated with FOREV-2.The pressure profiles of the plasma shield confined in the external magnetic field for more than 4 ms is between 4 and 7 bar and the pressure profiles show a half width of only 4 cm as is shown in Fig. 5. The upstream shift of the pressure profiles follows the upstream movement of the heat load which is due to reradiation from the expanding plasma shield [22]. For the given target heat load the maximum static melt layer thickness is about 470 microns as shown in Fig. 6 with the upstream direction as positive and the downstream direction as negative direction. The melt profile because of the upstream shift of the heat load shows a rather constant depth over a width of 15 cm. The external pressure gradient from the plasma shield causes a drastic melt layer erosion as shown in Fig. 6 with a rather symmetrical profile . The crater depth after resolidification is up to 410 microns and thus comparable to the melt layer thickness. In tokamaks during disruptions electric currents are flowing from the plasma into the structure [22].The current density of that component crossing the melt layer perpendicularly to the target surface is typically .1 to 1 $kA/cm^2$.The resulting volumetric Lorentz force being parallel to the armour surface causes melt motion in either downstream or upstream direction depending on the direction of the toroidal magnetic field. Taking pressure gradient and Lorentz force due to a current of .1 $kA/cm^2$ into account results in a maximum crater depth of about 350 microns. For a current of 1 $kA/cm^2$ the maximum crater depth is 700 microns thus being up to a factor of 1.4 larger than the thickness of the melt layer. Calculated average melt velocities in the tungsten melt layer for the two forces pressure gradient

and Lorentz force for a current of 0.1 $kA/cm^2$ are shown in Fig.7.
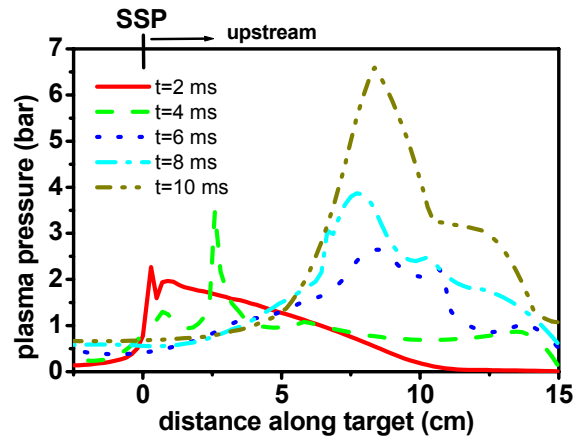


Fig. 5: Time dependent profiles of the external pressure from the plasma shield as calculated with FOREV-2 for a disruption case with 30 $MJ/cm^2$ and a time duration of 10 ms
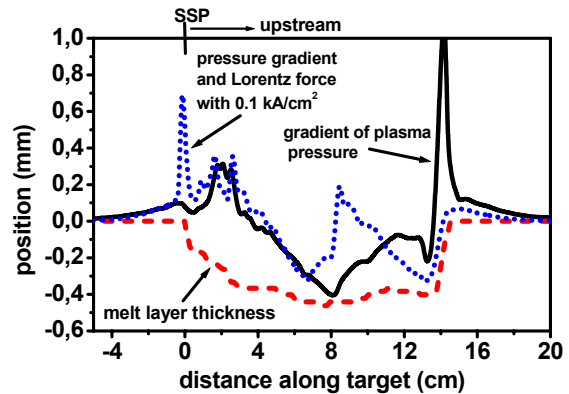


Fig. 6: Numerical results on crater depth for tungsten armour during a disruption with peak heat load of 3 $GW/m^2$ and time duration of 10 ms for the two different forces gradient of plasma pressure only and sum of plasma pressure and Lorentz force due to a current density of .1 $kA/cm^2$.For comparison the melt layer thickness without melt motion is also shown

The Lorentz force results in larger melt velocities than the pressure gradient of the external plasma shield. For the direction of the toroidal magnetic field as chosen here both velocities close to the SSP are directed downstream and add together to values of up to 800 cm/s. As a consequence the crater profile becomes asymmetrical and the mountains depending on the direction of the toroidal magnetic field appear either at the down or upstream crater edge. Moreover due to the rather large melt velocity considerable droplet splashing will occur in the tungsten divertor armour (the Reynolds number becomes rather large and a turbulent flow can arise).

There might also exist a current flowing parallel to the armour surface. The resulting body force which is perpendicular to the armour surface further amplifies the melt motion and contributes to droplet splashing.
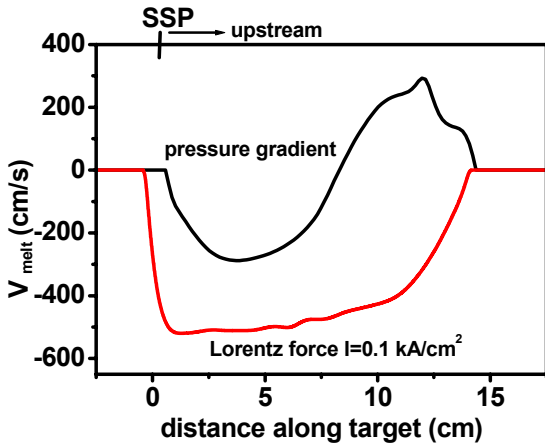
Fig. 7: Comparison of calculated average melt velocities in the tungsten melt layer for the two different forces Lorentz force with current density of 0.1 kA/cm$^2$ and gradient of plasma pressure. Close to the SSP both velocities are directed downstream

### 3.2 Vertical displacement events (VDEs)

Besides disruptions vertical displacement events (VDEs) are heating the FW, the baffle and the dome armour via surface heat loads. For VDEs it is assumed that the energy density deposited to the structure is up to 30 MJ/m$^2$ per event. The maximum impact energy of the hot plasma is assumed to be 1 keV. The duration of the heat load is assumed to be .1 s. The heated area has a width of 30 cm with a constant power density. It is assumed further that the Halo current is up to 1 kA/cm$^2$ flowing into the structure during the event. Calculated crater profiles are shown in Figs. 8a and b for Beryllium. In Fig 7a results are shown for two cases of the Halo current density with 0.1 and 1 kA/cm$^2$. Fig. 8a is valid for no armour shielding and for Fig. 8b it was assumed that the impacting plasma ions
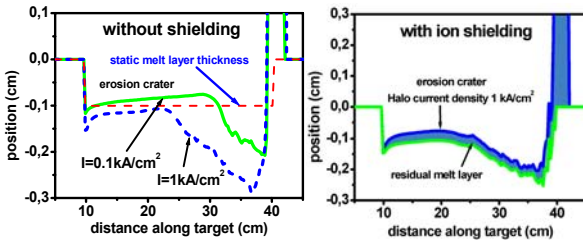


Fig. 8a                    Fig. 8b.

Calculated crater profiles in a Be FW armour for a VDE with 30 MJ/cm$^2$ for the two values of the Halo current of 0.1 and 1 kA/cm$^2$ without shielding (a) and with shielding (b)

are stopped in an evolving plasma shield. The crater depth for both cases are rather comparable despite the fact that the static melt layer thickness in the case with ion shielding becomes only 250 microns. The positive velocity of the melt motion shifts the melt to the right. The maximum crater depth is 2.8 mm for a current density of 1 kA/cm$^2$ and 2mm for .1 kA/cm$^2$ and thus drastically exceeds the static melt layer thickness which is 1 mm without shielding. Fig.9 shows the calculated crater profiles for
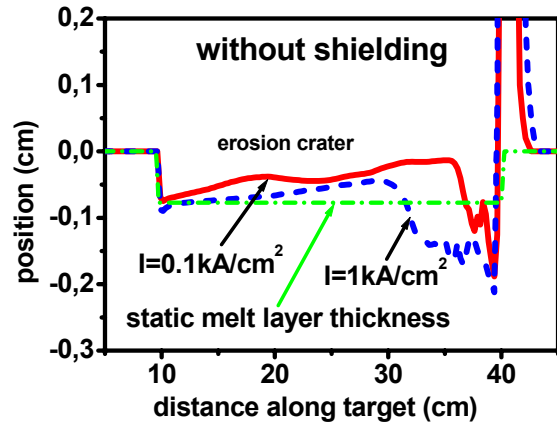


Fig. 9: Calculated crater profiles for a W FW armour for a VDE with 30 MJ/m$^2$ without shielding

tungsten armour again without shielding for the same heating conditions. The maximum crater depth is up to 2 mm. Fig. 10 shows calculated melt velocities for Be and W armour. The high velocity causes considerable droplet splashing [23] by the evolving interfacial instability [24] of the film flow. Because of the higher velocity of the Be melt the droplet splashing there is larger. The given numbers at the curves describe the fraction of melted mass splashed away by droplets.
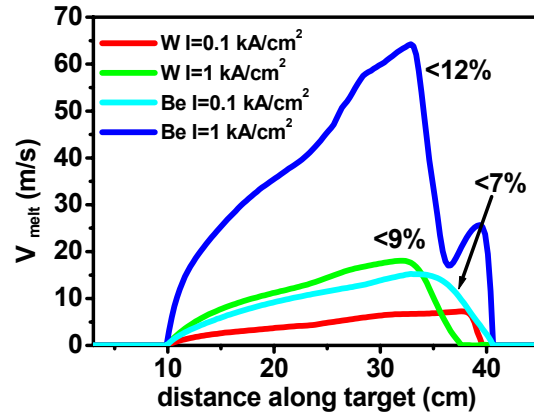


Fig. 10: Typical melt velocities for Be and W for a VDE with 30 MJ/m$^2$ and .1 sate indicated numbers describe the fraction of the melted mass which is splashed by droplets

## 4. Divertor erosion during ELMs

Triggered by the observation of giant ELMs at JET, in which up to 5% of the plasma thermal energy content was dumped to the divertor [25], the problem of ITER-FEAT divertor armour erosion during ELMy H-mode operation was addressed recently [26]. However another problem related with ELMs is the enhanced impurity production at hot spots, at leading edges and at redeposited layers which consist of mixed materials with drastically reduced heat conductivity from which beryllium predominantly evaporates under the high heat load of the hot spots.

In order to decide whether ELMs are tolerable for the divertor armour one has to be aware that during a 400 s discharge approximately 1000 ELMs will occur and that the lifetime of the armour evaporation and melting because of melt layer erosion are unacceptable. This defines the tolerable ELM energy for virgin plane divertor armour tiles without hot spots.

Disruptions produce a rather large surface roughness in metallic and CFC armour. Redeposited layers of sputtered and evaporated material mixed with dust and droplets have drastically reduced heat conductivities. Erosion at hot spots and at redeposited layers does not influence the armour lifetime during ELMs but enhances the impurity production and thus might limit the tolerable ELM energy from another point of view, namely from preventing ELMs to trigger a disruption. To guarantee this the tolerable ELM energy has to be limited to such values that the impurity production at hot spots and redeposited layers remains at such a level that the impurity cloud when finally arriving at the x-point is unable to dissipate a considerable fraction of energy from the plasma edge by radiation. Such a scenario for the first time was discussed in [7]. Meanwhile more detailed studies on hot spot ablation and impurity cloud expansion in the divertor were performed for different combinations of divertor and FW armour materials [8]. The impurity production from tungsten hot spots covering up to 10 % of the armour area during an ELM having a peak heat load of $1 GW/m^2$ and a duration of .5 ms and the tungsten impurity transport in the divertor are shown in Fig.11 at the end of the ELM and at two later time moments. The tungsten impurity cloud after the ELM mainly downstream of the separatrix moves towards the x point which for ITER-FEAT is at a distance of 1.5 m from the separatrix strike point (SSP). In the Fig. there are shown density profiles (solid lines) and plasma particle fluxes (arrows) given as product of plasma density times velocity. The time dependence of the tungsten density at the x-point is shown
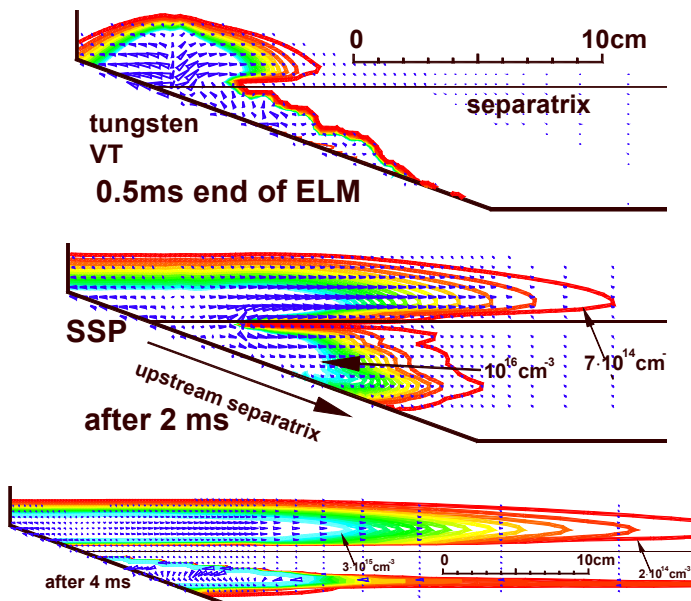


Fig. 11: Tungsten plasma density contours (thick lines) and plasma particle flux (plasma density times velocity, arrows) at 3 time moments. Peak target heat load at the SSP is 1 GW/m$^2$. (10 GW/m$^2$ at the hot spot), wetted area 5%

in Fig. 12. After 20 ms the tungsten density becomes about $3 \cdot 10^{14}$ cm$^{-3}$. Such a large impurity density is able to dissipate the thermal energy of the edge plasma and thus has a large potential for triggering a thermal quench disruption. CFC armour would yield a more unrenewable result because ablation from carbon flakes is more intense than ablation from tungsten hot spots. In this case the allowable ELM energy has

to be limited to values below .5 MJ. This is a factor of 5 less than what is tolerable for virgin CFC armour and about a factor of 25 less than what is presently estimated to occur for ITER-FEAT ELMs derived from a physics based scaling [26].
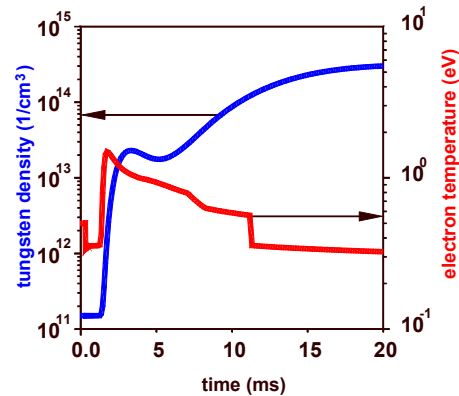


Fig. 12: Tungsten plasma density and temperature evolution at a distance of 1.5 m from the target at the position of maximum density

## 5. Conclusions

Melt layer erosion of metals is dominated by melt flow. Pressure gradients and Lorentz forces in the case of disruptions and only Lorentz forces in the case of VDEs trigger a pronounced melt motion which sweeps away a considerable part of the melt layer. For disruptions of 10 ms time duration the crater depth in the tungsten armour of a vertical target reaches 700 microns and the melt motion towards the crater edge is so violent that considerable droplet splashing occurs and any castellation will be destroyed by filling of the gaps with melted material. A moderate VDE on a Be FW armour results in crater depths of up to 2.8 mm and on a tungsten armour a depth of up to 2 mm. The high melt velocity results in considerable droplet splashing. Melt layer erosion at leading edges of metallic armour material and droplet splashing during normal operation produce hot spots. Enhanced impurity production at tungsten hot spots limits the tolerable ELM energy to values below 2,5 MJ. This is a factor of 5 below what is tolerable for a virgin plane metallic armour target [8]. Therefore the use of any metallic armour in the divertor requires mitigation of disruptions and a tile arrangement which excludes leading edges. The use of Be as FW armour because of its large damage during VDEs becomes problematic.

Brittle destruction of CFC occurs for volumetric heating and its quantification by numerical modelling is possible. The potential of brittle destruction under pulsed and quasistationary cyclic surface heat loads presently is not clear. Available experimental results and results from numerical modelling indicate formation of open pits of rather large depth due to preferential crack propagation into the depth of the sample. However the minimum surface temperature required for intense pit formation and onset of macroscopic erosion under cyclic surface heat loads is not known. The large erosion potential of macroscopic erosion makes further investigations on brittle destruction mandatory.

Staff:

B. Bazylev
I. Landman
S. Pestchanyi
V. Safronov
H. Wuerz

Literature:

[1]  G. Federici et al., Assessment of erosion and tritium codeposition in ITER-FEAT. J. Nucl. Mater 290-293 (2001) 260.

[2]  H. Würz et al., Damage Evaluation of Vertical Targets and First Walls during ITER-FEAT off-normal events. FZKA 6582, 2001.

[3]  H. Würz et al., Erosion of ITER-FEAT vertical targets during off-normal events. Accepted for publication in Fus. Eng. and Design, 2001.

[4]  H. Würz et al., Macroscopic erosion in tokamak off-normal events. Accepted for publication in Fus. Eng. and Design, 2001

[5]  B. Bazylev, H. Würz, Melt layer erosion of metallic armour targets during off-normal events in tokamaks. Submitted to J. Nucl. Mater

[6]  H. Würz et al., Macroscopic erosion of divertor and first wall armour in future tokamaks. Submitted to J. Nucl. Mater

[7]  H. Würz et al., Vertical target and FW erosion during off normal events and impurity production and transport during ELMs typical for ITER-FEAT. J. Nucl. Mater 290-293 (2001) 1138.

[8]  S. Pestchanyi, H. Würz, Impurity production and edge plasma pollution during ITER-FEAT ELMs. Submitted to IAEA-TCM Sept. 2001, Aix-en-Provence.

[9]  V.T. Astrelin et al., Nucl. Fusion 37 (1997) 1541.

[10]  J. Linke et al., Fus. Eng and Design 1, 49-50 (2001) 101

[11]  O.I. Bushinsky et al., J. Nucl. Mater 266-269 (1999) 793.

[12]  A. Huber et al., Physica Scripta T91 (2001) 61.

[13]  H. Würz et al., accepted for publication in Fus. Science and Technology.

[14]  G. Miloshevsky, H. Würz, FZKA report 6482, 2000.

[15]  S. Pestchanyi, H. Würz, Brittle destruction of Carbon Based Materials under off-normal ITER-FEAT conditions. Phys. Scripta T91 (2001) 84.

[16]  M. Araki et al., Fus. Eng and Design, 19 (1992) 101.

[17]  C.H. Wu et al., J. Nucl. Mater 258-263 [1998] 782.

[18]  N. Arkhipov et al., Erosion mechanism and erosion products in carbon based material. Submitted to J. Nucl. Mater.

[19]  A. Huber, IPP Jülich, private communication.

[20]  K. Nakamura et al., Fus. Eng. and Design, 39-40 (1998) 285.

[21]  T. Tanabe et al., J. Nucl. Mater 241-243 (1997) 116.

[22]  B.J. Azzopordi, Int. J. Multiphase Flow 23 (1997) 1.

[24]  W. Shyy, R. Narayanan, Editors, Fluid dynamics at interfaces. Cambridge University Press, 1999.

[25]  H. Würz et al., Plasma shield dynamics and target erosion in disruption simulation experiments. Fus. Eng and Design 49-50, 389, 2000.

[25]  S Clement et al., J. Nucl. Mater 266-269 (1999) 285.

[26]  G. Janeschitz et al., J. Nucl. Mater 290-293 (2001) 1.

## TW1-TVP/TUMO1
## Molecular Dynamics Simulations of Oxygen Impact on D Sputtering Threshold

The sputtering yield of tungsten is one of the critical issues for its use as armor material in future tokamaks. Impurities in the impacting scrape-off-layer plasma and especially oxygen may significantly deteriorate the good tungsten erosion performance. Therefore the investigation of consequences of this impurity impact is important. The process of the plasma-target interaction is shown in Fig. 1.
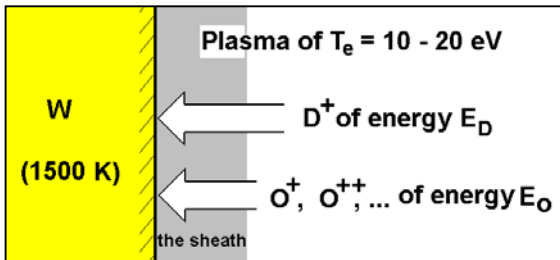


Fig. 1: The scheme of the plasma-target interaction

To investigate this process the molecular dynamics simulation (MDS) code 'CADAC' ('Classical Atomic Dynamics Analysis Code'), now under development, is applied. The processes in the target surface layer of size of 10 nm are simulated with about $3 \times 10^3$ atoms during a time interval of $10^{-11}$ s. Kinetic coefficients for the main chemical reactions between oxygen and tungsten under deuterium and oxygen ions bombardment across the electrostatic sheath are preliminary calculated. The scrape-off-layer plasma has typical electron temperature $T_e$ of $10 - 20$ eV, and the incident ion energies $E_D$ and $E_O$ below $10^2$ eV are assumed. The tungsten surface is heated up to 1500 K.

The surface reactions of type $W + O = WO_2$ and $WO_2 + O = WO_3$ are modeled taking into account the diffusion of the oxygen along the tungsten surface and destruction of the molecules by direct impact of the fast plasma particles and by the target thermal motion. The sputtering yield of W is assumed due to the removal of these molecules from the surface. Direct W sputtering, which starts at larger incident energies, surface clusters from W and O, which form at lower temperatures, volumetric oxygen diffusion and the influence of D-T on the surface chemistry are not yet considered. First results for the sputtering yields are obtained based on a solution of the reactions kinetic equations.

Essential modeling features are pair-wise potential interactions of participating atoms and simultaneous Newton dynamics motion of the tungsten target atoms and hydrogen isotopes and oxygen atoms. A model on three-atomic potentials in which the influence of oxygen on the W-W bonds is accounted for is now under development.

A new numerical instrument: the time cluster solver is introduced into CADAC allowing significant acceleration of the calculations, especially for assemblies of atoms of large mass differences, keeping exact conservation of momentum and fairly good conservation of energy. The time cluster scheme is shown in Fig. 2. All atoms in the simulation are subdivided into several groups called clusters. Each cluster has its own time step. Instead of usual meaning of atomic clusters as groups of atoms in close spatial proximity to one another,

here their proximity in time is implied, but in space they may be arbitrarily far or near of each other.
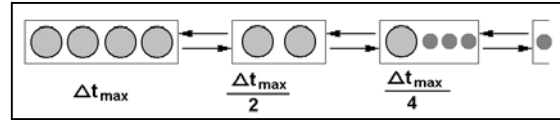


Fig. 2: Time step cluster structure of CADAC schematically. Large circles are the heavy atoms and small ones are the light atoms. The arrows indicate the movement of atoms from a cluster to its neighbor clusters

Staff

I. Landman
H. Würz

# Coil System

# M 31
## Development of 60 kA Current Leads Using High Temperature Superconductors

### Introduction

According to the European Fusion Technology Programme, the Forschungszentrum Karlsruhe and the Fusion Technology Division of the Centre de Recherches en Physique des Plasmas of the Ecole Polytechnique de Federale de Lausanne (CRPP-EPFL) are responsible for the design and construction of a 60 kA current lead for the ITER Toroidal Field Coil system using high temperature superconductors (HTS) in the temperature range between 4.5 K and 70 K to reduce the steady state heat load at the 4.5 K level.

### Design of a 10 kA HTS module using Bi-2212 tubes

As an extension to the development programme, an alternative design of a 10 kA current lead using Bi-2212 tubes cladded with AgAu sheath was investigated. This option was not available yet at the beginning of the task but has the advantage of being much cheaper than the tape option. Two 5 kA tubes were connected in parallel to form a 10 kA HTS module and tested at CRPP.

During the test, two questions were answered, i.e., what is the safety margin in case of a quench (this was the main reason to use the tape option in the stages A-2 and B of the development programme), and what is the current balance between the two tubes in both steady state and transient operation.

Fig. 1 shows the binary 10 kA current lead consisting of a wire bundle heat exchanger wrapped with superinsulation, a copper interconnection between the heat exchanger and the two Ag/Au cladded Bi-2212 tubes connected in parallel and a cold end copper contact. The HTS tubes were soldered to the copper contacts using a Bi 34 % In 66 % solder with a melting point of ≈80°C.



Fig. 1: 10 kA HTS current lead consisting of two conduction-cooled Bi-2212 tubes and a gas-cooled copper wire bundle heat exchanger

### Test results

The heat load at the 4.5 K level was measured to be (1.13 ± 0.11) W whereas 0.96 W were calculated. The difference may be due to tolerances in the thickness of the AgAu sheath and its thermal conductivity data.

There is a reasonable agreement between the temperature profiles measured and calculated (Fig. 2).
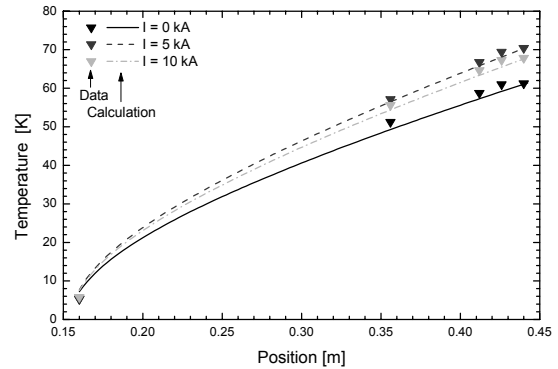


Fig. 2: Measured and calculated temperature profiles along the HTS part (Tube B) of the current lead during steady state operation.

It was not possible to evaluate the single contact resistances $R_c$ at 70 K/4.5 K due to the very high current imbalance between the two tubes (voltage taps are not on equipotential line). The total $R_c$ at 4.5 K is 2.4 nOhm (calorimetric evaluation).

From the measurement of local magnetic field at four positions of both tubes, the current distribution was estimated. There is a large current imbalance between tubes A and B, independent of the transport current. Simulations based on a strongly uneven current distribution within each tube can reproduce the field data. Transport current in tube A beyond the expected critical current (resistive signal observed). The transport current in tube B is very small.

During quench, there is a current transfer from tube A to tube B at voltages below 1 mV (Fig. 3).
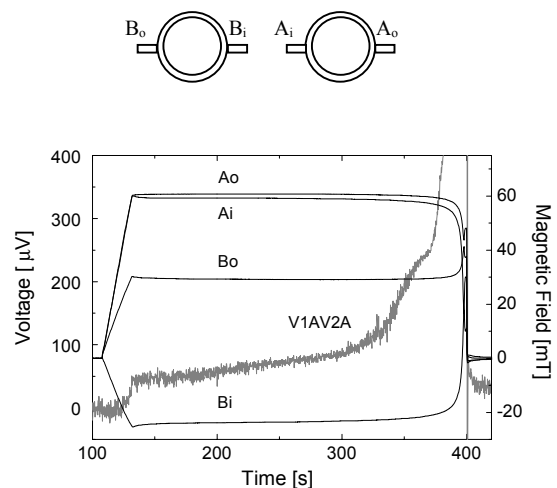


Fig. 3: Azimuthal magnetic fields measured by Hall probes close to the surfaces of Tubes A and B at a current of 10 kA indicating that the current flows mainly in Tube A. The voltage V1AV2A across Tube A suggests that the current in this Bi-2212 superconductor is close to the critical current. The nomenclature used is indicated in the scheme shown above

The measured quench current is much higher for tube A and much lower for tube B than expected from short sample data provided by Nexans at 77 K.

The rapid increase of the voltage from 10 to 100 mV within a time of 3.5 s observed for loss of flow is a consequence of the uneven current distribution. This time would be considerably prolonged for an even current distribution. The results suggest that a design based on two Bi-2212 modules in parallel is unfavorable because of the reduced effective critical current and the deteriorated quench behavior in the case of a large current imbalance.

The existing technology is not adequate to manufacture a single 70 kA Bi-2212 module which requires an outer/inner diameter of 27/25 cm. Considerably more development work is indispensable.

**Conclusions and Outlook**

The tests of the Bi-2212 tubular current lead has been finished, the task M31 is completed. Summing up the results of the 10 kA and 20 kA HTS current lead tests, the robustness of the Bi-2223 tape material design for HTS current leads was demonstrated.

In a new task the design, development and testing of a 70 kA HTS current lead for ITER-FEAT will be performed. For this lead, Bi-2223 tapes will be used. It is planned to perform the new task again in collaboration with CRPP Villigen, Switzerland. The test of the lead will be done in the TOSKA facility because the required infrastructure and components are available.

Staff:

R. Heller
M. Tasca (until 28/02/01)

Literature:

M. Tasca, "Entwicklung und Verifizierung einer modularen Hoch-stromzuführung unter Verwendung von Hochtemperatur-supraleitern", *Doktorarbeit, Wissenschaftliche Berichte FZKA 6608,.* (2001)

R. Heller, G. Friesinger, A.M. Fuchs, R. Wesche, " Development of High Temperature Superconductor Current Leads for 70 kA ", *presented at 17th International Conference on Magnet Technology, Geneva, Switzerland*, Sept. 24 –28, 2001

A. M. Fuchs, R. Wesche, A. Anghel, F. Roth, R. Heller, M. Tasca, " Test Results of a 10 kA Current Lead using Ag/Au cladded Bi-2212 Tubes ", *presented at 17th International Conference on Magnet Technology, Geneva, Switzerland*, Sept. 24 –28, 2001

# M 44
# TFMC Test and Installation

The TOSKA facility at Forschungszentrum Karlsruhe was upgraded for testing the ITER TF model coil. The facility had been qualified for this task in two steps:

- Test of the LCT coil at 1.8 K (1996/1997)

- Test of the stellarator prototype coil W 7-X (1999)

The first step demonstrated the ability of the LCT coil for being used as background coil for the TFMC test configuration. The basic facility with its electrical and cryogenic supply system as well as data acquisition and control was taken into operation. The test of the W 7-X coil counted besides the test of the coil as an intermediate step for gaining operation experience and improving the facility components. The specific facility configuration needed for the TFMC test was complete December 2000. The assembling of two 80 kA current leads with the cryostat extensions was ready in March 2001.

The test of the TFMC is being performed in two phases as it has been concluded by the TFMC Coordination Group and the EURATOM Association Forschungszentrum Karlsruhe Steering Committee:

- Test Phase I of the TFMC without LCT coil (June – October 2001).

- Test Phase II of the TFMC in the background of the LCT coil (2002)

The intention of the testing in two phases is to achieve results of the TFMC as soon as possible in less sophisticated configuration with a lower risk of occurring faults.

For the performance of the TFMC test, an organization scheme was approved for decision making and handling the daily work of testing. The management of the test is handled by the Coordination Group which is supported by the Operation and the Test Group. Members of the groups are delegates from the ITER JCT and the Home Teams.

The acceptance tests and the preparation of the test program of the TFMC are accompanied by the special skills of the European superconducting laboratories. The task areas of the Association Forschungszentrum Karlsruhe EURATOM are:

- Instrumentation (included in M 44)

- Conductor measurements (NET Contract No.: NET/97-458 concluded)

- Mechanical material and component testing (EU Task No: M 45, concluded)

- High voltage component delivery and testing (NET Contract No.:NET/96-438, concluded)

- Finite element analysis (EU Task M 12)

- Electromagnetic and thermohydraulic analysis (included in M 44 and 3 D quench analysis with code system MAGS, IRS, EU Task SEA 5)

- Transient voltage behavior of the TFMC (included in M 44)

- Leak testing acceptance tests during fabrication (included in M 44)

The acceptance tests of the TFMC at European industry site (Alstom SA) were completed in December 2001. The TFMC arrived at the TOSKA site in January 11, 2001.

After performance of the TFMC acceptance test at TOSKA site the test configuration for testing without LCT coil was assembled and installed in the TOSKA vacuum vessel. The test run very successful from June to October 2001.

## 1 The TOSKA facility

Cryogenic system: The cryogenic system was prepared as far as possible without the TFMC. All the piping work including instrumentation was performed. The supply pipes running to the TFMC were closed by welded plugs. The piping and the modified LCT coil were leak tested under pressure by a vacuum leak test with closed lid of the TOSKA vacuum vessel. All the instrumentation, control and interlocks were pre-tested.

Current leads: The repair of the non brazed $Nb_3Sn$ inserts at the cold end was completed by soft soldering of suitable copper profiles. The 80 kA current leads were then assembled with the cryostat extensions under performance of suitable sequence of leak and high voltage tests. The so called power feedthroughs containing superconducting bus bars type II and current leads in the cryostat extensions were ready for installation end of March 2001 (Fig. 1).



Fig. 1: One of the assembled power feedthroughs ready for installation at the flange of the TOSKA vacuum vessel

High current supply system: The commissioning of the 20 kA power supply and the 80 kA safety discharge circuit were completed in December 2000.

Signal conditioning and data acquisition: Low and high voltage signal conditioning were pre-tested to confirm that the correct data values were processed.

## 2 Assembling and installation of the ITER TFMC

After arrival of the TFMC at the TOSKA site at January 11, 2001 tests (leak, high voltage and sensor tests) were performed to

assure that no damage was caused during shipping. The TFMC was lifted into and aligned in the intercoil structure (ICS). The ICS and TFMC were put upright in the vertical position. It was lifted onto the gravitational support and assembled with the auxiliary structure (Fig. 2). The acceptance tests were performed partially outside (high voltage and sensor continuity test series) and inside (leak test) the TOSKA vacuum vessel (Fig. 3). The helium circuits of the test configuration were temporary connected for pressurizing them with helium for a vacuum leak test for achieving the highest sensivity. The measured leak rate was $< 2 \bullet 10^{-7} \bullet mbar \bullet l/s$ and therefore acceptable for going ahead with the further installation work. The TFMC configuration was connected to the TOSKA facility (helium supply, current supply, sensors). The power feedthroughs were installed at the vacuum vessel flanges. A joint between the superconducting bus bars type I coming from the coil terminals and the superconducting bus bars type II coming from the current leads had to be fabricated including the piping, the electrical insulation and finally the support structure of the superconducting bus bars in the TOSKA vacuum vessel.

in reports [1], [2] and the test procedure [3]. The test procedure contains the sequence of the testing steps.

The cooldown of the 63 t test configuration needed about 2 weeks and achieved the superconducting state at July 6, 2001 (Fig. 4). The temperature difference across the TFMC was kept < 40 K and across the structure < 55 K. Some temperature sensors on poor cooled areas of the ICS were eliminated from the computer controlled cooldown program as agreed by all partners in order to keep the temperature gradient of about 1 K/h.

Before starting the tests with current final acceptance tests (high voltage, sensor function, flow distribution, vacuum leak tests) were performed. The Paschen minimum insulation problems disappeared as expected under the low vacuum pressure. The full insulation strength at 10 kV DC were achieved. Pulse voltage tests showed a breakthrough between 5 – 7 kV. No breakthroughs at 4 kV were observed for the two polarities.



Fig. 2: The ITER TFMC configuration in the TOSKA assembling area
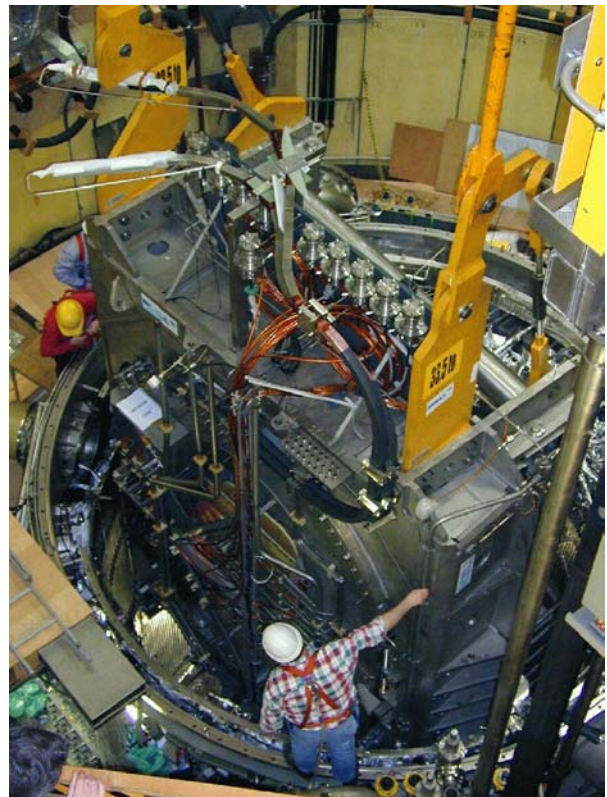


Fig. 3: The ITER TFMC configuration during lifting into the TOSKA vacuum vessel

After completion of the installation work a series of tests were performed (high voltage tests, sensor continuity check, vacuum leak tests of the different helium circuits). Some problems were found with a pressure dependent insulation fault (Paschen minimum effect) which should vanish when a vacuum of about $10^{-6}$ mbar can be achieved at low temperature. The overall leak rate was $< 1 \bullet 10^{-7} \bullet mbar \bullet l/s$ at the maximum operation pressure of the different circuits. The boundary conditions for start of the cooldown of the test configuration were acceptable to all partners. The cooldown was started June 25, 2001.

## 3   The test of the ITER TFMC

The testing of the TFMC configuration was performed according to test program elaborated by the European superconducting laboratories. It consists of preparing analysis work summarized

There was sufficient margin available for the safety discharge of the magnet at 535 V. At a test pressure of 3.5 bar the total leak rate increased to $2 \bullet 10^{-5} \bullet mbar \bullet l/s$. The ownership of the TFMC was transferred from the manufacturer AGAN to EFDA/EU. The non conformities found were summarized in a list. The assignment of non conformities to the parties has to be done after the conclusion of the test phase I.

The current test were started with low current tests for checking out the interlocks of the facility and the proper function of the quench protection. The TFMC was then ramped in steps to current levels which represent quarters of the stored magnetic energy. At each current level an inverter mode discharge (max. voltage of the power supply) and safety discharge were performed. The coil achieved the rated current of 80 kA on July

27, 2001. The test were continued by heating tests of two coil pancakes to determine the current sharing temperature of the
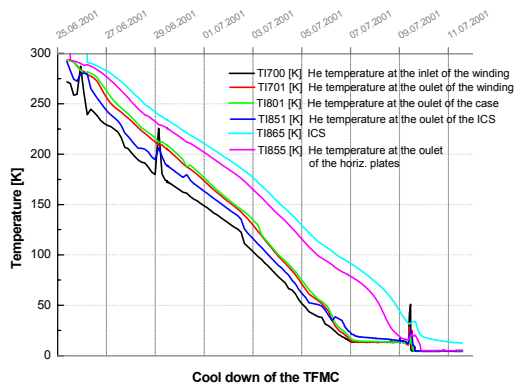


Fig. 4: The temperature traces during the cooldown of the TFMC test configuration

conductor and consequently the operation limits of the coil. Ramping tests with different ramp rates were performed to determine the AC losses of the coil including the eddy current losses of the heavy steel structure.

Besides the testing of the TFMC also cooling modes of the facility and the 80 kA current leads were tested.

## 4    Test results of the TFMC

Electromagnetic properties: The coil was operated in total 11.3 hours at 80 kA in 19 runs. This current level is the highest one ever achieved for a large superconducting coil. It exceeds the ITER FEAT toroidal field coil design current by about 18 %. During the test operation 15 safety discharges were performed from current levels larger than 50 kA. 10 safety discharges were initiated by a quench. From that 7 took place from 80 kA.

The operation of the coil was very stable no resistive voltages above the noise level (~ 0.1 mV ) were observed.

The current sharing measurements at 56.6 kA, 69.3 kA and 80 kA agree according the first evaluation with the expected values. No degradation was found after cycling and 7 current sharing temperature measurements over the testing time.

The resistance of all type of conductor joints were in the range of 1 – 2 n$\Omega$.

The AC losses were somewhat higher than expected and have to be analyzed in detail.

Thermal hydraulic properties: The TFMC operation parameters, steady state losses and the max. temperatures after a safety discharge are presented in the following:

The coil was operated first at 80 kA with the following mass flow distribution:

| | |
|---|---|
| Winding: | 70 g/s |
| NbTi bus bars: | 2 x 10 g/s |
| Case: | 10 g/s |
| Auxiliary structure: | 10 g/s |
| Intercoil structure: | 10 g/s |

| | |
|---|---|
| Inlet temperature: | 4,52 K |
| Inlet pressure: | 5.0 bar$_{abs.}$ |

No systematic change of the pressure drop was observed across the winding during operation under current.

The steady state losses without current were as following:

| | |
|---|---|
| Winding: | 12 W |
| NbTi bus bars: | 2 x 50 W |
| Case: | 10 W |
| Auxiliary structure: | 11 W |
| Intercoil structure: | 30 W |

After a safety discharge from 80 kA the following maximum temperature and pressure values were measured:

He-Temperature

| | |
|---|---|
| Winding: | 18 K |
| Case: | 21 K |
| Intercoil structure: | 12 K |

Pressure

| | |
|---|---|
| Winding, Case and ICS: | 7 bar |

Energy removed by recooling

| | |
|---|---|
| Winding: | 3.6 MJ |
| Case: | 1.7 MJ |

Mechanical properties: The mechanical properties measured are in fair agreement with the expectation (details see Task M12).

## 5    Results of the TOSKA facility

Cryogenic system: The availability of the TOSKA facility was better than 98%. The operation of the cryogenic system fulfilled the request of the experimenters very well. All safety discharges of the TFMC were handled without Helium gas release to the atmosphere. The recooling time was about 2 hours. Typical operation parameters during ramping are presented in Fig. 5.

The time for achieving steady state conditions after ramping was between 0.5 to 1 hour.

The Tcs test by gas heating mentioned above with 600 W additional load, far above the cooling capacity of the refrigerator, could be mastered several times for 30 min in a reproducible way.

The very low heat load of the different components inside the vacuum vessel was achieved by a vacuum pressure of $2\bullet10^{-6}$ mbar, by additional superinsulation blankets on the test configuration and by a LN$_2$ baffle at the diffusion pump suction port. After cool down the measured leak rate was $2\bullet10^{-5}$ mbarl/s During all current tests the vacuum remained stable without additional leaks.
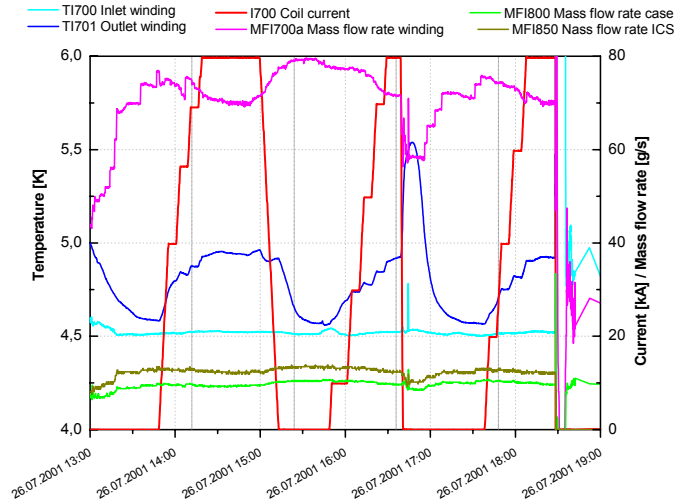
Fig. 5: Typical cryogenic operation parameters during operation with current (slow ramp down, inverter mode discharge, safety discharge)

Current leads: The two current leads were operated at 80 kA without showing any instability. A test series was made to optimize the operation parameters at zero, 40 kA and 80 kA. The current leads were successfully operated under stable conditions at calculated mass flow.

Electrical supply system: The parallel operation of the 50 kA and 30 kA power supply used to feed 80 kA in the TFMC was mastered successfully. The three different current ramp down modes (controlled ramp down, inverter mode discharge and safety discharge) were optimized and checked against a computer model based on the Power System Blockset running under SIMULINK. The current commutation from the power supplies across short circuit path into the discharge resistor for the safety discharge worked very well within about 625 ms from the trigger of the safety discharge to complete the sequence and start the exponential current decay with a time constant of 4 s.

A total number of 15 safety discharges with coil current larger than 50 kA were performed successfully. Typical voltage and current traces for current commutation are presented in Fig. 6.

Fault conditions (switch off of one power supply in the parallel operation mode) were successfully tested up to 40 kA.

Data acquisition, signal conditioning and protection: The complex data acquisition system in combination with the process control worked well. Arising problems were solved in a short time and with no real impact on the operation of the experiment.

The voltage ripple of the thyristorized power supplies induced a quite high noise level to some signals as joint voltage drops. Introducing low pass filters at 10 Hz it was possible to reduce such noise substantially and achieve with the signal conditioning and data acquisition system a resolution in the range of 10 $\mu$V. The high voltage patching area offered the possibility to arrange the signal conditioning in a way that also the joint resistance of the outer joints could be measured. The

patching scheme was sufficient flexible to cover nearly all requests of experimenters.

The quench detection system for winding and superconducting bus bars worked very reliable no unintentional safety discharge was triggered during the whole operation time at voltage levels of 100 mV for the TFMC pancakes and 10 mV for superconducting NbTi bus bars (positive and negative polarity) Each protection circuit included also a low pass filter with a response time of 0.5 s.

## 6    Summary

The ITER TFMC was assembled, pre-tested and installed in the TOSKA facility.

After cooldown and acceptance tests the ownership was transferred from the manufacturer AGAN to EFDA/EU.

The test results fulfill the expectations and demonstrate the availability of the technology for the construction of the ITER FEAT toroidal field coils.

The operation of the TOSKA facility was very smooth and reliable. All components achieved their rated values. It was demonstrated that the cooling system can be operated over a short time (30 min.) far above the cooling capacity of the refrigerator. Current leads and power supply including safety discharge circuit were the first time successfully operated at 80 kA current level. Signal conditioning and protection as well as data acquisition and process control run stable over about 6 month.
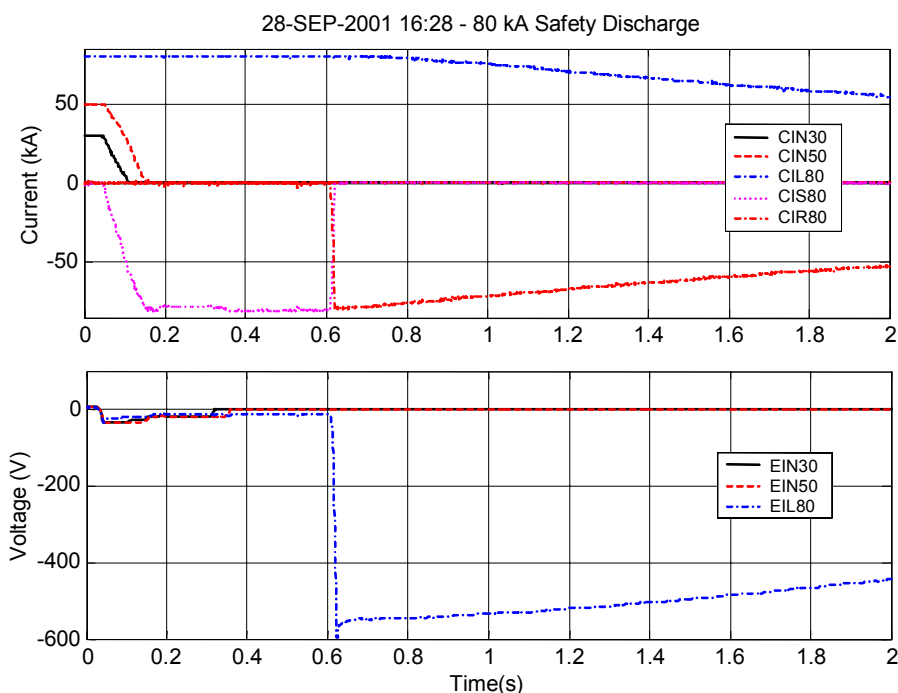
Fig. 6: Current and voltage traces during the current commutation from the power supply across the short circuit path in the dump resistor

Staff:

A. Augenstein
E. Bobrov (since Sept. 28, 2000)
S. Darweschsad
I. Donner
G. Dittrich
P. Duelli
W. Eppler
S. Fink
G. Friesinger
A. Grünhagen
R. Heger (since July 1, 2001)
R. Heller
W. Herz
R. Kaufmann
A. Kienzler
O. Langhans
W. Lehmann
V. Leibbrand
V. Marchese
I. Meyer
J. Müller
G. Nöther
U. Padligur
P. Rohr
G. Schleinkofer (till August 30, 2001)
V. Schulmeister
E. Specht
H.-J. Spiegel
M. Süßer
A. Ulbricht (for 3, 4, 6)

D. Weigert
F. Wüchner
G. Zahn (for 1, 2, 5)
H.P. Zinecker (till June 30, 2001)
V. Zwecker

Lierature:

[1] P. Libeyre, ITER TFMC, Test and Analysis Summary Report, Chapter 1: Specific Analysis Results Needed for Testing, CEA Cadarache, DRFC, AIM/NTT-2000.005, April 12, 2001

[2] A. Ulbricht, ITER TFMC, Test and Analysis Summary Report, Chapter 3: TOSKA Facility, Forschungszentrum Karlsruhe, Wissenschaftliche Berichte , FZKA 6614, Mai 2001

[3] E. S. Bobrov, ITER TFMC Test Program, Outline of the Test Procedure, Forschungszentrum Karlsruhe, Interner Bericht, Institut für Technische Physik, June 2001

## M 45 (N 11 TT 15)
## ITER Coil Casting and Intercoil Structures

During the current investigation period, cryogenic mechanical data were established with respect to two full-scale TF coil mockups, called Model 1 and Model 2. These two models represent the portion of the inner leg and part of the outer intercoil structure. Model 1 is a forged [1] heavy part (Type 316LN) of 40 tons, which after forging was pierced and cut into two C-halves to insert the superconducting TF winding pack. The tensile and fracture data for the base metal were already published [1] and the present paper gives the FCGR results of those obtained at 7 K. The produced heavy weld closure (~240 mm deep) by narrow-gap welding and their repair welds were tested to determine the weld tensile and fracture properties. For Model 2 a 25 ton heavy piece of modified Type 316LN casting (higher manganese) was produced and representative samples in all three spatial orientations were tested. These data were compared with a one ton trial cast sample. Here, beside the static mechanical properties, also fatigue life and FCGR measurements were carried out to complete the database.

For the CS coil the fatigue properties of the superconducting cable jackets were extensively tested for both candidate materials, Incoloy 908 and Type 316LN. The results show so far [1] that the static properties of both alloys are comparable but the weld metal mechanical properties are worthwhile to be investigated further. Therefore, tensile measurements were performed using small 3 mm gauge length extensometers to establish weld metals database. Concerning cyclic behavior the Type 316LN (base metal) showed in the past a lower resistance against fatigue crack growth than Incoloy 908. Therefore, cyclic tests of the base and weld metals of the jackets were extensively carried out. Furthermore, to avoid weld metal cracking during the jacket compaction process, a low Nb content filler wire was used for the orbital butt welds of the extruded tubes made of Incoloy 908 material. Also a new series of weld samples were produced for the Type 316LN extruded jacket material. The FCGR data of the Type 316LN jacket were compared with several commercial 316LN base metals already used in cryogenic applications. These results show the

possibility to improve the FCGR behavior of the extruded 316LN jacket in principal. Other than FCGR measurements, where the crack starts from a defined micro scale fatigue pre-crack, fatigue life tests show the material property in its original virgin state, where the total life time covers the crack nucleation, propagation, and failure process. Therefore, both materials were tested with usual smooth hourglass shaped flat and circular specimens carefully machined from the jacket materials weld section. The determination of the cryogenic materials properties of the TFMC intercoil structures, produced by thick plates of Type 316LN wrought material was an important part of the task.

In order to perform large scale loading investigations, the existing 200 kN screw driven machine [2] was upgraded with a four column servo hydraulic 630 kN load capacity testing machine. The first large scale tensile tests up to 20 mm Ø tensile specimens, made of Model 2 one ton cast material were performed in LHe. One of the goals of this installation was to supply cryogenic cyclic data of the full size CS jacket welded sections.

**Results with tensile and fracture toughness measurements**

The results with tensile and fracture toughness tests are reported in Table 1. The first four rows of this Table give the data of 25 ton cast steel, which shows an anisotropic behavior. However, the obtained values for this 25 ton heavy casting is more homogenous than the one ton trial casting already reported [1], which showed a higher degree of anisotropy. The new values determined from the one ton trial casting with different size specimens, but from same orientation show the large scatter of the material (the rows 5–8). The data of the 20 mm Ø specimen (row 8) was determined using two independent extensometer systems (each of them with two extensometers) attached at different regions of the reduced section. It is obvious that even for the same specimen the results of yield strength and Young's modulus may vary depending on the measured zone. These results reveal the high inhomogeneous nature of the one ton trial cast steel (15% total elongation).

The tensile and fracture mechanical data obtained with the two repair welds of the narrow-gap weld joints show that weld

Table 1: Tensile and fracture toughness results of modified 316LN casting (25 ton & one ton), repair weld samples, jacket materials, and Type 316LN 80 mm thick wrought plate sample at 7 K and 4 K

| Material / specimen orientation and positions | Young's Modulus GPa | Yield Strength MPa | Ultimate tensile strength MPa | Uniform Elongation % | Critical J JETT [4] N/mm | $K_{IC}$ (converted) MPa m |
|---|---|---|---|---|---|---|
| 25 t cast steel Y, 7 K [a] | 159 / 124 | 944 / 852 | 1086 / 1055 | 25 / 40 | 193 / 241 | 175 / 172 |
| 25 t cast steel Y, 4 K [a] | 179 / 173 | 800 / 870 | 1231 / 1183 | 26 / 17 | - | - |
| 25 t cast steel X, 7 K [a] | 162 / 176 | 911 / 847 | 1216 / 1048 | 33 / 27 | 242 / 202 | 198 / 188 |
| 25 t cast steel Z, 7 K [a] | 214 / 168 | 877 / 869 | 1060 / 984 | 20 / 20 | 300 / 252 | 253 / 205 |
| 1 t cast steel, 4 Ø, 7 K | 176 / 148 | 694 / 688 | 1144 / 858 | 21 / 32 | - | - |
| 1 t cast steel, 6 Ø, 4 K | 126 / 190 | 695 / 766 | 964 / 1044 | 30 / 23 | - | - |
| 1 t cast steel, 12 Ø, 4 K | 170 | 825 | 1255 | 25 | - | - |
| 1 t cast steel, 20 Ø, 4 K | 113 / 158 | 676 / 738 | 1126 / 1126 | 34 / 9 | - | - |
| Repair weld No 1 | 157 / 161 | 1064 / 1127 | 1471 / 1495 | 30 / 26 | 118 / 125 | 153 / 158 |
| Repair weld No 2 | 192 / 186 | 1164 / 1190 | 1518 / 1527 | 22 / 25 | 131 / 84 | 161 / 130 |
| 316LN jacket weld | 203 / 181 | 1143 / 1124 | 1476 / 1476 | 19 / 18 | 95 / 96 | 138 / 132 |
| Incoloy 908 jacket weld | 148 / 163 | 1038 / 1108 | 1377 / 1313 | 14 / 5 | 111 / 130 | 128 / 145 |
| 316LN / T-L surface* | 209 / 193 | 1051 / 1002 | 1662 / 1631 | 40 / 43 | 251 / 306 | 226 / 250 |
| 316LN / T-L mid plane | 204 / 206 | 1000 / 1015 | 1619 / 1641 | 42 / 40 | 280 / 255 | 239 / 228 |
| 316LN / S-T** | 210 / 211 | 1009 / 1003 | 1551 / 1616 | 38 / 43 | 232 / 246 | 218 / 224 |
| 316LN / L-Tsurface*** | 210 / 192 | 991 / 1026 | 1620 / 1565 | 43 / 42 | 220 / 296 | 212 / 246 |
| 316LN / L-T mid plane | 204 / 198 | 977 / 994 | 1614 / 1639 | 44 / 42 | 290 / 259 | 243 / 230 |

[a] X, Y, and Z are spatial orientation of the block as given in reference [1]
* T – L  (Transverse long) orientation of specimen according to ASTM designation
** S - T (Short transverse)
*** L - T  (Long transverse)

sample No 1 welded with GMAW (Gas Metal Arc Welding) process has slightly lower properties than sample No 2 welded with SMAW (Shielded Manual Arc Welding) concerning the tensile values, whereas the fracture toughness of weld sample No 2 is higher than No 1. However, both repair welds fulfill the 4 K design requirements ( $K_{IC}$ > 130 MPa√m).

For the CS jacket structures of Incoloy 908 and Type 316LN (Valinox) the weld metal tensile and fracture toughness data are given in the two rows (11 and 12) of Table 1. To ensure the measurement of weld metal data these tests were carried out using the double extensometer system with a gauge length of 3 mm, thus enabling the record of the strains only in the weld metal region. The low elongation (~5 %) of one of the tests for the Incoloy 908 weld metal can be attributed to weld defects, which were often observed for several specimens during fatigue life tests. These defects were in the range of 0.1 – 0.3 mm and result mainly from the welding process. Another fact is also the significantly low Young's modulus of the weld zone compared to the 316LN weld metal.

The last 5 rows of Table 1 present the data for the 80 mm thick Type 316LN wrought plate at 7 K at different orientations obtained by two specimens machined from the same position. The results show a well-balanced isotropic behavior of the measured tensile and fracture toughness values. In addition, the obtained data show a small scatter for the Young's modulus (mean = 204 GPa, standard deviation (SD) = 7 GPa), yield strength (mean = 1007 MPa, SD = 20 MPa), tensile strength (mean = 1616 MPa, SD = 34 MPa), and elongation (mean = 42 %, SD = 2 %). For fracture toughness the determined average value using the JETT [4] test method results to 232 MPa√m with a SD of 12 MPa√m.

**Fatigue life and fatigue crack growth rate tests**

To characterize the cyclic properties of the structural materials mainly two type of investigations were carried out. These were the classical axial fatigue life experiments using small scale (4 mm Ø) specimens and FCGR tests under the load ratio ($P_{min}$/$P_{max}$) R = 0.1, all at 7 K. Major attention was focused on the CS jacket butt weld fatigue life characterization. In a similar way, the base metal of the cast 25 ton steel was investigated at 7 K with the same type of specimens in as received condition. The fracture surface obtained after the fatigue life tests of the CS jacket weld materials delivered valuable information about the weld performance and the determined defects were correlated to the fatigue life. Figure 1 shows the set of experimental results for Incoloy 908, Type 316LN (Valinox) weld metals, and cast steel. The jacket material Valinox was tested additionally with flat hour glass type specimens. Here the weld metal represented the thinnest wall area (4 - 5 mm) of the CS jacket section. All Incoloy 908 specimens were in aged condition (200h / 650°C at vacuum), whereas for Valinox, tests were conducted with both aged and unaged materials. The cast material 7 K fatigue life results show that the obtained line is significantly lower than that of common Type 316LN materials due to the lower ultimate strength. For the Valinox weld metals the values obtained with the flat specimens show a slightly lower fatigue life property compared to round specimens. Almost in all cases the failure started from the surface of the specimen. The lower cyclic performance is due to the rectangular cross section of the loaded area, where the sharp edge increases the possibility of an earlier crack nucleation. For Valinox there are no differences in the final results between aged and unaged conditions. The derived line gives the best estimate of the conducted test results. In fact, between Incoloy 908 and Valinox there is hardly any difference in fatigue life. For Incoloy 908 welds the fracture surfaces show clearly defects and the defect size dictates the achieved total cyclic number. However, even in practically defect free state both materials are comparable as these experiments confirm. The two dotted lines in Figure 1 represent the design

approach based on cumulative damage rules (ASME Boiler and Pressure Vessel Code Section III), where the experimental curve is modified by applying a factor of two on stress or 20 in cycle number, whichever is more conservative [5]. The derived lines show that the allowable fatigue life is governed by stress rather than number of cycles. Therefore, for both materials (even with small weld defects) the allowable stress is within the range of 500 MPa for one million cycles at 4 K. Figure 1 shows also the failure of survived aged flat specimen with > 1 million cycles at second time loading (plot *) with elevated stress level of 1000 MPa, indicating the crack nucleation during the first cycling set at 900 MPa.

The FCGR characteristics of the Valinox and Incoloy 908 base and weld metals are shown in Figure 2. The determined average lines show the following facts: Between aged and unaged Type 316LN jacket materials there is no significant difference. For Incoloy 908 the weld and base metals show similar FCGR behavior. Type 316LN weld metal FCGR has a higher resistance against crack propagation above ∆K ~29 MPa√m, whilst below this stress intensity range the Incoloy 908 has a better performance. Solution heat treatment (1050 °C / ½ h, and water quench) of Type 316LN jacket material improves the FCGR behavior considerably if compared to jacket materials without any treatment. The reason of this finding seems to be the grain size, which in case of the extruded jacket material is very small (~70 µm) with a high amount of twins. By solution heat treatment the size of the grains are increased with fewer twins. An investigation program for the material 316LN showed that a variation of FCGR properties exist between different batches resulting from the microstructure. Figure 3 shows the obtained data for different groups of Type 316LN materials. In this diagram the old published data of 50 mm thick 316LN plate obtained with 24 mm thick CT specimens at 4 K are plotted [6]. In this work it was possible by using large specimens to determine the FCGR up to > 100 MPa√m, which in case of 4 mm thick specimens was not possible because of specimen collapse beyond the 40 MPa√m regime. The test results with modified cast steel (Model 2), the forging (Model 1), and a commercial 20 mm thick plate (average grain size ~300 µm) are all in line with the old 4 K data. However, the 80 mm plate (TFMC intercoil structural material) is significantly inferior to Valinox (Figure 2). The investigated microstructure of the 80 mm plate indicated also a smaller average grain size (~120 µm) than usual with a high twin density.

In addition to the above given jacket materials FCGR and fatigue life tests (small scale specimens) a fatigue life investigation program was started with full size jacket materials having a butt weld in mid section. The measurement took place inside the 400 mm diameter cryostat at LHe using the 630 kN servo hydraulic machine. A special equipment designed beneath the 4 K rig made a 4-point cyclic bend loading possible with peak loads at ~ 400 kN. The carried out preliminary tests at 4K show the applicability of such measurements at a frequency of circa 1 Hz with a LHe consumption of about 250 liters per day. The first fatigue life test results performed with full size jacket structures are expected in near future.

Staff:

A. Nyilas
H. Kiesel
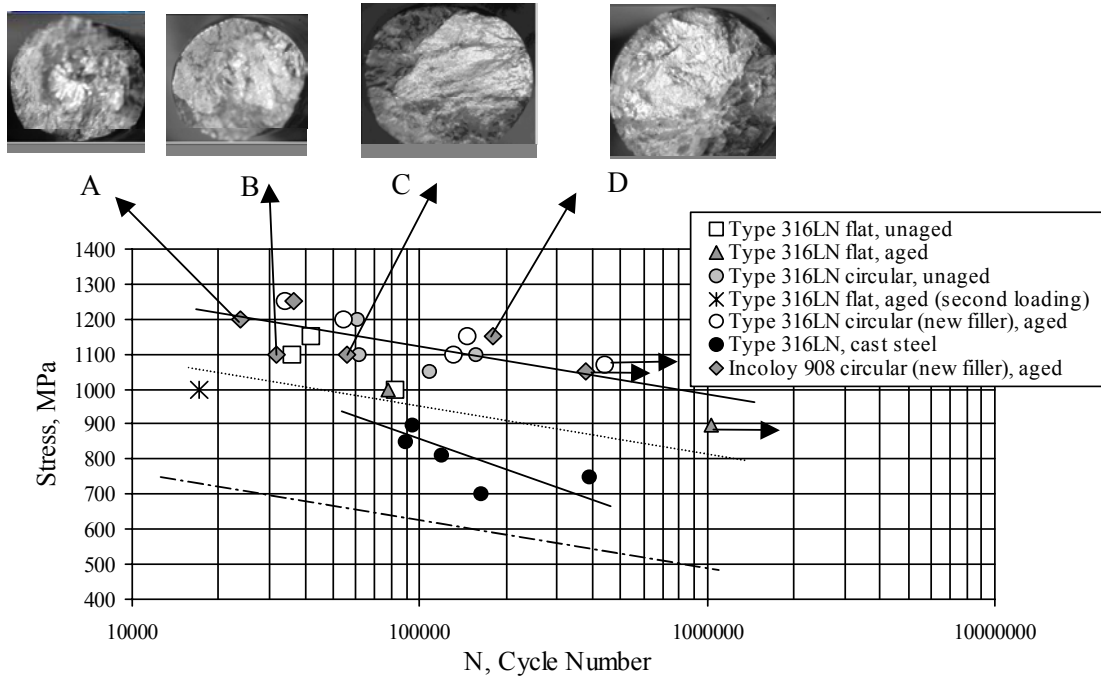
Fig. 1: Fatigue life results with Type 316LN (aged / unaged), Incoloy 908 (aged) jacket material butt-welds, and cast steel at 7 K (load ratio, R = 0.1). The photographs A to D show the fracture surface of fatigue life specimens of Incoloy 908 weld sections. The specimen A failed by an internal small weld defect of ~0.3 mm. For specimens B and C failure started from the surface by small flaws of ~0.3 and ~0.2 mm lengths. For specimen D the failure started from the surface of the specimen without an initial weld defect
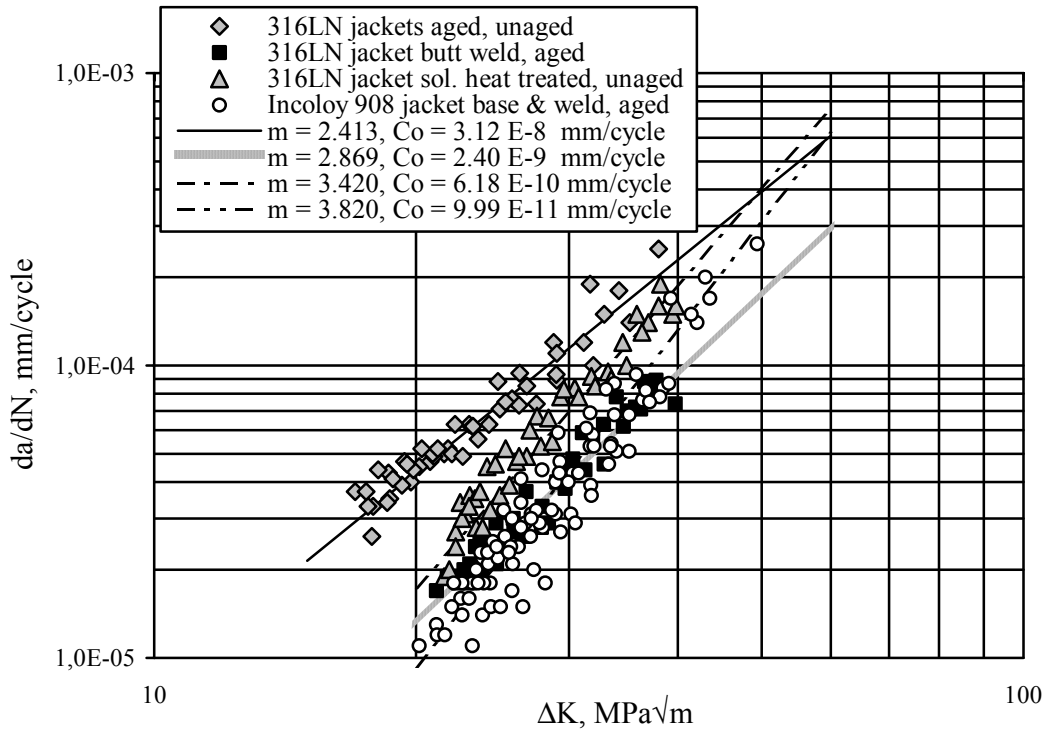


Fig. 2: FCGR of Type 316LN (Mat.: Valinox, aged and unaged) and aged Incoloy 908 (base/weld) jacket materials at 7 K (R = 0.1). The lines for m and $C_o$ show the mean of the determined Paris constants (m is dimensionless)
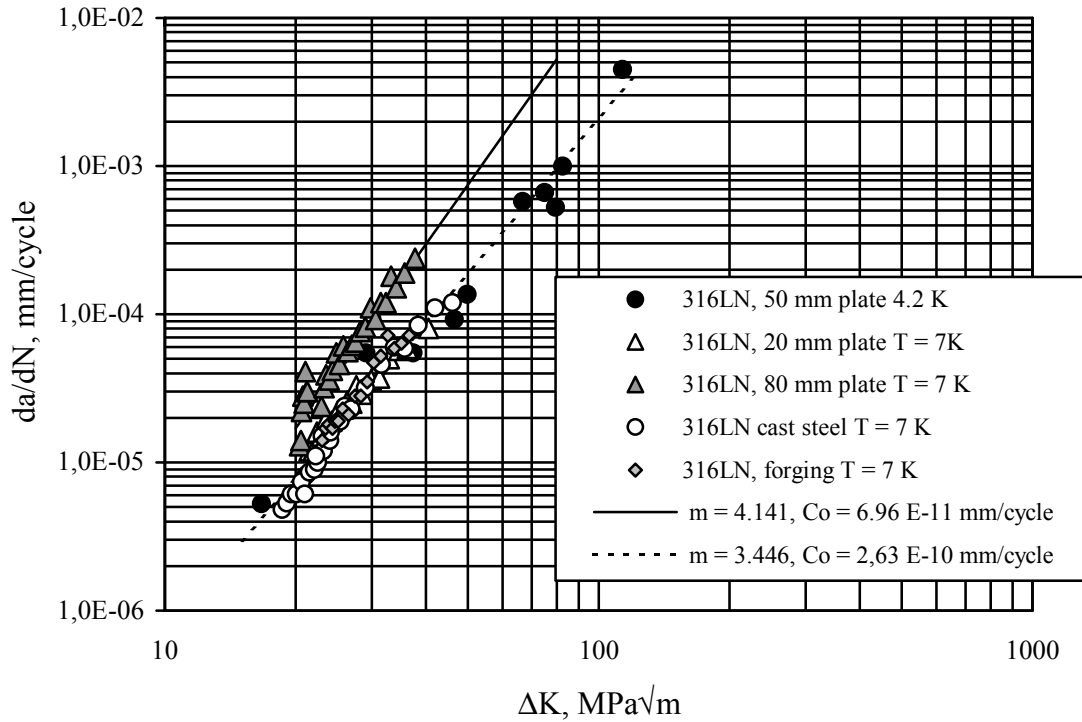
Fig. 3: FCGR of Type 316LN base materials at 7 and 4 K (R = 0.1). The lines along with m and $C_o$ show the mean of the determined Paris constants (m is dimensionless)

Literature:

[1] Nyilas A., Harries R. D., and Bevilacqua G., "Status of European material testing program for ITER model coils and full size mockups", in *Advances in Cryogenic Engineering (Materials)* 46A, edited by U. B. Balachandran et al., Plenum, New York, 2000, pp. 443-450.

[2] Krauth H. and Nyilas A., "Fracture toughness of nitrogen strengthened austenitic steels at 4 K", in *Fracture and Fatigue* in ECF 3, edited by J. C. Radon, Pergamon Press, Oxford (1980), pp. 119-128.

[3] Nishimura A., Yamamoto J., and Nyilas A., "Fatigue crack growth of SUS 316 and weld joint with natural crack at 7 K", in *Advances in Cryogenic Engineering (Materials)* 44A, edited by U. B. Balachandran et al., Plenum, New York, 1998, pp. 81-88.

[4] Nyilas A., Obst B., and Nishimura A., "Fracture mechanics investigations at 7 K of structural materials with EDM notched round and double edged-bars", in *Advances in Cryogenic Engineering (Materials)* 44A, edited by U. B. Balachandran et al., Plenum, New York, 1998, pp. 153-160.

[5] Darleston B. J. L., "The influence of fatigue on the energy scene", in *Fatigue 84,* Vol. III, edited by C. J. Beevers, Proc. of 2nd International Conference on Fatigue and Fatigue Thresholds, Birmingham (1984) pp. 1581-1595.

[6] Nyilas A., Krauth H., Metzner M., Munz D., "Fatigue response of materials used in large superconducting magnets for fusion technology", in *Fatigue 84,* Vol. III, edited by C. J. Beevers, Proc. of 2nd International Conference on Fatigue and Fatigue Thresholds, Birmingham (1984) pp. 1637-1649.

## T400-1/01
## Stress Analysis for the TFMC Tests in TOSKA

Under this task finite element electromagnetic and mechanical stress analysis is performed to prepare, support and evaluate the TFMC tests in TOSKA (Task M 44).

The work to perform test predictions reported in [1, 2] was continued. The global FEM-model [3] was improved further on to meet the final geometry of the TFMC joint leg. Also the coil clamping in the ICS had to be improved (side wedge covers and coil clamping screws at the front wedge). The actual extended global model consisting of the model coil (TFMC), the Intercoil Structure (ICS), the LCT-coil and the supporting structure is shown in Fig. 1.
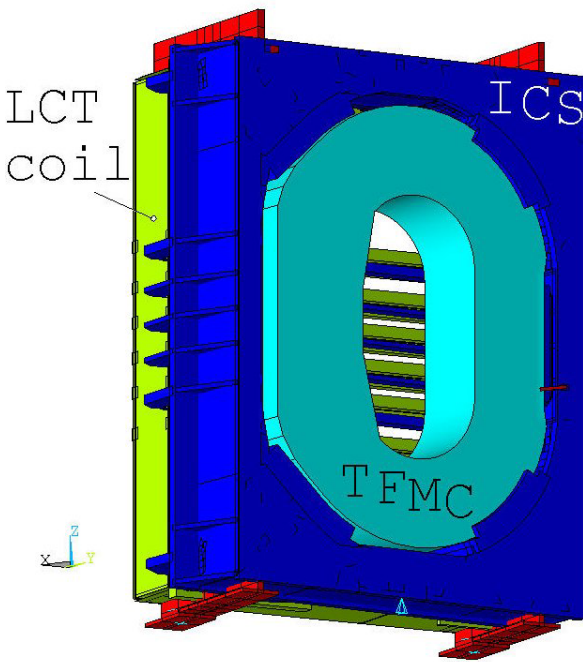


Fig. 1:  Mechanical model with TFMC fixed in the Intercoil Structure and the LCT coil behind

This model was used to calculate the predictions for the mechanical sensor positions shown in Fig. 2. The predictions for the displacements (sensors GDI), the stresses (rosette gauges GRI) and the uniaxial strains (gauges GEI) are reported in [4] for the two test phases:

Phase I:    TFMC loaded by 80 kA without LCT coil
Phase II:   TFMC loaded by 70 kA with LCT coil loaded by 16 kA.

All values in [4] are given for the maximum current of each test phase with parametric friction coefficient values.

During the installation of the test rig the global model was also used to calculate the required clearance, e.g. between ICS and TFMC considering some misfits of the components. Further on the bus bar movements have been calculated during cool down and loading. It turned out that taking into account the real supporting structure the bus bar movements are lower than assumed for the design where some idealized supporting conditions were used.

The study concerning plastic deformations at the highly loaded ICS side wedge, reported in [5], was continued by a sensitivity study of the side wedge tilt [6]. During the design [3] the wedge

tilt was introduced to reduce some stress concentrations on the side wedge edges. The question now was whether expected imperfections could have detrimental effects on the optimised stress distribution. The study showed that the imperfection sensitivity is rather low and that the stress reduction due to tilting is quite moderate, too.

In the meantime test phase I has been finished (see also task M44 'TFMC installation and test'). The evaluation of the sensor data is being done right now. Concerning the strain gauges some problems occurred due to an unexpected temperature sensitivity producing considerable data scatter. The displacement sensors suffered under sporadic drop outs, but nevertheless they gave satisfactory values in the average, except one sensor which totally failed.
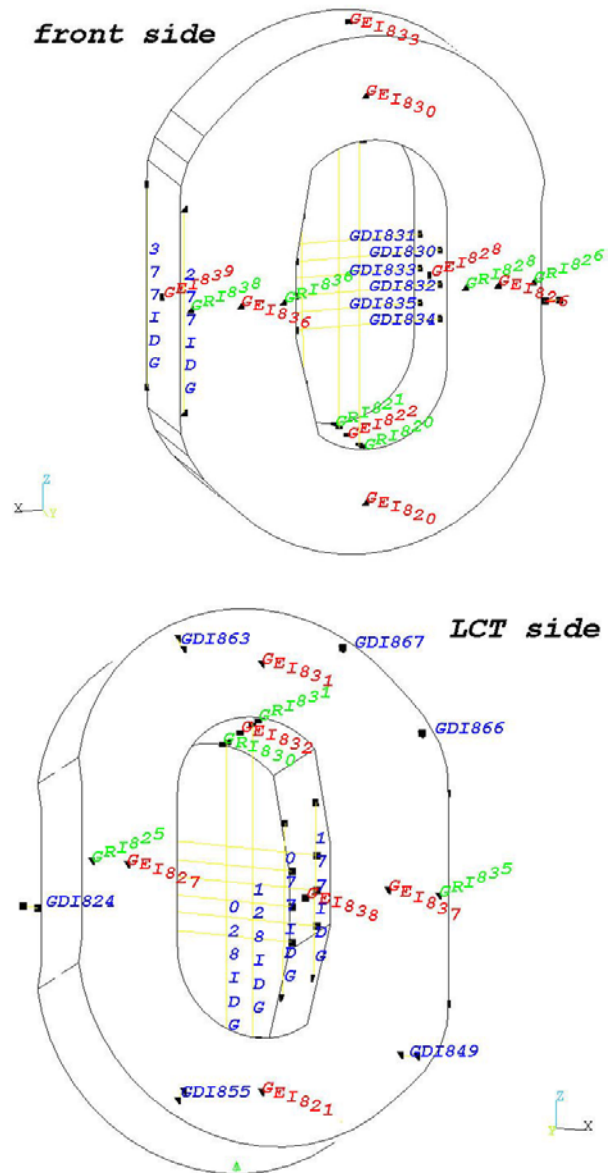


Fig. 2:  Mechanical sensors on the TFMC:
GDIxxx  displacement devices,
GRIxxx  rosette strain gauges,
GEIxxx  uniaxial strain gauges

A first evaluation shows that the measured global coil deformation and the stress level of the coil case is predicted quite well by the global model. Fig. 3 e.g. shows the comparison between predictions (continuous line) and measurements (cross

points) of the joint leg elongation inside and outside and the vertical coil diameter behaviour during a ramp cycle test with 80 kA maximum current. Considerable deviations from the calculations and also unexpected behaviour is observed by some strain gauges on the coil case side walls. There are some hints that this may be at least partly due to discrepancies between the real coil geometry (some out-of-plane asymmetry of the coil) and the relatively rough idealized FEM-model. Some clarification is expected by a more detailed mesh refined analysis.

To qualify the test data an extensive evaluation of all test data concerning the reproducibility and data scatter has been started. One question e.g. is, whether the data will allow for clear identification of non-linearity, such as the contribution of friction effects. Also some work concerning the observed sensor behaviour have to be done. With regard to the coming phase II tests with the more complex unsymmetrical coil loading it will be most important to have well characterized sensors.
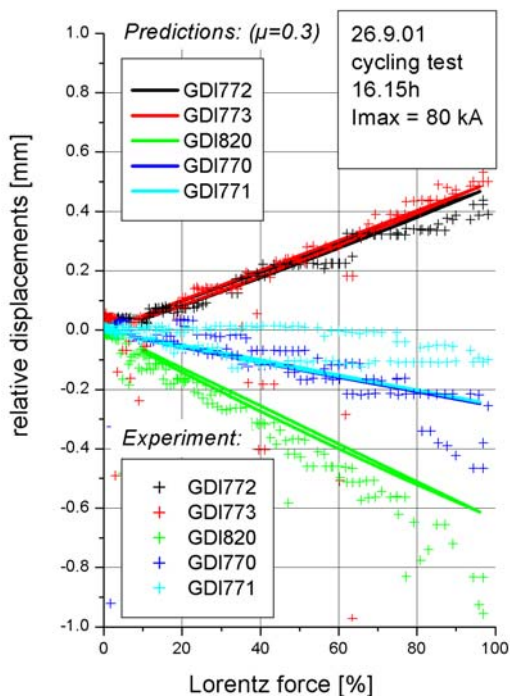


Fig. 3: Predicted and measured coil deformation of a cycling test

Staff:

G. Hailfinger
S. Raff
P. Schanz

Literature:

[1] Nuclear Fusion Project Annual Report of the Association Forschungszentrum Karlsruhe/Euratom, FZKA 6400, EUR 19326EN, p. 43

[2] Nuclear Fusion Project Annual Report of the Association Forschungszentrum Karlsruhe/Euratom, FZKA 6550, EUR 19707EN, p. 45

[3] B. Glaßl: Structural Analysis of the Inter Coil Structure ICS by a 3D FE Programme (Load 70/16 kA). Final Report, AGAN Technical Report TR-No-004, Cosortium AGAN, February 1998

[4] P. Libeyre, ed.: ITER Toroidal Field Model Coil (TFMC) - Test and Analysis Summary Report, Chapter 1: Specific Analysis Results Needed for Testing, CEA Internal Report AIM/NTT-2001.005

[5] P. Schanz, S. Raff: Stress Analysis for the TFMC Tests in TOSKA – Plastic Analysis of the Intercoil Structure, FZK Internal Report, Febr. 2001

[6] P. Schanz, S. Raff: ITER TFMC – Sensitivity study of side wedge tilting, FZK Internal Report, Mai 2001

## T400-1/01
## TF Model Coil (TFMC)

**Subtask : 3d quench analyses with the code system MAGS**

Before the TFMC tests got started the question arose whether a fast discharge can lead to a quench of the conductor or not. To answer this question several MAGS runs have been performed assuming a discharge time constant of 4 s starting from maximum current and another discharge time constant of 0.058 s starting with a current of 21.7 kA.

The analysis did show that there is no quench to be expected. Even though the maximum temperature in the radial plate ranges between 20 K to 25 K no quench occurs. This is because the heat transfer through the insulation to the cable takes time and flowing Helium can remove some of the introduced heat. If later critical temperatures at the strands are reached, the current has decayed to practically zero.

Staff:

R. Meyder

Literature:

[1] R. Meyder, R. Heller: Thermohydraulic Analysis of Discharge Scenarios of the TFMC using the MAGS code. Contibution to 14th TFMC T&A meeting May 2001

## T 400/1-01a
## Test of the ITER Model Coils, Contribution to the Test of the ITER Central Solenoid Model Coil (CSMC)

The goal of the task is the participation of members of the European Home Team (EUHT) in the installation and test of the CSMC at Naka, Japan as well as application of existing and new developed codes for the evaluation of the test results. The Task shall assure the transfer of experience of the CSMC test to the EUHT.

The Forschungszentrum Karlsruhe is involved in the following fields:

- Assessment of the cryogenic system and the operation during testing of the CSMC

- Behavior of the CSMC against transient voltages

Since the test of the TF insert in the CSMC coincided with the test of the TFMC in the TOSKA facility no staff member was available for participating in the test in Naka, Japan.

### 1 Behavior of the CSMC against transient voltages

Counteracting switches are applied in the dump circuits of superconducting coils if the discharge voltage rises to about 5 kV. Fast capacitor discharges generate fast voltage transients across magnet winding which can lead to nonlinearities of the voltage distribution in the winding (Fig. 1). These effects were previously studied by an electrical network model for the ITER TF full size coil and the TFMC.

With this experience, a network model for the CSMC was developed in collaboration with Institut für Energiesysteme und Hochspannungstechnik (IEH) of the University of Karlsruhe [1] for the CSMC.
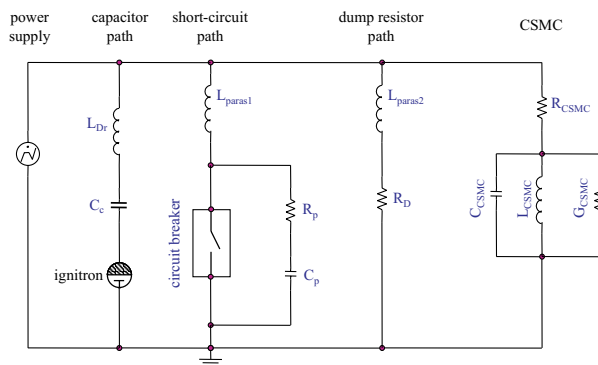


Fig. 1: Schematic discharge circuit of the ITER CSMC. $L_{Dr}$ represents and inductor adjustable to 10 to 20 µH in series to a parasitic inductances of 9 µH, $L_{paras1}$ and $L_{paras2}$ are parasitic inductances of 1µH and 30 µH, respectively

The transient electric behavior of the ITER CSMC has been studied by a detailed network model. The total inductance and the first natural frequencies could be verified by measured values and showed good agreement. It turned out that the capacitance of the instrumentation cables and the eddy current losses inside the conductor have a considerable influence on the frequency response of the coil. Transient oscillations with a frequency of about 2 kHz have been excited in the model by a safety discharge (Fig. 2).
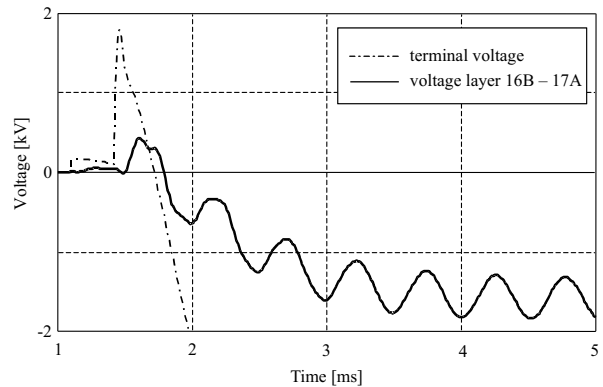


Fig. 2: Voltage at location of maximum transient insulation stress. At t = 1.42 ms the arc in the circuit breaker extinguishes and the current starts to commutate to the dump resistor path

However, the maximum allowable insulation stress has not been exceeded. It was found that the origin of the excitation is a short voltage pulse prior to the main discharge voltage. Its size and shape depends primarily on the charge of the capacitor bank $C_C$ and the values of the RC circuit parallel to the circuit breaker. This should be considered for the design for the design of the discharge circuit of the full size CS coil. Due to the lower natural frequencies, oscillations will be more likely to be excited.

Assuming a linear behavior of the coil a low voltage pulse generator with pulse rise times down to 1 µs was constructed and tested for experimental investigation of the ITER model coils and validation of the network model codes.

The final report about the CSMC network calculations were transmitted to EFDA / CSU in April 2001

Staff:

S. Fink
A. Ulbricht

Literature:

[1] C. Meinecke, A. M. Miri, S. Fink, A. Ulbricht, Investigation of the transient electrical behavior of the ITER Central Solenoid Model Coil (CSMC) during safety discharge, Proc. MT-17, Geneve, Sept. 24-28, 2001

# Fuel Cycle

# 99-514
# ITER Tritium Plant Design

The ITER tritium Fuel Cycle within the Tritium Plant shall accomplish safe handling, processing and recycling of the fuel gases needed for tokamak operation during the D-D and D-T phases of the machine. Already in early operational stages of the tokamak the Tritium Plant will be required as tritium is generated by D-D reactions. The central design guidelines for the Fuel Cycle are the minimization of tritium inventories (and therefore occupational exposure and the potential for unplanned releases), low generation of effluents and wastes, reduction of costs by standardization of components and simplicity of installation, commissioning and operation of the Tritium Plant.

To cope with the main Fuel Cycle duties, such as the collection and purification of unburned deuterium and tritium from the tokamak, the isotope separation into certain $Q_2$ mixtures (Q = H, D, T), the safe storage of deuterium-tritium mixtures, the supply of deuterium and tritium into the machine and the need for characterization of the gases handled, the ITER Fuel Cycle consists of four major systems:

- Analytical System (ANS)

- Isotope Separation System (ISS)

- Storage and Delivery System

- Tokamak Exhaust Processing (TEP)

In addition a distributed computer control system was required to be developed.

With the exception of the ISS, which was covered by ITER Canada, the different systems have been fully designed in detail at the TLK and integrated to constitute the complete Fuel Cycle of ITER. A detailed design is indispensable for tritium inventory considerations, and a credible Failure Mode and Effect Analysis (FMEA) can only be made against a detailed design. The flow diagrams with corresponding lists of components, heaters, instruments, pipes, and valves along with process descriptions are also essential for a reliable cost estimation. The design documentation of the tritium plant is structured in a way and developed to a level of detail which will facilitate procurement of all the tritium processing systems.

The ITER numbering system was extended to achieve a common format of the ISO standard Process Flow Diagrams (PFD's) and Pipe and Instrumentation Diagrams (P&ID's) for all systems of the tritium Fuel Cycle. Safety functions such as overpressure and/or overtemperature protection have been implemented into the detailed design. The design is based upon well-proven technology to ensure the safe handling of tritium together with credible accountancy and a high reliability of all components and high availability of the Tritium Plant throughout the lifetime of ITER.

An outline flow diagram (OFD) showing all major components and processing routes has been developed to provide a consistent overall design basis for the tritium Fuel Cycle of ITER. It identifies and defines all interfaces within the Fuel Cycle, served as a basis for the preparation of clear and coherent design documentation and allowed a proper identification of the interfaces to systems external to the Fuel Cycle. These external interfaces have been described in Interface Data Sheets including Chemical Flow Sheets and Pipe and Instrumentation Diagrams.

The tritium Fuel Cycle Systems are interconnected as follows: The TEP receives tritiated gas mixtures from the tokamak during various operational phases of ITER, from neutral beam injectors (NBI), and waste gas streams from the SDS, ANS, and the Fuelling System. The impurity-free hydrogen isotope streams from the TEP permeators are routed to the ISS and the detritiated impurities forwarded to the normal Vent Detritation System (N-VDS). The ISS receives all of its feed gas from TEP, and forwards isotopically adjusted mixtures to the SDS and a detritiated protium stream to a monitored plant discharge point. The SDS handles both incoming and outgoing tritium shipments to and from ITER, receives deuterium and tritium from the ISS, and stores and delivers to the Fuelling System (including NBI) fuel grade hydrogen isotopes and other gases. This system is also used for periodic tritium accountancy and recovery of the He-3 tritium decay product. The ANS has multiple connections for the receipt of gas samples for analysis from the TEP, ISS and SDS, and a single discharge of waste gas to the TEP.

Tritium inventories have been optimized and buffer vessel sizes have been established taking trade off between systems into account. The ISS and TEP sizes were optimized so that the ISS can operate without modification from 450 s burns up to 3,000 s burns with minimum overall tritium requirement for the campaign. (The optimum ISS size is 1.8 kW as measured by the sum of condensing power in all four columns.) The complementing TEP size must progressively increase from 100 to 400 molhr$^{-1}$ as the burn cycles extend from 450 to 3,000 s with corresponding dwell times equal to three times the burn time. This is feasible due to the modular character of the front-end permeator subsystem of TEP.

As some systems interconnected to tritium Fuel Cycle System, such as the Water Detritation System (WDS) and the Atmosphere Detritation Systems, operate even during ITER maintenance periods, the ISS will continuously receive (via TEP) a tritiated protium stream. The separated tritium (and deuterium) will normally be sent to the SDS, irrespective of the ITER operational status.

One of the next steps would be an overall FMEA on the basis of the FMEA's for the different systems and the implementation of the consequences into the design, for example buffer vessels for off-normal operations.

Staff:

C. Caldwell-Nichols
L. Dörr
M. Glugla
R. Lässer
P. Schäfer

# TR 1
# Tokamak Exhaust Processing

The principal techniques developed by different research groups for the detritiation of primary gaseous wastes are altogether based on multiple process stages comprising at least one step involving heterogeneously catalyzed chemical reactions. While the permeation of hydrogen isotopes through palladium/silver membranes combined with heterogeneously catalyzed reactions were proven to be particularly suitable for highly contaminated gases, isotopic swamping is the method of choice in ITER for the final detritiation and recovery of residual amounts of tritium. Such a process step is essential from the viewpoint of tritium economy even if the quantities of tritium to be retrieved may be comparatively low: Tritium lost into any atmosphere or vent detritiation system either needs to be finally wasted or recovered after regeneration of the molecular sieves via water detritiation and isotope separation.

Experiments with the CAPER facility at the TLK have demonstrated that in a closed loop comprising a catalyst bed and a palladium/silver permeator the detritiation of gas mixtures containing $Q_2$, $CQ_4$, $Q_2O$, CO, $CO_2$, He and other inert gases proceeds irrespective of the gas composition as long as carbon is present on the catalyst surface. A complete set of reactions describing the chemistry is:

$$CQ_4 \leftrightarrow C + 2\,Q_2 \qquad (1)$$
$$C + CO_2 \leftrightarrow 2\,CO \qquad (2)$$
$$CO + Q_2O \leftrightarrow CO_2 + Q_2 \qquad (3)$$
$$CO + 3\,Q_2 \leftrightarrow CQ_4 + Q_2O \qquad (4)$$
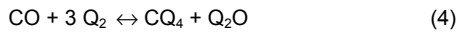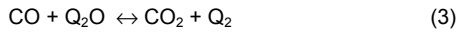
Nickel on kieselguhr ($SiO_2$) in the form of a precipitated catalyst was found to be the most robust catalyst material for this purpose.

The final clean-up detritiation step is based on counter current isotopic swamping in a permeator catalyst (PERMCAT) reactor. To promote the exchange reactions

$$H_2 + CQ_4 \leftrightarrow CH_4 + Q_2 \qquad (5)$$
$$H_2 + Q_2O \leftrightarrow H_2O + Q_2 \qquad (6)$$
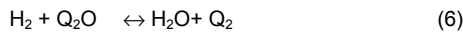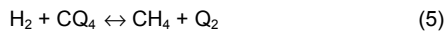
also a catalyst is required, which if possible should not promote the methanation reaction (4). The production of methane and water during isotopic swamping locks up some hydrogen and thereby reduces the driving force for permeation in the PERMCAT. A systematic study was therefore carried out to develop the most favourable catalyst for the PERMCAT reactor. Numerous catalysts have been prepared, characterized and compared along with commercially available catalysts for their ability to support isotope exchange reactions and methanation reactions. Aluminum oxide and silicon dioxide or kieselguhr was used as a catalyst support material. Not only precious metals, such as palladium, rhodium and platinum, but also nickel and nickel-copper alloys and palladium-gold alloys were investigated.

The results from screening the activity of pure nickel, nickel/copper alloys and pure copper with respect to the methanation reaction and the $CH_4$ - $D_2$ exchange reaction are shown in Figure 1 and Figure 2, respectively. For both reactions the catalytical activities of pure nickel commercial catalysts and catalysts prepared at the TLK are comparable; the temperature at which these catalysts were activated by reduction in a hydrogen atmosphere have no observable effect. The activity of the catalysts for both reactions decreases with increasing copper content and activation temperature. Neither methanation nor isotopic exchange was observed on pure copper catalysts.
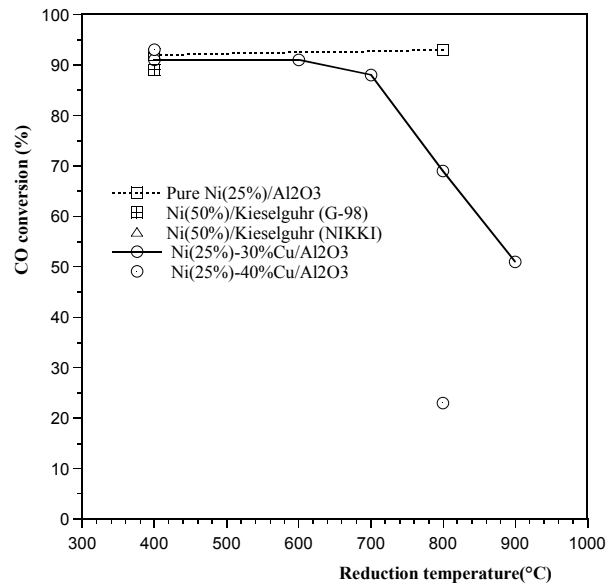


Fig. 1: Methanation activity on Ni/Cu catalysts at 400°C
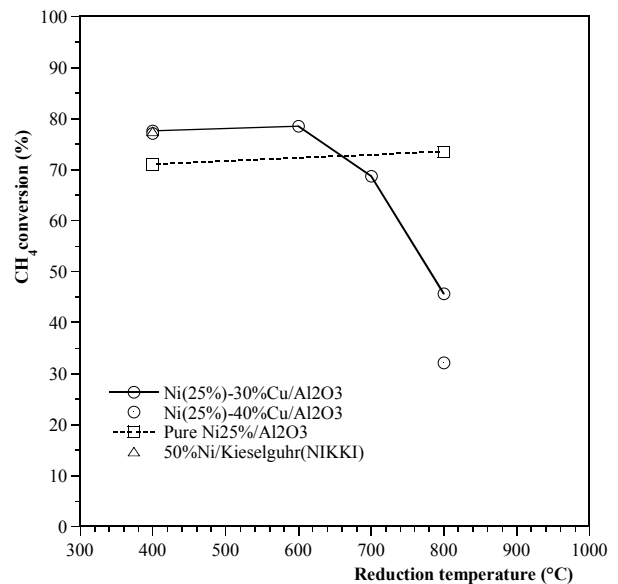


Fig. 2: $CH_4$ - $D_2$ exchange activity on Ni/Cu catalysts at 400°C

On commercial platinum, palladium and rhodium catalysts a complete methanation was observed at 400°C. Regular platinum group metal catalysts have therefore no advantage in a PERMCAT as compared to a nickel catalyst.

The catalytical activities measured on palladium and palladium/gold alloys specifically prepared have shown an initially promising effect. Depending on the support material and the reduction temperature during activation the catalytical activities for the methanation reaction and the $CH_4$ - $D_2$ exchange reaction are quite different, as seen in Figure 3 and Figure 4, respectively. Silica supported palladium based catalysts undergo a strong metal support interaction (SMSI) leading to a substantial decrease in the catalytical activity for methanation, while the catalytical activity for the $CH_4$ - $D_2$ exchange reaction remains essentially constant. The catalyst with 20% palladium on Aerolyst 350 ($SiO_2$, Degussa -Hüls) activated under hydrogen at 800°C shows the selectivity sought: The catalyst activity for the $CH_4$ - $D_2$ exchange is essentially the same as for palladium catalysts reduced at lower temperatures, while the catalyst activity for the methanation reaction is negligible.
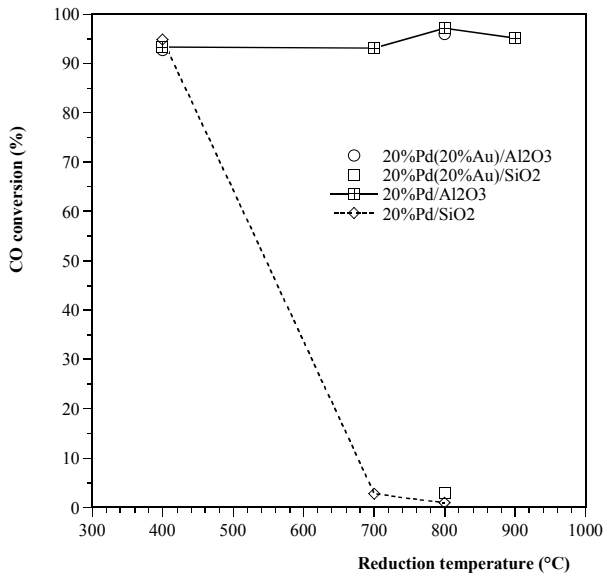
Fig. 3: Methanation activity on Pd/Au catalysts at 400°C
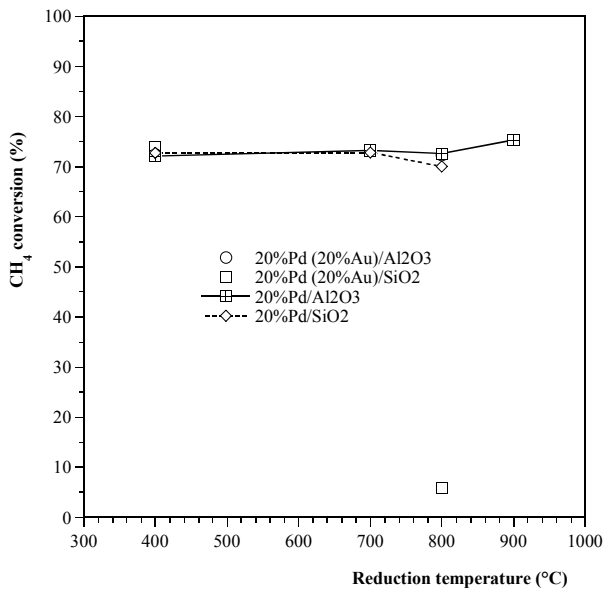


Fig. 4: $CH_4$ - $D_2$ exchange activity of Pd/Au catalysts at 400°C

The work has shown that catalysts can be designed such that only certain reactions are supported and the selectivity of the material can be tuned within certain limits. However, even though CO is not converted into methane on high temperature activated $Pd/SiO_2$ catalysts, the initially high activity of the material for the $CH_4$ - $D_2$ exchange reaction is almost completely blocked in the presence of CO. Such a catalyst poisoning was not observed for $CO_2$. As a consequence the PERMCAT reactor for isotopic swamping should either be operated with the robust nickel catalyst or any CO present in the gas to be detritiated must previously be oxidized. The operation of the CAPER facility at the TLK will finally disclose the optimal method.

Staff:

B. Bornschein
M. Glugla
K. Günther
R. Lässer
T.L. Le
K.H. Simon
Fa. D. Niyongabo

# TR 12
# Development of Tritium Analytical Devices

## Introduction

The knowledge of the chemical composition of gases in any processing plant is of fundamental importance for safe operation and achievement of well characterised product streams. This is particularly relevant in tritium handling plants regardless of whether they are used for basic research, preparation of products for external applications or constituents of the fuel cycle of fusion reactors. Tritium containing mixtures do not only change due to the decay of T into $^3$He, but also due to radiation induced processes. Thermodynamically stable gas species may be split into ions, radicals and fragments by the energy released during tritium decay and new molecules can be created which were not initially present. It is well known that tritium reacts with gases adsorbed on inner walls of their containments and is capable of removing dissolved materials, such as carbon in steel.

One of the major tasks of the Tritium Laboratory Karlsruhe (TLK) is the development or enhancement of effective and new methods for the analysis of tritium containing gas mixtures as well as their technical and practical demonstration in the daily applications of a tritium processing plant. The main methods [1] used for the analysis of tritium in gases at the TLK are mass spectrometry (Quadrupoles and Omegatrons), gas chromatography, laser Raman spectroscopy, calorimetry and ionisation chambers. Among these techniques, gas chromatography plays a special role. Three gas chromatographs are employed with packed columns, two are used for the routine applications in the Tritium Measurement Techniques (TMT) System and one is dedicated to the CAPER experiment. In the latter the processing of fusion exhaust gases is simulated by in situ mixing of various impurities with tritium and measurement on their detritiation aiming to achieve a detritiation factor of $10^8$.

## Gas chromatography

Gas chromatography is a well proven analytical tool for determination of a large variety of gas compositions. Commercial separation columns and special detectors are available for almost any gas analytical application. The injected sample is forced through a separation column by the carrier gas. Various gases of a sample exit the column at different retention times due to different interaction between the gas species and the material inside the column. The retention time characterises the type of gas and the area of the peak the concentration. The separation of hydrogen mixtures by gas chromatography is possible at temperatures lower than 170 K. In most cases liquid nitrogen is used. Therefore, other gases which condense or are absorbed by the column material must bypass the low temperature column to be detected. Very recently micro gas chromatographs with special packed or capillary columns were developed which have retention times of less than 3 minutes, require very small amounts of gas for analysis and employ special detectors (micro thermal conductivity detectors) built using semiconductor processing technology with the high sensitivity. Disadvantages of gas chromatography are the long retention times in the case of packed columns, that the separated tritium is mixed with the carrier gas requiring special clean-up systems if the release is not acceptable and that components might not fulfil the stringent leak tightness requirements of a tritium plant.

## Laser Raman spectroscopy

Laser Raman spectroscopy has been developed to a powerful tool and is now well capable to give an accurate knowledge of the gaseous composition of $Q_2$ mixtures within a short measurement time. Various experimental set-ups with laser and spectrometer positioned either outside or inside a glove box or by sending the laser light via optical fibres to the Raman cells have been tested in recent years. Disadvantages of laser Raman spectroscopy are the use of windows, possible darkening of windows due to deposition of material on the surfaces, that noble gases are not detected and that quantitative analysis of more complex molecules such as $CQ_4$ or even higher hydrocarbons is very difficult because the spectra of all possible combinations of H, D and T in these molecules need to be measured and analysed.

## Mass spectrometry

Various types of mass spectrometer (quadrupoles, omegatrons, single or double focusing instruments, time of flight instruments, etc.) are nowadays commercially available. The mass resolution of these instruments varies generally from 100 to 3000 and with the exception of $^3$He and T most gas molecules of interest can be separated. The instruments need special gas inlet systems as the usual operating pressure is below $10^{-4}$ Pa and use electrons to create ions which are then detected. Cracking products are created inside the electron gun. If the mass resolution is not high enough the analysis of a mass spectrum is difficult due to the presence of cracking products with similar masses originating from different gas species - especially if all three hydrogen isotopes and multiple ionised gas species are present. Furthermore, the composition of a gas mixture is modified by the electron impact and the high temperature of the filament in the ion source which means that only the atomic concentrations are correctly determined.

## Result of the comparison of the three analytical tools

A comparison between the three techniques showed that gas chromatography is the simplest one, the one most often used, by far the cheapest, demanding only a small amount of space, can be placed fully into a glove box, does not need ultra high or high vacuum pumps, does not use any type of window material, is easy to be learnt, operated and maintained. Due to these reasons the analytical equipment chosen for the Analytical System [2] of the ITER Tritium Plant are 3 micro-gas chromatographs (µGCs) and two packed gas chromatographs (GCs).

## Gas chromatographic studies performed at TLK

At the TLK three gas chromatographs [3] with packed separation columns are in daily use, but the experience in micro gas chromatography and its use in tritium applications is limited. Very recently a micro-gas chromatograph was purchased with two separate modules each containing a special injection system (sampling volume and purging pump), its capillary column (either Hayesep (25 cm long) or molecular sieve 5A (4 m long)) and a micro-thermal conductivity detector (built in semiconductor technology). First measurements were performed with various gas mixtures.

For comparison, chromatograms obtained with the conventional gas chromatograph GC-2 which is part of the Tritium Measurement Techniques (TMT) in TLK and employs packed columns, and with the micro-gas chromatograph mentioned above are presented in Fig. 1 and Figs. 2/3, respectively, for the same gas mixture. The gas mixture used contained the following species: 5.09% He, 1.01% $N_2$, 0.99% $CH_4$, 0.987% CO, 1.00% $CO_2$, 0.964% $C_2H_6$, 1.04% $C_3H_8$ and 88.919% $H_2$. He is used as carrier gas in the three gas chromatographs. In case of GC-2 only one sample is injected and analysed by the various columns and detectors, whereas in the case of µGCs each module is fed by a single gas sample.
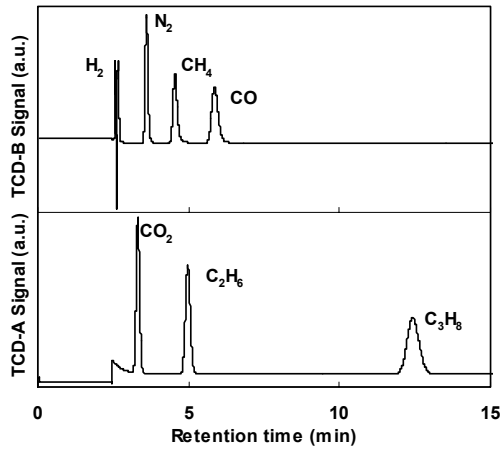
Fig. 1:  TCD-A and TCD-B chromatograms of GC-2

The TCD-A spectrum (Fig. 1) of the conventional chromatograph contains only three peaks $CO_2$, $C_2H_6$ and $C_3H_8$, because the fast eluting gases He, $H_2$, $N_2$, $CH_4$ and CO were injected into a further column packed with molecular sieve 5A (3 m long, 100°C). After CO passed a Valco valve it is switched and the gases $CO_2$, $C_2H_6$ and $C_3H_8$ later eluting from the two other columns (Porapak (3m long) and Chromosorb (2 m long) in series and at 120°C) are transferred to the TCD-A and detected. After 8 minutes the temperatures of the 3 columns are ramped up to 150°C with a speed of 10°C/minute. The splitting and injection of the gas mixture into the different columns (Porapak/Chromosorb and molecular sieve) is necessary because otherwise $CO_2$ and the higher hydrocarbons would be trapped in the molecular sieve bed and would not be observed. The retention times for CO and $C_3H_8$ are 5.9 minutes or 354 seconds after passage through the Porapak/Chromosorb and molecular sieve columns and 12.4 minutes or 744 seconds after exiting the Porapak/Chromosorb column, respectively. The first peak of the TCD-B shows a very sharp and deep minimum. This shape of the $H_2$ peak is caused by the anomaly in the thermal conductivity behaviour of He-$H_2$ mixtures. The signal to noise ratio of the measurements are very good, because large sample amounts (210 kPa times 0.2 $cm^3$) were injected.
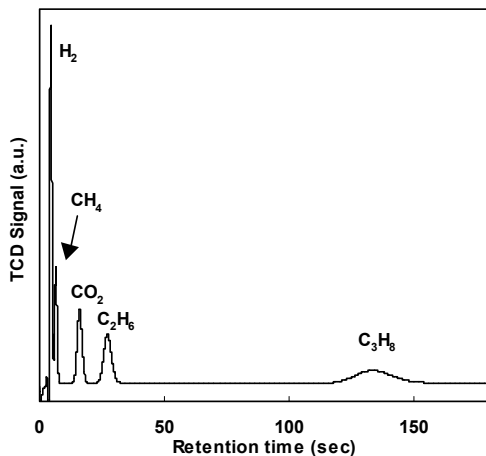


Fig. 2:  µTCD chromatogram with molecular sieve capillary

Fig. 2 and Fig. 3 present the micro-GC chromatograms obtained with the capillary molecular sieve column at 40°C and the capillary HayeSep column at 60°C, respectively. The µTCD chromatogram of Fig. 2 is very similar to the corresponding one of Fig. 1 with respect to the number and shape of the peaks especially if one considers that the area under the CO peak in Fig. 1 is larger than the $CH_4$ area due to the increased peak width. The main differences between Fig. 1 and 2 are the far shorter retention times although the column temperatures were far lower than the ones used in GC2. Fig. 3 shows the peaks of $CO_2$ and of the hydrocarbons $CH_4$, $C_2H_6$ and $C_3H_8$. The retention time of the last eluting gas specie $C_3H_8$ is 130 seconds, approximately 6 times shorter than for GC2.
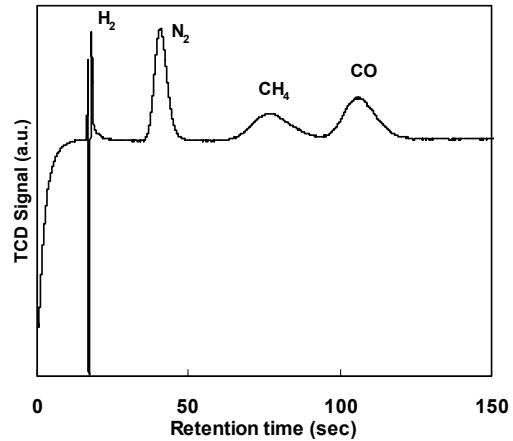


Fig. 3:  µTCD chromatogram of the µGC with HayeSep capillary

The results indicate that the impurities to be handled in a tritium processing plant can easily be measured with micro-gas chromatography. A further advantage of micro gas chromatography is that the amount of sample to be injected for detection is far smaller than in the case of conventional systems due to the capillary columns and the more sensitive µTCD. With respect to tritium this means that the tritium amounts to be injected for analysis are also far smaller than with packed columns.

**Future analytical work in the field of gas chromatography**

Further work will involve the application of special external columns which are cooled because the gas chromatographic separation of tritium gas mixtures can only be performed at temperatures < 150K. This requires modifications of commercial micro-gas chromatographs. The development of these techniques for the analysis of hydrogen mixtures with µGCs will be one of the main analytical tasks in the near future.

Staff:

S. Grünhagen
R. Lässer

Literature:

[1] R. Lässer, C. Caldwell-Nichols, L. Dörr, M. Glugla, S. Grünhagen, K. Günther, R.-D. Penzhorn: Analytic of Tritium-containing Gaseous Species at the Tritium Laboratory Karlsruhe, to be published in 21th SOFT, Madrid.

[2] R. Lässer, M. Glugla, T. Hayashi, P. Schuster, H. Yoshida: The analytical system of the ITER Tritium Fuel Processing Plant, to be published in 6$^{th}$ Int. Conf. Tritium Science and Technology, Tsukuba 2001, Japan.

[3] R. Lässer, M. Glugla, S. Grünhagen, K. Günther, R.-D. Penzhorn, J. Wendel: Use of gas chromatorgraphy in the Tritium Laboratory Karlsruhe, to be published in 6$^{th}$ Int. Conf. Tritium Science and Technology, Tsukuba 2001, Japan.

**TEP 13A**
**Self-assay, Fast Delivery Tritium Storage Bed Development**

**Introduction**

In the tritium plant of ITER large amounts of tritium (approximately 800 g for a 3000 seconds long plasma pulse assuming a tritium supply rate of 100 $Pam^3s^{-1}$) have to be injected into the tokamak and kg tritium inventories have to be stored and processed in a safe and efficient manner.

In the present design of the Storage and Delivery System (SDS) [1] of the ITER tritium plant 19 hydrogen storage beds are foreseen. Each bed will have a storage capacity for 100 g tritium, a hydrogen supply rate of up to 200 $Pam^3s^{-1}$ and the capability of in-situ calorimetry. In-situ calorimetry is required to determine the tritium inventory of each bed by measuring the temperature increase due to the decay heat of 0.324 W per g tritium. The advantage of a self-assaying storage bed is that the tritium does not have to be removed from the bed into a large reservoir as required when the accountancy method using pressure, volume temperature and tritium concentration (pVT-c) measurements is employed. In addition, the bed must be equipped with secondary containments to collect tritium permeated at higher temperatures, built with fully tritium compatible construction materials, and to be easily operated in a safe way. 10 further beds are used in the so-called Long Term Storage (LTS) of SDS where the large tritium amounts expected to be trapped in the ITER tokamak, especially in the carbon of the divertor, during extended plasma campaigns will be stored after dedicated clean-up phases to regain the temporarily trapped tritium. The only difference is that the beds of LTS will not need in-situ calorimetry as they are loaded and de-loaded relatively infrequently.

**Use of tritium storage beds**

The storage of tritium in metals as metal tritides is considered to be the simplest, safest and most compact way. The advantages of metal hydrides (hydrogen here refers to protium, deuterium and tritium) storage beds are:

- Appropriately chosen metals used as storage material have very low hydrogen equilibrium pressures ($< 10^{-5}$ Pa) at room temperature. These beds function as pumps for hydrogen at room temperature (without any moving mechanical parts) because they can absorb large amounts of hydrogen and the final pressure is the hydrogen equilibrium pressure which is a function of temperature and atomic hydrogen concentration in the metal. A further advantage is that permeation is negligible at room temperature. At higher pressures due to radiation induced processes, tritium reacts with impurities on and dissolved in the surrounding wall. As a consequence, the purity of the tritium gas will decrease with time. All these effects can be neglected at the very low hydrogen equilibrium pressure above the storage material at room temperature.

- The hydrogen density in metal hydride alloys can be very high allowing a very compact design. Even under the consideration that during hydrogen intake most metals disintegrate into powder and that powder needs far more space than bulk material, storage beds can be built in a very compact way.

- The hydrogen equilibrium pressures over storage materials at moderately low temperatures (approximately 400°C) are in the 100 kPa range. The getter beds work at these temperatures as compressors and function as a hydrogen source supplying the hydrogen gas at constant pressure in the two phase regions. It is clear that over-pressurisation by heating the getter bed with the valves closed must be strictly avoided.

- Due to the high affinity of storage materials to oxygen, water, nitrogen, higher hydrocarbons, etc. the purity of the hydrogen gas after even one absorption cycle in the getter bed improves resulting in very clean hydrogen mixtures. Most of the impurities are irreversibly trapped by the metal storage material with the main disadvantage that the amount of the getter material available for hydrogen absorption decreases. Therefore, the introduction of large amounts of impure gases into storage beds should be avoided. Especially the introduction of air or pure oxygen into beds is to be prevented as high temperatures may be achieved due to the high heat generated by the exothermic reaction and the low thermal conductivity of powder.

**Design criteria of a self-assay, fast delivery tritium storage bed for ITER**

The power needed for a hydrogen desorption rate of 200 $Pam^3s^{-1}$ is calculated to be 7.7 kW by means of the slope of the plateau pressure in the two phase region of $ZrCoQ_x$ (Q = H, D, T) as a function of the reciprocal temperature. Approximately the same amount of heat is generated during absorption and needs to be removed if fast absorption is required.

The power of 8 kW is supplied to the getter material by internal and external thermocoax heaters. The largest fraction of heat is generated by two internal heaters mounted into grooves machined into the outer surface of a Cu-cylinder. The Cu cylinder is placed parallel to the cylinder axis in the middle of the whole getter bed. External heaters are placed into grooves machined into the outer stainless steel surface of the primary containment. They loose a certain fraction of their power to the surroundings and are not so efficient as the internal heaters.

Getter materials disintegrate into powder upon hydriding. Powder is known to have a very poor thermal conductivity. To overcome this problem 45 Cu sheets of 1mm thickness (in the following called fins), separated by 6 mm, are installed between the inner and outer cylindrical stainless steel walls of the primary containment. The space between the fins is to be filled with coarse ZrCo powder which will disintegrate further upon hydriding. A further disadvantage of powder is that it can be easily spread through the pipe work by high gas streams. This needs to be strictly avoided because powder can lead to damage (e.g. valve seats may loose their leak tighness or flow controllers may get plugged). Furthermore, powder deposited in cold regions where heating is impossible can absorb large amounts of tritium without the possibility of recollection. Filters are to be installed and care needs to be taken to avoid plugging of the filters. Large filter areas are to be provided to reduce large pressure drops.

During accountancy the decay heat generated by the tritium inventory absorbed in the bed is removed by He gas circulated through a U-shaped 6x1 stainless steel tube installed in the middle of the ZrCo powder and in good thermal contact with the fins. To achieve high temperature differences by the tritium decay the various material masses needed to build the primary containment should be minimised as far as possible.

A further coaxial tube is installed in the Cu cylinder to remove the heat generated during absorption of the hydrogen in the getter material. If necessary, this tube could also be used to remove the decay heat. A further possibility to determine the decay heat is to simply measure the temperature increase of the primary containment by temperature sensors installed in the Cu cylinder. This method would be far simpler than the circulation of He through an external closed loop.

The storage beds are designed with inlet and outlet connections to permit circulation of hydrogen through the bed. This is important whenever hydrogen is to be absorbed from mixtures with inert gases. In the absence of a circulation facility the hydrogen would be only well absorbed at the very beginning, but the concentration of the inert gases which are not absorbed would increase above the storage material and finally stop the further uptake of hydrogen by the storage material due to the very long diffusion times of hydrogen through the inert gases.

The goal to design and manufacture a storage bed with fast delivery properties is directly linked to the use of materials with high thermal conductivity, the application of powerful heaters and the achievement of optimum heat transitions between the various parts involved and of a compact structure of the storage bed.

**Vacuum brazing**

For optimum heat transfer between the heaters, the coaxial tube, the Cu-cylinder, the walls of the primary containment, the fins, the U-shaped tube and the powder optimum vacuum brazing of the various materials is of greatest importance. This requires the installation of reservoirs for the brazing materials and very accurate machining of the various parts to achieve the optimum gaps of approximately 50 microns between the various materials. The following parts need to be brazed together:

- The coaxial tube for cooling and the Cu cylinder in the centre,

- The two internal heaters (placed into the grooves of the outer surface of the Cu cylinder) and the Cu cylinder,

- The outer surfaces of the Cu cylinder and the outer surface of the inner stainless steel tube of the primary containment,

- The 45 fins and the inner surface of the inner stainless steel tube of the primary containment,

- The 45 fins and the U-shaped 6x1 stainless steel tube,

- The 45 fins and the inner surface of the outer stainless steel tube of the primary containment,

- The two external heaters (placed into the grooves of the outer surface of the outer stainless steel tube of the primary containment) and the outer stainless steel tube.

The primary containment is surrounded by a secondary containment to collect tritium permeated at higher temperatures, e.g. during heating. The secondary volume is normally filled with He gas to transfer the tritium decay heat to the outer walls. The helium gas will be pumped off only before heating of the getter beds or before accountancy runs.

The beds are designed to withstand the highest possible hydrogen equilibrium pressures which can be achieved at a certain maximum temperature. Furthermore, hardware and software interlocks for temperatures and pressures are installed to switch off any power to the getter bed in case temperature or pressure limits are reached.

**The status of the project**

The design of a tritium storage bed for ITER incorporating the requirements and specifications mentioned above has been finalised. Manufacturing drawings have been approved and contracts for manufacture of a self-assay, fast delivery tritium storage bed have been placed.

Staff:

W. Jung
R. Lässer

Literature:

[1] R. Lässer, L. Dörr, M. Glugla, T. Hayashi, D.K. Murdoch, R.-D. Penzhorn and H. Yoshida: The storage and delivery system of the ITER tritium plant, to be published in 6th Int. Conf. Tritium Science and Technology, Tsukuba 2001, Japan.

# TR 4
# Tritium Recovery from Plasma Facing Components

Tritium in first wall materials of fusion machines is a matter of concern not only for inventory but also for safety reasons as it may produce volatile compounds potentially hazardous during handling. In first wall carbon tiles of D-D and D-T operated fusion machines tritium is found predominantly in a very thin co-deposited layer and/or as implanted layer with a thickness of few tens of micrometers. Since the tiles must eventually be disposed off in a repository it is desirable to reduce the total tritium inventory in the tiles down to the corresponding Low Level Waste (LLW) category. In this context, the development of detritiation techniques for graphite and CFC tiles recovered from the first wall of fusion machines is of paramount importance. However, the experimental techniques investigated until now are limited by the conditions permissible inside of the torus. When dealing with the tiles outside of the reactor more severe treatment conditions are acceptable. Working in that direction, numerous screening tests have been carried out at the Tritium Laboratory in Karlsruhe (TLK) trying various techniques as mechanical abrasion, ultrasonic bath, heating under moist air, argon, or ozone and Radio-frequency (RF) under moist noble gas atmosphere.

Among them the preliminary tests using RF under moist argon appeared to be very promising not only in terms of tritium release but also because it could be possible to be used inside the torus.

In these experiments the specimens were heated by radio frequency heating in a stainless steel apparatus (Fig.1).
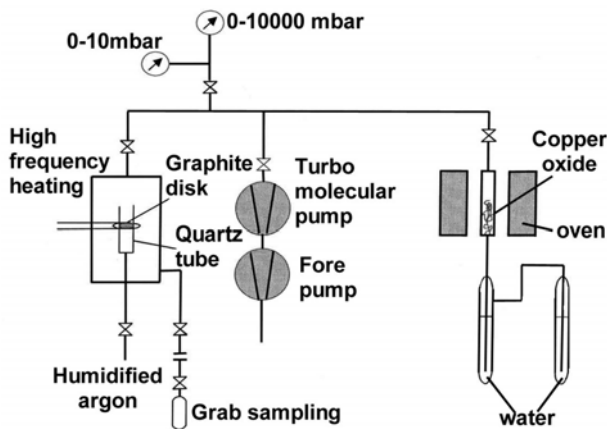


Fig. 1: Experimental set-up for the RF detritiation

The disk was heated very rapidly by RF heating up to a temperature of 850°C. Of the total activity in the disk more than 96 % are liberated after heating under moist argon for 24 hours at 850°C. Moreover, when the stainless steel reactor was opened it was observed that a very thin disk had spalled off from the main disk. After combusting both disks it appeared that only the thin disk contained the rest of the tritium activity (Fig. 2).

We concluded that the spalled off thin disk constitutes actually the co-deposited layer.



Fig. 2: Thick and thin disc after the RF heating under moist argon

In order to test that technique in full scale using complete tiles, an experimental Tritium Decontamination facility (TIDE) installed in a glove box was prepared at the TLK. The facility is able to handle complete tiles up to 900 $cm^3$ in realistic conditions with a simultaneous treatment of the released gas. The decontamination factor will be calculated either using full combustion of selected specimens before and after the RF treatment or using a new calorimeter capable to measure the tritium activity of a whole tile.

The new calorimeter is expected to be operational by the middle of next year. Currently the RF technique is under optimisation and the necessary calibration tests are carried out with tiles containing low tritium levels.

Staff:

N. Bekris
H. Dittrich
W. Jung
P. Haeffner
W. Hellriegel
M. Sirch

## TSW-001
## Tritium in CFC and Graphite Waste

Present-day tokamaks like JET use tiles of graphite and carbon fibre composite (CFC) as first wall materials. Merits of carbon are its low Z, high heat conductivity, neutron compatibility and good mechanical properties. For the divertor strike point region CFC is the preferred material because it sublimes rather than melts during disruption thermal quenches or giant edge localised modes. A drawback of carbon is its relatively high erosion rate resulting in co-deposition with hydrogen isotopes and beryllium in cold regions of the vessel close to the areas of greatest erosion and in the gaps between the tiles.

After campaigns with tritium carbon tiles become contaminated to various degrees, the extent depending upon the tile location in the vessel and the type of plasma / wall interaction to which they were exposed. The most likely mechanism of tritium retention is co-deposition together with eroded carbon. In fact, tritium measurements in tiles removed from the JET vessel have revealed that the tiles contain less tritium than expected. More than 90 % of the tritium still remains in the machine, probably incorporated into flakes and dust accumulated on water-cooled louvres or in the sub-divertor region.

Once tiles are retrieved a careful estimation of the total tritium inventory in representative tiles is necessary prior to their conditioning for disposal in a repository. This permits classification of the tiles into accepted waste disposal categories. Tiles must be treated thermally or otherwise to eventually reduce the tritium content down to established allowable levels. As a rule, the efficacy of the conditioning treatment must be verified by further measurement.

The total tritium content in a single outer base MarkII divertor tile retrieved from JET after the DTE1 (first deuterium/tritium experiment) campaign was carefully determined for the first time. Two fully diverse techniques were selected: a) full combustion of small "coring" specimens and b) calorimetric decay heat measurements of large "coring" specimens.

Complementary determinations to verify these measurements included deuterium depth profiles by ion beam analysis (IBA) and deuterium/tritium depth profiles by accelerator mass spectrometry (AMS), specially suited for the measurement of very small tritium concentrations. Another valuable technique involved temperature programmed heating of samples in a flow tube and registration of the released tritium via the integrated signal from a calibrated scanning tritium detector.

*Measurements by full combustion*

Cylindrical coring specimens were removed from graphite/CFC tiles with a hollow drill and numerous 1 mm thick disks sliced off. Every single disk was then fully combusted under a moist air stream at 800 °C in the presence of a copper oxide oxygen donator, the released tritium being trapped in two sequentially arranged bubblers containing water. From liquid scintillation counting analysis of tritium in the water the tritium content in each specimen was calculated. The technique was found to be extremely sensitive, highly reproducible and accurate. The combustion of a 1 mm thick disk obtained from the plasma-exposed side of the specimen yields the total tritium retained on the tile surface, irrespective of its chemical form or type of trapping. In addition, the incineration technique allows measurement of the tritium content in the bulk, particularly when the tiles have considerable tritium inventories after machines have been operated with DT plasmas. From the combustion measurements the average tritium concentration in a particular tile can be assessed and the total tritium content for that type of tile can be integrated toroidally over the vessel.

*Calorimetric measurements*

Another technique used for the determination of tritium in tiles is calorimetry. The maximum sample size for the calorimeter used at TLK is limited to < 0.5 l. Owing to this and aiming at maximising the sample volume it was necessary to manufacture a special core drill. The large CFC "coring" cylinders were either analysed singly or stacked in a sample container (max. three cylinders).

The sample volume and reference heat capacity of the prototype precision IGC-V calorimeter of TLK are vacuum insulated for improved performance. The base temperature stability is specified to $\pm 10^{-4}$ K. The detection limit given by the manufacturer is 1 $\mu$W (or $\approx$ 0.03 Ci). Calibrations were performed by applying a precisely measured electric heating power to a resistor attached to the sample volume. The arrangement allows measurements in the power range 0 - 10 W. The calorimeter is installed in an air conditioned room whose temperature is constant to $\pm 0.5$ °C.

All measurements were performed on a single IBN7 outer base divertor tile belonging to the first wall of JET during the DTE1 campaign. Simple visual inspection revealed a rather inhomogeneous tile surface with large dark and light grey zones. The tritium concentrations on the surface of tile IBN7 varied within a factor of up to 25.

The results obtained with tile IBN7 have been compiled in the Table below. Four cylinders of approximately 90 $cm^3$ volume each were analysed by calorimetry. Three separate measurements were carried out with each large cylindrical specimen or group of specimens. Numerous base line determinations were carried out, usually one before and one after each tritium measurement. Specific average total tritium concentrations (surface plus bulk) of each specimen are given in the Table. Taking into account that the tile surface shows important variations in concentration, it is apparent that the reproducibility of the tritium concentration measurements in the large specimens is probably even better than what these measurements indicate.

Table: Comparison between full combustion and calorimetry of divertor tile IBN7 specimens

| Full combustion (1.5 $cm^3$ specimens) | | Calorimetry (90 $cm^3$ specimens) | |
|---|---|---|---|
| Cyl. N° * | Tritium concentration [Bq/$cm^3$] | Cyl. N° | Average tritium concentration [Bq/$cm^3$] |
| 7 | 0.72 x $10^8$ | 10 | (1.03 ± 0.07) x $10^8$ |
| 8 | 0.16 x $10^8$ | 11 | (0.82 ± 0.24) x $10^8$ |
| 9 | 1.11 x $10^8$ | 12 | (1.34 ± 0.14) x $10^8$ |
| 13 | 0.17 x $10^8$ | 14 | (1.00 ± 0.07) x $10^8$ |
| Average | (0.54 ± 0.46) x $10^8$ | Average | (1.05 ± 0.18) x $10^8$ |

* The small 1.5 cm3 cylinders were cut centrally from the large 90 cm3 cylinders. The average tritium concentration in the small cylinders was obtained from the total in disks and cuttings.

The results obtained by full combustion after mechanical sectioning of four small cylindrical "coring" specimens of tile IBN7 are also listed in the Table. To allow a more accurate comparison between calorimetry and full combustion the small cylinders were cut from the centre of the large cylinders used for calorimetry. This type of sampling is only associated with a minor diminution of the total activity in the large cylinders, i.e. approx. 1.7%. The tritium activities given in the Table are the results of the full combustion of up to 23 disks (tile thickness ≈ 32 mm). The tritium inventories in the cut material were obtained by interpolation and added to that found in the disks. The values therefore reflect the activity co-deposited / implanted on the surface plus that trapped in the bulk. The average total tritium concentration in six small cylinders was found to be $(0.81 \pm 0.57) \times 10^8$ Bq/cm$^3$. While this value agrees fairly well with that obtained from calorimetry, the accuracy is considerably poorer. This is attributed to the small size of the combustion samples, in which small variations in tritium surface concentration play a much more important role than in the large cylindrical specimens, where variations in surface concentration average out.

A direct comparison between the tritium concentrations in the inner cylinders and in the corresponding outer cylinders indicates that the tritium concentrations in the small cylinders vary by a factor of up to six with respect to concentrations found in the large cylinders. As anticipated, by combustion a sufficiently reliable overall result can only be achieved when a sufficiently large number of small coring specimens is analysed. This undoubtedly will have an impact on the diagnostic categorisation of waste specially when the tritium inventories in the tile approach tolerable limits.

The "coring" technique used in this work is considered cumbersome and risky from a safety point of view. Owing to the non-homogeneous distribution of tritium on tiles, the achievable degree of accuracy by sampling may not be sufficient to satisfy authorities. This will be even more the case when dealing with very low overall tritium concentrations. It is concluded that there is a great need to develop reliable methods for the determination of tritium in whole tiles. For waste certification the detection limit should be in the nW range in samples of several litres volume size.

*Total tritium content of tile IBN7*

The volume of tile IBN7 was estimated to be 1620 cm$^3$ and its weight 2493 g. On the basis of the calorimetric measurements the total tritium inventory of tile IBN7 was calculated to be $1.7 \times 10^{11}$ Bq.

*Required decontamination factor to achieve LLW category*

From an economical and safety point of view the most advantageous category for the disposal of tritiated waste is the low level waste category (LLW). The demanded low specific activity is, however, quite difficult to attain.

The decontamination factor, DF, can be defined as

$$DF = \frac{initial\ activity}{final\ activity}$$

Since LLW activity is specified to $\leq 12 \times 10^6$ Bq/kg it follows, at least for the outer base divertor tile IBN7 having a tritium inventory of $1.7 \times 10^{11}$ Bq or $6.8 \times 10^{10}$ Bq/kg, that a DF of no less than $6 \times 10^3$ must be achieved. If the surface layer is removed successfully by some appropriate mechanical procedure and it is assumed that about 90% of the tritium is in the plasma-exposed surface region (assumption based on a

limited number of bulk measurements), the required DF reduces to 600. Clearly, considerable efforts will have to be invested to meet this challenge. In other JET tiles, i.e. outer wall graphite tiles or inner wall limiter tiles the bulk fraction was found to be much smaller. For these tiles the mechanical removal of the surface layer is expected to have a higher beneficial effect.

The data reported in this work permit predictions on the degree of detritiation needed for an outer base divertor tile to allow sentencing within the low level waste category values. As evident, rather high decontamination factors, i.e. >> 100, will have to be achieved and verified to reduce the tritium concentration down to margins of acceptability for a disposal within the LLW category. Appropriate conditioning technology for tiles still needs to be developed and demonstrated.

Staff:

N. Bekris
U. Berndt
L. Doerr
R.-D. Penzhorn
M. Sirch
B. Schweigel

# TR 16
## Tritium Extraction and Helium Purification

Tritium extraction from the ITER Helium Cooled Pebble Bed (HCPB) Test Blanket Module (TBM) will be executed by freezing out the tritium arising in aqueous form by a cold trap and the molecular tritium by a liquid nitrogen cooled molecular sieve adsorber.

A cold trap design with a series of cooled copper plates as surfaces for water condensation has been installed in a pre-test facility in the TLK and a variety of tests have been carried out. The main parameters investigated were the helium flow rate, the inlet concentration of the water vapour and the number of cold plates i.e. the cooling surface offered for freezing the water vapour. The gas to be processed was simulated by a humidifier, working with ethanol as medium to control the dew-point, which was capable of providing a gas stream containing water vapour from 0,5 to more than 6000 ppmv. Test runs with low (1.7 l/min), medium (8 l/min) and high (33 l/min) throughputs of helium were carried out containing water vapour ranged from 10 to 16 ppmv. The efficiency of the cold trap was evaluated by the number of copper plates that have to be cooled by liquid nitrogen to reach a residual water vapour concentration in the gas stream of less then 0.1 ppmv

Staff:

N. Bekris
H. Dittrich
E. Hutter
F. Kramer
J. Rodolausse

Literature:

N. Bekris, E. Hutter, J. Rodolausse: Parametric studies and scale-up of a cold trap in the tritium extraction loop of a HCPB-breeder blanket for ITER, to be published in 6th Int. Conf. Tritium Science and Technology, Tsukuba 2001, Japan
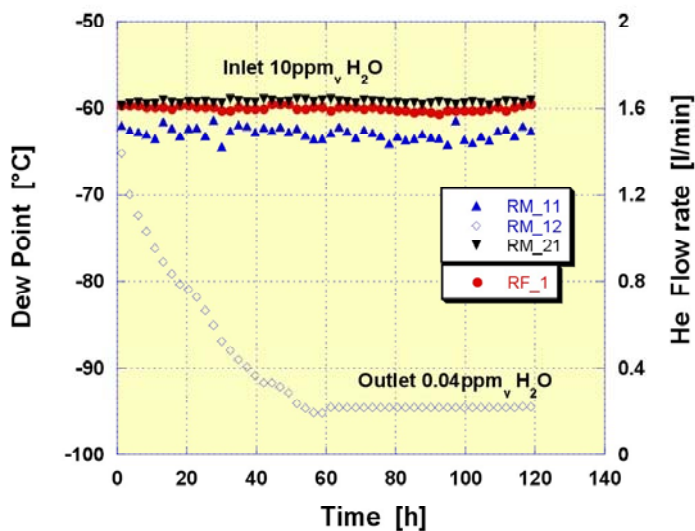
The second main component of the tritium extraction process, the molecular sieve adsorber bed, has been specified and designed. It will be operated at liquid nitrogen temperature to adsorb all hydrogen species in the purge gas of the blanket. The design allows for two steps of regeneration: the desorption of the adsorbed hydrogen while raising the temperature of the adsorbent up to 150 K and the complete regeneration by warming up the bed to 300°C. In this second step all co-adsorbed impurities are liberated. It was not possible for this apparatus to be purchased from industry. It is now under construction in the workshops of the Forschungszentrum.
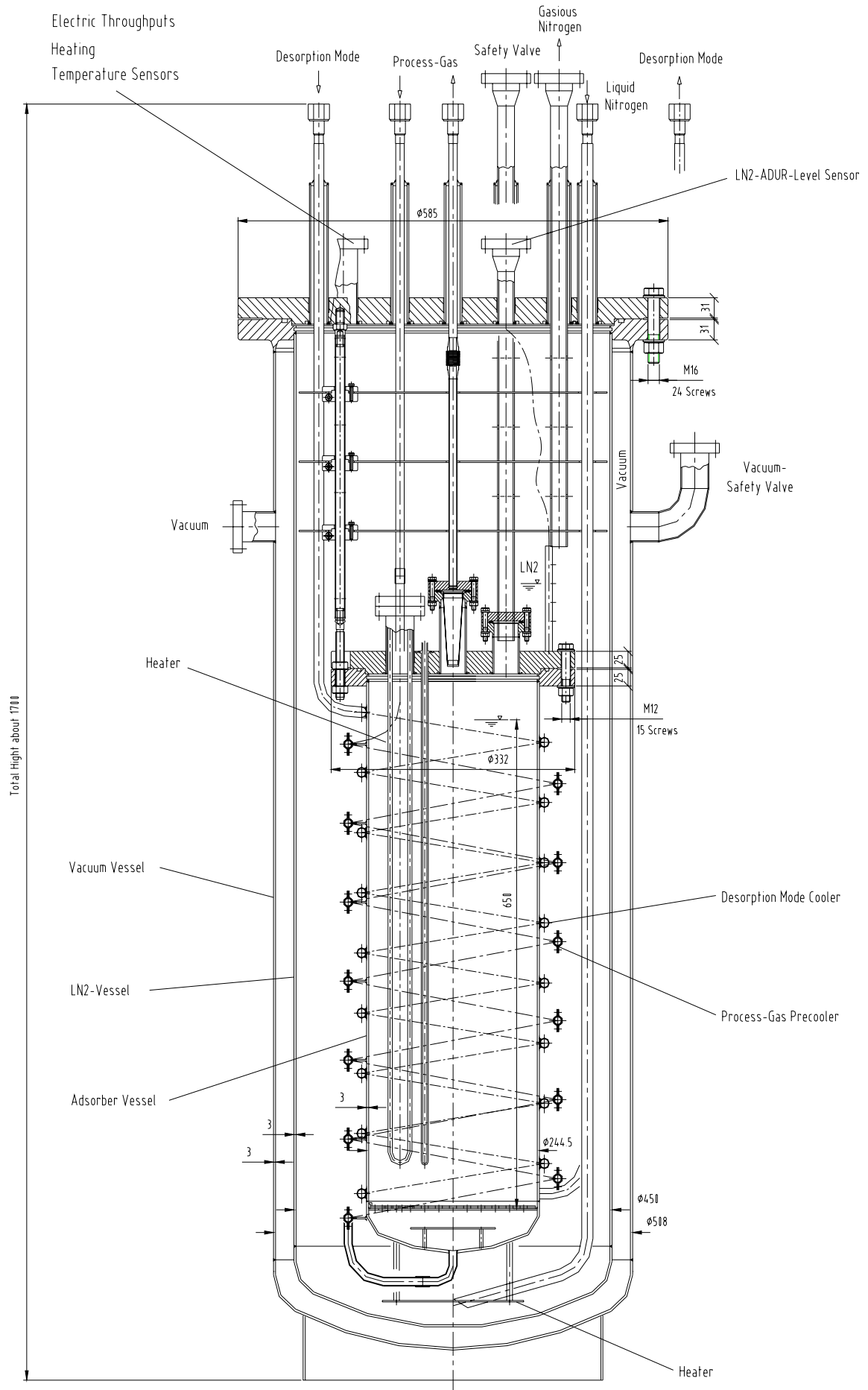
Fig. 2:  Cryogenic Molecular Sieve Adsorber

## T 456 / 02
## Development of a Tritium Compatible Roots Pump

### Introduction

Any tritium handling component for ITER must fulfil stringent requirements with respect to safety and reliability. In these systems the only materials to be used are those which do not deteriorate in the presence of tritium – this excludes the use of elastomers, plastics, etc. where exchange of protium with tritium occurs with subsequent β⁻-induced radiation damage and $^3$He embrittlement. Heated walls of primary containments are to be surrounded by secondary containments to collect tritium permeated through hot walls. The overall leak rate of tritium processing components must be smaller than $10^{-9}$ Pam$^3$s$^{-1}$; this requires the use of metallic seals.

### Pumps for ITER

Pumps to be used in ITER have to fulfil the same requirements. In addition, if oil lubricated pumps are used, the contamination of the oil by tritium needs to be minimised or fully avoided because properties of the oil may change upon irradiation and tritiated oil requires special precautions during maintenance/repair and generates a waste disposal problem. Special tritium compatible pumps were developed and are commercially available, e.g. Normetex scroll pumps, metal bellows pumps, membrane pumps, etc. Disadvantage of these pumps are their limited pumping speed, their huge size in the case of Normetex pumps with a pumping speed ≥ 600 m$^3$/h and their costs.

Each of the four pumping trains of the ITER mechanical forevacuum system consists of a first stage Roots pump (4200 m$^3$/h) backed by two second stage Roots pumps (each with 1200 m$^3$/h) and two third stage rotary pumps (each with 180 m$^3$/h). Roots pumps were chosen because of their high pumping speeds, reliable performance and compact construction. However, commercial Roots pumps are generally manufactured with elastomer O-rings as body seals and do not fulfil the requirement for leak tightness mentioned above. In addition, gas flowing from the pumping volume to the oil filled volumes along the rotating shafts can contaminate the oil, whereas gas flowing in the opposite directions can transport oil vapour to the gas to be processed. In the absence of perfect shaft seals these gas streams will always occur whenever a pressure difference exists between the pumping and the oil filled volumes. Therefore, standard commercial Roots pumps cannot be used in tritium handling facilities.

Roots pumps can be made fully tritium compatible by three modifications: i) the use of metal seal as body seals instead of the O-ring, ii) the installation of ferrofluidic seals between the rotors and the bearings to stop gas exchange between the pumping and the oil filled volumes and iii) the use of tritium compatible material wherever tritium has a chance to get in contact.

Well known Roots pump producers were contacted, but none was interested. Finally a special, small company was found with experience in building Roots pumps and installation of ferrofluidic seals in blowers for application at higher pressures.

The supplier of ferrofluidic seals could not guarantee the leak tightness of their seals in the application mentioned above. Therefore, the decision was made to build first a test rig to check the performance of ferrofluidic seals under the typical conditions occurring in a Roots pump. Depending on these results the decision for manufacture of a Roots pump should be made.

### Experimental test rig

A special rig was built for the testing of ferrofluidic seals under Roots pump relevant conditions. The integral leak rate determination of the test rig did not show any leak indication in the $10^{-10}$ Pam$^3$s$^{-1}$ range as only metal seals and metals are used as construction materials. The shaft (simulating the shaft of a Roots pump) is rotated by a magnetic drive and kept in position by two bearings. The rotational speed of the shaft is frequency controlled from 0 to 1500 rpm. Further shafts of different diameter can be connected to the shaft between the two bearings to test other ferrofluidic seals of various inner diameters. The ferrofluidic seal is mounted between three C-metal rings in such a way that gas can pass the ferrofluidic seal only along the shaft. The main mechanical parts of the ferrofluidic seal are the strong magnet of cylindrical shape in the middle and steel cylinders on each side with precisely machined teeth on its inner cylindrical area and a very small gap to the shaft. The magnetic field lines pass preferably from the teeth through the gap, attract the ferrofluidic liquid to these locations and return back to the magnet via the shaft. On each side of the magnet seven very small volumes between the stationary teeth and the rotating shaft are created which are filled with very small amounts (μ-litres) of the ferrofluidic liquid. These liquid filled volumes prevent gas streaming along the shaft. Due to the strength of the magnetic field and the very small gap between the stationary and revolving parts the ferrofluidic seal is capable of withstanding pressure difference higher than 100 kPa. For the tests $^4$He is introduced into the volume with the bearings, kept at constant pressures (between 25 and 100 kPa) and a leak detector is connected to the other side of the ferrofluidic seal to determine the actual leak rate.

### Short term measurements of the leak rate of a ferrofluidic seal

First trial leak test measurements performed within a few hours demonstrated clearly that the leak rate of the ferrofluidic seal stayed constant in the $10^{-10}$ Pam$^3$s$^{-1}$ range independently of changing the $^4$He pressure in the bearing volume between 0 and 100 kPa and the rotational speed of the shaft from 0 to 1500 rpm.

### Long term measurements of the leak rate of a ferrofluidic seal

The leak rate of the ferrofluidic seal is shown in the Fig. 1 for 0, 25, 750, 1500 rpm and 100 kPa He pressure and in Fig. 2 for $^4$He pressures of 25, 50, 100 kPa and 1500 rpm. The leak rate was continuously measured by a $^4$He leak detector, but the data shown in the plots represent the leak rates obtained in 12 hours intervals. The values presented are the leak rates already corrected for the background signal. The observed leak rates increase almost linearly with time with exception of the rpm
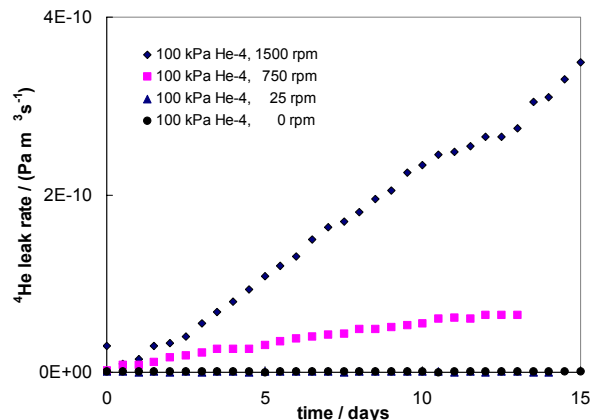


Fig. 1: $^4$He leak rate of ferrofluidic seal for various rpm's
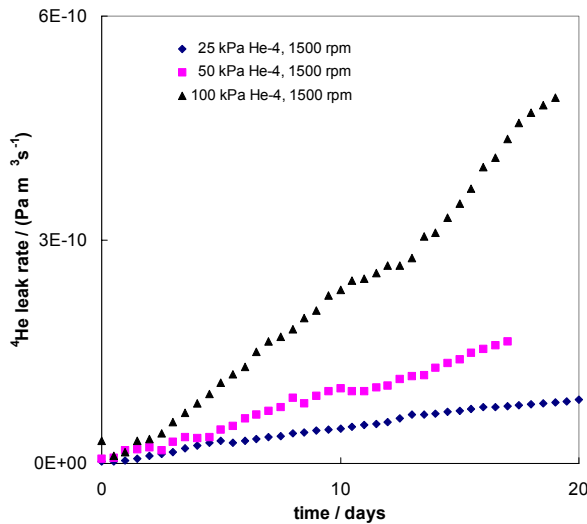
Fig. 2: $^4$He leak rate of ferrofluidic seal for various pressure differences

values of 0 and 25. No saturation behaviour is detected within the two weeks measurement times. No increase of the leak rate is observed for the 0 and 25 rpm. This means that only a non-detectable uptake of He in the liquid occurs at rotations below 25 rpm within the observation times. The cause is probably the very smooth surfaces of the ferrofluidic liquid at low rpm due to laminar flow conditions. At higher rotational speed more gas is introduced into the now turbulent liquid and capable of passing through the liquid because the liquid experiences high velocity gradients as one side of the liquid rotates with the same speed as the shaft whereas the other side of the liquid stays stationary as the ferrofluidic seal. With this in mind one would expect that doubling the rotational speed gives approximately twice the leak rate. Fig. 1 seems to indicate that this is not true. It is necessary to consider further effects: due to doubling the speed of the magnetic drive and of the shaft higher eddy currents are introduced by the magnetic drive into its metallic surrounding and by the magnet of the ferrofluidic seal into the rotating shaft causing higher temperatures of the housing and of the ferrofluidic seal. Also the gas temperature inside the bearing volume increases with higher rotational speed of the shaft due to friction. With increasing temperatures the properties of the ferrofluidic seal change and helium can pass mare easily through the liquid resulting in the approximately three times higher leak rate at 1500 rpm than at 750 rpm. A thermocouple connected to the outer surface clearly measured these temperature changes. As a consequence it was decided to install water cooling in the neighbourhood of the four ferrofluidic seals of the Roots pump to be built. The zero leak rate at 0 rpm is also an important result because it indicates that the distribution of the ferrofluidic liquid around the shaft stays unchanged for long times meaning that the ferrofluidic seal will keep its performance for long shutdown periods. Fig. 2 shows within the experimental accuracy that doubling the $^4$He pressure results in approximately twice the leak rate.

Until now the ferrofluidic seal has been operated for more than one year under Roots pump relevant conditions. Repetition of the first leak rate run resulted in very similar results demonstrating that the performance of the ferrofluidic seal has not changed. Furthermore, during the whole testing period of more than one year no ferrofluidic liquid was added to the ferrofluidic seal.

The observed leak rates for helium are very small, although no saturation behaviour was observed for the times studied. If a pressure of 25 kPa He is chosen in the volume with the bearings the leak rate after 2 weeks is $6.7 \cdot 10^{-11}$ Pam$^3$s$^{-1}$ according to Fig.

1. Assuming a linear increase as a function of time gives a leak rate of approximately $10^{-8}$ Pam$^3$s$^{-1}$ after 6 year of continuous operation, a leak rate still far smaller than achievable with normal shaft seals. This clearly shows the usefulness of the ferrofluidic seal.

**Conclusions**

The ferrofluidic seal showed very small leak rates and behaved very well during all tests.

As a consequence of the observed performance of the ferrofluidic seal a contract for manufacture of a Roots pump which fulfils the tritium requirements for ITER was placed. This Roots pump comprises

- a pumping speed of up to 250 m$^3$/h,

- metal body seals to achieve the required leak tightness of $10^{-9}$ Pam$^3$s$^{-1}$,

- four ferrofluidic seals between the rotors and the bearings to stop gas exchange between the pumping and the oil filled volumes,

- one magnetic drive.

A more detailed description of the behaviour of the ferrofluidic seal and its application in Roots pumps is given in Ref. 1.

Staff:

W. Jung
R. Lässer
K.-H. Simon

Literature:

[1] R. Lässer, D.K. Murdoch, R.-D. Penzhorn and K.-H. Simon: Use of ferrofluidic seals in the design of tritium compatible pumps, to be published in 6th Int. Conf. Tritium Science and Technology, Tsukuba 2001, Japan.

# VP 11
# Torus Exhaust Cryopump Development and Testing

## 1. Introduction

In the preceding test campaign the final acceptance tests and the parametric tests of the 1:2 model cryopump were performed [1], [2]. It was shown that all contractual requirements of the model cryopump could be achieved. During the parametric tests the ITER-relevant pumping speeds and loading capacities for pure gases and ITER-relevant gas mixtures were demonstrated [3].

For the ITER pumping cycles a total time period of 750 s is required, including 150 s cooling down from 85 K to 4.5 K, 450 s steady state pumping at 4.5 K, 150 s heating up from 4.5 K to 85 K and pumping down from about $10^4$ Pa to 10 Pa in parallel.

The formerly used control cryostat with a buffer volume of 700 l liquid helium (LHe) and an available supercritical helium (SCHe) mass flow of 30 g/s didn't allow the fast cooling down times. Moreover no ITER-relevant cycle numbers could be achieved.

For testing these ITER requirements the TIMO facility at Forschungszentrum Karlsruhe is being upgraded. The old control cryostat was replaced by a new one with a buffer volume of 3000 l LHe, a high pressure storage tank for cryogenic

gaseous helium and a cold blower with a maximum mass flow rate of 250 g/s. It was installed and connected to the cold valve box by cryotransfer lines.

The reference sorbent material to be used for the ITER cryopanels was characterised with respect to helium and hydrogen sorption in the COOLSORP facility. Direct experimental sorption data at cryogenic temperatures are very scarce in literature. Thus, this investigation provides important design and optimisation data for regeneration and inventory limitation issues.

## 2. Upgrading of TIMO

### 2.1 New control cryostat

For cooling the circuit of the pumping panels in the ITER-model torus cryopump gaseous helium at 4 bar and 4.5 K is used. This makes sure that no two phase flow conditions will occur which can produce uncontrollable instabilities inside the cooling channels.The cryogenic helium is supplied by a refrigerator with a maximum capacity of 600 W at a pressure level of 1.5 – 1.8 MPa and a temperature of 7 K in front of the control cryostat.

The pump runs through three operation modes within one pumping cycle: cooling down from 85 K to 4.5 K, steady state pumping, heating up from 4.5 K to 85 K. Within all these three modes the baffle and the shielding structure is kept at 80 K by
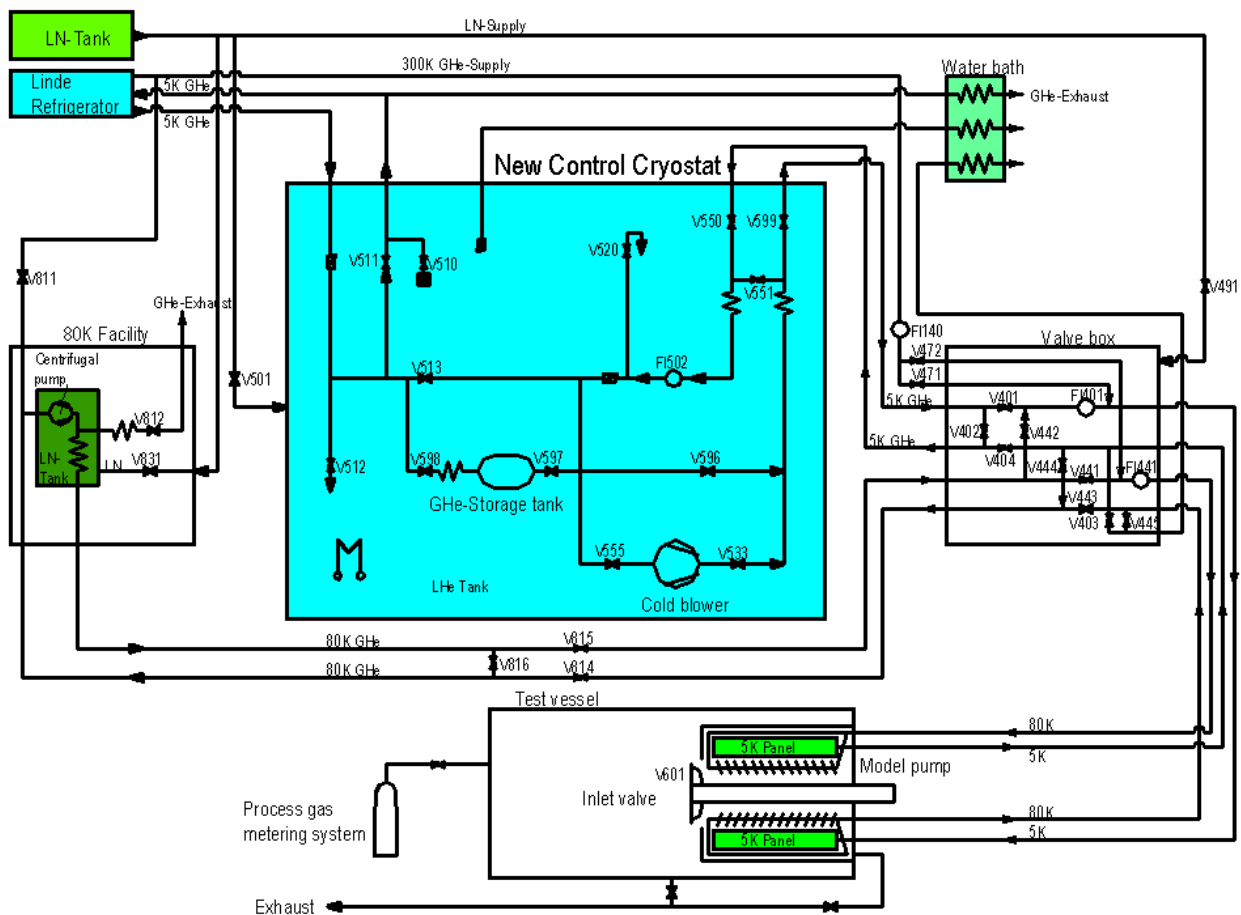


Fig.1: Simplified flow scheme of TIMO with upgraded new control cryostat

gaseous helium.

A critical issue is the cooling down step for which a time period of 150 s is allocated according to the current ITER operation concept. However, the capability for fast cool-down in 75 s shall also be demonstrated. 120 kg stainless steel must be cooled down within this interval. Additionally 27 l cryogenic helium are needed for refilling the loop. The available He refrigerator cannot deliver online the needed helium flow rate. For this reason a new control cryostat with storage systems for gaseous and liquid helium has been installed in TIMO.

A simplified flow scheme is given in Fig. 1. Fig. 2 shows the internal structures which are dipped into the LHe bath. The control cryostat consists of an inner dewar vessel with a storage volume of 3000 l LHe. The maximum allowable design pressure is $10^5$ Pa. This vessel is supported by an outer vessel with a height of 3880 mm and a diameter of 2200 mm. In between the two vessels there is a vacuum insulated gap with a liquid nitrogen-$(LN_2)$-cooled thermal shield. Gaseous helium can be stored in a pressure vessel with 250 l volume and a maximum pressure of $2·10^6$ Pa. A heat exchanger in front of the vessel cools the 7 K He flow from the refrigerator to 4.5 K. A cold Barber Nichols blower, Type BNHEP-17-00 is installed. It allows a mass flow rate of 250 g/s at a differential pressure of $4·10^4$ Pa with an inlet pressure of $3.5·10^5$ Pa.



Fig. 2: Internal structures of 3000 l control cryostat

Two heat exchangers in the panel circuit transfer the compression heat load upstream of the cold blower and the heat load in the return line coming from the pumping panels to the LHe bath. The cold valves for operation of the 4.5 K loop are installed in the LHe-bath.

Before starting the cycling operation of the model pump 3000 l LHe are filled into the dewar and the buffer vessel is pressurized with cryogenic gaseous Helium to a pressure level of $1.8·10^6$ Pa. Over a period of 150 s a mass flow rate of about 60 g/s is injected into the panel loop passing the cold blower. At the beginning the loop is opened to the water bath and only a small fraction of the injected gas remains in the loop. The rest is

rejected to the refrigerator passing through the water bath. The cold blower is working with 250 g/s and is bypassed in the cryostat to the return line.

As the panel temperature decreases the bypass is slowly closed and the flow to the model pump goes up. When the panel temperature reaches 10 K the loop is closed to the water bath. At that point, because of steep variations of the GHe density the flow from the buffer tank fills up the panel loop. At the end of cooling down, the connection between buffer tank and panel loop is shut down and steady state pumping mode is started.

## 2.2 Cryotransfer lines

The distance between the position of the new 3000 l control cryostat and the cold valve box is now 14.0 m.  With an inner diameter of 39.2 mm a total pressure difference of $2.8·10^4$ Pa at a mass flow rate of 250 g occurs in the panel loop. This is well below the achievable $4·10^4$ Pa pressure difference of the cold blower. To ensure heat in-leaks of less than 0.2 W/m the cryogenic lines are $LN_2$-shielded and vacuum superinsulated.

Aside from the go and return lines to the cold valve box, cryogenic transfer lines to the helium refrigerator and a He exhaust line to the He-storage system via the water bath have been installed. The total new installed cryogenic piping is shown in Fig. 3.



Fig. 3: TIMO facility showing new 3000 l control cryostat and cryotransfer line to cold valves box

## 2.3 Water bath

The helium exhaust gas which cannot be returned directly to the refrigerator is heated up to room temperature in three heat exchangers which are installed in a water bath. Within the upgrading activities a totally new system was installed which fits for the enlarged mass flow rates. It consists of three heat exchangers in quilted design dipped into a water bath with a volume of 2.0 m³. The three heat exchangers are attached to:

- the warm exhaust gas from the panel circuit when operating with opened loop,

- the evaporated gas from the liquid helium in the control cryostat,

- the gas coming from the refrigerator return line when controlling the pressure level.

Downstream of the water bath measuring and control devices for flow, pressure and temperature are assembled. The helium is fed into a central storage system and then returned to the refrigerator.

### 3. Acceptance tests with control cryostat

After finishing the mechanical installation and the electrical wiring, leak tests and tests of the measurement techniques were performed. During first cool down of control cryostat the Joule Thomson valve and the valves for controlling the pressure in the panel circuit failed. There was a misalignment of the guiding tubes and the 1600 mm long actuator rods. The consequence was a strong friction between the conical valve seat and the valve body which caused a non continuous characteristic of the throttling behaviour, thus, not allowing a steady state control of the refrigerator.

The actuator rods were dismantled and two swivel systems installed which allow the actuator rods adjusting to the guiding tubes. After the repair work acceptance tests have been restarted with a delay of 3 months.

### 4. Capacity tests

A key issue of the cryosorption pumping system is the pumping of helium, which is, together with protium, the gas species with the smallest sticking coefficient of only about 20% [5]. Consequently, the pure helium plasma shot, which is foreseen in the initial operation scenario of ITER, represents the most stringent scenario. The target would be a pumping curve for helium providing a high pumping speed of 1 l/(s·cm²) at a constant level over the complete ITER relevant gas load range (maximum 2.2 (mbar·l)/cm²).

This performance was checked experimentally in TIMO for two different gas throughputs, i.e. the ITER-relevant throughput and only 20% of that, see Fig. 4.
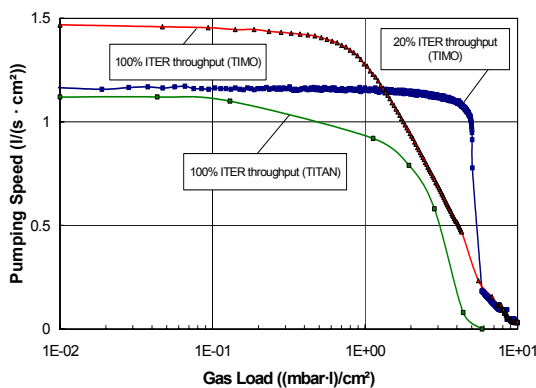


Fig. 4    Helium capacity

The pumping speed is constant, at least up to about 50% of the ITER-relevant gas load and well beyond the required value in the whole ITER range of gas load. The capacity limit (zero pumping speed) is approximately the same for both throughput curves and is about a factor of 10 higher than what is required. This means that the very demanding requirement of full gas throughput under He plasma shot conditions can be complied with. For comparison, an older pumping speed curve as derived in the single panel test facility TITAN is also given in Fig. 4. This curve is somewhat worse, both with respect to speed and capacity limit. This comparison illustrates the advancements incorporated in the new pump design compared to the older TITAN test design.

### 5. COOLSORP

The COOLSORP facility was operated continuously throughout the year. The experiments were made to measure the sorption isotherms of different gases on the same carbon material, namely the ITER reference material. This is a coconut-shell derived granular activated charcoal.

The first stage of the experiments was done to check the validity and applicability of the experimental method used [6]. As being a natural product, one important aspect was to study the change of sorption characteristics with different batches out of different production years of the same charcoal type. In this respect, the measured sorption isotherm curves differed within a boundary of about ±2.5%, whereas the reproducibility for the same sample is one magnitude better. A second aspect, which has to be kept in mind when using isotherm data, is the influence of the experimental method itself. The only system for which a comparison with literature data could be made, was the sorption of nitrogen at 77.3 K at the same charcoal product. In this case, we found differences between our own data (measured with a continuous method) and literature data (measured with a static method) of up to 10%. This illustrates the complexity of the sorption process.

In the second stage of experiments, He and $H_2$ were measured at several temperatures from vacuum up to atmospheric pressures.

The results for helium are shown in Fig. 5. All the isotherms, except the one for 4.2 K, relate to the supercritical temperature range ($T_{crit}$(He) = 5.2 K). The curves show a distinctive plateau in the higher pressure range. The change in slope of the 4.2 K curve indicates the formation of multilayers.

Fig. 6 presents the analogous results for hydrogen. However, in this case, the investigated temperature range covers both sub- and supercritical temperatures ($T_{crit}$($H_2$) = 33.2 K). The subcritical range can be further subdivided in measurements above the normal boiling temperature (T = 20.38 K), where the investigated pressure range corresponds to relative pressures $p/p_0$ less than unity, and below the normal boiling temperature, where condensation takes place already for smaller pressure values. Despite these differences from the thermodynamic point of view, all curves look quite similar. This clearly reveals that capillary condensation which could in principle happen in the subcritical range, cannot be of predominant importance, but a pore filling mechanism seems to prevail. The adsorbed volumes are consistently higher than for the corresponding He isotherms. The hydrogen data can now be used to estimate the semi-permanent inventory in the cryopump panels under various stages of regeneration.

In the next stage of the experimental programme measurements with deuterium will be performed. Furthermore, a gas analyser will be installed to be able to measure sorption isotherms of gas mixtures and to monitor potential composition drifts during the sorption process so as to reveal any competitive sorption effects. Another issue which shall be investigated in close detail is the influence of the charcoal particle bonding, by direct comparison of loose material and bonded material behaviour.
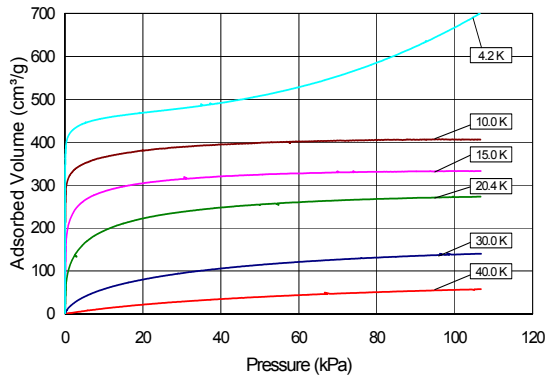
Fig. 5: Measured isotherms for helium
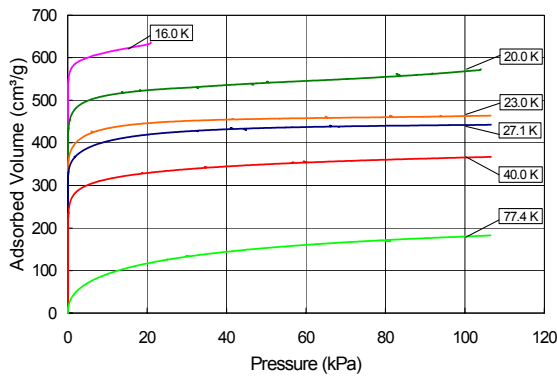


Fig. 6: Measured isotherms for hydrogen

## 6. Microwave regeneration

Special R&D has been performed to develop an alternative technology for the heating step within panel regeneration. It had been shown earlier that a temperature of at least 85 K is needed to have a sufficient release of the hydrogens. This is currently done convectively by passing a forced flow of warm gas through the cooling channels of the cryopanels. As a consequence to that, the whole panel mass is warmed up, which has to be rapidly cooled-down again afterwards. To further optimise this energy-consuming operation, the use of microwave heating was brought into discussion. The advantage of this technique would be the limitation of the heating on the charcoal part on the surface of the panel.

Screening tests have been performed with 2.45 GHz microwaves at ambient temperature and with $LN_2$-precooled samples. It was shown that the loose bulk material has a good absorptivity in the whole temperature range. However, the charcoal coated layer of only 1 mm thickness, which is typical for the cryopanel set-up, was found to be too thin relatively to the wave length, to absorb effectively. This problem could be solved when using high frequent gyrotrons, which are anyway installed at the fusion machine for heating of the plasma. Therefore, further tests were performed in close collaboration with the Institute for Pulsed Power and Microwave Technology. For these tests, a 1MW 140 GHz gyrotron was employed to heat a dummy panel with a charcoal coating corresponding to the ITER cryopanel set-up. The influence of heating power (pulse length) and panel inclination relative to the focussed beam were investigated (at ambient conditions) and a good heating behaviour was measured, cf. Fig. 7. The measurement data are now used to validate a heat transfer model, which would then be used to simulate the heating process under vacuum and at cryogenic temperatures. If the simulation supports the feasibility of this technique, more experiments are planned.
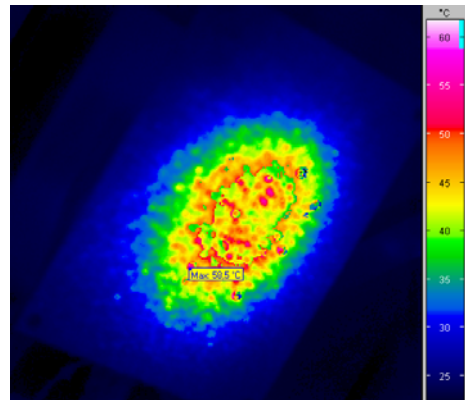


Fig. 7: Surface temperature distribution after a focused 6 ms 140 GHz gyrotron beam pulse on a 20x20 cm coated panel mock-up as target

Staff:

A. Antipenkov
G. Dammertz
Chr. Day
A. Edinger
J. Grimm
H. Haas
V. Hauer
T. Höhn
H. Jensen
A. Mack
R. Simon
Th. Waldenmaier
J. Weinhold
St. Zabeschek
D. Zimmerlin

Literature:

[1] Chr. Day; H. Haas; A. Mack: Development of the cryovacuum pump system for ITER-FEAT. Jahrestagung Kerntechnik 2001, Dresden, 15.-17. Mai 2001, S. 603-06

[2] Chr. Day; H. Haas; A. Mack; D.K. Murdoch: New operational aspects of the ITER-FEAT primary vacuum pumping system. 21st Symp. on Fusion Technology (SOFT), Madrid, E, September 11-15, 2000

[3] A. Mack; Chr. Day; H. Haas; D.K. Murdoch; J.C. Boissin; P. Schummer: First operation experiences with ITER-FEAT model pump. 21st Symp. on Fusion Technology (SOFT), Madrid, E, September 11-15, 2000

[4] D.K. Murdoch; A. Mack; Chr. Day; H. Haas; J.C. Boissin; I. Viniar; P. Ladd; A. Antipenkov; G. Saksagansky; S. Pimanikhin: ITER-FEAT vacuum pumping and fuelling R&D programmes. 18th IAEA Fusion Energy Conf., Sorrento, I, October 4-10, 2000

[5] Chr. Day: The use of active carbons as cryosorbent. Colloids and Surfaces A, 187-188 (2001) S. 187-206

[6] Chr. Day; V. Hauer: Pore characterisation of cryosorbent carbon materials at cryogenic temperatures. 7th Internat. Conf. on Fundamentals of Adsorption (FOA7), Nagasaki, J, May 20-25, 2001

**T 228.1**
**Influence of Higher Hydrocarbons on Vacuum Pumping**

The existence of higher hydrocarbons in fusion machines with graphite first wall materials is a central issue. Besides others, one aspect is the impact of these, potentially tritiated substances on pumping performance of the cryosorption pumps in the torus high vacuum system. Because the radioactive decay of tritium takes place without activation energy, the accumulation, and also the progressive formation directly on the cold charcoal contact in cryopump adsorption panels cannot be excluded. It has already been demonstrated that the pumping speed of a cryosorption pump can become very poor when a certain amount of hydrocarbons is accumulated on the panels [1]. Preliminary tests have shown that the poisoning effect intensifies with increasing size of the hydrocarbon moleculares. Thus, to make any quantitative predictions, it is essential to understand the radiation chemistry on cold activated charcoal and to identify the chemical products.

A new test facility is being built-up at the TLK. It will include a two-stage closed loop He-cooled Gifford McMahon cryocooler as cold source. A sample adsorption chamber is connected to the cold head with an achievable minimum temperature of about 10 K. The sample holder allows to investigate charcoal in the form of loose granule material or bonded to a metal substrate to simulate cryopanel conditions most neatly. The temperature of the sample can be monitored by cryogenic silicon diodes. The second stage of the refrigerator is equipped with a resistance heater to make the whole temperature range between 10 K and ambient temperature available. Gas analysis will be provided by a standard unit resolution quadrupole mass spectrometer, which is currently being upgraded for additional high resolution operation in the mass range up to 16 amu by working in the second Matthieu stability region. It was aimed to develop a robust and versatile facility design, which covers a number of different experimental issues. Consequently, as primary objective, the facility can be used to investigate cryosorption on freshly activated and/or tritium pre-loaded charcoal to study poisoning, and has a powerful gas analytical device for monitoring radiochemical reactions. Moreover, the desorption behaviour of cryosorbed gases from charcoal can be studied using the temperature controlled second cryocooler stage, and sorption characteristics for sorbent characterisation can also be determined. The latter combines both measuring sorption isotherms and sorption isosteres depending on the way how the gas is contacted with the charcoal. In this respect, the new facility for tritiated gases is an ideal complement of the existing COOLSORP facility for non-active conditions. The whole facility is inserted in a glove box and will be fully included in the tritium cycles available at TLK.

The design of the facility and its integration in the former ALTEX glove box is currently under work. In preparation of the active experiment, the refrigerator part of the facility has already been set up and tested under non-active conditions with $H_2$, $D_2$, CO and a $D_2$/CO-mixture.

Staff:

U. Berndt
Chr. Day
M. Glugla
K.H. Simon

Literature:

[1]  Chr. Day et al., New operational aspects of the ITER-FEAT primary vacuum pumping system, 21st SOFT, Madrid, E, September 2000.

## T 450
## Leak Testing of Water Cooled Circuits

The work of K.S. Forcey and R.A.H. Edwards of JRC Ispra (Reports T364 and EU Task VP3) on detection and localization of leaks from cooling circuits for ITER has been reviewed in the light of operational experience on large tokamaks and the design of the pumping and cooling systems of ITER. The proposed method involves having tracer compounds permanently in the cooling water circuits and looking for these compounds in the exhaust gases from the tokamak. The equipment proposed for detection is a standard gas chromatograph / mass spectrometer (GC/MS) with additional selective traps to improve the detectability of the trace compounds. This is a well established technique used in the detection of trace compounds in the environment and other applications. ITER has several water circuits so at least the same number of trace compounds is required for this technique.

The major recommendation of the review is that leak localization should only be attempted when tokamak operations have stopped. This means that tracers should be added when leak localization is necessary rather than being permanently maintained in the cooling circuits. The major reasons for this recommendation are:

- If a leak is sufficiently large then plasma operations are either difficult or are no longer possible. At this point the tokamak should be shut down and leak localization started.

- ITER will be equipped with many other devices to detect leaks and identify their composition so there is not likely to be a problem in determining if a water leak is present, the problem is then to locate it.

- Any trace compound in the cooling water will be subject to radiolysis and may be severely degraded and no longer identifiable. Also it will be difficult to maintain the water purity and tracer concentration simultaneously.

- Any trace compound leaking with water into a plasma would be highly ionised by the plasma and its molecular structure broken up so it would not be identifiable in the vacuum exhaust.

- The regeneration regime for the ITER cryo-pumps required for permanent leak localization will not be acceptable for proposed ITER plasma pumping scenarios.

However, adding tracers to suspect water circuits in a shut down period has many advantages. Apart from avoiding the disadvantages listed above, other benefits are:

- The concentrations of the tracers in the cooling water can be higher leading to better detectability.

- The proportion of hydrogen isotopes in the exhaust gases from the tokamak will be considerably lower leading to easier separation of the exhaust gases.

Suitable equipment for experimental work has been identified from two manufacturers and an experimental plan is under consideration. Eventually it is hoped that a technique can be tested at JET as it has a live tokamak and a cryogenic pumping system. However, initial testing of the technique can be performed at the Forschungszentrum using the TIMO facility and preliminary discussions have been held on this proposal. A critical part of the detection technique is provided by the separation of hydrogen isotopes and impurities by selective regeneration of the cryopumps and this is a feature being examined with the TIMO facility.

It should also be noted that a technique used at Tore Supra to identify leaking high pressure water circuits is simply to reduce the pressure in these circuits sequentially and monitor the leak rate. This additional technique should also be considered for ITER.

Once a particular water circuit has been identified as having a leak, the next problem is to locate the particular section. Ice plugging of sections of the water circuits has been suggested as an alternative to valves for the isolation of individual circuits during leak localization. This is an established technique which should be pursued by ITER designers in collaboration with consultants if the inclusion of such devices is thought feasible.

The development of in-vessel probes to identify the area where a leak is located are further tasks subject to specific development task requests.

Staff:

C. Caldwell-Nichols

# JET Exploitation

**JW0-FT-1.1**
**Removal of Tritium Contaminated Flakes/Dust**
**from the Sub-Divertor Region of JET**

During the first Deuterium Tritium Experiment (DTE1) 34 g tritium were introduced into the JET torus mainly by neutral beam injection.

A fraction of the introduced tritium (about 4 g) remained in the form of co-deposited films, flakes, or was implanted in graphite tiles. The flakes are mainly, found in the inner leg of the divertor zone in relatively cool areas. In some areas the flakes become so thick that they spall off from the structure.

As one of the key issues in JET is to close the tritium balance, in 1998 during the remote exchange of the divertor tiles, about 100 g of highly tritiated flakes were removed from the JET machine using a vacuum cleaner with a cyclone dust separator shown in Figure 1.
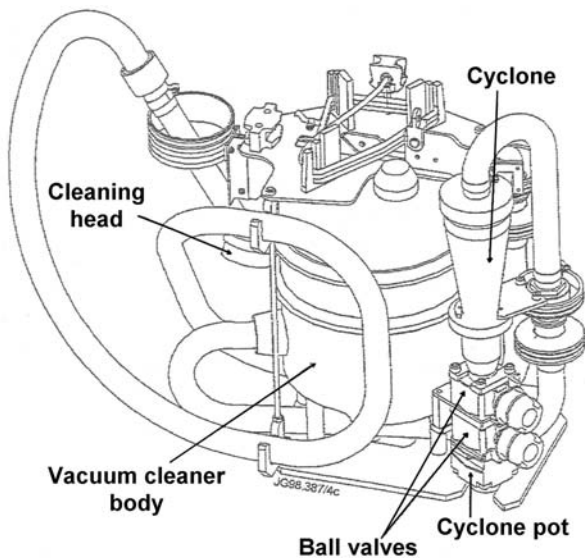


Fig. 1:  Remotely operated flake collection vacuum cleaner

In order to close the tritium balance approximately 1 g of these flakes were delivered to the Tritium Laboratory Karlsruhe (TLK) during 1999, contained in a small aluminium bloc (the vacuum cleaner cyclone pot) of about 200 cm³ under argon atmosphere. The pot was sealed in a plastic PVC bag filled with air and introduced in a first aluminised bag (inner bag) also under air atmosphere together with a linen bag containing about 40g silica gel. A second aluminised bag (outer bag) houses the whole package accompanied by linen bag containing 71 g of palladium catalyst (Fig. 2).

The flakes were introduced in a 6.7 m³ glove box at the TLK and the tritium released measured after the successive opening of the different containing bags.
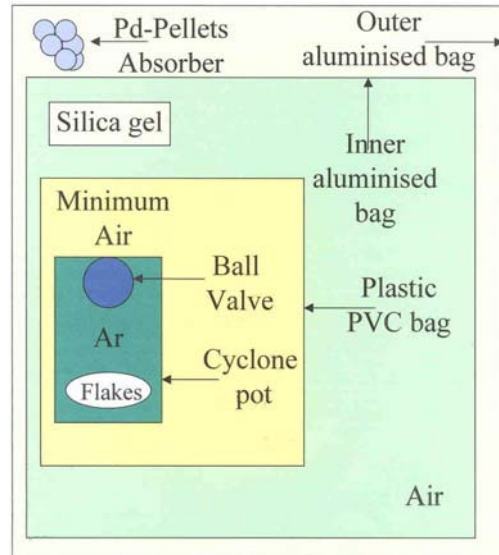


Fig. 2:  Transport concept of the JET flakes

The following table shows the parts of tritium trapped by each packing barrier and measured in the glove box.

| Tritium barrier | Tritium amount |
|---|---|
| Outer aluminised bag | 4 MBq |
| Pd pellets | 11.3 mCi |
| Inner aluminised bag | 5.1 Ci |
| Silica gel | 6.2 Ci |
| Plastic PVC bag | 0.2 Ci |
| **Average** | 11.5 Ci |

The flakes were then removed from the cyclone pot and introduced to a 10 ml glass bottle and sealed in a 20 ml codex bottle. The mass of flakes was determined to be 0.932 g and the total tritium released within 28 months was 15.7 Ci.

The remaining tritium activity was determined by calorimetry. Three measures in two different calorimeters gave an average remaining activity of $(6.04 \pm 0.01)10^{11}$Bq i.e. 16.3 Ci. These values give a specific activity of 34.4 Ci/g or 1.3 TBq/g.

Presently the chronic release measurement of tritium is continued and a physicochemical characterisation of the flakes is also planned.

Staff:

D. Adami
N. Bekris
U. Besserer
L. Doerr
M. Glugla
R.-D. Penzhorn
M. Sirch

## JW0-FT-1.6
## Surface and Depth Profiling of Tritium in Selected JET Tiles

During plasma discharges hydrogen isotopes are implanted into the graphite tiles as ions or as energetic charge-exchange neutral atoms.

Hydrogen atoms may also be co-deposited with carbon, whereby the eroded carbon combines with the plasma to eventually form a deposited amorphous, hydrogenated carbon film. The tritium retention via co-deposition and implantation including migration through the network of interconnected pores and diffusion across the grains depends on the plasma operation conditions and on the degree of neutron and alpha irradiation damage.

As the erosion and re-deposition of plasma facing components together with plasma fuel material constitutes an important issue for every fusion machine, especially in terms of tritium inventory, a research program was launched in the Tritium Laboratory Karlsruhe (TLK) since 1997 on the determination of tritium concentration on the surface as well as in the bulk of tiles.

During a preliminary research campaign accomplished with graphite tiles obtained from operating fusion machines (JET, TFTR), a quantitative determination of the depth and surface concentration of tritium was carried out using full combustion. These analysis have shown that almost all of the tritium trapped in such tiles (99%) is located in a layer of 50 microns as implanted and/or co-deposited material.

In addition, tritium depth profiles for Carbon Fiber Composite (CFC) tiles have also been analysed because they are mainly used as first wall material.

For that purpose a complete set of JET MKIIA divertor poloidal tiles were retrieved after the first Deuterium Tritium Experiment (DTE campaign) and shipped for analysis to the Forschungszentrum Karlsruhe (FZK). Using the coring technique cylindrical specimens from tiles were taken at the Hot Cells and analysed at the TLK.

Numerous analysis were performed using the well known and firm full-combustion/liquid scintillation technique.

In contrast to the results obtained for graphite tiles the CFC tiles showed a depth profile for the tritium concentration all over the thickness of the tile. As the tiles used at JET have a 2D CFC structure i.e. successive graphite weaves planes deposited one to the other, it is logical to assume that the tritium distribution profile is related to a diffusion of material between the weave planes. The diffusion depends of the tritium surface concentration, the nature and the surface temperature of the tile.

Moreover, a diffusion process was also discovered taking place from the backside of the tile. Typical diffusion profiles for the outer divertor tiles 8 and 9 are illustrated in Figure 1.

As a large part of the tritium is trapped in the bulk of the CFC tile, thermal release rates of a plasma exposed disk as well as of a bulk sample were compared. Both specimens had a diameter of 7.8mm and were heated up to 1100°C with a heating ramp of 7°C/min.

As illustrated in Figure 2 the behaviour of both samples is almost the same.
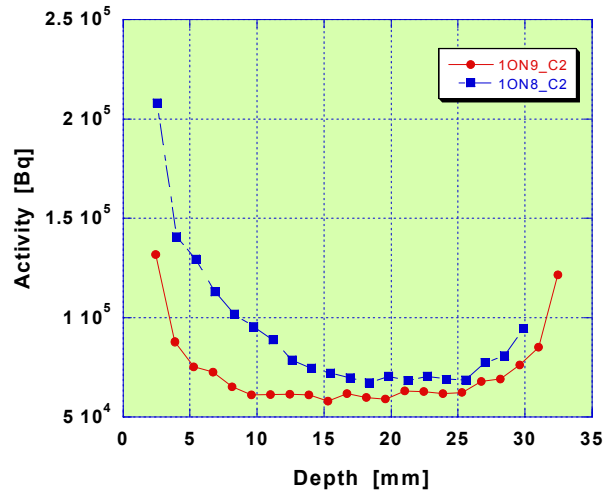


Fig. 1: Comparison between tritium diffusion profiles for tiles 8 and 9 retrieved from the JET outer divertor
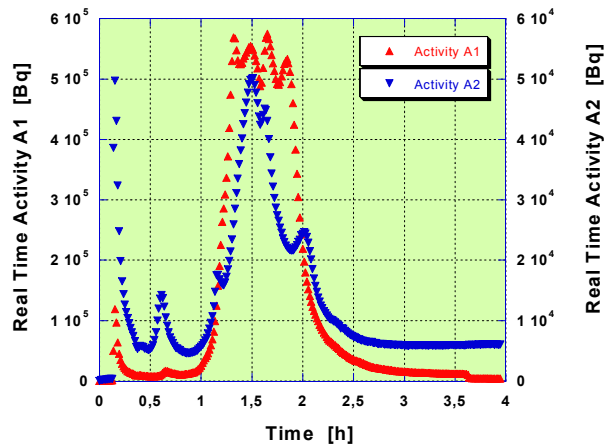


Fig. 2: Comparison between tritium thermal release of a bulk and a plasma exposed disk

After the release of the adsorbed water at approximately 150°C both specimens exhibits four peaks. For the A1 plasma exposed sample these peaks are close one to the other and are observed between 400°C and 800°C. In comparison to the A1 disk, the corresponding first and last peaks for the A2 sample (1.45mm below the plasma exposed surface) seems to appear earlier and later, respectively. For the time being it is not yet established if the 4 peaks corresponds to 4 different tritiated species, to 4 different trapping sites or to a combination of many tritiated species trapped in several sites.

Further experiments are in progress to understand this behaviour, namely by coupling the thermal release of such samples to a mass spectrometer.

Further experiments are also in progress to investigate the tritium retention and depth diffusion in the bulk for all type of divertor tiles.

From the results collected until now it becomes clear (at least for the 2D CFC type of tiles used at JET) that a surface thermal treatment of the tiles to remove the implanted/co-deposited tritium is not enough, as substantial amounts of tritium are trapped in the bulk of the tiles.

Staff:

N. Bekris
U. Berndt
D. Knebel
R.-D. Penzhorn
B. Schweigel

## JWO-FT-2.1
## Water Detritiation

During the operation of JET and tritium facilities of future fusion machines, active waste is generated in form of tritiated water (HTO), which has to be processed with full recovery of tritium.

At JET tritiated water is produced during the operation of the JET machine and the Exhaust Detritiation System in the Active Gas Handling System. Much tritiated water is also expected during the decommissioning of JET. Therefore a water detritiation system with a throughput of 20 000 kg/y needs to be developed and installed at JET. This aim will be realised in three steps: a laboratory test installation, an experimental facility on a semitechnical scale (500 kg/y) and finally the full-scale JET plant.

The most suitable process for water detritiation is the well known CECE process, a combination of electrolysis, where water is split into hydrogen and oxygen, and the catalytic exchange of hydrogen isotopes by a Liquid Phase Catalytic Exchange (LPCE) column for the tritium recovery from hydrogen.

Selection of the most suitable hydrophobic catalyst/packing combinations for the LPCE column and testing of parameters are the first important goals. At the Tritium Laboratory Karlsruhe (TLK) a laboratory sized catalyst test installation (Fig. 1) comprising an LPCE column and the required peripheral equipment was used for an inter-comparison of several hydrophobic catalyst/packing combinations, manufactured in Belgium, Romania, Russia and Japan.
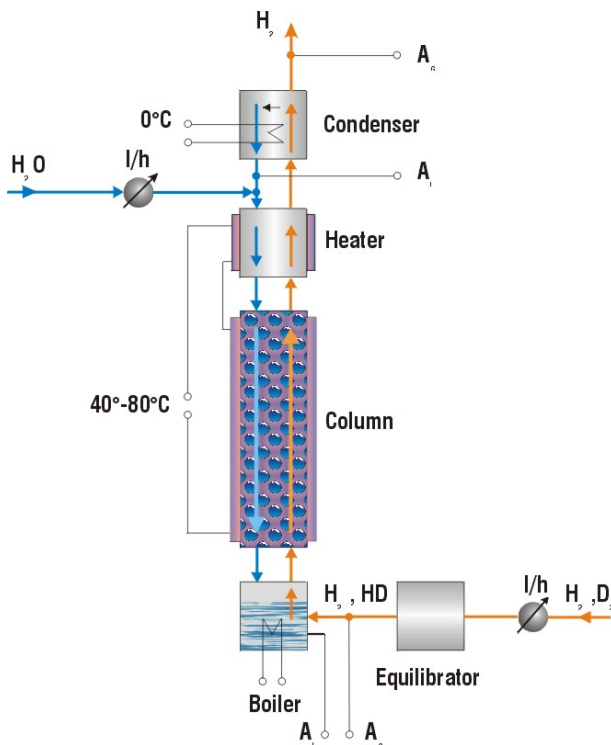


Fig. 1: Catalyst test installation

The main component of the test installation is a glass column with a length of 120 cm and a diameter of 40 mm. The column is filled with a mixture of hydrophobic catalyst and inert packing material (Fig. 2) with an active height of 90 cm. In the experiments water and hydrogen enriched with deuterium ($\leq$ 2 %) ar employed in a counter current mode. The molar ratios of gas to liquid flow are in the range of 2 – 4 at gas velocities of 0.1 – 0.2 m/s. The operation temperatures are 40 - 80 °C as recommended by the catalyst manufacturers.



Fig.2: Romanian catalyst/packing combination

The achieved degree of isotopic exchange for the different catalysts was evaluated under similar conditions by analysing the effluent gaseous and liquid phase by mass spectrometry (Quadrupole and Omegatron spectrometer) and infrared spectroscopy. In Table 1 the experimental results are presented.

Table 1: Experimental results

| Catalyst | Temp. (°C) | G/L | Concentrations at the bottom | | Concentrations at the top | | | HETP (cm) |
|---|---|---|---|---|---|---|---|---|
| | | | Liquid at. % | Gas at. % | Liquid at. ppm | Vapor at. ppm | Gas at. ppm | |
| Mend. Uni Moscow Russia | 60 | 2.2 | 1.42 | 0.99 | 1000 | 2750 | 2579 | 53 |
| | | 4.1 | 2.49 | 0.98 | 750 | 1360 | 3470 2320 | 29 |
| SCK·CEN Mol, Belg. | 40 | 2.1 | 1.19 | 0.99 | 370 | 2320 | 3475 | 82 |
| | | 4.0 | 2.22 | 0.99 | 510 | 2247 | 3525 | 45 |
| ICIT Romania | 70 | 2.3 | 1.51 | 0.99 | 210 | 305 | 862 | 28 |
| | | 3.7 | 2.33 | 0.99 | 360 | 480 | 3195 | 29 |
| Showa Co Japan | 70 | 1.9 | 0.95 | 0.99 | 3400 | 7750 | 5150 | 125 |

In addition, a mathematical model has been developed that allows comparison between experimental results and theory and will be used to design optimised large technical scale columns as required for JET. The objective of this model is the simulation of catalytic isotope exchange between tritiated water and hydrogen/deuterium to describe the deuterium enrichment performances of the columns which were tested with several catalysts at the TLK. The model and the corresponding software were verified by the experimental results. To describe the performance of the separation process two approaches were considered:

- A graphical approach (classical) that uses the operating line and the equilibrium curve for the process (Fig. 3).

- An analytical approach that solves the transport equations characterising the isotopic exchange process.
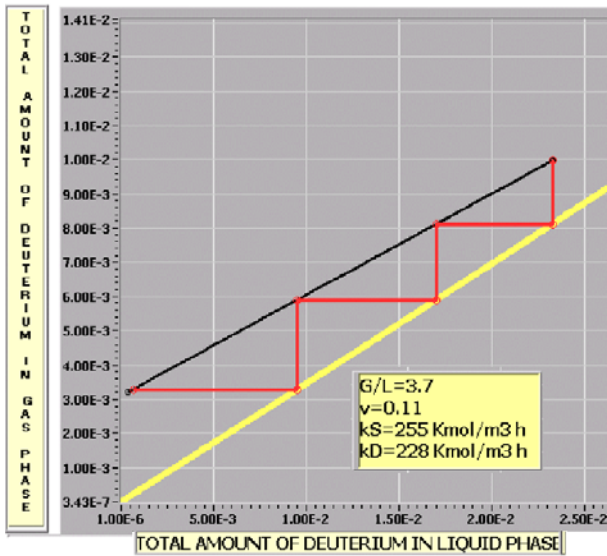


Fig. 3: Graphical determination of HETP

With this simulation model different types of catalysts having different geometrical shapes can be compared. Evaluation criterion of the single transfer rates of deuterium from deuteriated hydrogen to water is the Height Equivalent to Theoretical Plates (HETP). By this approach a general assessment of the efficiency of a column is possible.

On the basis of the obtained data several configurations of catalyst/packing can be proposed for JET. In order to maximise the surface of the catalyst packing, a new catalyst/packing material was manufactured in Romania, which will be tested now.

To evaluate the influence of the deuterium transport on the tritium transport when the two processes take place simultaneously, a further experimental installation was designed and is presently under construction in the TLK to get further data and to develop the present model to include the transport of tritium.

Staff:

C.J. Caldwell-Nichols
I. Cristescu
I.R. Cristescu
W. Jung
U. Tamm
S. Welte

Literature:

[1] I.-R. Cristescu, I. Cristescu, R.-D. Penzhorn, U. Tamm, Model for the simulation of catalytic isotope exchange between tritiated water and hydrogen/deuterium, Proceedings of the Annual Meeting on Nuclear Technology, Dresden, Germany, May 15–17, 2001, pp. 593-596.

# JWO-FT-6.1
# Impact of Tritium on the Performance of a Prototype Cryosorption Panel

## Introduction

This task is an essential complement to the parallel assessment of the pump performance of the ITER model cryopump (Task VP11), where the tritium fractions have been replaced by deuterium, and aims on full qualification of the cryopanel design for operation with tritiated gases. Before this task, this has only been investigated qualitatively and on a small scale level. The main goal is to reveal the isotopic effect clearly and to show any systematic differences for pumping non-tritiated and tritiated gas mixtures.

In the first stage of this task, an existing cryogenic module of the Active Gas Handling System (AGHS) at JET will be modified and adapted so as to house a test cryopanel arrangement. The panel set-up exactly meets the ITER point design and the test results are, therefore, fully representative. The major parts of the modification are the integration of a separate test vessel and the adaptation of the peripherical gas and cryogen supply systems.

In the experimental programme for this test unit, the cryopanel will be investigated with respect to pumping speed and capacity. The tests shall also establish appropriate regeneration conditions for tritiated species and assess the residual inventories associated with them.

## Design status

The basic design of the new installation and the intended experimental procedures have been discussed and agreed upon together with JET. The interfaces (mechanical, cryogenic, electrical, analytical etc.) and the requirements (safety, vacuum, quality, tritium compatibility etc.) were defined. The current design, which is still under approval discussion with the JET representatives, is shown in Fig. 1. An ultra high vacuum vessel is housing a series of three cryosorption panels, fed by liquid helium. The panels will be fabricated in quilted design and will be equipped with electrical resistance heaters to provide defined heating and to allow for a robust and versatile temperature control. This is an essential aspect for determining accurately the regeneration conditions needed after pumping tritiated gases. The design offers two operational alternatives, on one hand, the operation with the real JET plasma exhaust gases by direct connection with the JET torus matrix line, on the other hand, the operation with defined and pre-mixed gas mixtures via an internal gas circuit. The latter case is the standard case for tests with highly tritiated gas mixtures.

The manufacturing of the new test unit will be divided into three different parts, two smaller ones (vacuum bellows, panel substrates) and a big one concerning the integration and the complete vessel manufacturing. The delicate part of cryopanel finish will be done in-house at FZK involving the patented charcoal coating procedure. A step-by-step procedure for the complete manufacturing process has been developed to identify any critical points and to define inspection and monitoring actions.
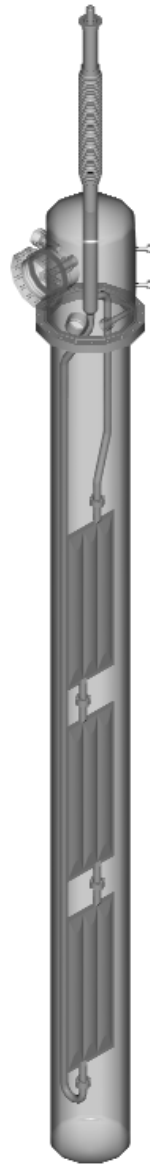


Fig. 1: Design of the cryopanel arrangement for tests under tritium at JET. The overall height is about 3 m.

Staff:

Chr. Day
H. Jensen
A. Mack
R. Simon

## JWO-FT-6.2
## Technical Permcat for the AGHS of JET

Staff:

M. Glugla
R. Lässer
T.L. Le
Fa. D. Niyongabo
K.H. Simon
S. Welte

Detritiation of tritiated hydrocarbons and water via hot metal getter beds in the Impurity Processing (IP) of the JET Active Gas Handling System (AGHS) during DTE1 resulted in an irreversible consumption of uranium due to the formation of carbides and oxides. In addition, the disposal of tritiated uranium constitutes a serious waste problem. Meanwhile the technology based upon heterogeneously catalysed reactions combined with permeation of hydrogen isotopes through palladium/silver as developed at the Tritium Laboratory Karlsruhe (TLK) has been adopted for the IP of the AGHS; uranium beds were replaced by a nickel catalyst reactor and a permeator.

In a next step a so called PERMCAT unit (*perm*eator/*cat*alyst hybrid) for counter current isotopic swamping will be installed at the outlet of the IP to further reduce the amount of tritium lost to Exhaust Detritiation System (EDS) of JET. The unit was constructed in Karlsruhe and shipped to JET for integration into the AGHS.

The PERMCAT reactor is designed for final clean-up of gases containing up to about 1 % of tritium in different chemical forms such as water, methane or molecular hydrogen. The unit is based on counter current isotopic swamping with protium, and experiments with laboratory scale Permcats have shown decontamination factors in the range of $10^4$ to $10^6$ under a variety of conditions. The prototype technical unit for JET was designed to cope with a tritiated gas flow rate of at least 1.5 molh$^{-1}$.

Because of the principle geometry of the PERMCAT a technical unit with the throughput required by the JET AGHS has to be based upon a multi-tube design and manifolds for the different gases. The JET Permcat comprise 21 tubes (instead of 6 for the CAPER facility operated at the TLK), each with a length of 900 mm (instead of 530 for the CAPER facility) manifolded. For an equal gas flow rate through each of the single 21 tubes of the JET PERMCAT the pressure drop in the tubes need to be uniform. The homogeneous filling of the catalyst into the PERMCAT was a challenging task and carefully examined. Figure 1 shows the individual pressure drops as measured in the final stage of the manufacture.
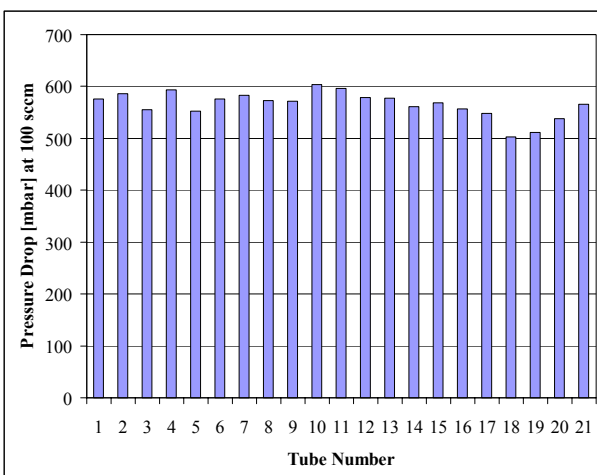


Fig. 1: Pressure drop of the different PERMCAT tubes

After careful leak testing and thermal cycling to check the function of the heaters and the response of the thermocouples the unit was shipped to JET for installation and testing with off gas from the JET tokamak.

# ITER Site Cadarache

## EISSG-SL3
## Strategy for the Management of Effluents and Releases

To evaluate potential sites for ITER in Europe a technical Site Study Group (EISSG) was established by the end of 2000. All the activities of the EISSG, which is chaired by the EFDA Associate Leader for Technology, are performed within the frame of EFDA. Since the French delegation announced the site of Cadarache at a European Consultative Committee on Fusion (CCE-FU) meeting the EISSG was asked to confirm the compliance of the Cadarache site with the ITER technical requirements, to identify key elements for the licensing procedure, to examine site specific aspects of the ITER construction and operation cost and to evaluate the social and infrastructure aspects of the project. The work was carried out through the Associations and by European industries via EFET.

The objective of task SL3 was to examine and to describe some possibilities to improve the basic ITER effluent and releases control designs, especially the detritiation systems.

It should be noted that in the case of tritium arising from a fusion plant there are practical and economic incentives to recover as much tritium as possible for reuse, as it is one of the fuels of the fusion reaction. Hence the ALARA principle is inherently followed in the design of fusion reactors.

Local conditions at a particular site may affect the quantities and concentrations of effluents and releases that will be permitted. Any such levels which are higher than the declared ITER Project Release Guidelines are unlikely to be adopted. If the permitted levels are lower than estimated values for the project then methods to reduce the effluents and releases have to be considered. It is likely that the liquid releases estimated for ITER in the Generic Site Safety Report, Volume IV, Normal Operation (GSSR Vol IV) may be too large for the Cadarache site.

The main sources for tritium contaminated gases and for tritiated water to be disposed of have been intensively studied.

Apart from the plume from the cooling tower, all gaseous releases are liberated to the environment from a single discharge point. The greatest source is the discharge from the ISS, which is estimated to be 67 TBqa$^{-1}$ of HT in $H_2$. This is the largest single source of tritium to be discharged in any form. However, while this is comparatively large it is in the form of HT, the most readily dispersable form, that is it will not be condensed or precipitated significantly close to the release point due to local weather conditions. The Water Detritiation System (WDS) waste stream is HT in $H_2$, there is also no water waste stream from the Atmosphere Detritiation Systems (ADS). The Heating, Ventilation, Air Conditioning (HVAC) and ADS systems will pass air containing small amounts of tritium, either as HT or HTO. The ADS systems have a finite detritiation factor but are designed to be consistent with ALARA and cover all likely eventualities. The plume from the (forced draught) cooling tower will contain tritium that may have leaked through the heat exchangers of the Tokamak Cooling Water Systems (TCWS) from the primary circuit. The volume of water evaporated per day is estimated to be 10,000 m$^3$day$^{-1}$.

Atmosphere from the active areas is detritiated by several ADS comprising of catalyst beds (to oxidize HT or tritiated hydrocarbons to HTO) and molecular sieve driers to remove as much of the HTO as practicable. The gases passing through these systems are discharged to atmosphere, these will include trace quantities of both HT and HTO due to the finite efficiency of the catalysts and driers. The driers will be regenerated periodically as they have a finite capacity and this will produce liquid water. The bulk of this water will have the normal moisture content of air but it will contain varying amounts of HTO, depending on the use of the particular ADS and the contamination level of the atmosphere being detritiated. This water is sent to one of five buffer tanks according to the concentration. The water that is sent to the tank for the lowest category (LL) of concentration is intended for direct discharge as liquid effluent, the limit is presently defined as 60 kBqkg$^{-1}$. The water in the remaining 4 tanks will be processed in the WDS. Condensate from the various HVAC systems will also be collected in the buffer tanks according to the tritium concentration. Before discharge, the water from the LL tank will be combined with water from the showers and laundry in the Personnel Access and Control Building and any water that has leaked from the TCWS and collected in the floor drain which has not been recycled and is sufficiently low in concentration. Blow-down from the cooling tower may contain tritium that has leaked through the heat exchangers of the TCWS from the primary circuit. The volume of water per day to be discharged in the current design is estimated to be 3,000 m$^3$day$^{-1}$.

If an intermediate loop in the cooling system would be used then a corresponding reduction of tritium released in the plume will be achieved, however the current estimated release is 0.36 Tbqa$^{-1}$ HTO, which is small compared to the total airborne releases.

The design and operational modes of the ISS and the WDS will result in a protium gas stream that has had the tritium content reduced to the lowest level that is practicably possible. If the release of this gas stream directly to the environment is the accepted route for disposal then there is little possibility to reduce the tritium content further. If release to the environment is not acceptable then the gas stream has to be collected and stored. Hydride beds are not practicable due to the mass of the protium vector involved, so conversion to liquid water is the most probable method for storage.

The exhaust gases from the ADS systems come from molecular sieve drier beds and are sent to the discharge point. It is unlikely that the drying performance (i.e. the removal efficiency of HTO) can be improved significantly, noting that the vector is a large volume flow of air. The HT content is a function of the catalysts which are optimally designed. Hence a significant decrease in releases of HT and HTO are unlikely to be possible.

The blow-down from the cooling tower has the characteristic of a large volume vector with very low contamination levels leading to a release of tritium. The concentration of tritium in this water and the large volume make tritium recovery impracticable. Two possible methods to reduce the tritium release are to reduce the loss of water or to reduce the potential for tritium leakage. A low-loss system would be to use a conventional cooling tower for the secondary cooling water, though this is perhaps not acceptable at the Cadarache site and moreover would result in a large volume of tritiated water to be disposed of on decommissioning. A possible alternative would be to use an intermediate cooling loop between the primary cooling water and the site water used in the forced draught cooling tower, thus creating an extra barrier to leakage. This would involve an additional pump and heat exchanger system but the water volume in this intermediate loop would be limited and can be conditioned/detritiated using the existing equipment.

The water from the HVAC and ADS systems designated for direct release can have a lower limit applied to it, this would reduce the integrated release and possibly the total volume of the water released but it would also increase the demands on the WDS. Any water leakage from the TCWS can also be treated in a similar fashion, however any contaminants it collects from the drainage system may make it unsuitable for the WDS.

Water from the showers and laundry will be contaminated with detergents etc. If this water contains any tritium, evaporation of the majority of the water followed by condensation and treatment in the WDS will inherently reduce the tritium content.

The estimated releases based on the ITER reference design are 0.12 TBqa$^{-1}$ and 0.02 TBqa$^{-1}$ from the blow-down and site waste water, respectively. The most significant reduction in releases is most likely to be obtained by an intermediate loop in the cooling system.

Dust and Activated Corrosion Products (ACP) are released due to the finite efficiency of the filters used in the various vector streams (water and air) and consist of particles smaller than the minimum size capable of being trapped. A reduction in releases is possible using better filters but there is a substantial penalty in the performance of the systems they are part of, hence a significant reduction is unlikely.

Staff:

C. Caldwell-Nichols
L. Dörr
M. Glugla

# EISSG-SL5
# Tritium Storage and Inventory Measurements

Beyond the initial hydrogen phase of ITER the Tritium Plant is essential for the operation of the machine as tritium will be produced from D-D reactions. The Tritium Plant has to process all tritiated gas streams from quite different sources, has to provide the deuterium and tritium fuel at specified flow rates and isotopic compositions and has to detritiate a number of waste streams prior to discharge into the environment. The Tritium Plant also handles incoming and outgoing tritium shipments and carries out tritium inventory measurements of these gases and the in-plant inventory.

The Fuel Cycle of the ITER Tritium Plant comprises a number of systems, namely the Analytical System (ANS), the Isotope Separation System (ISS), the Storage and Delivery System (SDS) together with the Long Term Storage (LTS) Vault, and the Tokamak Exhaust Processing (TEP) including auxiliary systems such as the Tritium Plant vacuum pumps. To assess completely the safety of the Tritium Plant by a Failure Mode and Effect Analysis (FMEA) or other safety considerations and to determine the tritium inventory and the tritium distribution within the Fuel Cycle a detailed design is necessary already at this stage of the project. Therefore not only an outline flow diagram of the Fuel Cycle, but Process Flow Diagrams (PFD's) including chemical flow sheets and even Pipe and Instrumentation Diagrams (PID's) along with the associated lists for components, heaters, instruments, pipes and valves have been prepared for all the Fuel Cycle systems of the ITER Tritium Plant. Interfaces between the systems and to other installations of ITER have been identified and described in Design Description Documents.

The Storage and Delivery System within the Fuel Cycle of the ITER Tritium Plant is crucial for inventory measurements and tritium accountancy. Specific regulations applicable in France concerning the storage of tritium do not exist. However, the design of the Storage and Delivery System (SDS) was briefly reviewed in view of ITER at Cadarache. In particular the hydride material options for the storage of tritium have been studied and the inventory measurement procedures examined.

Metal hydrides have been proposed for hydrogen storage because of the reversible absorption and desorption of hydrogen. For tritium applications of metal hydrides the equilibrium partial pressure of hydrogen isotopes at room temperature should be very low. The metal hydride would then not only act as a highly effective pump, but would also not leave any tritium in the gaseous phase and thereby substantially reduce the risk of tritium spill. Conversely the metal hydride temperature for an equilibrium pressure of hydrogen around atmospheric pressure should not be too high to allow the liberation of hydrogen isotopes from the metal hydride under moderate conditions. The two favourable tritium storage materials are uranium and zirconium-cobalt.

Uranium is probably the material most often used for storage and supply of ultra-pure hydrogen isotopes. The pressure / composition isotherms of the uranium / hydrogen system are an outstandingly good example of a metal hydrogen system with two phases: the $\alpha$-phase (dissolution) at very low concentrations and the hydride ($\beta$-phase) at very high concentrations. In the low concentration phase the equilibrium pressure increases sharply. When the hydride phase formation starts the equilibrium pressure stays essentially constant over a large concentration range. Only at an atomic ratio of uranium to hydrogen of almost 3 the pressure increases again strongly.

The reaction of uranium with hydrogen is exothermic with an enthalpy of about - 129 kJ per mol uranium or about - 86 kJ per mol hydrogen gas. The reaction heat need to be removed upon

uptake of hydrogen to keep the uranium hydride temperature and thereby the hydrogen equilibrium pressure low. During hydrogen desorption the reaction enthalpy needs to be introduced again into the system, which requires fairly powerful heaters for reasonable desorption rates. The supply of 200 Pam$^3$s$^{-1}$ of deuterium-tritium, the steady state fuel rate for ITER, would require to dissipate about 8 kW of power into the uranium hydride powder.

The total quantity of tritium stored in an uranium hydride getter bed can easily be limited by employing exactly the amount of uranium stoichiometrically required. An ITER getter bed with about 2650 g of depleted uranium would in effect restrict the inventory to 100 g tritium. The tritium equilibrium pressure above UT$_3$ at room temperature is less than $10^{-5}$ Pa. Even a fully loaded uranium bed will not show a significant pressure increase above the hydride for temperatures somewhat higher than ambient.

The zirconium-cobalt hydrogen system has been studied extensively because the Van't Hoff plot (logarithm of the hydrogen equilibrium pressure above the hydride versus the reciprocal absolute temperature) shows a slope very similar to uranium. This means that the reaction of hydrogen with zirconium-cobalt is exothermic to the same extent as with uranium. However, the reaction heat in case of zirconium-cobalt need to be removed more effectively upon uptake of hydrogen to keep the zirconium-cobalt hydride temperature and thereby the hydrogen equilibrium pressure low. The plateau pressures in the two phase region have a significant slope which increases with increasing temperature. For atomic ratios of zirconium-cobalt to hydrogen higher than about 2.0 the slope of the isotherms is rather steep. The plateau pressure of hydrogen above zirconium-cobalt hydride is higher for a given temperature in comparison to uranium hydride. This has the slight disadvantage that at room temperature zirconium-cobalt does not act as a getter pump as well as uranium, but the advantage that an equilibrium pressure of about 0.1 MPa is already reached at a lower temperature as for uranium. For zirconium-cobalt the amount of hydrogen which can be recycled at a given temperature and within certain pressure limits is very small and drastically reduced in comparison to uranium.

To principally restrict the total quantity of tritium stored in a zirconium-cobalt hydride bed to 100 g it shall not contain more material than stoichiometrically required. Since zirconium-cobalt will absorb hydrogen up to a ratio of 2.7, about 1850 g of the alloy is necessary for an ITER getter bed. However, a fully loaded bed will show significant tritium pressures for any temperature above ambient. It is therefore absolutely essential to watch the temperature of a fully loaded zirconium-cobalt hydride getter bed and to keep it sufficiently cold. The temperature of the bed during inventory measurements by in-bed calorimetry would typically be about 80°C. Under these conditions the equilibrium pressure above the fully loaded zirconium-cobalt hydride is already about atmospheric and hence the tritium inventory of the bed is not altogether retained in the metal phase.

A further disadvantage of zirconium-cobalt is its tendency to disproportionate at higher temperatures and at equilibrium (or higher) hydrogen pressures. Nowadays it is known that the disproportionation process can be reversed by subjecting the material to high temperatures under high vacuum conditions. Nonetheless the zirconium-cobalt bed would not be available for hydrogen isotope storage during such a regeneration.

To supply the steady state deuterium-tritium fuel rate for ITER of 200 Pam$^3$s$^{-1}$ about 8 kW of power would need to be dissipated into the zirconium-cobalt hydride powder in the getter bed. Seeing that this is already a challenging task for a technical getter bed, the control of the hydrogen pressure above the

zirconium-cobalt hydride at such a power input seems to be very difficult. Depending upon the actual temperature and hydrogen content the bed may easily be overheated during transients in the tritium removal rate because of the considerable slope of the isotherm. The resulting overpressure can cause the rupture disc of the metal hydride getter bed to blow or may initiate the disproportionation of the zirconium-cobalt hydride.

The reaction of metal hydride getter materials with oxygen, the temperature for a hydrogen equilibrium pressures of 0.1 MPa and the release of decay helium ($^3$He) have been employed as the main criteria in a scientific assessment and scientific comparison of metal hydrides for tritium storage at ITER about 5 years ago. As a result zirconium-cobalt was chosen at that time as the reference material for the ITER storage getter beds, also in view of the fact that uranium is a nuclear material. The necessity to strictly limit the inventory to 100 g tritium per metal hydride storage bed and in particular the requirement of a high tritium desorption rate were not considered at that time. From the discussion above it is clear that uranium is much safer than zirconium-cobalt as a storage material for a frequently used technical getter bed within a tritium process. It is therefore strongly recommended to reassess the choice of the ITER reference hydrogen getter material for the Cadarache site.

The general strategies for material balance and tritium inventory tracking for ITER at Cadarache are:

- The control and full accounting of tritium delivered to the ITER site and tritium removed or released from the plant.

- The evaluation of the amount of tritium generated in the breeder modules and bred in the beryllium of the first wall.

- An assessment of the amount of tritium burned by fusion reactions and generated by D-D reactions.

- The estimation of the amounts of tritium in waste material temporarily stored on site.

The arithmetical balance of these data is the tritium contained within the Mass Balance Areas for ITER, noting the uncertainties due to measurement and estimation inaccuracies.

The basic technique for on-line tracking of tritium and other gases within ITER are mass flow measurements and batch measurements via pressure changes in known volumes as gas is moved from one subsystem to another. Both techniques are rather limited in accuracy and require knowledge of the gas composition. Chemical analysis of the gases returned from the torus for example would involve a temporary storage in corresponding buffer vessels and thus would substantially increase the overall tritium inventory in the Fuel Cycle Systems beyond tolerable quantities.

The Long Term Storage Vault receives tritium which is delivered to the Cadarache site, exports (when necessary) tritium from site, but most importantly delivers and receives tritium from the remainder of the ITER Tritium Plant. Delivery from the Long Term Storage Vault will be required for initial loading of the Storage and Delivery System and routine top-up during operations, necessary because the tokamak will accumulate tritium over time in co-deposits and dust. The tritium accumulated in the machine during plasma operation will be periodically recovered and returned to the LTS getter beds. The period between such operations is expected to be of the order of a few weeks.

The tritium inventory in the LTS storage beds will be known at any point in time as all movements are properly accounted for. The Long Term Storage Vault is therefore proposed to be a separate Material Balance Area (MBA) of ITER.

The tritium inventory in the remaining various subsystems of ITER will normally be distributed. Therefore the inventory in the Fuel Cycle, in the tokamak and in the Hot Cell will only be known to a certain accuracy.

The methods feasible to determine the tritium inventory in the Fuel Cycle and the tritium inventory in the machine are limited. The amount of tritium held inside the tokamak will need to be continuously followed. This cannot be performed by any direct measurement of the inventory and can only involve calculating the difference between the known amount of tritium in the Fuel Cycle Systems, the estimated amount of tritium in the Hot Cell and the nominal inventory within this (second) MBA of ITER.

A more accurate measurement can only be made by emptying all the tritium from the Fuel Cycle Systems (and the Hot Cell) into the SDS which is by no means simple. Not only the tritium inventory in the cryogenic Isotope Separation System, but also the tritium inventories in catalyst vessel of the Tokamak Exhaust Processing or other components would need to be recovered. In addition, the amount of tritium lost into the Detritiation Systems of ITER would need to be accounted for. This is expected to take months rather than weeks and would severely interrupt the operation of ITER.

Three methods are proposed for the determination of the amount of total hydrogen and for the measurement of the total quantity of tritium in the SDS. The first method is the simultaneous determination of the hydrogen and tritium inventory by pressure, volume, temperature, concentration (pVTc) measurements. The accuracy of such a procedure is typically about 3-5%. The second method is the fast determination of hydrogen inventories. The overall content of one storage bed is transferred by heating and full evacuation into another getter. The values measured by flow meters at the inlet and at the outlet of the metal getter beds are integrated over time and thereby give an estimate of the gas inventory. The third method is in-bed calorimetry which allows the determination of the overall tritium content of a storage bed without removing the inventory from the bed. For an ITER getter bed with a design maximum inventory of 100 g tritium the accuracy of in-bed calorimetry is about ±3 g for a measuring time of 8-12 h and about ±1 g for a measuring time of 24 h. The method relies upon the exact determination of the heat generation rate of the tritium gettered in the storage material.

Book-keeping techniques may be sufficient to determine when the tokamak requires detritiation. If full inventory measurements of the Tritium Plant are required periodically for regulatory purposes a set of procedures for carrying out this task need to be established. The methods for tritium inventory measurements described and the limitations for tritium tracking have shown that further studies are required to quantify the possible accuracy of inventory and accountancy procedures.

Staff:

C. Caldwell-Nichols
M. Glugla
R. Lässer

# HCPB Blanket Concept

## TTBB-001
## TBM Adaptation to ITER FEAT

This activity has been performed in the frame of the Test Blanket Working Group in close collaboration with the ITER JCT and the other blanket design teams (EU-WCLL, JA, RF) involved in the ITER blanket test Programme during the extension of the EDA phase of ITER. The objective was the adaptation of the Test Blanket Module (TBM) System to the design and operational conditions of ITER-FEAT. This necessitated an assessment of blanket test program and objectives as well as a revision of the test module and the auxiliary system design.

Most of the work on the testing plan and conceptual design have been performed in 2000 and reported in [1,2,3]. In 2001 the conceptual design of the TBM System has been completed and the performance analysis on neutronics, thermo-hydraulics and thermomechanics has been carried out. Both the conceptual design and the related performance analyses have been reported in the Design Description Document of the of the HCPB TBM; this document has been delivered mid July 2001 to the ITER team. The HCPB contribution to the Safety Report of ITER has been prepared as well (see section TTBB-001-2). Furthermore, two additional documents have been prepared collecting all the material properties (relevant for ITER operation) of the ceramic breeders and beryllium pebble beds; these two documents are part of the Material Assessment Report of ITER.

An upgraded Design Description Document (Status December 2001) of the HCPB TBM including all the work (conceptual design, performance analyses including safety) performed in this task in year 2001 is under preparation and will be published next year as FZKA report.

In the next years a constant increase of the design activities is planned in the HCPB Programme. The final goal is to start the test of HCPB TBMs in ITER in 2015; milestones on this way are to "freeze" a HCPB blanket concept for DEMO and to complete a test programme for TBM in ITER in 2005, to "freeze" the design of the TBMs in 2010 after an extensive mock-up testing in a big Helium Test Facility and finally to fabricate, qualify and licence the TBM for testing in ITER.

## TTBB-001-1
## Test Programme and Conceptual Design of TBM's

The HCPB blanket testing programme for ITER-FEAT is based on four TBM's, each devoted to a family of objectives.

1. Electromagnetic (EM) TBM (3 years of tests during H plasma). Measurements of eddy currents and electromagnetic forces in normal operation and during disruption. Investigation of effects of ferromagnetic materials. Preliminary tests on TBM loops and remote handling.

2. Neutronics and Tritium production (NT) TBM ( 3 years of tests; D plasma and low-duty D-T plasma). Check of the tritium breeding capability and validation of neutronic code and data.

3. Thermomechanics (TM) TBM (2 years of tests: low and high-duty D-T plasma). Investigation of pebble bed behaviour, thermal creep, cyclic power operation, purged gas flow conditions.
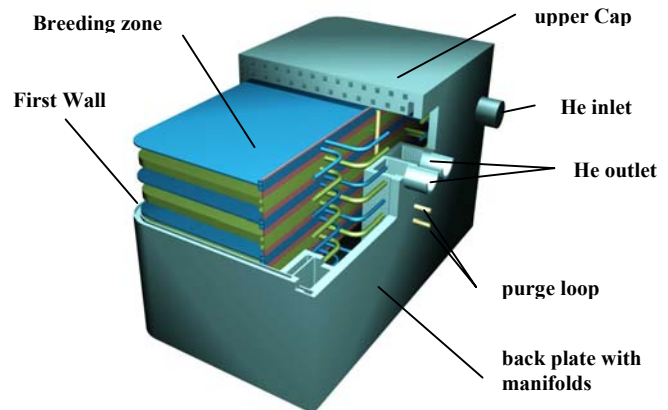


Fig. 1: Isometric view of the TBM without external manifolds and mechanical attachments to ITER

4. Plant integration (PI) TBM (2 years of test in high-duty D-T plasma). Integration tests: thermo-mechanics, thermo-hydraulics, tritium and activation products handling and cooling system operation

**TBM Design**

The HCPB TBM with outer dimensions of 1.27 m x 0.74 m x 0.8 m consists essentially of horizontal layers (with exception of the TM-TBM, in which also vertical beds are foreseen) of breeder and beryllium pebble beds, separated by cooling plates. The whole stack is encapsulated by a box that is formed by a First/Side Wall shell with integrated cooling channels, a robust backplate containing the manifolds and the mechanical attachment system and two massive caps at the upper and lower ends of the box able to withstand the internal pressure of the box (20 MPa is the max. design value in case of accident scenarios). Helium coolant is fed from the rear side via manifolds, at first through the box including the FW, and subsequently through the cooling plates in the internal breeder zone. The pebble beds are purged by a forced flow of low-pressure helium provided by the Tritium Extraction Subsystem (TES).

In 2001 the design of the TBM has been completed; in particular a new design of the backplate with manifold and of the external feeding manifolds has been elaborated.

**Auxiliary System Design**

The TBMs of the HCPB line have an own single-loop helium cooling system. Its components are located in the TCWS (Tokamak Cooling Water System) vault, approximately 100 m away from the TBM. The cooling system is designed to remove about 1 MW of heat from the TBM at inlet/outlet temperatures of typically 250/500°C and 8 MPa system pressure. The main pipe inner diameter is 68.3 mm.

The Tritium Extraction System has been designed for a mass flow of 6 g/s, a He pressure of about 0.1 MPa and a swamping ratio He/H$_2$ of 1000. The tritium production in the TBM is about 0.11 g/day (peak value during the pulses).

In 2001 the most important changes have been made in the design of the Coolant Purification System (CPS). The CPS has

been strongly reduced in dimensions and integrated into the Helium coolant system allocated in the TCWS vault.

**Nuclear Analyses**

The nuclear design calculations for the HCPB blanket test modules in ITER have been performed with the Monte Carlo code MCNP, version 4C and nuclear cross-section data from the FENDL-1 data library. A 20 degree torus sector model, developed on the basis of the current ITER design by the ITER Joint Central Team nuclear analysis group, formed the basis of the calculations (see Fig. 2). The horizontal test blanket port was modified in this model to allow the inclusion of test blanket modules. A water-cooled steel frame and two test modules of the HCPB type with a 5 mm thick Beryllium protection layer at the plasma facing surface were integrated into the port.

Nuclear calculations have been performed for the NT and the PI HCPB test blanket modules. Neutron wall loading, tritium generation, nuclear power generation and shielding efficiency have been assessed in the calculations.



Fig. 2: Radial-poloidal cut of the MCNP model of ITER (with integrated HCPB TBM in the horizontal port) used for the nuclear analysis
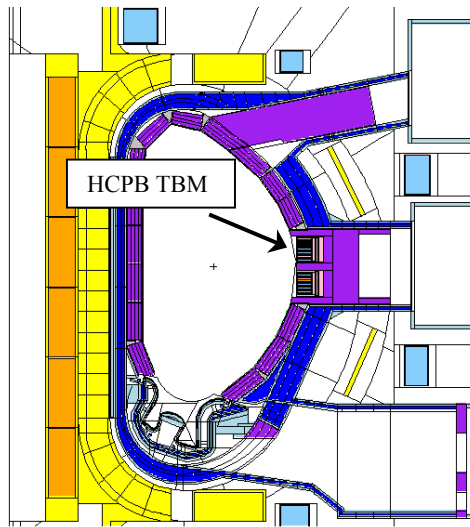
Afterheat and activity inventories were assessed for the NT TBM by making use of an appropriate code system that allows to perform three-dimensional activation calculations. The Monte Carlo transport code MCNP and the fusion inventory code FISPACT form the central modules of this system and are linked through an appropriate interface. While the MCNP-calculations are based on the FENDL-1 data library, the FISPACT inventory calculations make use of the activation and transmutation cross-section data of the  European Activation File EAF-99.

**Thermohydraulic - Thermomechanical Analyses**

Thermohydraulic analyses were carried out for the TBM using the finite elements (FE) code FIDAP. Two FE models were generated,  the first one representing the TBM box including a 5 mm thick beryllium protection layer at the plasma-facing surface and a part (10 mm thick) of the beryllium pebble bed at the inner box surface, and the second FE model representing the breeder zone consisting of the breeder and beryllium pebble beds, the cooling and the stiffening plates. The counter-current flow in the cooling channels of the first wall was taken into account. The

helium temperature at the outlet of the FW was used as inlet temperature for the cooling/stiffening plates of the breeding zone model. The flow direction in the cooling/stiffening plates is radial with headers at the back side and U-turns at the front side. To avoid overcooling of the stiffening plates, every third cooling channel is a dummy channel with stagnant helium, whereas in the cooling plates helium is circulating in every channel. The helium flow rates have been determined in such a way, that the sum of the temperature rises in the two FE models is equal to the temperature rise specified for the TBM's (200 and 250 K, respectively). Heat transfer coefficients have been determined using the usual correlations for turbulent channel flow. For the FW channels it has been additionally assumed that by roughening of the surface doubling of the coefficients is achieved.

Output of the thermohydraulic analyses are the temperature distribution of the structural material, the pebble beds and the coolant. The pressure drops have been estimated as well.

**Structural Analysis**

A preliminary structural analysis has been carried out using the CAD/FE code system CATIA/PERMAS. A poloidal section of the TBM has been modelled consisting of the FW box, two cooling plates, two half stiffening plates, and a simplified version of the helium distribution-collection system at the back side of the TBM. The mechanical interactions between the pebble beds, the beryllium protection layer, and the TBM structure has been ignored.

Only one case has been analysed so far: the PI-TBM under maximum load conditions. The calculated temperatures of the structures are in good agreement with the results of the thermohydraulic analysis. The calculated stresses are in general within acceptable limits. E.g. the maximum primary stress (v. Mises) amounts to only 44 MPa. The maximum primary stress in the region of the helium distributors/collectors is 162 MPa, but this stress can easily be reduced by further optimising the design. The total v. Mises stress (primary plus secondary) is in total acceptable, but some local maxima necessitate further attention, e.g. a detailed analysis by mesh refinement, local stress evaluation, or application of more sophisticated methods like inelastic analysis. However, this can reasonably be carried out only when the design of the TBM has been further elaborated.

In order to control the pressure in the TBM in the case of an internal helium leak, two rupture disks are foreseen. In order to limit their dimensions the maximum tolerable pressure inside the TBM should be about 2 MPa. For the breeding zone of the TBM this will be readily achieved by the stiffening plates. The stability of the back region of the TBM has recently been improved by two toroidal headers at the back wall of the TBM. This design modification has not yet been included in the structural analysis.

**Material Assessment Report on Beryllium and Ceramic Breeder Pebble Beds**

In the frame of this work two further documents have been completed as contribution of the Material Assessment Report of ITER. The first document contains a critical review of the available pebble and pebble bed properties of Beryllium 1mm-NGK pebbles. The second one describes the two Lithium ceramics (FZK- Orthosilicate and CEA Metatitanate) that are considered as breeder material in the HCPB concept. The work has been carried out with the contribution of CEA as far as the Metatitanate is concerned.

## TTBB-001-2
## Safety Analysis of TBM's and External Loop

A first safety assessment of the HCPB TBM has been performed during the ITER EDA phase in 1997. The effort was co-ordinated within the Parties and the ITER Joint Central Team with the aim for a consistent approach in the safety analysis between the ITER basic machine and the TBMs. On these grounds a re-evaluation has been performed in this year, considering the changes made since then to ITER as a whole, to the HCPB test strategy, and to the TBM and its cooling system in particular. Like in former work emphasis is placed on the analysis of off-normal events with slightly modified accident scenarios. The objective is to demonstrate that the introduction and operation of the test modules does not add significantly to the risks of the basic machine.

This study discusses three groups of accidents judged to cover all accident scenarios envisaged in Cat II to IV events involving the TBMs. Some limited effort has been spent to address the behaviour of the TBMs under Cat V accident scenarios as well in order to assess the ultimate safety margins of the TBMs. The three groups of accidents investigated with their parametric variations are summarised in Table 1.

Table 1: Accidents analysed for the HCPB PI-TBM

| |
|---|
| **1) Loss of coolant into the vacuum vessel, that is**<br>1a) In-vessel multiple breaks of FW cooling channels of the TBM<br>1b) as 1a plus failure of FW/breeder zone interface with steam ingress into the TBM<br><br>**2) Loss of coolant into the breeder box with various leak sizes (and with subsequent coolant release into the VV)**<br><br>**3) Loss of coolant into the heat transfer vault for the TBMs, that is**<br>3a) double-ended pipe break in the TBM cooling system with late passive shutdown at melting of FW<br>3b) as case 3a plus failure of the TBM box leading to steam/beryllium contact<br>3c) as case 3b but with early active plasma shutdown. |

The assessment addresses a number of concerns or issues that are directly caused by the TBM system failure. Any consequences which may result from subsequent damage to the ITER machine (e.g., via a heavy disruption) are beyond the scope of this work. The concerns addressed for the different event sequences are the following, where applicable: (a) vacuum vessel pressurisation, (b) reactor vault pressure build-up, c) purge gas system pressurisation, (d) temperature evolution in the TBM, (e) decay heat removal capability, (f) tritium and activation products release from the TBM system, (g) hydrogen and heat production from Be/steam reaction, and (h) Be/air reaction exothermic heat production.

The concerns identified for the individual event sequences revealed to be uncritical, except for some reservations made to case 3b (see below). The VV pressurisation upon release of the total helium inventory from the TBM system is very small (8700 Pa). In cases of large ex-vessel leakage from the loop the pressure rises in the reactor vault by 280 Pa within 2.2 seconds, i.e., 0.28 % above nominal. Pressurisation of the TBM box upon a leak inside the module occurs within a fraction of a second and is limited to about 2 MPa by appropriate burst disks. The pressure does not propagate significantly to the tritium extraction subsystem.

The temperature evolution in the TBM first wall during transients is dictated by the delay time needed to shutdown the plasma. At continued plasma operation after loss of coolant the first wall temperature rises at a rate of 1 to 2 K/s. The long-term temperature development in the TBM is a matter of decay heat and boundary conditions assumed. The 1D heat transport model showed that passive decay heat removal from the TBM is assured in all cases. As a result chemical heat from steam/beryllium reactions is tolerable if early shutdown (less than 20 s) is assured. In the hypothetical scenario of loss of coolant with plasma shutdown occurring at melting of the FW beryllium protection layer, the chemical reaction there is limited by the amount of beryllium present with acceptable hydrogen production. Unlimited steam access to pebble beds must be avoided in case 3b, for which means are indicated.

The tritium release from the TBM system is inherently small. The most mobile fraction of the order 0.3 mg only is carried with the helium coolant. The amount of tritium which could be liberated from the beryllium pebbles is bounded by the inventory to 18 mg. Activation products in the helium cooling system are expected to be small.

Uncertainties in the data base and in the analysis do not seem to have considerable impact on the outcome of the study. Most of the effects are inherently small (like pressurisation, heat production, radioactive inventory) compared to the consequences resulting for ITER as a whole from the postulated disruption damage. In conclusion, the HCPB TBM system does not add significantly to the safety risk of ITER.

Staff:

N. Bekris
L. Boccaccini
Y. Chen
U. Fischer
S. Gordeev
S. Hermsmeyer
E. Hutter
K. Kleefeldt
S. Malang
G. Piazza
E. Rabaglino
J. Reimann
K. Schleisiek
I. Schmuck
H. Schnauder
H. Tsige-Tamirat

Literature:

[1] L.V. Boccaccini, U. Fischer, K. Kleefeldt, S. Malang, K. Schleisiek; "Helium-cooled pebble bed blanket testing in ITER FEAT - Objectives and test strategy", FZK Internal report (February 2001).

[2] K. Kleefeldt; "Helium Cooling System Layout for the HCPB Test Blanket Modules to be tested in ITER FEAT", FZK Internal Report (February 2001).

[3] L.V. Boccaccini (comp.), N. Bekris, Y. Chen, U. Fischer, S. Gordeev, S. Hermsmeyer, E. Hutter, K. Kleefeldt, S. Malang, K. Schleisiek; " Design Description Document for the European Helium Cooled Pebble Bed (HCPB) Test Blanket Modules, FZK Internal report (December 2001).

## TTBB-002
## Blanket Manufacturing Techniques

## TTBB-002-1
## HIP Joining of Cooling Plates

**The 7th HIP experiment series using two-step HIP technique for diffusion welding of structure with cooling channels**

The objective of the work on hot isostatic pressing (HIP) experiments is to investigate the appropriate HIP technique, the boundary conditions, and parameters in order to achieve good mechanical properties of the diffusion welding joints as well as to achieve a transition to test specimens of larger dimensions. Typical specimens for the first wall and cooling plate (size: about 100x100 mm$^2$) consist of two halves of plates with complex arrays of internal coolant channels on each half.

In the past 6$^{th}$ experiment series [1] the two-step HIP process was already successfully applied for achieving high mechanical properties. In the first HIP step, the specimens protected by pressure plates were encapsulated and diffusion welded with relatively low gas pressure at max. 12 MPa (1050 °C, about 2 h) corresponding to a surface pressure at the welding joint of about 30 MPa. After dismantling and separating, the specimens with now open cooling ducts were HIPped at a high pressure of 200 MPa (1050 °C, 1 h). With this second HIP step the still existing defect zone in the HIP joint are pressed together so that the strength and ductility of the HIP joints are improved by further diffusion process. In the following 7$^{th}$ series specimen plates of the same first-wall and cooling plate geometry were used, while the welding preparation was modified.

**Specimens preparation**

In the 7$^{th}$ experiment series four sets of specimens were welded. The first two sets were manufactured with each dry-milled (Rt ≤ 3 μm) and ground joining surfaces in order to check the reproducibility of the 6$^{th}$ HIP. In a further specimen set the dry-milled joining surfaces were sealed at the edge by EB welding and in the last specimen set EUROFER was used for the first time. Cleaning took place in an ultrasonic bath with acetone. As getter material, zirconium wires had been inserted into the cooling channels of every second plate.

| Specimen set No. | Material *) | joining surface preparation | | |
|---|---|---|---|---|
| | | dry-milled | ground | EB seal welding **) |
| 1 | M | x | - | - |
| 2 | M | - | x | - |
| 3 | M | x | - | x |
| 4 | E | x | - | - |

*) M=MANET, E=EUROFER, **) at the edge of joining surface

Quartz glass mats of a fine structure were used as separators between the specimens, the pressure plates and the encapsulating jacket during the first HIP step.

**Experimental results**

After the execution of the experiments six of eight specimen plates were intact. The deformation of the channel webs of the MANET specimens was in the range desired, while it was somewhat too high for the EUROFER specimens. For the first time, strong deformation of two specimen plates was observed after the first HIP step. This deformation was due to the pressure break-through at the sheet-jacket during the HIP process. All intact specimen plates, except for the first wall plate with the ground joining surface, were found to have strengths (Rp0.2, Rm) and ultimate elongation (A) that corresponded to those of the basic material (MANET: Rp0.2~605 MPa, Rm~725 MPa, A~14%; EUROFER: Rp0.2~471 MPa, Rm~608 MPa, A~16%). It could be confirmed again that better results were achieved by specimens with dry-milled joining surfaces in comparison with those with ground surfaces. Evaluation in case of EB seal welded specimens showed higher value of ultimate elongation and lower strength values. For the first time, the notch impact test was carried out but the strength values obtained were subjected to considerable large scattering so that the measurement should be repeated in the future experiments especially with EUROFER specimens. Fig. 1 shows for example the metallurgic photographs of the MANET first wall specimens with dry-milled and ground joining surfaces (Table, No. 1 and 2) after the second HIP step. The welding zones are only recognizable from the partly existing preferred direction of the grains. This is particularly clearly recognizable in the case of ground joining surface.

joining surface →



500x

FW specimen with dry-milled joining surface

joining surface →



500x

FW specimen with ground joining surface

Fig. 1:  Micrographs of the MANET FW specimens with dry-milled and ground joining surface after the 2$^{nd}$ HIP step

**Conclusion and Outlook**

With the use of two-step HIP process in these experiments good diffusion welding results for grooved plates with cooling channels were achieved. The values of tensile and yield strength in the welding zones lie in the range of the base material. The values of the uniform elongation are useful. First measurement results for notch impact strength showed large scattering and should to be repeated with some improvement of sample preparation in the following experiments. As significant knowledge gained from these experiments the following parameters for preparation of HIP joining surfaces were found suitable for improving the welding results: dry-milled surface, Acetone ultra sonic bath (no etching) and the use of zirconium wires as getter material. A transition from the use of MANET to EUROFER as specimen material has been introduced. In future experiments the continuation of this work will emphasis on the

HIP joining of EUROFER/EUROFER and ODS-EUROFER/EUROFER which is considered necessary e.g. for the development of the advanced dual coolant blanket concept [3].

Staff:

P. Norajitra
G. Reimann

Literature:

[1] G.Reimann, Diffusionsschweißversuche in Heißisosta-tischen Pressen zur Herstellung von Plattenbauteilen mit inneren Kühlkanälen für Fusionsblankets - sechste Versuchsreihe -, FZK-PKF report Nr. 158, August 2000.

[2] G. Reimann, H. Kempe, P. Norajitra, R. Ruprecht, R. Vouriot: Diffusionsschweißversuche in Heißisostatischen Pressen zur Herstellung von Plattenbauteilen mit inneren Kühlkanälen für Fusionsblankets – siebente Versuchsreihe - FZK-PKF Report Nr.175, Mai 2001.

[3] P. Norajitra, L. Bühler, U. Fischer, K. Kleefeldt, S. Malang, G. Reimann, H. Schnauder, G. Aiello, L. Giancarli, H. Golfier, Y. Poitevin and J.F. Salavy, The Second Advanced Lead Lithium Blanket Concept Using ODS Steel as Structural Material and SiCf/SiC Flow Channel Inserts as Electrical and Thermal Insulators, FZKA 6385, 1999.

## TTBB-003
## Pebble Bed Assembly Development and Testing

## TTBB-003-1
## Operation and Analysis of HEBLO Test Section

**Temperature transient experiments with limited heating plate temperature at 700°C**

After termination of the first HEBLO experiment series [1] under steady-state operation with altogether 61 measurements (each with constant temperature levels between 300 and 700 °C) following temperature transient experiments with altogether 123 temperature cycles were carried out successfully till the end of 2000. For safety reasons and to avoid an excessive strain of the heating plates, the maximum heating plate temperatures were limited to the moderate value of 700°C in these first transient experiments. By means of cyclic power control of the gas heaters and the pebble bed heaters a maximum temperature ramp of about 200 K within the pebble beds could be reached. All components functioned well so far and the reproducibility of the operating conditions and the measured temperatures was always given. This indicates that the pebble beds, the heating plates and the steel structure are still intact. All measurement data (temperature, flow rate, heat power, purge gas flow, and pressure drop, etc.) were recorded online fully automatically.

**Temperature transient experiments with maximal heating plate performances**

After an increase of the heating plate performances to an extremely high level the maximal steady-state temperatures of the ceramic and beryllium pebble beds of 900 °C and 650°C, respectively, (Fig. 1) could be successfully achieved now corresponding to the DEMO conditions. The maximal first wall temperature was also reached at about 500-510°C after additionally adjusting the power of the gas heaters. Based on this new condition with high temperature level following cyclic temperature transient experiments with 12 temperature cycles were carried out in the first quarter of 2001. Fig. 2 shows the cyclic temperatures measured in the ceramic and beryllium pebble beds and in the first wall. Applying the same technique of cyclic power control of the gas and pebble bed heaters as before a maximum temperature ramp within the ceramic and beryllium pebble beds of about 400 K and 250 K, respectively, could be reached with the maximum value of pebble bed temperatures (curve b) at the vicinity of the heating plates of about 900°C for ceramic and about 640°C for beryllium, respectively.
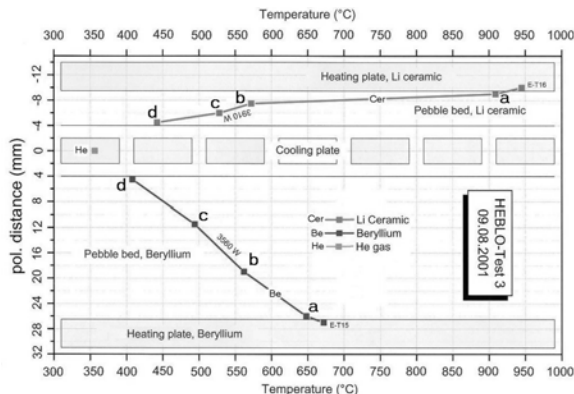


Fig. 1: Steady-state temperatures measured across the Be and ceramic pebble beds at highest heating plate performances.
(Measuring positions: a: NW-HP, b: PB, c: PB, d: NW-CP;
CP= cooling plate, FW= first wall, HP= heating plate, NW = near-wall, PB = pebble bed)
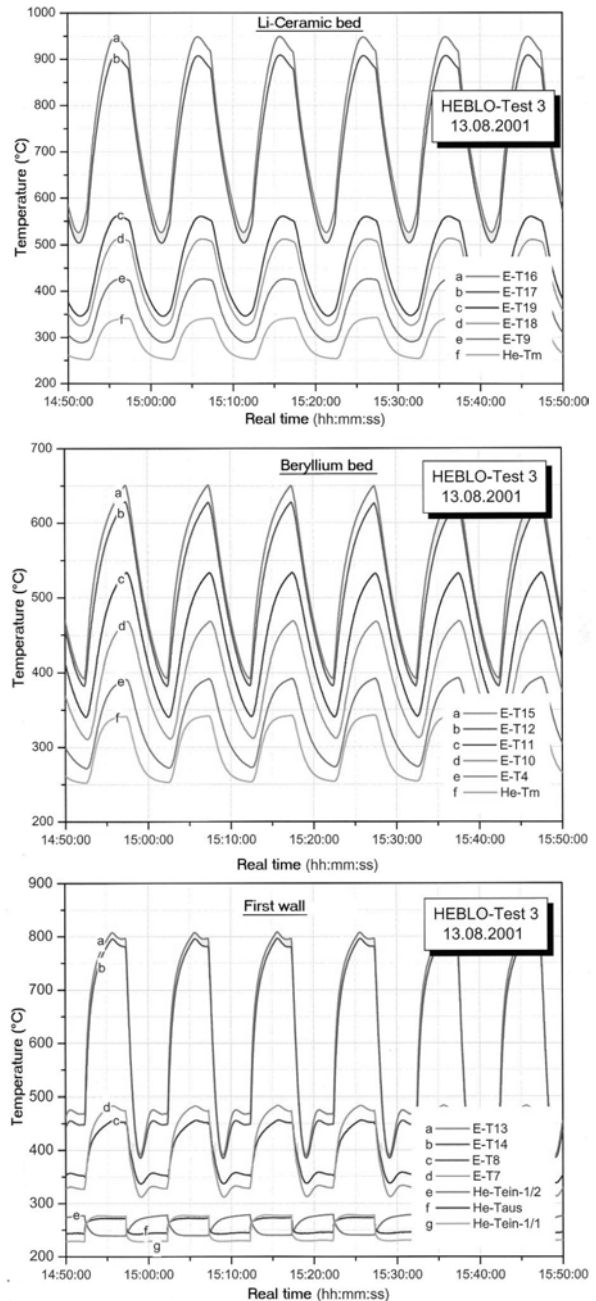


Fig. 2: Cyclic temperature transient experiment at highest heating plate performances, measured temperatures within the pebble beds and the first wall

**LOFA experiments**

Preparations for the 'loss of flow' accidental case (LOFA) experiment were made including installation and testing of an additional software for the automatic control of the LOFA experiments based on the shutdown scenarios assumed for ITER [2,3] (Table). The LOFA functions were simulated by a successive shut-down of the helium blower and all the heaters within the test section (gas, pebble bed and first wall heaters). The LOFA experiments were tested first with moderate heat power of the heating plates and afterwards the complete programme of LOFA experiments was run successfully with extreme heating plate performances. In case of the normal shut-down the maximum temperatures of the steel structure before and during LOFA amount to 504/625°C for the first wall and 450/620 °C for the cooling plate, respectively. The maximum ceramic and beryllium pebble bed temperatures dropped from

908°C and 657°C at the beginning of LOFA to a value of about 635°C and 580°C, respectively, at about 10 min later.

Postulated Plasma Shutdown Scenarios for Accident Analysis

| Shutdown Scenario | Delay time (s) | Ramp-down time from full power to zero (s) | |
|---|---|---|---|
| | | of internal heat | of surface heat |
| Normal | 1 | 100 | 100 |
| Accelerated | 1 | 20 | 20 |
| Fast | 1 | 0 | 20 |

**Conclusion and outlook**

The experiments with the HEBLO test section have shown that the components of a blanket concept similar to the actual HCPB blanket withstood the relevant DEMO conditions. After extensive preparations and function tests the temperature cyclic transient and the LOFA experiments were carried out and have been successfully completed. It seems that all components of the test section and the helium loop withstood all thermal-mechanical loads with maximal temperature of up to 900 °C in the ceramic and 650 °C in the Be pebble bed, respectively. Work on post-examinations of the individual components (e.g. integrity of the diffusion welds, interactions between pebble beds/steel structures) is under-way. Simulation post-calculations related to the temperature transient experiments are in preparation.

Staff:

P. Norajitra
D. Piel
G. Reimann
R. Ruprecht

Literature:

[1] P. Norajitra, D. Piel, G. Reimann, R. Ruprecht: The First Series of the HEBLO Experiment with the HCPB Small-scale Test Section (Task TTBB-003), FZK Internal Report, Juni 2000.

[2] K. Kleefeldt, K. Gabel, I. Schmuck: Safety studies for the HCPB DEMO blanket and ITER test module, FZK Internal Report, March, 1997.

[3] L.V. Boccaccini, Editor: European Helium-Cooled Pebble Bed (HCPB) Test Blanket, ITER Design Description Document Status 1.12.1998, FZKA 6127, March 1999.

## TTBB-005
## Development of Ceramic Breeder Pebble Beds

### TTBB-005-1
### Characterisation of $Li_4SiO_4$ Pebbles

In the frame of the development of ceramic breeder pebbles for the HCPB blanket, slightly overstoichiometric lithium orthosilicate ($Li_4SiO_4$ + $SiO_2$) pebbles are considered as candidate ceramic breeder. The pebbles have diameters in the
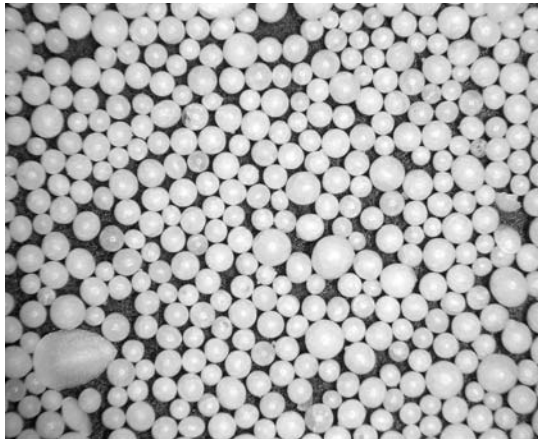


Fig. 1:     $Li_4SiO_4$ pebbles (natural enrichment)

range 0.25-0.63 mm and are produced by the melting-spraying process in the laboratories of the firm Schott Glaswerk Mainz. In particular, for pebbles with natural [6]Li–enrichment lithium orthosilicate and $SiO_2$ powders are molten and sprayed. During the flight the sprayed material solidifies in dendrite structure assuming spherical shape. This method allows to produce
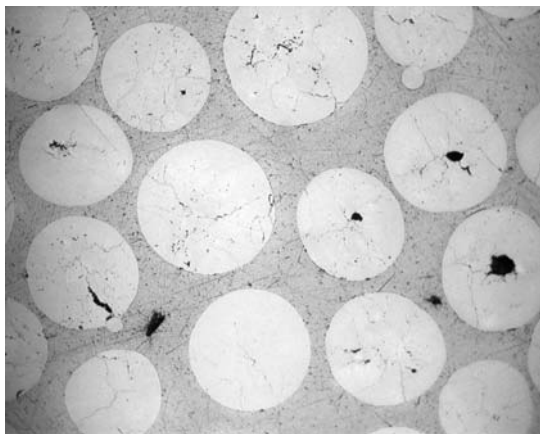


Fig. 2:  Cross section of $Li_4SiO_4$ pebbles (natural enrichment)

spherical pebbles with high density (figs. 1 and 2). [6]Li-enriched pebbles are produced by mixing and melting together of lithium orthosilicate, lithium carbonate (95% 6Li-enriched) and $SiO_2$ powders. The quality of each batch of pebbles delivered to FZK is controlled by:

- analyses of chemical composition of the pebbles;

- optical and electron microscopy (microstructure);

- crush test (mechanical stability);

- porosity and density measurements;

- annealing tests;

In conditioning experiments (pebbles annealed at 1000 °C for two weeks in air) and in long term annealing experiments (96 days at 970 °C in He + 0.1 vol% $H_2$ purging flow), performed to study the pebble behaviour at high temperature, it was observed that, a larger porosity was generated in pebbles produced starting from lithium carbonate (enriched pebbles) than in the not enriched ones (fig. 3 and fig. 4). The increased porosity strongly reduced the mechanical stability of the pebbles (crush tests). For this reason a study was started to optimise the production of enriched pebbles. The work is still ongoing and has to be completed till the end of the year 2001, in order to supply relevant material for the high fluence irradiation to be started at HFR Petten in the first months of next year.
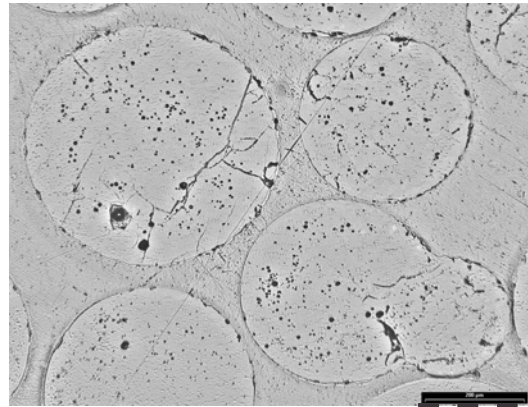


100 : 1                                    200 µm

Fig. 3:  Cross section of not enriched pebbles after 96 day annealing at 970 °C
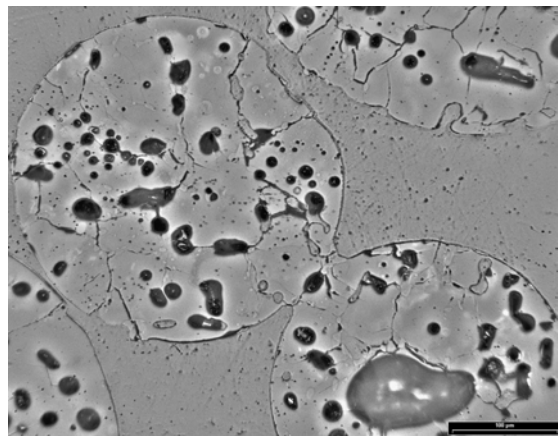


200 : 1                                    100 µm

Fig. 4:  Cross section of enriched pebbles after 96 day annealing at 970 °C

Staff:

C. Adelhelm
E. Günther
R. Knitter
G. Piazza
R. Rolli
O. Romer
B. Schweigel

## TTBB-005-7
## Thermal-Mechanical Pebble Bed Tests

Present ceramic breeder blanket designs are based on ceramic breeder and beryllium pebble beds. For power reactor blankets maximum temperatures in the breeder and the beryllium pebble beds are in the range of 900°C and 650°C, respectively. Because of different thermal expansions of the pebble beds and the structural material and irradiation effects, large compressive stresses occur in these beds which might cause considerable plastic deformations of pebbles. Thermal creep of pebble beds will partly release the build-up of stresses, might improve heat transfer due to increased contact areas between the pebbles and might compensate a further stress build-up due to irradiation induced swelling.

For the proper design of ceramic breeder blankets the knowledge of thermal creep and thermal conductivity of deformed pebble beds, therefore, is of large importance.

### Thermal creep strain of metatitanate pebble beds

Previous experiments[1] showed that the thermal creep behaviour differed significantly for two types of metatitanate pebble beds differing only by grain size. In this year, detailed experiments were performed[2] using other batches of metatitanate pebbles developed by CEA and JAERI. These granular materials differed in sintering temperature, grain size and density. The experiments were performed in an uniaxial test facility with a maximum pressure of 8MPa and a maximum temperature of 850°C.



Fig. 1: Thermal creep strains of different metatitanate pebble beds

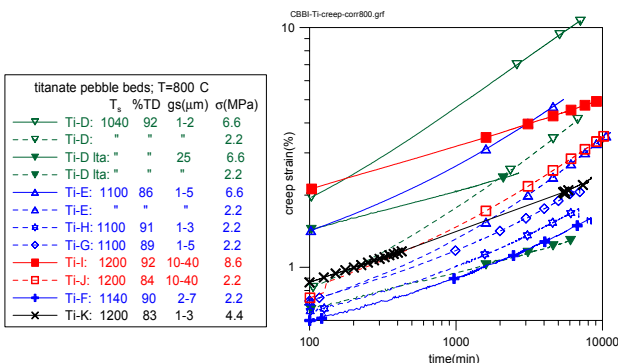The experiments showed that thermal creep of metatitanate pebble beds can vary significantly depending on the microstructural characteristics of the pebbles, as shown Fig. 1. The most significant parameter appears to be the grain size. The largest creep rates were determined for a material with very small grains (1-2μm), a low pebble density($\approx$ 83% of theoretical density), produced at a low sintering temperature ($T_{sint}$ = 950°C). For small creep rates, grains should be > 5μm, the percentage of theoretical density > 90%. This would probably require a sintering temperature of > 1100°C. However, other pebbles characteristics, such as shape, size, and surface roughness, are likely to be considered before clear conclusions on parameters governing thermal creep behaviour of metatitanate pebbles can be drawn.

The most recently produced CEA metatitanate pebbles, Ti-H, with smaller pebbles (d = 0.7-1mm) compared to other batches (0,8-1,2mm) showed very satisfactory results (although the grain size was smaller than the value recommended above). This might be caused by the larger achievable packing factor which is also desired for other reasons (breeding ratio, heat transfer).

For the group of materials characterised by quite small creep rates, thermal creep can be described sufficiently well by correlations proposed in [1]. There is another group of materials which exhibit a second creep regime connected with higher creep rates. Data were also presented for these materials[2] to be used in numerical codes to describe the thermomechanical interaction between pebble beds and structural materials.

The necessity of the knowledge of thermal creep for the second creep regime will decrease remarkably if it proves that stress relaxation processes in blanket structures are very fast. Additional experiments and theoretical predictions[3] showed that for 770°C the uniaxial pressure dropped to $\approx$ 25% of the initial value in only 2 hours.

### Thermal conductivity of compressed ceramic breeder pebble beds

For ceramic breeder beds, the increase of the bed conductivity with increasing bed deformation is expected to be much smaller compared to beryllium pebble beds due to the much smaller difference between the solid material conductivity and the conductivity of the surrounding gas. Quantitative results, however, still were missing.

Experiments were performed[4] with orthosilicate and different metatitanate pebble beds for bed deformations up to 4% and maximum temperatures of 800°C using the pulsed hot wire technique. The measurements at high temperatures were performed in air; at ambient temperature also helium and argon was used.

Fig. 2 contains results for both types of granular materials for ambient temperature and 800°C. At 800°C, the dependence of the conductivity on bed deformation is very small; at ambient temperature this dependence is somewhat more expressed for metatitanate pebble beds. For non-deformed pebble beds, the measurements agree well with previous results obtained by other authors. For the blanket design at nominal operation (high temperature) the moderate increase of conductivity with bed deformation may be neglected; during cooling down and heat-up phases (low temperature periods) this increase might be beneficial.
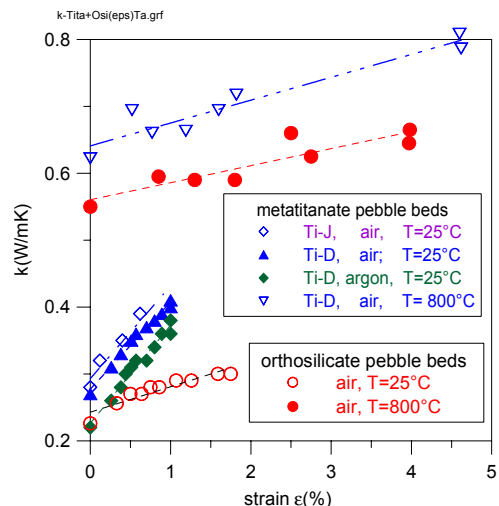


Fig. 2: Thermal conductivity of deformed orthosilicate and metatitanate pebble beds

Staff:

J. Reimann
G. Wörner
S. Hermsmeyer

Literature:

[1]  J. Reimann, G. Wörner; Thermal creep of ceramic breeder pebble beds, CBBI-9, Toki, Japan, Sept.27-29, 2000.

[2]  J. Reimann; J.-D. Lulewicz; N. Roux; G. Wörner, Thermal creep of metatitanate pebble beds, CBBI-10, Karlsruhe, Germany,Oct.22-24, 2001.

[3]  L. Bühler, J. Reimann, Thermal creep of granular breeder materials in fusion blankets, ICRFM 10 Baden-Baden, Oct. 14-18, 2001.

[4]  J. Reimann; S. Hermsmeyer, G. Wörner Thermal conductivity of compressed orthosilicate and metatitanate pebble beds, CBBI-10, Karlsruhe, Germany,Oct.22-24, 2001.

## TTBB-005-8
## Model Development

### Background

Deformation of granular material (pebble beds (PB)) in fusion blankets (Fig. 1) is supposed to release stress caused by non-uniform temperature distribution due to non-uniform volumetric heating. For accurate predictions FE models can be applied. The models have to be adjusted to the material parameters measured during experiments. Main objective of this task is improvement of Drucker-Prager model calibration in view of application of models to blanket-relevant geometries (Cer PB/cooling plate/Be PB and blanket box wall) taking into account the thermal creep as well as the thermal conductivity in both deformed un-irradiated Ceramic and Be pebble beds (Task TTBB-007-5).

### Preliminary modelling and ABAQUS calculations

The modelling is performed using standard material models for granular material and creep from the literature. For the modelling calculations the FE code ABAQUS was used. It allows calculations for granular materials using special material options. The input parameters for the code have to be adjusted using existing experimental data. A preliminarilly calibrated model for the temperature dependent mechanical behaviour of the Li4SiO4 pebble beds is available. The modelling approach - with no regard to the impact on the thermal behaviour, i.e. thermal conductivity as function of stress and temperature - is reported in [1]. Following the uniaxial experiments creep-modelling for Li4SiO4 pebble beds has been completed for a temperature range up to 800 °C. A Drucker-Prager-Cap (DPC) model has been calibrated based on a bi-axial experimental result at 400 °C. This DPC model accounts for granular shear and compaction flow of particles independent of temperature, while the complete temperature dependence is included in the creep law that describes thermally activated creep. Numerical simulations of experiments show good agreement with the experimental data.

The ABAQUS pre-calculations [2] for an in-pile HCPB test module to be tested in Petten were carried out still without consideration of the creep model for the breeder and Be pebble beds. To continue these calculations with consideration of thermal creep behaviour of the pebble beds the thermal creep model for the Li4SiO4 pebble beds described in [1] was taken into account which is based on the corresponding isothermal creep experiments. In the first stage, this thermal creep model was compiled into a user subroutine interacting with the Drucker-Prager-Cap model for granular flow with cap plasticity/cap hardening. First test runs for reaching numerical stability are under way.

Similar proceeding for consideration of thermal creep model for Be pebble bed will also be taken into account, as soon as the respective input from TTBB-007-5 is available.

Staff:

L. Bühler
S. Hermsmeyer
P. Norajitra
G. Reimann

Literature:

[1] L. Bühler: Continuum models for pebble beds in fusion blankets, FZKA 6561, 2001.

[2] F. Wolf: Strukturmechanische Berechnungen für das Submodul des HCPB-Blankets, FZK Interner Bericht, August 2000.
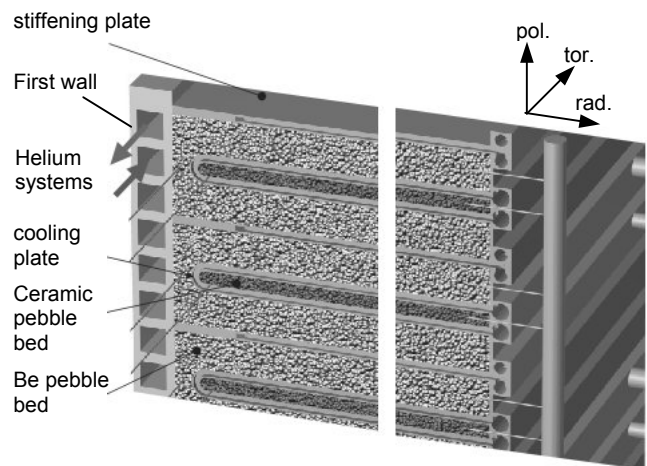


Fig. 1: Improved HCPB blanket concept, poloidal arrangement of the components: first wall, cooling plate, stiffening plate and layers of Li4SiO4 and beryllium pebble beds

## TTBB-007
## Development of Beryllium Pebble Beds

### TTBB-007-1
### Characterisation of Beryllium Pebbles

In the European helium cooled pebble bed blanket (HCPB) for power reactors the neutron multiplier and the breeder material are arranged as pebble beds between flat cooling plates. Reference neutron multiplier material are 1 mm diameter NGK pebbles produced by the rotating electrode process (Fig. 1). In the reporting period particular importance has been devoted to the study of the effects of impurities in beryllium pebbles. In particular, the effect on the pebble mechanical properties and on the activation during blanket operation were investigated.
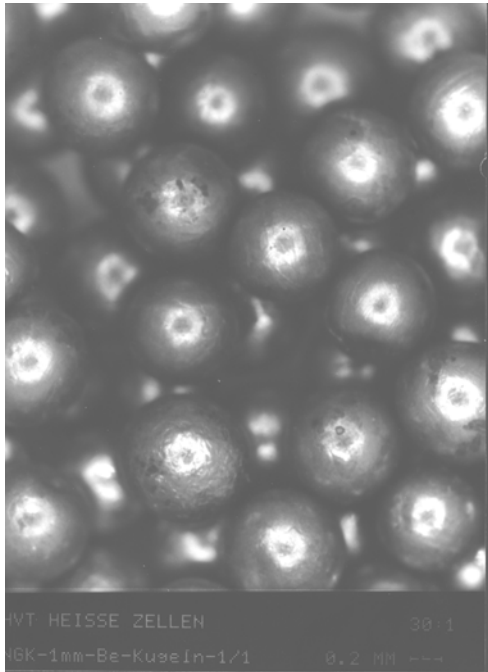


Fig. 1: NGK beryllium pebbles

Al and Mg impurities can influence the ductility of beryllium pebbles, in fact, they tend to segregate at grain boundaries as low-melting phases (Al-Mg-phases melt at about 450°C) [1]. Thus, it is important, if the impurity amounts are higher than the solubility limit, that Al and Mg are tied up by impurities such as Fe and Si, to form solid intermetallic phases stable at high temperatures ($Al_5Fe_2$ with melting temperature $T_{melt}$ = 1169 °C and $Mg_2Si$ with $T_{melt}$ = 1085 °C). This is possible if the mass ratios Al/Fe and Mg/Si are:

Al(wt %) / Fe(wt %) < 0.5     (atomic ratio Al/Fe < 1)

Mg(wt%)/ Si(wt%) < 1.7     (atomic ratio Mg/Si < 2)

Table 1 shows an example of impurity amounts (wt%) which could be acceptable in the Be pebbles in the present R&D phase.

In order to form the high temperature stable phases the produced pebbles should be annealed with a high temperature (T > 850 °C) heat treatment program. This thermal treatment should be optimised as far as temperature and time at temperature are concerned.

| Table 1 | |
|---|---|
| Be | 99.5 |
| BeO | 0.23 |
| Al | < 0.04 |
| Fe | 0.09 |
| Mg | 0.03 |
| Si | >0.02 |
| U | <0.01 |
| Co | <0.001 |
| Sc | < 0.005 |
| Mn | 0.01 |
| Others | ~ 0.065 |

If, in the industrial production, the quantities of Al, Fe, Mg and Si are different from those proposed in Table 1, and higher than the respective solubility limits in beryllium, the ratios given above should be in any case kept.

In the present R&D activities uranium impurities higher than 0.01 wt% don't represent a concern, but, as far as the activation product inventory in a reactor is concerned, the uranium content has a strong impact on it. There both fission products and long-lived actinide are produced (e.g. [239]Pu, [241]Am) dominating the radiological hazard potential. Therefore, for safety reasons, the amount of U in the pebble to be used in the reactor should be as low as possible (less than 0.0050 wt %).

As far as other impurities are concerned, major contributors to the γ-dose rate of beryllium are [56]Mn, [24]Na and [60]Co (activation products of [55]Mn, [24]Mg and [59]Co respectively) at short term, [137m]Ba (fission product) at medium term and actinides at long term cooling times. Therefore, for both safety and waste management reasons it would be desirable that the above listed impurities be kept as low as reasonably possible.

Staff:

H. Kleykamp
H. D. Gottschalg
G. Piazza

Literature:

[1] H. Kleykamp, "Selected thermal properties of beryllium and phase equilibria in beryllium systems relevant for nuclear fusion reactor blankets", Journal of Nuclear Materials, 294 (2001) 88-93.

## TTBB-007-2
## Improvements, Verification and Application of ANFIBE Code

In the beryllium pebbles of the Helium Cooled Pebble Bed (HCPB) blanket, large quantities of helium and a non-negligible amount of tritium are produced under fast neutron irradiation. The code ANFIBE (ANalysis of Fusion Irradiated BEryllium) is being developed in order to predict swelling due to helium bubbles and tritium inventory in the range of operating and accidental conditions of a fusion power reactor. Due to the absence of data in this range, ANFIBE has to be extrapolated. Consequently, in comparison to codes which predict gas retention in $UO_2$ fuel pellets [1], the development of a more sophisticated solid state physics model for the description of gas kinetics and a more careful and detailed validation procedure are required. The on-going programme for the improvement of ANFIBE runs on a period of five years (2000 – 2004) and is carried out in collaboration with the JRC – ITU (Karlsruhe, Germany), the NRG (Petten, The Netherlands) and the SCK-CEN (Mol, Belgium), as far as a part of the experimental studies are concerned. The theoretical processing of experimental data and related development of ANFIBE, as well as the definition of open key issues to be solved with further experimental studies, is under the responsibility of FZK. The contribution of FZK to the experimental activities is focused on the following points: (1) measurement of helium and tritium diffusion coefficients and, in general, study of gas release modes up to the melting point; (2) study of the microstructure of irradiated beryllium and its evolution with temperature. The final aim of these studies is to validate ANFIBE from the microscopic point of view, i.e. to verify if the different gas diffusion phases (atomic diffusion, precipitation into bubbles, bubble diffusion and growth, release pathways) are correctly described. In 2001 weakly irradiated beryllium pebbles were analysed, with the following characteristics: 2 mm diameter, produced by Brush Wellman by Fluoride Reduction Process, irradiated in the BERYLLIUM experiment (HFR Petten, 1994) at 780 K up to a fast fluence of $1.24 \cdot 10^{25}$ m$^{-2}$, resulting in 480 appm helium and 12 appm tritium final inventory.

**Study of helium and tritium release from irradiated beryllium**

Helium and tritium release from beryllium has been studied in collaboration with the JRC-ITU, by the so-called Knudsen-cell technique [2]. The samples are heated in vacuum up to the melting point and gas release rate is measured by a mass spectrometer. A typical result is shown in figure 1. Below 800 K, no release of helium is observed. At higher temperature, three release stages appear: (1) helium atomic diffusion to grain boundaries (800 – 1300 K); (2) helium precipitation into intragranular bubbles (1300 – 1450 K); (3) sudden release of the trapped helium inventory via extensive bubble venting. The first and second phases are suitable to assess the diffusion coefficient, provided that an inverse analysis model that takes into account gas atomic diffusion and bubble precipitation is used. As far as tritium is concerned, the experimental procedure has been optimised in order to distinguish it from helium-3. It has been proved that tritium is released mainly in the form of di-tritium gas. As a consequence, tritium release modes due to atomic diffusion to grain boundaries are also influenced by surface recombination phenomena. It appears that a small part of tritium gets trapped by helium bubbles and it is released as they are vented.

**Study of the microstructure of irradiated beryllium**

The study of the microstructure of irradiated beryllium is of fundamental importance to understand gas microscopic kinetics and to relate them to macroscopic release modes. In particular,
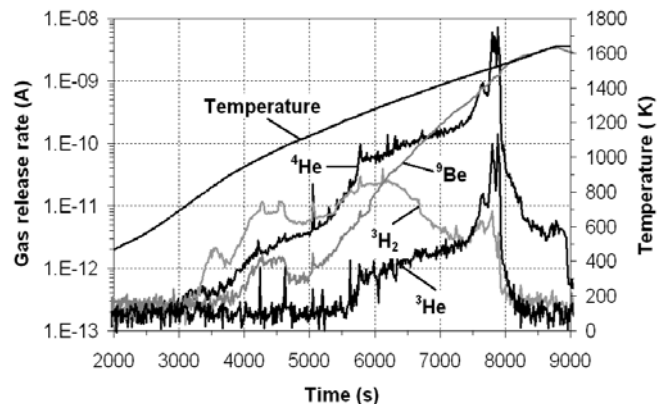


Fig. 1: He and 3H release from irradiated beryllium during a fast heating up to the melting point. Material: pebbles from the BERYLLIUM experiment. [2]

it allows to study the interaction between gas diffusion, bubble nucleation and defects induced by irradiation. Under irradiation, *both* dislocations *and* a relatively high quantity of gas are produced *at the same time* in beryllium, which does not happen in steels. Dislocations act as traps for gas atoms, so their presence affects bubble nucleation. The magnification needed to study radiation damage and the formation of $\approx$ nm size bubbles requires the use of the Transmission Electron Microscopy technique. A procedure for the preparation of $\approx$ 100 nm thin foils, starting from 2 mm diameter pebbles, was developed at the JRC-ITU. The pebbles of the BERYLLIUM experiment were analysed by TEM in the following states: as fabricated, after irradiation, after irradiation and out-of-pile heating up to 1000 K [3] . In the original state, no dislocations are present inside the grains. After irradiation, in spite of the low dose and the relatively high temperature, a high density of dislocations is present (fig. 2, [3]), but no bubbles: this suggests that gas is trapped in the free space near dislocations. At 1000 K small ellipsoidal bubbles ($\approx$ 5-6 nm diameter) appear on dislocations. A technique of image processing is under development to assess the bubble concentration and the related swelling, as well as the average diameter: a key issue of this processing is the assessment of the foil thickness. An optical microscopy investigation has been also performed at 1300 K: at this temperature, in spite of the limited gas inventory, large gas bubbles are present (some micron diameter, fig. 3), due to the poor mechanical properties of beryllium. At grain boundaries, elliptical bubbles with a big elongation are connecting to each other to form gas release pathways [3].
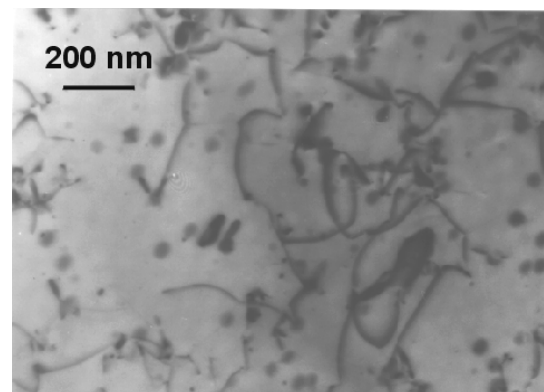


Fig. 2: Dislocations and Mg impurities (black dots) in beryllium after irradiation at 780 K: no gas bubbles are present. Material: pebbles from the BERYLLIUM experiment [3]
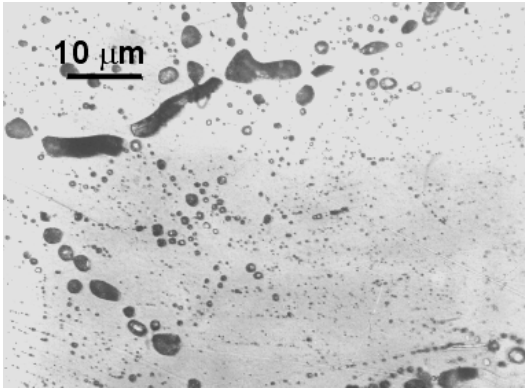
Fig. 3: Large bubbles inside the grains and at grain boundaries in irradiated beryllium after out-of-pile heating up to 1300 K: the formation of gas release pathways at grain boundaries is in progress. Material: pebbles from the BERYLLIUM experiment [3]

Staff:

E. Rabaglino

Contributors at the JRC-ITU:

C. Ronchi
F. Capone
J. Y. Colle
J.P. Hiernaut
W. Huber
M. Murray-Farthing
H. Thiele
T. Wiss

Literature:

[1]  K. Lassmann, Personal communications, 2001.

[2]  E. Rabaglino, C. Ronchi, F. Scaffidi-Argentina, "Helium and tritium kinetics in irradiated beryllium pebbles", contributed paper to the ICFRM-10, Baden-Baden, Germany, 2001.

[3]  E. Rabaglino, C. Ronchi, F. Scaffidi-Argentina, T. Wiss, "Helium and tritium release and sub-microscopic restructuring in irradiated beryllium pebbles", oral presentation at the 5th IEA International Workshop on Beryllium Technology for Fusion, Moscow, Russia, 2001.

**TTBB-007-4**
**Thermal-Mechanical Pebble Bed Tests**

In a helium cooled pebble bed blanket (HCPB) for power reactors the neutron multiplier and the breeder material are arranged in pebble beds between flat cooling plates. The maximum temperatures in the breeder and in the beryllium pebble beds are in the range of 900 °C and 650 °C respectively. Because of temperature differences and different thermal expansion coefficients between pebble beds and structural materials, and because of irradiation effects, constrained strains occur. The large compressive stresses in the pebble beds might result in plastic deformations of pebbles, which influence the thermal conductivity of the beds. Therefore, for the proper thermal mechanical design of the blanket, the thermal conductivity of these beds as a function of deformation and temperature as independent parameters must be known.

**HECOP experiment**

Measurements of thermal conductivity and heat transfer coefficient to the containing wall of strongly deformed pebble beds have been started at FZK using the test section HECOP. In the experiments beryllium pebble beds are heated up to about 600°C bed average temperature and uniaxially compressed up to 6 MPa. Temperature and strain in the beds can be adjusted independently. Minimisation of uncontrolled heat losses, and reliable measurement of the temperature gradients in the bed guided the design of HECOP.



Fig 1:    Glove-box with the press used in the HECOP experiments (laboratory of the firm Goraieb Versuchstechnik)

Because of the toxicity of beryllium powder HECOP was built-up in a glove box filled with He at constant temperature (Fig. 1).

Fig.2 shows a schematic of the HECOP test section. The beryllium pebbles are poured into a steel cylinder which is then vibrated in order to obtain the initial packing conditions (about 63 % packing factor). A system of 5 heaters is used to generate the temperature gradient in the bed and to c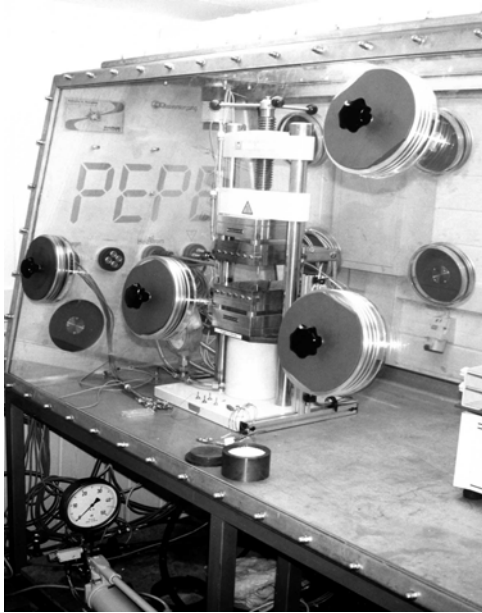ontrol heat losses (H1, H2, H3, H4, H5). Two further heaters (H6, H7) belonging to the press contribute, by additional heating, to reach 600 °C

average temperature in the bed. The temperatures in the pebble bed are measured using two pairs of thermocouples at two defined bed's heights. Heater H2 generates the heat which flows in axial direction through the bed and is used to calculate the thermal conductivity of the pebble bed. To reduce lateral heat losses a guard heater (H4) is placed around H2, so that the
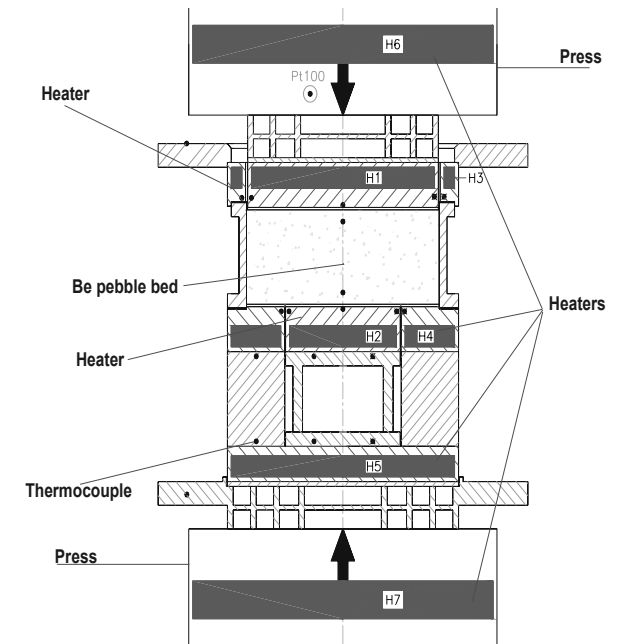


Fig. 2:   Schema of the HECOP test facility. Black points indicate thermocouples. In the pebble bed each black point corresponds to two thermocouples at the same bed height

temperature of the basis of the cylinder is as uniform as possible. The heating power of H4 is controlled by the temperature difference between two thermocouples which are very near each other and belong respectively to H2 and H4. To perform a measurement this temperature difference must be constant in time and practically equal to zero. A similar system of guard heaters (H1 and H3) is used in the upper part of the cylinder to control the uniformity of temperature in the upper part of the pebble bed. H5 is the guard heater impeding the heat produced in H2 from flowing to the press bottom part. Also in this case thermocouple pairs control the power produced in the heater. The test section was wrapped up with insulating material and has a steel lateral containment (fig. 3).

First preliminary results are already available on the heat transfer parameters of a beryllium single size pebble bed at two different temperatures: 250 °C and 350 °C and for mechanical pressure on the pebble bed up to 6 MPa. Isothermal experiments (no temperature gradient in the pebble bed) at these two temperatures and at different pressures, were performed to evaluate heat losses in the device. These losses influence the obtained thermal conductivity values. The error in evaluation of thermal conductivity due to heat losses is less than 10 %.

Fig. 4 shows the thermal conductivities as a function of the applied pressure at 250 °C average temperature in the pebble bed. Due to the increase in the contact surface between the pebbles in the bed, the increasing of uniaxial pressure on the pebble bed corresponds to an increase of its thermal conductivity. By decreasing the mechanical pressure the thermal conductivity does not change significantly up to about 2 MPa, afterwards it decreases. The final thermal conductivity is in any case higher than the value at the beginning of the

experiment, and this is due to the compaction of the bed. By increasing again the pressure also the thermal conductivity increases following, practically, the precedent pressure decrease curve.

The behaviour is the same at 350 °C bed average temperature.
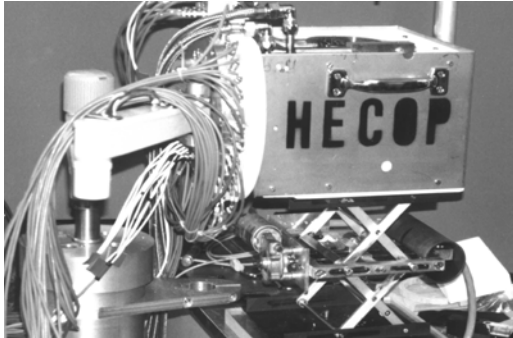


Fig. 3:     HECOP test section with external insulation
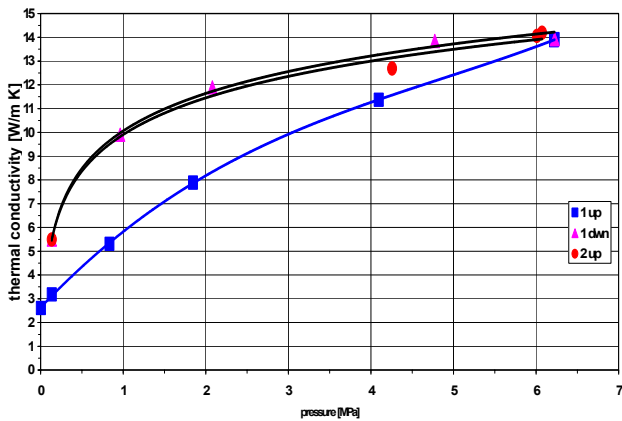


Fig. 4:  1 mm beryllium pebble bed's thermal conductivity at 250 °C
        bed average temperature  as a function of pressure
        (temperature gradient in the bed about 50 °C)

Staff:

A. Goraieb
H. Harsch
G. Hofmann
G. Piazza
J. Reimann

Literature:

[1]  G. Piazza, G. Hofmann, J. Reimann, S. Malang, A. Goraieb,
     H. Harsch" Thermal conductivity measurements of deformed
     beryllium pebble beds". Proceedings of the 5th International
     Workshop on Beryllium Technologies for Fusion, October
     10-12, 2001, Moscow, Russia

## TTBB-007-5
## Model Development

### Background

Irradiation swelling of beryllium during the blanket life time may endanger the blanket integrity because unacceptably large stresses could result. Thermal creep of beryllium may help in reducing such stress. In order to enable reliable predictions for the blanket geometry FE codes have to be adjusted to experimental data regarding deformation-dependent thermal conductivity, and thermal creep. Models have to be flexible enough to incorporate irradiation effects, like swelling and embrittlement, that will be investigated in the future.

### Thermal-mechanical modelling and ABAQUS calculations

Using recent data from uni-axial and tri-axial compression tests, a reference Drucker-Prager-cap pebble bed model for 1mm NGK Beryllium pebbles has been calibrated. This model was applied to finite-element predictions of the cold pre-compression of a test element for the HCPB in-pile experiment to be carried out at NRG Petten/NL from 2002. The model was applied within efforts of predicting the steady state of the same test element under in-pile conditions. Finally, a model with deformation-dependent conductivity was used in analyses of S-PEHTRA Beryllium pebble bed conductivity experiments: by adapting the unknown mechanical initial conditions, model predictions can match the radial temperature profile better than the fit previously applied.

On the thermal modelling of pebble beds, a literature review was carried out to establish and/or confirm key elements of a model. It is foreseen that a better understanding of pebble contact properties will improve modelling. As part of the activity, a unit-cell pebble contact model was implemented in the finite-element code FIDAP and unit cell conductivities calculated for different levels of pebble contact.

Currently, ABAQUS finite element applications are a continuation of in-pile test element analyses [1] carried out in 2000, the key modification being the introduction of creep [2] in the ceramic breeder model. Beryllium pebble beds are part of the model and are critical for the convergence of the overall model. In the reporting period a new mesh for an in-pile test element as to be tested at HFR Petten has been created. First test runs for reaching numerical stability, with increasing model complexity, are under way.

The work needs to be continued in several respects. New experimental data will be used to improve models as they become available. The model will be extended to incorporate irradiation swelling. And finally, the model will be applied to blanket-relevant geometries, and numerical stability problems will be addressed that are likely to spring up during application.

Staff:

L. Bühler
S. Hermsmeyer
P. Norajitra
G. Reimann

Literature:

[1] F. Wolf: Strukturmechanische Berechnungen für das Submodul des HCPB-Blankets, FZK-interner Bericht, August 2000.

[2] L. Bühler: Continuum models for pebble beds in fusion blankets, FZKA 6561, 2000.

# WCLL Blanket Concept

**TTBA-003**
**Coating Qualification and Irradiation Tests**

**TTBA-003-32**
**Fabrication and Characterisation of Hot Dip specimen**

Previous experiments with steel samples of sheet geometry have shown that tritium permeation can be significantly reduced by an adapted surface coating. In combination with adjusted heat treatments the Hot-Dip aluminising process (HD) fulfils the necessary requirements of tritium permeation barriers (TPB). However, for technical applications more complex structures are required and it has to be demonstrated that the process can be applied to such shapes as well.

In the frame of the European Permeation Barrier Qualification, hot-dip aluminised EUROFER 97 tubes (one end closed) were prepared for permeation testing in $H_2$-gas and in Pb-17Li-$H_2$ in the VIVALDI apparatus at ENEA-Brasimone. The HD coating was performed with the same process parameters as reported earlier for disc shaped samples [1].

The VIVALDI apparatus is a specially designed test unit and allows permeation tests in gas atmosphere as well as in liquid Pb-Li up to temperatures of 500 °C. A schematically layout of the VIVALDI apparatus is given in Fig. 1.



Fig. 1: VIVALDI apparatus for permeation tests

The VIVALDI apparatus is a UHV-equipment consisting of the following main components:

UHV chamber with two test positions and surrounding heating. The chamber is designed for working with pure gas atmosphere or PbLi filling and $H_2$ bubbling

Two symmetrically test lines for measuring $H_2$ permeation (UHV-layout)

UHV supply system for Ar or $H_2$ to permeation chamber including pressure detection

The permeation test is performed by mounting the coated test sample into the first test position and by inserting a reference sample (uncoated, bare one) into position two. The test is started by evacuating the whole test system. In a second step the UHV chamber is heated to the desired test temperature and filled with $H_2$ to start the permeation test.

The permeation is evaluated from the pressure increase in the test lines.

In the first testing sequence 2 samples were delivered to ENEA which showed similar behaviour in the gas phase testing. In table 1 the results for sample HD 2 are given.

Tab. 1: Permeation values and reduction factors (PRF) for coated and bare EUROFER 97 in gas phase

| T (°C) | Sample HD-2<br>P (mol $m^{-1}s^{-1}$ $Pa^{-1/2}$) | Bare EUROFER 97<br>P (mol $m^{-1}s^{-1}$ $Pa^{-1/2}$) | PRF |
|---|---|---|---|
| 280 | 1.80e-14 | 3.53e-12 | 196 |
| 320 | 4.64e-14 | 6.50e-12 | 140 |
| 370 | 8.19e-14 | 1.14e-11 | 139 |
| 420 | 1.28e-13 | 1.82e-11 | 141 |

From these results it is clearly seen, that permeation can be reduced significantly by coating with the developed Hot-Dip process. The planed reduction by a factor of 100 is achieved in $H_2$-gas. However the PRF ratio vs. temperature is not constant or monotonic. This behaviour may indicate that defects are present in the scale (inhomogeneous scale thickness caused by the coating process) or that microcracks are formed for example during low temperature cycling. At 400 °C a recovery of scale properties may take place indicated by a slightly growing PRF ratio. This can be explained by a self healing process of the $Al_2O_3$ scale on top of the EUROFER 97 caused by diffusion of metallic Al from the intermetallic phase in the interlayer between scale and matrix to the surface. Additional tests are required to confirm the observed behaviour and to improve the coating process as well as to lead to a understanding of the foregoing mechanisms. Nevertheless, the results show, that coating of steels by Hot-Dip have the potential to reduce permeation by the required ratio and that this process have the enormous advantage of scale self healing by forming a reservoir of Al compared to thin film coating techniques. In the next phase, permeation tests in Pb-17Li-$H_2$ have to confirm the good results obtained in pure hydrogen gas.

Staff:

H. Glasbrenner
J. Konys
W. Krauss
Z. Voß
O. Wedemeyer

Literature:

[1] H. Glasbrenner, J. Konys, 21st SOFT conference, 11 – 15 September 2000, Madrid, Spain.

# TTBA-006
# Magneto-Hydrodynamics (MHD)

## TTBA-006-61
## Test and Modelling of Forced Convection

### Introduction

In currently investigated water-cooled liquid-metal (LM) blankets for fusion reactors (EU-WCLL) the LM - a lithium-lead alloy - serves mainly as breeding material [1] and not as coolant. A crucial issue of lquid metal cooled blankets is the magneto-hydrodynamic situation in the header where the flow is distributed/collected from the individual ducts. There, high flow velocities appear which, due to the large amount of structural material in the header, generate high pressure drops. An even more peculiar feature of the MHD flow in the header is that uneven flow rates in the individual feeding and draining ducts may appear, which are caused by the electric coupling of channels via the electrically conducting structural material.

New fabrication technologies allow an electrical separation of the individual feeding/draining ducts and hence drastically reduce the MHD pressure drop and avoid uneven flow rates (the so called multi-channel effect). The electrical separation is performed via an electrically insulating coating being plasma-sprayed on the ducts. Afterwards the individual ducts are hipped to a full header module.

Another feature of the EU-WCLL blanket design is that MANET is considered as structural material which is ferro-magnetic, owing a magnetic permeability significantly larger than unity ($\mu_r \approx 50$). This ferro-magnetism may lead to changes of veloctiy profiles whithin the duct and probably to reduced MHD pressure drops, due to the modified electro-magnetic boundary conditions at the liquid-solid interface. This effect becomes most appearent  especially if the magnetic saturation field strength is exceeded, which holds for the blanket.

The R+D program in the reporting period has been focussed on the theoretical and experimental investigation of a forced convective MHD flow in ducts of circular cross-sectional shape for three different duct flow types:

a)  MHD flow channels with an electrical separation between structure material and liquid metal containing duct.

b)  MHD flow in thick electrically conducting ducts.

c)  MHD flow in thick-walled ferromagnetic ducts.

All these issues are subsenquently discussed below.

### Blanket relevant MHD- flows in circular ducts

One important question for the design of liquid metal blankets is the availability of a long term reliable electrical insulation of the duct walls, which is capable to withstand the high neutron fluxes present in the reactor. The research to develop such electrically insulating materials is still an ongoing task although the insulation requirements for such a material with respect to MHD are far below the ones setup by the electric industry. In the absence of an electric insulation of the duct walls global electric currents induced by the fluid motion can circulate within the blanket structure. This effect known as multi-channel effect (MCE) may lead especially for self-cooled blankets to pressure drops exceeding the allowable material stresses. But also the WCLL blanket can be significantly affected by the MCE since it yields uneven flow distributions in the individual ducts.

The pressure drop caused by MHD flows in most of the relevant duct geometries may be minimized by the use of thin conducting walls or by direct insulations (coatings or ceramics). Thin conducting walls can be achieved by the use of so-called Flow-Channel Inserts (FCI), where an electrically insulating ceramic sheet is sandwiched by thin steel plates. These FCI's are fitted loosely in the ducts. The physical effect leading to the reduced MHD pressure drop is that the electric current density is minimized, because the thin steel sheets represent a higher ohmic resistance than a thick wall facing the liquid metal. A second advantage are the low requirements on the FCI's with respect to their stiffness, since the pressure level in- and outside the FCI is nearly the same. Nevertheless, the usage of FCI's in long geometries requires the insertion of several FCI's. At the junctions where the FCI's overlap, three-dimensional MHD flows appear due to the jump of the electrical conductivities.

Another technical method to overcome the disadvantage of the overlapping of FCI´s and their fitting into the ducts bores is discussed in the frame of the manufacturing of the WCLL test blanket module (TBM) for ITER [2]. This specific type of FCI is illustrated in figure 1. The manufacturing of such a FCI is performed as follows:

a)  Fabrication of semi-circular grooved thick MANET steel plates (using the hot isostatic pressing or HIP method.

b)  Spark-erosion of a thin-walled MANET steel tube and final machining of this tube.

c)  Plasma spraying of the thin walled MANET tube with alumina oxide $Al_2O_3$.

d)  Seal welding of the thick plates with the thin tube using an electron beam

e)  Finally, diffusion bonding of the semi plates in a HIP facility at 50MPa and 980°C for three hours.
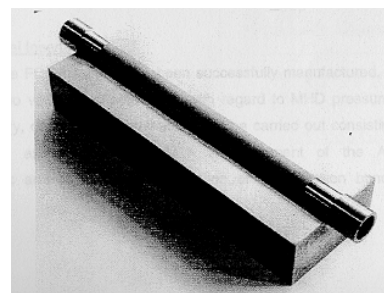


Fig. 1:  Photograph of the semi-fabcricated specimen foreseen for MHD flow tests in the MEKKA-facility of the FZK [2]

### Analytical description of the MHD flow in thick- walled ducts with and without ferromagnetic structural material

The MHD pressure drop in ducts with electrical separation is given by the electric wall conductivity of the liquid metal facing thin steel duct. The leading parameter there is the wall conductance ratio $c$ which is defined by relation (1a):

$$c = \frac{\sigma_W \cdot t_W}{\sigma \cdot a} \quad (a); \nabla p = \frac{c}{1+c} \quad (b). \qquad (1)$$

Herein, $\sigma_W$ is the specific electrical conductivity of the duct wall, $t_W$ the wall thickness of the liquid metal facing structure, $a$ the ducts and $\nabla p$ the dimensionless pressure gradient scaled with the electromagnetic pressure given by a$\sigma$v0B2. The dimensionless pressure gradient to be expected in a two-dimensional fully developed MHD flow in a circular tube is given by relation (1b).

In case of thick walled electrically conducting ducts the pressure gradient is by orders of magnitudes larger than in case of electrical separation; but, as shown by Bühler [3,4] significantly lower than that of a Hartmann-flow, where the pressure gradient per unit length is 1. The Hartmann flow assumption has been formerly used as a design tool in blanket designs. The pressure gradient in a fully developed MHD flow in a thick walled duct is given by equation 2.

$$\nabla p = -\frac{1}{1+\dfrac{\sigma}{\sigma_w}\dfrac{R^2+1}{R^2-1}}, \qquad (2)$$

where R is the radius of the thick-walled duct as depicted in sketch 2.
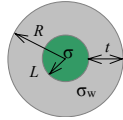


Fig.2:   Sketch for the definition of an MHD- flow in a thick walled duct

The structural material considered for the EU-WCLL blanket (MANET) owns a ferromagnetic behavior ($\mu_r \approx 50$) and a magnetic saturation field strength of 1.64Tesla. Unfortunately, the magnetic field strength being present in a Tokamak are around 4-7 Tesla and hence far above the saturation value. As a consequence the electro-magnetic boundary conditions at the liquid metal-duct interface are different than in the case of non-ferromagnetic materials. Especially, the magnetic field produced by the electric current (, which originates form the interaction of moving liquid and plasma confining magnetic field) circulating within the liquid metal and the magnetic field lines compressed in the ferro-magnetic duct interact with each other, leading to other current pathes. This modification of the boundary condition leads to different MHD flow features than investigated in the past.

A new model was derived capable to describe the two-dimensional MHD flow in a ferromagnetic duct. If the plasma confining magnetic field is above the saturation value of material the magnetic field leading to the MHD pressure drop is reduced significantly. Nevertheless, in this case the field lines remain parallel so that the velocity distribution is the same as in a non-ferromagnetic duct. The figures 3 show the magnetic field lines and the electric current distribution in a ferromagnetic material (figure 3b) compared to a non-ferromagnetic material (figure 3a).

If the magnetic field is in the range of saturation value a non-linear regime evolves, which is expressed by curvilinear magnetic field lines inside the pipe. This effect is shown in figure 4. These curvilinear field lines yield velocity profiles, which differ from the well-known classical solutions.

All computational results yield the following pressure gradient results for the 2D MHD flow in a circular tube.
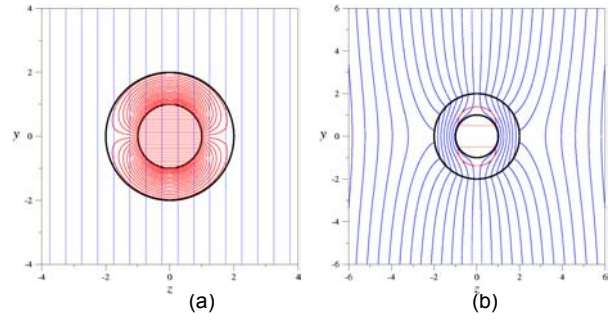


Fig. 3:   Magnetic field lines and electric current distribution in a 2D MHD flow in a circular duct above the magnetic saturation field. (a) Non-ferritic wall ($\mu$=1); (b) ferritic wall ($\mu$=100)
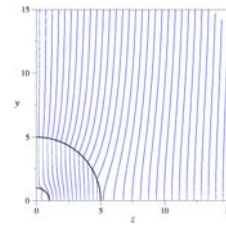


Fig. 4:   Calculated magnetic field lines in a magnetic field strength regime close to the saturation field of the material

a)   MHD flow in a electrically conducting thick walled duct

$$\nabla p = -\frac{\alpha^2}{1+\dfrac{\sigma}{\sigma_w}\dfrac{R^2+1}{R^2-1}} \quad \text{with } \alpha = -\frac{4}{\mu_r}\frac{R^2}{R^2-1} \text{ for } \mu_r \gg 1 \;(3)$$

(b)   MHD flow in an electrically insulating ferromagnetic duct

$$\nabla p = -\frac{3\pi}{8Ha}\alpha \qquad (4)$$

**Experimental investigation of the MHD flow in ducts of circular shape**

Three different test sections (two ferritic and one non ferritic, from left to right respectively on the figure 5) are mounted in the NaK loop of the Mekka facility.

In order to demonstrate the feasibility of the electrical separation method proposed for the EU-WCLL-blanket concept the test section in figure 5a was installed. Here, the pressure drop between three locations will be performed and the electric potential on the structural material will be measured in order to quantifiy the order of magnitude of electrical separation being achieved.

The MHD flow in thick-walled ducts will be examined in the other two test sections shown in figure 5. Here, pressure drop measurements between 5 positions along the flow direction will be performed. Simultaneously electric potential measurements inside the material will be conducted at two axial positions and 46 points within the material of the test section. For this reson small multipole electric potential sensors have been developed and fabricated in FZK. Figure 6 shows a five pole potential probe.

The flow near the magnetic saturation (non linear regime) will be studied carefully in order to adjust the analytical and numerical models.
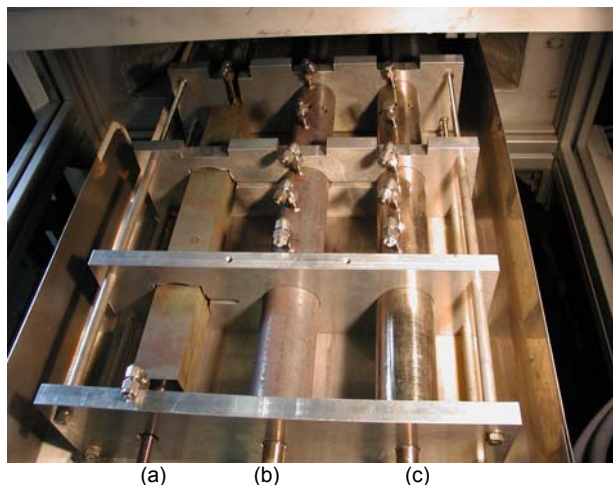


(a)　　　　　(b)　　　　　(c)

Fig. 5: Test sections being installed in the MEKKA-facility of the Forschungszentrum Karlsruhe. (a) Test section with electrical separation of liquid metal containing duct from rectangular shaped structure material. (b) ferromagnetic thick walled test section. (c) non-ferromangetic stainless steel test section



Fig. 6: Five pole electric potential probe for installation in the test sections (b) and (c)

The magnetic characterisitcs of the test sections has been evaluated experimentally. Figure 7 shows the measured values of the magnetic field within the duct as a function of the magnetic field being imposed on the outside. One can cleary see in the figure where the saturation of the material begins, which is expressed by a linear behaviour. Also the damping of the external imposed field by the magnetic permeability is depicted.

An electrical wetting procedure with liquid metal temperaures of 300°C for more than a week has been performed and real MHD measurements are currently ongoing.
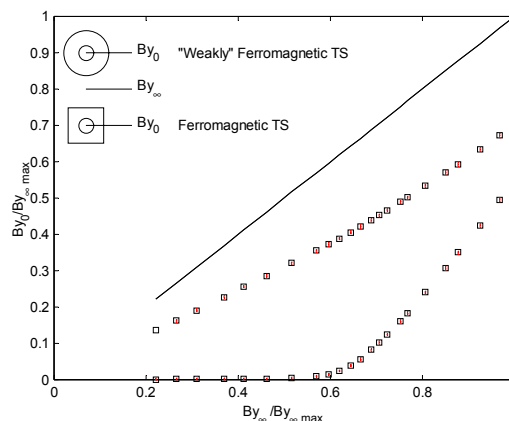


Fig. 7: Measured magnetic field inside the test section as a function of the externally applied magnetic field $B_0$ for the MANET test section (a) and the ferromagnetic test section (b)

Staff:

R. Stieglitz
E. Arbogast
L. Bühler
K. Messadek
F. Pfeffer
J. Reimann

Literature:

[1] Giancarli, L. et al. (1992), Water-cooled lithium-lead blanket design studies for DEMO reactor, Fusion Technology 21, 2081

[2] Fütterer, M.; Giancarli, L. (1996) Design Description Document for the European Water-Cooled Pb-17Li Blanket. DMT 96/349 SERMA/LCA/1911.

[3] Bühler, L. (1998) MHD-flows in thick-walled ducts, FZKA-6066.

[4] Bühler, L. (1998) Magnetohydrodynamic flows in thick walled ducts. Proceddings of 20th Symposium on Fusion Techn., Marseille, Sept. 7th-11th 1998.

# Structural Materials Development

**TTMS-001**
**Irradiation Performance**

**TTMS-001/5**
**HFR Irradiation Programme**

HFR Phase IA and Phase IB irradiation programmes complement the former MANITU investigations on promising low-activation ferritic/martensitic steels. KLST charpy subsize specimens (3x4x27mm), irradiated in the Petten High Flux Reactor at temperatures of 250, 300, 350, 400, and 450°C up to 2.4 dpa, are subjected to post irradiation examinations (Charpy tests). The result consists of force-deflection-curves, further evaluation delivers impact energy, dynamic yield stress, ductile to brittle transition temperature (DBTT) and upper shelf energy (USE).

**MANITU, HFR Phase IA**

The final report of the MANITU irradiation programme is published [1]; special attention is dedicated to the influence of the different irradiation doses of 0.2, 0.8, and 2.4 dpa. The report mentions all 700 experiments carried out in the MANITU programme, including the second 0.8 dpa irradiation phase [2].

The F82H mod. steel, included in the Phase IA, was tested and compared to the formerly investigated F82H steel, which provided better properties. Detailed results are mentioned in the figures below and in [3].

**HFR Phase IB**

The irradiated specimens were obtained in May 2000. Decontamination and testing started immediately and will take place until end 2002.

The aim is to define the influence of the alloys heat treatment, especially lower austenitization temperatures, and the effect of strongly reduced boron contents on the embrittlement behaviour (cf. Tables 1 and 2). The OPTIFER-V alloy – providing outstandingly good results - corresponds to OPTIFER-Ia and is very similar to the EUROFER 97 which became available after the irradiations.
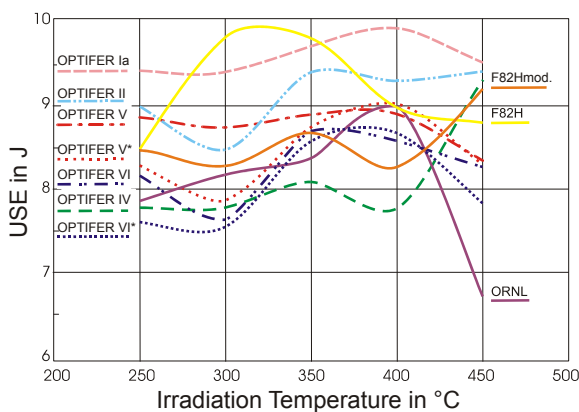


Fig. 1: Upper shelf energy vs. irradiation temperature

High upper shelf energy is found for all LAA's at all temperatures (Fig. 1). OPTIFER-Ia steel has the highest impact toughness, OPTIFER-Ia, -II, and –V are significantly better than the reference steels F82H and ORNL 3971. OPTIFER-Ia, OPTIFER-V, and F82H mod. steels show the lowest decrease of USE - not more than 12% even in the low temperature range. All materials show irradiation hardening which decreases with higher irradiation temperatures.

For low irradiation temperatures, the worsening in ductile-to-brittle transition temperature is significantly reduced (Fig. 2). OPTIFER-Ia, -IV, and -VI steels are in the range of the best LAA (ORNL 3791) formerly investigated and significantly better than the F82H mod. steel. The OPTIFER-V alloy shows the lowest DBTT-values of all investigated materials for both heat treatments, 50 – 100°C lower than F82H mod..
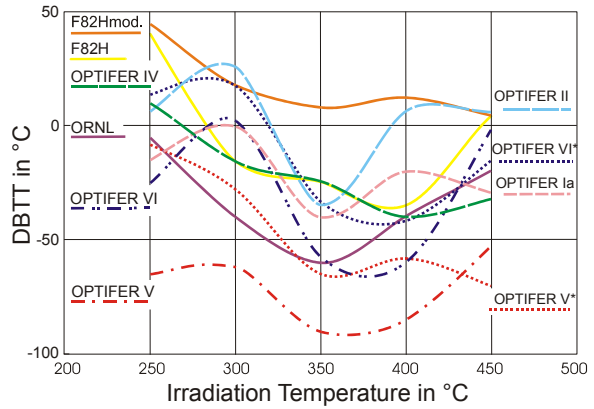


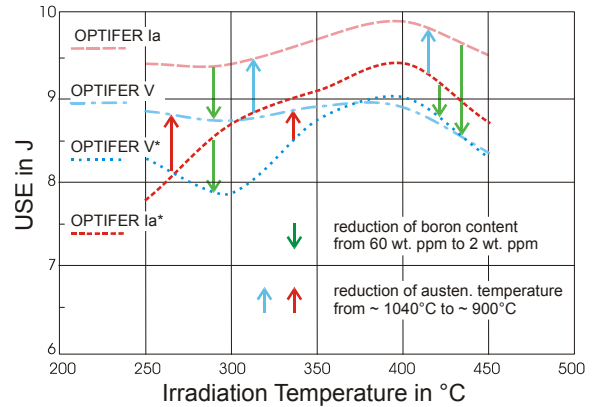Fig. 2: DBTT vs. irradiation temperature



Fig. 3: Influence of heat treatment and boron content

Lower austenitization temperature leads to higher impact energies for both boron contents before and after irradiation. The influence of the heat treatment is not affected by the irradiation: both heat treatments show approximately the same shift in USE and DBTT (Figs. 2 and 3).
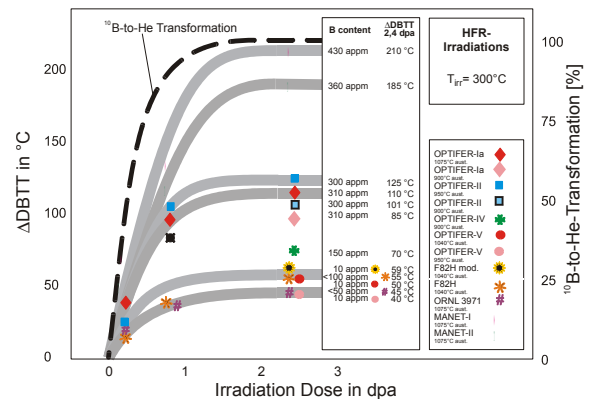


Fig. 4: Irradiation-induced shifts of ductile-to-brittle transition temperature and $^{10}$B-to-He transformation vs. irradiation dose

For the lowered boron content, DBTT is about 50 °C lower in both cases, the shift in DBTT after irradiation is reduced to 30%. The higher is the boron concentration, the steeper are the embrittlement slopes in Fig. 4. The shift of DBTT for the newly investigated materials, especially for the boron-reduced OPTIFER alloys, nicely fits to the former results; the negative influence of boron on the embrittlement behaviour is confirmed by the present investigation.

The following results are expected for the ongoing investigations:

- A study of EB and TIG weldings with F82Hmod and of diffusion weldings with MANET-II.

- A characterisation of the F82Hmod HIP base material and the influence of the notch root.

- The influence of different annealing treatments on the mechanical properties of OPTIFER-IV and F82H mod.

- Further insights for the improvement of the chemical composition (OPTIFER-IV without boron, JLF1).

Table 1: Heat treatment and selected properties

|  | Heat treatment | USE [J] | DBTT [°C] | $\sigma_{Dy\,26°C}$ [MPa] |
|---|---|---|---|---|
| OPTIFER-Ia* | 1075°C/ 0.5h + 780°C/2h | 10.1 | -80 | 543 |
| OPTIFER-Ia | 900°C/ 0.5h + 780°C/2h | 10.6 | -85 | 500 |
| OPTIFER-V* | 1040°C/ 0.5h + 750°C/2h | 9.5 | -80 | 605 |
| OPTIFER-V | 950°C/ 0.5h + 780°C/2h | 9.7 | -100 | 592 |
| OPTIFER-II | 900°C/ 0.5h + 780°C/2h | 9.7 | -75 | 470 |
| OPTIFER-VI | 950°C/ 0.5h + 780°C/2h | 9.1 | -70 | 540 |
| OPTIFER-IV | 900°C/ 0.5h + 750°C/2h | 9.3 | -80 | 519 |

Table 2: Chemical composition in wt.% of OPTIFER-alloys

| OPTIFER | Ia | V | II | VI | IV |
|---|---|---|---|---|---|
| Cr | 9.3 | 9.48 | 9.5 | 9.35 | 8.5 |
| W | 0.965 | 0.985 | 0.006 | 0.005 | 1.16 |
| B | 0.006 | 0.0002 | 0.0059 | 0.0002 | 0.003 |

**HFR Phase IIB (SPICE)**

The objectives are to evaluate the mechanical properties of material samples after irradiation at doses of 15 dpa and at different irradiation temperatures. The material is the reduced activation alloy EUROFER97 in different variations: different heat treatments, a HIP powder steel, and various boron contents to investigate the effect of He-embrittlement. The "quasi-saturation" of irradiation induced embrittlement between 10 and 15 dpa, found for conventional steels in former programs (SIENA), will be investigated for the EUROFER alloys. The low irradiation temperature ranges of the High Flux Reactor will give a look at embrittlement effects increasing progressively with decreasing temperature in all bcc-alloys irradiated up to now.

Three different sample holders, each of them placed in a central core position of the High Flux Reactor at Petten, are being irradiated at 5 different temperature levels of 250/300/350/400/450°C. Post Irradiation Examinations (PIE) will be carried out in the Fusion Materials Laboratory of FZK. Activation detectors in the sample holders and active thermocouple control of the liquid sodium cooling are additionally applied to ensure the high quality level of HFR irradiations even at higher doses (Fig. 5). The design provides space for 130 charpy, 91 tensile, and (for the first time simultaneously) 160 fatigue specimens; for details,

see [4]. Result will be a full data set of the irradiation effects on Charpy impact, tensile and fatigue behaviour. During the irradiation phase, unirradiated reference samples are investigated. Regarding the EUROFER steel, an embrittlement behaviour comparable to the best alloys investigated in former irradiation programmes is expected, accompanied by good mechanical properties. The higher irradiation dose of 15 dpa will be a step towards fusion-relevant doses.

Mechanical preparations, sample holder fabrication and sodium filling were finished in July 2001. The neutron irradiation has started in August, the target dose of 15 dpa will be reached by end 2003. After dismantling, transportation and decontamination, the PIE will start in mid 2004, they will be completed by mid 2006.
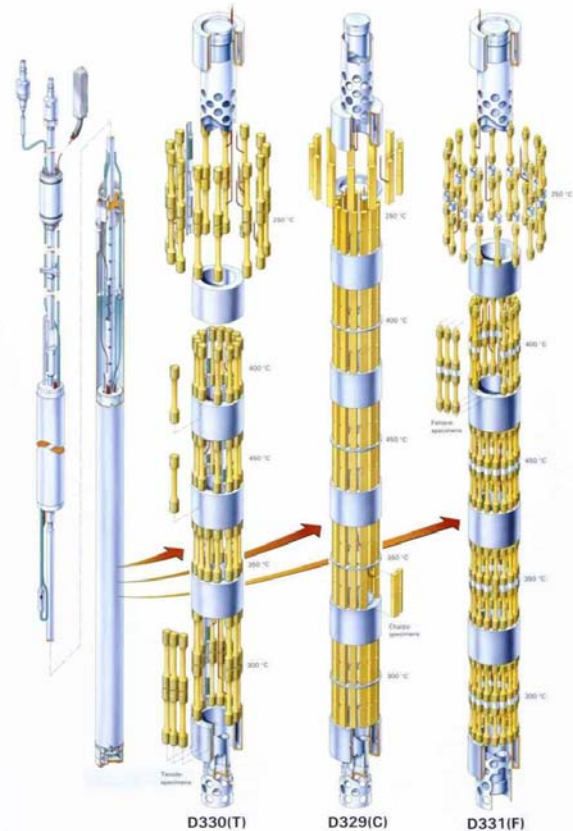


Fig. 5: Irradiation capsule with sample holders. D330: 91 tensile specimens; D329: 130 charpy specimens; D331: 160 fatigue specimens

Staff:

J. Aktaa
B. Dafferner
W. Kunisch
H. Ries
R. Rolli
O. Romer
H.-C. Schneider

Literature:

[1] H.-C. Schneider, B. Dafferner, H. Ries, O. Romer, Bestrahlungsprogramm MANITU, FZKA 6605, May 2001

[2] H.-C. Schneider, B. Dafferner, J. Aktaa, J. Nucl. Mater. 295 (2001) 16-20.

[3] H.-C. Schneider, B. Dafferner, J. Aktaa, ICFRM-10, Baden-Baden, Germany, October 2001.

[4] H.-C. Schneider, SPICE Irradiation Programme Status Report, internal report, Forschungszentrum Karlsruhe, December 2000.

## Work on OPTIFER and F82H mod. Alloys

Former mechanical tests and structural investigations of irradiated samples in the programs of SIENA, Manitu, etc., confirmed the good irradiation properties of the RAFM alloys. However, a critical effect of low-temperature irradiation-induced hardening and embrittlement occurs in the fusion-relevant temperature range of 250 – 400 °C. Here a remarkable shift of DBTT towards higher temperatures can be observed, together with an increase in the ultimate strength. This behavior occurs at moderate neutron doses of only few dpa up to 15 dpa as observed e.g. in SIENA. However, it was also shown that the effect can be reduced by chemical modifications, for example, by operating with Cr contents in the range of 9 wt.% and strongly reduced B contents.

Martensitic 7-10%CrWVTa alloys were irradiated in the HFR Petten up to an accumulated dose of 2.4 dpa in the temperature range between 250 and 450 °C. The tensile specimens were manufactured of the alloys OPTIFER II, OPTIFER IV, and the Japanese steel F82H mod.. After the post-irradiation tensile tests in the Hot Cells of Forschungszentrum Karlsruhe, the maximum of strength could be determined at 300 °C irradiation and test temperature; Fig. 1.
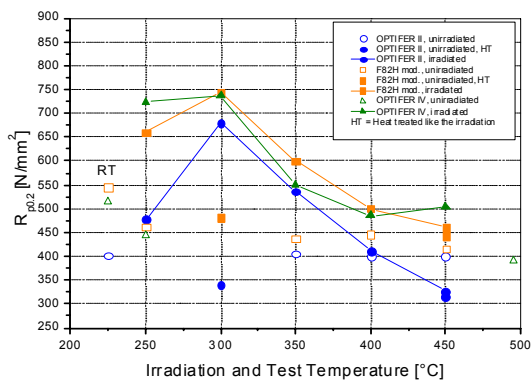


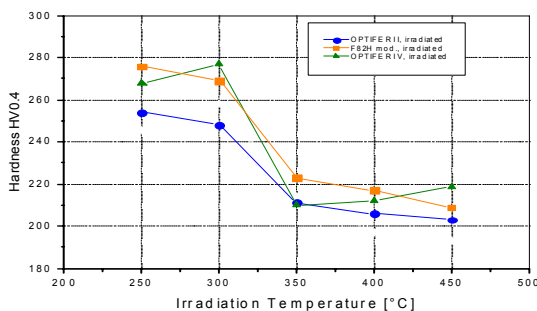Fig. 1:  Yield strength, $R_{p0.2}$, of HFR Ia specimens



Fig. 2:  Vicker Hardness HV0.4 of HFR Ia specimens

The materials were investigated in metallographic cuts. The ASTM grain-size of the OPTIFER alloys was 6 – 7.5, and the grain-size of the former austenitic grain of the alloy F82H mod was ASTM 5. There was no irradiation influence to this structure. Irradiation induced hardening could be found at the lower irradiation temperatures at 250 and 300 °C, as the softening to the higher temperatures of 350, 400, and 450 °C; Fig. 2. These data are in a good correlation to the tensile results.

Comparisons of tensile data with the DBTT values of the Charpy samples reveal that softening of the alloys F82H mod. and OPTIFER IV correspond to the trend of the DBTT values during dynamic tests, with a maximum DBTT at 250 °C irradiation temperature; Fig. 3.
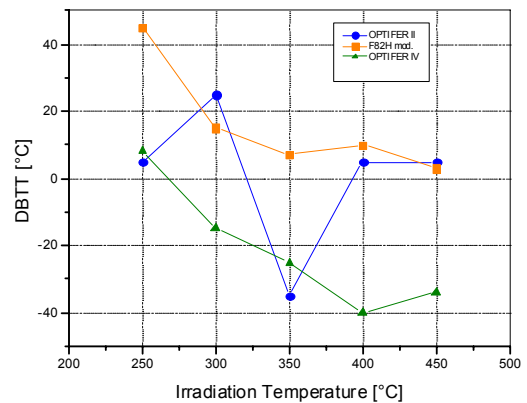


Fig. 3:  DBTT of HFR Ia specimens vs. irradiation temperature

Staff:

B. Dafferner
P. Graf
M. Holzer
M. Klimiankou
W. Kunisch
E. Materna-Morris
A. Möslang
B. Neufang
D. Preininger
H. Ries
R. Rolli
O. Romer
H. Zimmermann

Literature:

E. Materna-Morris, H.-C. Schneider, B. Dafferener, R. Rolli und O. Romer: Irradiation Influences on Mechanical Properties and Structures of Martensitic Low-Activation Alloys. 10th Int. Conf. on Fusion Reactor Materials, October 14 – 19, 2001 Baden-Baden, Germany.

# Modelling and Analysis of Irradiation Effects on Strength, Tensile Ductility and Impact Behaviour

The displacement damage dependence of irradiation strengthening, tensile ductility loss and Charpy-impact behaviour have been modelled [1,2]. Additionally, the effects from a superimposed helium (≤ 85 appm) generation [1,3] via the $10B(n,\alpha)7Li$ transmutation and particle strengthening [2] have been considered. The predictions were compared with experimental results obtained on various RAFM-Optifer and conventional 9-12CrMoVNb steels like MANET-I,II, irradiated in the HFR at temperatures of TI=250-475°C to 0.2-15 dpa. Besides, the effect of particle strengthening on work hardening, tensile ductility and impact behaviour have been modelled and compared with results observed on various Y2O3- particle strengthened unirradiated ODS-(9-13)Cr and high nitrogen containing martensitic 9-13Cr steels. At last for optimization regarding improved impact and ductility behaviour of RAFM and ODS-RAFM steels at simultanious high strength, also the effect of alloy composition (B, N, C, Cr) have been considered in detail including the irradiation behaviour.

## Irradiation hardening and DBTT

Taking into account interstitial-driven defect nucleation and growth a logarithmic displacement damage dependence of irradiation strengthening according

$$\Delta\sigma_i = B \ln(dpa) + A \qquad (1)$$

is predicted [2] for lower irradiation temperatures of ≤ 300°C, still without saturation. The coefficients A, B describe growth and defect nucleation rate which weakly diminishes with increasing displacement damage. Irradiation strengthening of 7-12Cr steels at this low temperatures according TEM examinations is mainly caused by small defect clusters, interstitial loops and under specific condition also α`-precipitates. Taking additionally into account stress-induced dynamic fracture appearance, from eq. 1 a logarithmic displacement damage dependence

$$DBTT_i \cong R_1 \ln(dpa) + R_2 \qquad (2)$$

results [2] too for the ductile-to-brittle transition temperature $DBTT_i$ of irradiated material. The slope $R_1$ decreases with diminishing defect nucleation rate B, strain rate sensitivity of strength and loading rate as well as increasing difference of dynamic fracture stress $\sigma_f^*$ and athermal strength $\sigma_o$, but does not depend on maximum thermal strength P at T=0 K. Parameter $R_2$ again depends on the same parameters but not on defect nucleation rate B. A superimposed structural-induced embrittlement with reduction of dynamic fracture stress $\Delta\sigma_f^*$ as could be the result of a helium or hydrogen generation increases both $R_2$ and slope $R_1$. At higher irradiation temperatures above 300°C vacancies strongly become mobile causing pronounced defect annealing. By considering of such competitive action of defect nucleation, growth and vacancy-driven defect annealing the displacement damage dependence of irradiation strengthening, $DBTT_i$ and their normalized shift $V_i=\Delta DBTT_i/DBTT_o$ change to a distinct saturation behaviour described by

$$\Delta\sigma_i = \Delta\sigma_{i,s}[ 1 - \exp(-k_a dpa/2p)]^p \qquad (3)$$

$$V_i \cong K_d \Delta\sigma_{i,s}/P\{\Delta\sigma_f^*/ \Delta\sigma_{i,s} + [1 - \exp(- k_a dpa/(2p))]^p\} \le V_s$$

with the material dependent exponent of about p≅1/4 to 3/4 and $K_d \ge$ e=2.718. The saturation strength $\Delta\sigma_{i,s} \infty (k_n/k_a)^p \infty \exp(Q_s/kT)]$ depends on coeffcients for defect nucleation $k_n$ and annihilation $k_a$ and their temperature dependence is described by an activation energy $Q_s=\Delta Ep$ of about 0.25-0.8 eV,

dependent on difference $\Delta E=E_{m,v}-E_{m,i}\approx 1eV$ of migration energies for vacancies and interstitials. For lower damages, eq.3 asymptote finally to the power-law dependence $\Delta\sigma_i \infty [k_n dpa]^p$ and $V_i \infty K_d/P[k_n dpa]^p$ with the exponent p.

As shown in Fig. 1 for both 7-9CrW(Ge)VTa and 10-12CrMoVNb steels at mean irradiation temperatures of $T_I$=250/300°C and 0.2-2.4(15) dpa, the obtained $DBTT_i$ values from Charpy tests increase in accordance to predictions of eq. 2 logarithmically with displacement damage. The conventional 10-12CrMoVNb steels with $R_1$=75.2-78 °C, $R_2$=76-131°C show due to enhanced defect nucleation rate higher slopes $R_1$ and also $R_2$ values compared to 7-9CrW(Ge)VTa steels, where $R_1$=16-62 °C and $R_2$= -38 to 58 °C. Within both steel groups particularly parameter $R_2$ is increased with increasing B content. By extrapolation to 50 dpa a $DBTT_i$ value of 150°C is predicted for F82H at $T_I$=250°C which comparably lower to that ≈210°C found on MANET-I at the low damage of 2.4 dpa.
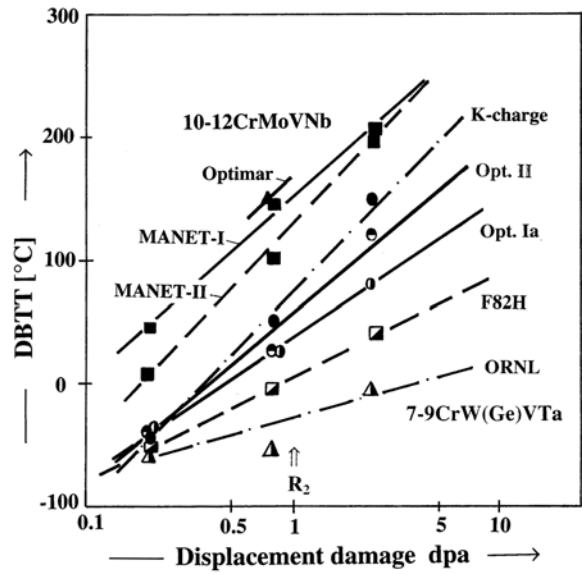


Fig. 1: Displacement damage dependence of $DBTT_i$ vs. ln (dpa) for various RAFM and MANET-I,II steels at $T_I=T_T$=250°C and ≤ 15dpa

In contrast to low temperatures $T_I=T_T$=250/300°C, the irradiation strengthening of 7-12Cr steels at higher irradiation temperatures clear saturates at the level of about $\Delta\sigma_{i,s} \le$ 480 MPa as shown in Fig. 2 by the plot $\Delta\sigma_{i,s}$ vs. $1/(T_I=T_T)$ for $T_I=T_T$=250-475°C. Saturation strengthening decreases sensitively with increasing irradiation temperature described by an energy of about $Q_s \cong 0.735$ eV. Compared to martensitic 7-12Cr, austenitic Cr/Ni steels show distinctly higher saturation strengths $\Delta\sigma_{i,s} \le$ 750 MPa together with a weaker temperature-induced reduction described by $Q_s \cong 0.473$ eV for $T_I=T_T \cong 350-605$°C. Besides, irradiation strengthening disappears almost at the about 175°C higher temperature of ≈600°C. Assuming $E_{m,v}$=1.3eV, $E_{m,i}$=0.3 eV from the energy $Q_s \cong 0.473$ eV a value of p≅3/4 is observed for martensitic 7-12Cr steels which is somewhat larger as that for austensitic steels.

As for the as saturation strength $\Delta\sigma_{i,s}$ also the irradiation-induced embrittlement shift $V_s$ at saturation decreases with increasing irradiation temperature above 300°C. Against 7-9CrW(Ge)VTa the 10-12CrMoVNb steels show with $V_i \le 1.1$ distinct higher shifts which distinctly decrease above 300°C according to an activation energy of $Q_v \approx 0.79$ eV as observed for irradiation strengthening too.
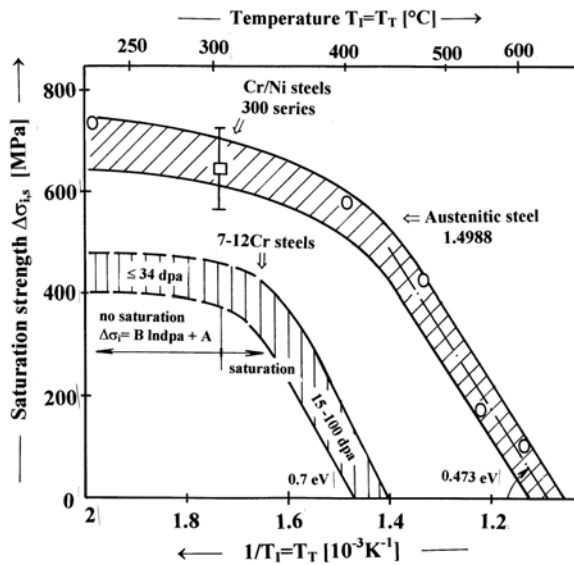
Fig. 2: Irradiation temperature dependence of saturation hardening of martensitic 7-12Cr and austenitic Cr/Ni steels by the plot $\Delta\sigma_{i,s}$ vs. $1/T_T=T_I$

**Effect of He**

As already previously shown [1] a neutron-induced helium generation via the $^{10}B(n,\alpha)^7Li$ reaction strongly reduces tensile ductility as fracture strain and total elongation of all boron containing 7-12Cr steels with maximum amount around $T_I=T_T\cong300°C$. It is caused by He-bubble/cluster formation at interfaces of $M_{23}(B,C)_6$ boroncarbides strongly enriched with boron together with their structural modifications which promotes interfacial decohesion and decreases ductile fracture stress at higher $He(^{10}B)$ contents. As for ductility also the ductile upper shelf energy of dynamic Charpy tests is reduced with increasing $He(^{10}B)$ content particularly at the low irradiation temperature 250°C, 2.4 dpa of strongest dynamic irradiation hardening as demonstrated in Fig. 3. It indicates, that the same process of He- induced ductility reduction acts also under dynamic loading conditions. However, in contrast to tensile ductility, the 10-12CrMoVNb steels show distinct higher helium-induced USE- reductions compared to RAFM steels. This different behaviour seems to be due to their higher $DBTT_i\lesssim$ 210°C values which obviously is a necessary condition for a well-marked He- induced reduction of the dynamic energy USE. It would mean that pronounced USE reductions by helium arises at strong dynamic irradiation strengthening and high damage dpa as well as initial $DBTT_0$ values. The DBTT shift, however, is mainly caused by the irradiation-induced increase of dynamic strengthening, which is only weakly additionally increased by helium below $T_I\lesssim300°C$.

The fracture strain as for uniform strain and work hardening in accordance to predictions generally decreases hyperbolically with increasing yield strength as observed for unirradiated and at $T_I=300°C$ irradiated 9-12Cr steels. Irradiation of the 85 appm B containing MANET-I at $T_I=T_T=300-475°C$ to 5-10 dpa strongly reduces fracture strain more pronounced at the high irradiation temperature $T_I=T_T=475°C$ due to a combined reduction of ductile fracture stress. Pronounced particle strengthening of ferritic-martensitic ODS-(9-13)Cr steels like ODS-Eurofer97 and the ferritic 20CrAlTiC ODS-steel PM 2000 with 0.5 wt.% $Y_2O_3$ also distinctly reduces fracture strain to about similar amount as through irradiation of MANET-I at 475°C. This ductility reduction in accordance with predictions, however, is mainly caused by the strongly enhanced work hardening due to presence of a high volume content of small (<50 nm) $Y_2O_3$-particles.
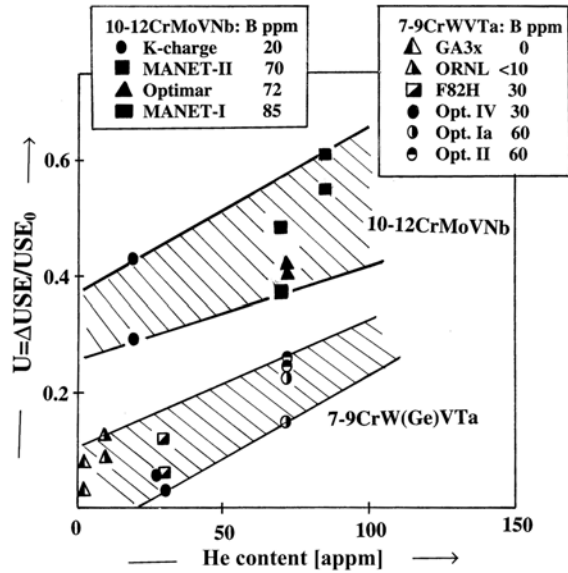


Fig. 3: Effect of He- content generated by $^{10}B$ on relative decrease of ductile energy USE for various 7-12Cr steels at $T_I=250°C$, 2.4 dpa

Staff:

D. Preininger

Literature:

[1] D. Preininger; Modelling of the effect of microstructure on the shape of cleavage fracture transition in martensitic 7-12Cr steels, Marc, 2001, Proc. of the Materials Week`2000, http//www.materialsweek.org

[2] D. Preininger; Modelling of the irradiation dose dependence of strength, ductility and impact properties of martensitic 7-12Cr steels, 7th European Conference on Advanced Mareials and Processes – EUROMAT 2001, 10/14. June 01, Rimini, Proc. p. 272

[3] D. Preininger; Mechanisms of the effect of helium on tensile ductility and impact behaviour of ferritic-martensitic 7-12Cr steels, ICFRM-10, 14/19. Oct. 2001, Baden-Baden, Book of abstracts p.456

[4] D. Preininger; Modelling of the effect of precipitates on work hardening, tensile ductility and impact behaviour of ferritic-martensitic 7-12Cr steels, ICFRM-10, 14/19. Oct. 2001, Baden-Baden, Book of abstracts p.455

[5] D. Preininger; Mechanism of Boron Addition on Impact and Ductility Behaviour of Ferrritic-Martensitic Low-alloyed and 7-12Cr steels, Materials Week`2001, 1./4. Oct. 01, München; Advanced Metallic Materials, I4 Steel: Recent Developments Abstract in http//www.materialsweek.org

## TTMS-001/9
## Irradiation in a Temperature Controlled Test Rig of BOR 60

### Objectives

In an energy generating fusion reactor structural materials will be exposed to very high levels of irradiation damage of about 100 dpa. Due to the fact, that fast reactor irradiation facilities in Europe are not available anymore, a cooperation with the Russian institution: State Scientific Centre of Russian Federation-Research Institute of Atomic Reactors (SSC-RIAR) has been implemented.

### The irradiation project ARBOR

In the irradiation project "ARBOR" (for Associated Reactor Irradiation in BOR 60 and the Latin name for tree) 150 mini-tensile/low cycle fatigue specimens and 150 mini-charpy (KLST) specimens of different RAFM steels are under irradiation in a special designed irradiation rig of BOR 60 at a temperature less than 340°C since November 2000. The irradiation started in position D-23, where temperature measurement is possible and is continued in an identical position G-23 of the 5th row of BOR 60 until 30 dpa will be reached.

1040°C; F82H mod., as received; OPTIFER IVc, normalised at 950°C EUROFER 97 with 82 wppm nat. B, as received; EUROFER 97 with 83 wppm B10, as received; EUROFER 97 with 1160 wppm B10, as received (as model alloys); EUROFER 97 with ODS as received and EUROFER 97 electron-beam welded as well as reference bulk material, from NRG, Petten.

### State of the art of ARBOR

At the end of October 2001 a damage dose of 17 dpa has been accumulated. The target dose of 30 dpa will be reached end of 2002. The postirradiation tests together with microscopy will be performed in the hot cells of SSC-RIAR beginning in 2003.

Staff:

C. Petersen
D. Rodrian

Literature:

C. Petersen, V. Shamardin, A. Fedoseev, G. Shimansky, V. Efimov and J.W. Rensman: "The ARBOR irradiation project", to be published in the ICFRM 10-issue of Journal of Nuclear Materials.



1- thermometric probe;
2- detachable head;
3- spacer tubes;
4- probe thermocouples;
5- wrapper;
6- gas gap;
7- internal tube;
8- ampoule assembly;
9- core center;
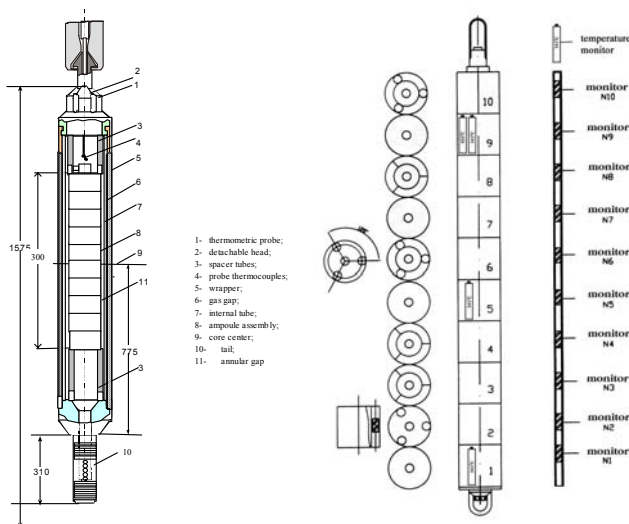10- tail;
11- annular gap

Fig. 1: Dismountable irradiation rig with a thermocouple

Fig. 2: Scheme of the neutron and temperature monitors location in the suspensor

The irradiation rig is equipped with neutron monitors in the central tube and of three of the ten levels of specimen positions as well as with three temperature detectors also at three of the ten levels.

### Specimens and materials

For tensile and low cycle fatigue testing a small size cylindrical specimen has been developed and for charpy testing the KLST specimen was chosen. Tensile, low cycle fatigue and charpy specimens of the following materials are under irradiation: EUROFER 97, as received; EUROFER 97, normalised at

**TTMS-002**
**Metallurgical and Mechnical Characterisation**

**TTMS-002/10**
**Thermal and Isothermal Fatigue Properties of Base Metal**

**Introduction**

A structural component like a Test Blanket Module (TBM) is subjected during service to alternating thermal and mechanical stresses as a consequence of the pulsed reactor operation. Of particular concern is the fatigue endurance of Reduced Activation Ferrite Martensite (RAFM) steels like F82H mod., OPTIFER IV and EUROFER 97 under cyclic strains and stresses produced by these temperature changes. To design such structures, operating under combined mechanical and thermal cycling, fatigue life has to be examined in isothermal fatigue tests for materials data generation and in thermal fatigue for verification of design codes.

In this report isothermal mechanical Low Cycle Fatigue (LCF)-behaviour of the RAFM steels F82H mod. and EUROFER 97 is described from a microscopical point of view.

Thermal low-cycle fatigue (TCF) experiments of EUROFER 97 are compared to F82H mod. and OPTIFER IV. TCF-data of F82H mod. show a dramatic influence of the application and duration of hold times.

**Experiments**

The LCF tests have been performed on solid cylindrical specimens (77 mm length, 21 mm initial gauge length and 8.8 mm diameter) with MTS servo hydraulic testing machines operating in triangular strain controlled push-pull mode (constant strain rates of $3 \times 10^{-3}$ 1/s).

The TCF test rig consists of a stiff load frame for mechanical clamping of the sample, which is directly heated by the digitally controlled ohmic heating device. Cylindrical hollow specimens with a wall thickness of 0.4 mm have been used for TCF-experiments. Variable strain rates are applied at TCF test mode, due to the constant heating rate of 5.8 K/s and variable temperature changes.

Since both, temperature and mechanical strain cycling are taking place, mechanical strain is available only after subtraction of the thermal strain from the net strain.

**Results**

LCF-behaviour:

LCF results in the temperature range between room temperature and 600°C of the RAF steels F82H mod. and EUROFER 97 show under these test conditions after the first few cycles a pronounced cyclic softening that continues up to failure. The softening during LCF tests, more pronounced for EUROFER 97, is dependent on temperature but independent on the total strain amplitude of the tests. From the analysis of the hysteresis loops and correlated electron microscopic observations it can be concluded that the cyclic softening is produced by a softening observed in the internal stress as a consequence of the evolution of the microstructure from a carbon saturated high dislocation density to a softer dislocation cell structure.
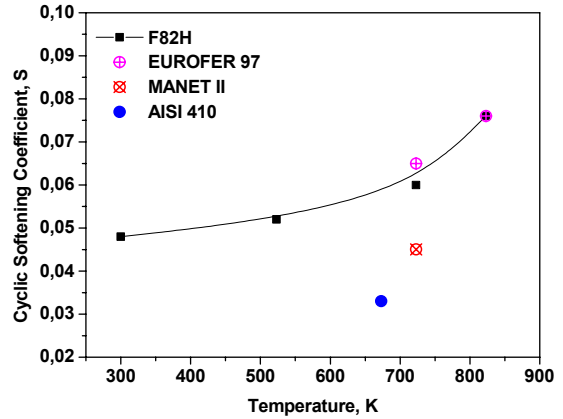


Fig. 1: The cyclic softening coefficient S for both steels under examination and similar steels cycled at the referred temperatures

The cyclic softening coefficient S-data for F82H mod. and EUROFER 97 indicate that for temperatures up to 450°C the cyclic softening taking place on the tempered steels is only slightly dependent on temperature. At 450°C the softening coefficient increases dramatically indicating that synergetic effects of cycling and temperature become important. From figure 1 it can be seen that EUROFER97 and F82Hmod., represent almost similar cyclic softening behaviour.

In order to understand the mechanism producing the cyclic softening observed on these steels a method originally suggested by Cottrell and employed by Kulhman-Wilsdorf and Laird was used. Upon this method, the flow stress obtained from the hysteresis loop is the result of a short distance interaction or "internal stress". Information about the type of obstacle to dislocation movement can be obtained from the data of these tested steels.

TCF-behaviour:

F82H mod., EUROFER 97 and OPTIFER IV are thermally cycled in the temperature range between 100 to 500 until 600°C.

Comparing total mechanical strain $\Delta\varepsilon_{t,m}$ vs. number of cycles to failure $N_f$, F82H mod. and OPTIFER IV show in the temperature range of 100 to 550°C at a $\Delta\varepsilon_{t,m}$ of about 0.4 %, $N_f$-values between 3000 and 5000 cycles (figure 2). Whereas EUROFER 97 at a similar $\Delta\varepsilon_{t,m}$ remains a factor of 2.5 lower in life time. In the temperature range of 100 to 600°C the behaviour is similar.

TCF-hold time experiments of 100 and 1000 s had been realised on F82H mod. (figure 3). The hold time definition is: HTH, hold time at the higher temperature $T_H$, HTL, hold time at the lower temperature $T_L$ and HTHL, hold time at both temperatures. Normally for 100 s hold time the results of HTL- and HTH-tests in temperature ranges of 100 to 500 °C are found in a smaller scatter of $\Delta\varepsilon_{t,m}$~0.3 % and of $N_f$ around 16000 cycles.

Staff:

J. Aktaa
M. Klotz
C. Petersen
M. Pfeifenroth
D. Rodrian
R. Schmitt

Literature:

L. A. Belyaeva, A. A. Zisman, C. Petersen, V. A. Potapova and V. V. Rybin: "Thermal Fatigue Crack Nucleation in Ferritic-Martensitic Steels before and after Neutron Irradiation", Journal of Nuclear Materials 283-287 (2000) 461-464.

A. F. Armas, I. Alvarez-Armas, C. Petersen, M. Avalos and R. Schmitt: "Internal and effective stress analysis during cyclic softening of F82H mod. martensitic stainless steel", presented at SF2M-ESIS conference, Paris, 29. – 31.5.2001.

A. F. Armas, C. Petersen, R. Schmitt, M. Avalos and I. Alvarez-Armas: "Mechanical and Microstructural Behaviour of Isothermally and Thermally Fatigued Ferritic-Martensitic Stainless Steels", presented at ICFRM 10, Baden-Baden, 14. – 19.10.2001 and to be published in a special issue of Journal of Nuclear Materials.

C. Petersen and D. Rodrian: "Thermo-mechanical Fatigue Behaviour of Reduced Activation Ferrite/Martensite Stainless Steels", presented at ICFRM 10, Baden-Baden, 14. – 19.10.2001 and to be published in a special issue of Journal of Nuclear Materials.
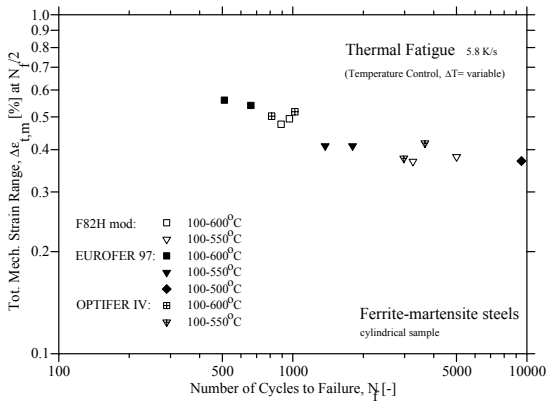


Fig. 2: Comparison of total mechanical strain range $\Delta\varepsilon_{t,m}$ of thermal fatigue behaviour between F82H mod., EUROFER 97 and OPTIFER IV
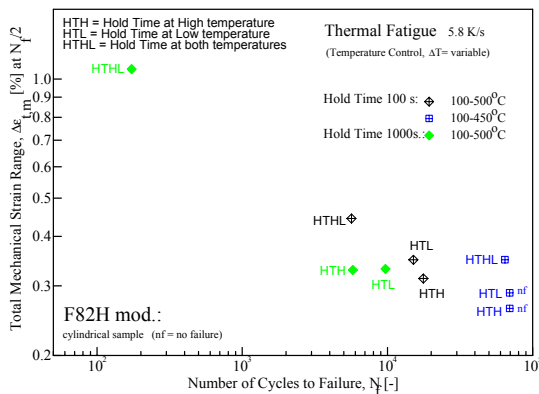


Fig. 3: Comparison of total mechanical strain range $\Delta\varepsilon_{t,m}$ of thermal fatigue behaviour of F82H mod. with 100 s and 1000 s hold times

In case of a continuous 100 to 500 °C temperature range the $N_f$ - values without hold times are found around 10000 cycles (Figure 2). So these hold times lead to a slight increase in life time. But at the HTHL condition for 100 s hold time with increasing $\Delta\varepsilon_{t,m}$ up to 0.45 % a reduction in life time down to 6000 cycles i.e. a factor of 1.6 lower was found. At increasing hold time of 1000 s even the HTL- and HTH-values are found to be less than 1000 cycles, but the HTHL-condition shortens the $N_f$ - values down to 200 cycles at a very high $\Delta\varepsilon_{t,m}$ - value of around 1.1 % strain. This is a reduction in life of rather two orders of magnitude resulting from increasing creep effects with increasing hold times. The reason for this behaviour is not yet understood and therefore structural examinations are planned.

# TTMS-002/13
# Metallurgical and Mechanical Characterization of RAFM Steels

Within the framework of the European Technology Programme, the Japanese steel F82H-mod is being investigated parallel to the European development line of OPTIFER and the new common European steel EUROFER. Further improvement/tailoring of the reference alloy EUROFER 97 and data generation for a step-by-step qualification are the main goals of activities.

## Work on F82H-mod and OPTIFER

Characterization work on F82H-mod was completed and documented [see Annual Report 99/00 and [1]]. The same holds for the work with regard to the mechanical properties (tensile strength, toughness and creep tests) [[2-6] and Annual Report 99/00].

## Work on EUROFER 97

In addition to the activities published in [7, 8], characterization work was continued. Concerning the notch impact behavior, a complete $A_v/T$ curve was plotted using specimens made of 14 mm plate material (transverse to rolling direction). Longitudinal and transverse specimens made of forged $\varnothing$ 100 rod material were compared. 5 ISO-V specimens were tested at each test temperature in order to obtain parameter scattering (Fig. 1). The $A_v/T$ curve obtained for specimens taken along forging direction corresponded to the mean curve of the 14 mm material. The transverse specimens were found to be far below the results obtained for the longitudinal specimens with accordingly smaller FATT and DBTT values. This was attributed to the marked deformation direction by forging. In both cases and for both materials, transition from the upper shelf to the lower shelf was reflected by a significant jump.

To determine the influence of hardening temperature, two heat treatments at increased hardening temperatures (1050°+750°C or 1075°+750°C) were tested in comparison to the state as delivered (=980°+760°C). Increase in the hardening temperature (to improve creep rupture behavior), however, was associated with a decrease in notch impact toughness. The DBTT/FATT values were reduced from 70-78°C to 54-57°C. Meanwhile, creep tests in the temperature range of 450°-650°C using specimens made of $\varnothing$ 100 and 14 mm plate material cover the time period up to $10^4$ h. The results obtained so far with regard to creep strength and creep behavior allow the preliminary statement to be made that EUROFER can be ranked between F82H-mod (minimum) and OPTIFER (maximum) [9] (Figure 2).

Aging behavior of EUROFER is considered to be very good. Specimens subjected to stabilization annealing treatments at 580°C for 3300 h or at 600°C for 1050 h (= at 550°C for 20 000 h) were tested in tensile tests in the temperature range between RT and 600°C and did not exhibit any significant differences in the parameters as compared to the state as delivered. Creep test results in the temperature range of 450°-650°C for a duration of up to 5000 h do not reveal any influence of aging treatment as well.

The results obtained so far will be compiled to an FZKA report with the homogeneity studies being taken into account. Current creep tests will be continued up to the time range of 20 000 h. However, up to 550°C, the stress range below 160 MPa will be covered only (see Fig. 2). Hence, no data are available for the design-relevant stress range of $\leq$ 100 MPa. This also holds for F82H-mod and OPTIFER. For experimental confirmation of the necessary extrapolations, special creep tests will be performed at 500°C and 550°C in the stress range of 180-60 MPa. These

creep tests will provide data on the technically relevant time-yield limits and the stress dependence of minimum creep rates of up to $10^{-9}$/h (see Fig. 2).


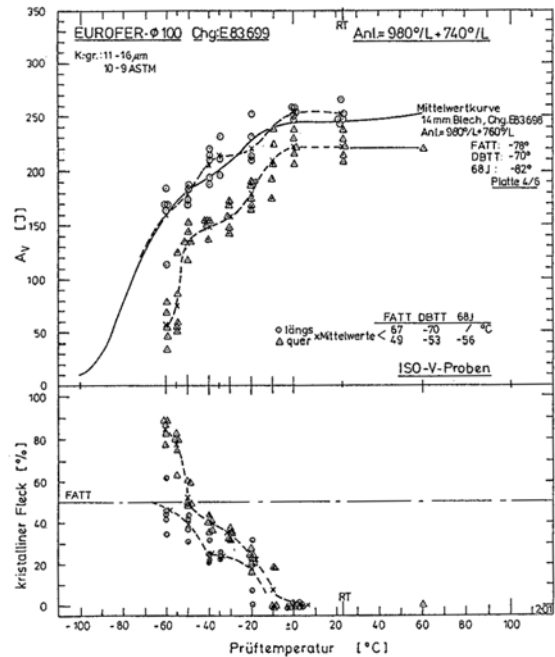
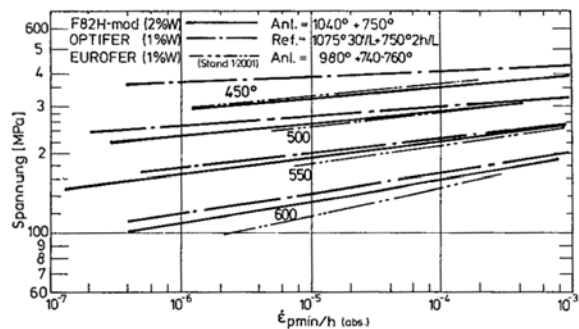Fig. 1: Fracture toughness curves for $\varnothing$100 bars and 14 mm plates



Fig. 2: Stress dependency of minimum creep rate for 3 RAFM-steels

Staff:

S. Baumgärtner
P. Graf
K. Ehrlich (until 11/2000)
A. Falkenstein
S. Heger
R. Lindau
E. Materna-Morris
M. Schirra

Literature:

[1] M. Schirra, S. Heger, A. Falkenstein: El comportamiento a la rotura y a la fluencia lenta del acero martensitico de baja activación F82H-mod (informe final). La résistance à la fatigue et le vomportement au fluage e l'acier martensique de faible activation F82H-mod (Rapport final) Spanische und französische Version von FZKA 6265, Febr. 2001

[2] M. Schirra, A. Falkenstein, H. Kempe*, M. Klotz* : Influence de la température de trempe sur les caractéristiques physiques et mécaniques des aciers martensiques de faible activation. Rapport IMF No. 055, Rapport PKF No. 154, März 2001

[3] M. Schirra, P. Graf, S. Heger, A. Falkenstein, H. Kempe, M. Klotz, J. Lapena, P. Fernandez: Untersuchungen an 4 Chargen der W-haltigen Legierung OPTIFER-IVc. Interner Bericht Juni 2000, Estudios sobre 4 variantes de la aleación OPTIFER-IVc con W. Analyse de 4 variantes de l'alliage OPTIFER-IVc au W., Spanische und französische Version

[4] M. Schirra, H. Kempe, E. Materna-Morris: Einfluss der Vergütungsbehandlung und verschiedener Stabilisierungsglühungen auf Kriterien der Kerbschlagzähigkeit von 8-12% Cr-Stählen. Interner Bericht, Sept. 2000

[5] S. Heger, M. Schirra: Zusammenstellung von Kriechkurven aus verschiedenen Versuchsprogrammen, Teil XIV (OPTIFER IVc, V-VII). Interner Bericht, Juni 2001.

[6] M. Schirra, A. Falkenstein, S. Heger, J. Lapena: Das Zeitstandfestigkeits- und Kriechverhalten der niedrig-aktivierenden martensitischen OPTIFER-Legierungen (Abschlussbericht). FZKA 6464, Juli 2001. Le comportement de résistance à la rupture et au fluage des alliages martensitiques de faible activation OPTIFER (rapport final). Französische Version FZKA 6464

[7] K. Ehrlich, R. Lindau, A. Möslang, M. Schirra : IEA-Workshop on RAFM-Steel, Tokyo, 2. + 3. Nov. 2000. EUROFER 97 and Development Strategy for RAFM Steels in Europe.

[8] M. Schirra, R. Lindau: 23. Vortragsveranstaltung VDEh-"Langzeitverhalten warmfester Stähle und Hochtemperatur-werkstoffe", Düsseldorf 1.12.2000, Tagungband Seite 36-49, Untersuchungen zu physikalischen und mechanischen Eigenschaften des niedrigaktivierenden martensitischen 9% Cr-Stahles EUROFER 97".

[9] M. Schirra: Jahrestagung Kerntechnik 2001, Dresden, 15.-17. Mai 2001, Beitrag 815, S. 597-601, "Das Kriech- und Zeitstandfestigkeitsverhalten von EUROFER 97 im Vergleich zu F82H-mod und OPTIFER".

[10] R. Lindau, M. Schirra: Status of investigations on the thermal and mechanical behaviour of EUROFER 97. Workshop on Data Base Evaluation of RAFM Steels, Brasimone, I, Nov. 27-28, 2000

**TTMS-002/19**
**Creep Fatigue Testing at High Temperatures**

**Introduction**

A structural component like a Test Blanket Module (TBM) is subjected during service to alternating thermal and mechanical stresses as a consequence of the pulsed reactor operation. Since the operating temperatures of a future DEMO reactor increase due to economic considerations, the knowledge of the creep fatigue endurance of Reduced Activation Ferrite Martensite (RAFM) steels like F82H mod. and EUROFER 97 becomes more important.

**Experiments**

The LCF hold time tests have been performed on solid cylindrical specimens of EUROFER 97 (77 mm length, 21 mm initial gauge length and 8.8 mm diameter) with MTS servo hydraulic testing machines operating in triangular strain controlled push-pull mode (constant strain rates of $3 \times 10^{-3}$ 1/s) at 550°C with a total strain range of 1%.

**Results**

First results of isothermal LCF tests with hold times in tension up to 600 seconds are compared with those on MANET II and F82H mod.. Figure 1 shows that lifetime of EUROFER 97 specimens seems not very different in comparison to F82H mod. values.
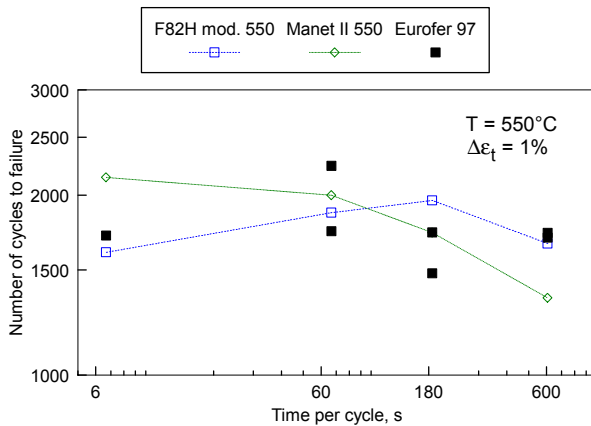


Fig. 1:  Comparison of EUROFER 97 with two reference materials with tensile hold times under LCF loading conditions

Staff:

C. Petersen
M. Pfeifenroth
R. Schmitt

**TTMS-003**
**Compatibility with Hydrogen and Liquid**

**TTMS-003/3**
**Thermal Fatigue Scoping Tests under Hydrogen Atmosphere**

**Introduction**

During service structural components of a Test Blanket Module (TBM) are subjected - under corrosive atmospheres - to alternating thermal and mechanical stresses as a consequence of the pulsed reactor operation. Of particular concern is the thermal fatigue endurance of Reduced Activity Ferrite-Martensite (RAFM) steels under test conditions and in atmospheres close to that prevailing in the reactor.

**Test facility**

The Vacuum Thermal Cycling Fatigue (VTCF) test facility consists of a stiff load frame, built in a vacuum vessel, for mechanical clamping of the sample, which is directly heated by the digitally controlled ohmic heating device. To apply a hydrogen partial pressure of $10^{-3}$ to $10^{-1}$ mbar, valves, transducers and the pump were modified and first calibration tests have been performed.

**State of the art**

The hydrogen feeding system to operate a prototype vacuum facility for thermal fatigue tests under hydrogen atmosphere is installed and in operable condition. But in the actual phase wish reference experiments under air atmosphere different number of cycles to failure are found in the modified system, foreseen for tests under hydrogen atmosphere. As long as it is not possible to obtain identical results under air in both facilities the start of tests under hydrogen atmosphere is postponed.

Staff:

C. Petersen
D. Rodrian

## TTMS-003/14
## Corrosion of RAF/M Steels in Liquid Pb-17Li

In fusion technology tritium permeation barriers (TPB) are required to reduce the tritium permeation through structural materials. It is known e.g. European fusion technology programme 1996 - 1998 that special ceramics or alloys have lower permeation rates as RAFM steels devoted as construction materials for a future fusion reactor. In the water cooled liquid lead-lithium blanket concept (WCLL) the structural materials are in contact with liquid metal and have to possess high enough corrosion resistance including the TPB on the steel surface. Therefore long term corrosion tests are necessary to confirm the compatibility with the flowing Pb-17Li alloy.

For this purpose low activation ferritic-martensitic (RAFM) steels coated by the Hot-Dip Aluminising (HDA) process as MANET I, Optifer IVa, F82H-mod or EUROFER 97 were inserted into the PICOLO Pb-Li corrosion loop to characterise the stability of the formed surface scale. Corrosion experiments are performed at 480 °C for test duration up to 10000 hours. The longest test time is reached for MANET 1 whereas EUROFER 97 tests started recently. The cylindrical samples had a diameter of 8 mm and a length of 35 mm. The corrosion attack was qualified by post test analysis consisting of metallurgical examination and EDX analysis on cross sections of the tested samples.

Corrosion tests with uncoated samples show that corrosion by Pb-17Li starts not immediately after exposure. First inhomogeneous corrosion attack will be registered after a certain time a so called incubation period of up to 3000 h. After this time a serious dissolution of the steel takes place. This process is mainly governed by depletion of Fe from the steel and forming a porous surface scale with bad adherence and nearly no protective character in flowing Pb-17Li. These results are described in more detail in Ref 1 - 3 .

In contrast, HDA coated samples exhibit a complete different behaviour. The first impression is that a corrosion attack is not visible even after test times of up to 10000 h as can be concluded from metallographic analysis. A SE image of a typical cross section is depicted in Fig. 1. This roughly concluded corrosion behaviour is evaluated from the smooth sample surface in the contact area to the Pb-17Li melt.

Furthermore, the Al treated surface shows a clearly structuring into two zones. A thin about 25 µm thick phase, which is separated by pores (Kirkendall effect) from a thick layer of roughly 100 µm. This layer has a smooth boundary to the steel matrix. The Al concentration detected by EDX analysis increases from this boundary line to near surface regions nearly linear to about 20 %, whereas in the surface scale values up to 40 % Al can be measured. From this EDX result and form XRD analysis it can be concluded that a thin $Al_2O_3$ scale may be formed on top of the sample, which protects the steel against Pb-17Li attack.

More detailed analytical work is required to understand the ongoing mechanisms and to clarify the Al profile in the surface near region versus time. Only this knowledge will lead to a better valuation of the protective scale characteristics. Nevertheless, the corrosion behaviour will be strongly influenced by the development of the coating process and the uniformity of formed scales.

The next step in testing the HDA coating and reaching a sufficient base for comparing RAFM steels will be the analytical work on EUROFER 97. First samples with a exposure time of 3000 h are now available.
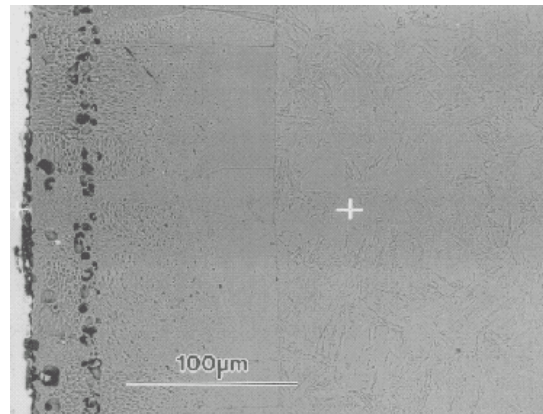


Fig. 1: Cross section of a HDA coated sample after 10000h exposure to flowing Pb-17LI
Right side:steel matrix
Left side: coating zone with adherent PbLi

Staff:

H. Glasbrenner
J. Konys
W. Krauss
Z. Voß
O. Wedemeyer

Literature:

[1] K. Stein-Fechner, J. Konys, H. Glasbrenner, Z. Voß: Tagungsbericht Jahrestagung Kerntechnik '99, 18.-20. Mai, Karlsruhe (1999), 677.

[2] K. Stein-Fechner, H. Glasbrenner, J. Konys, Z. Voß: EUROCORR 99, 30 August – 2 September 1999, Aachen, Germany.

[3] H. Glasbrenner, J. Konys, Z. Voß: J. Nucl. Mater., to be published.

# TTMS-005
# Rules for Design, Fabrication and Inspection

## TTMS-005/1
## Development and Assessment of Design Code

The objective of this task is the assessment and further development of a design code for blanket test modules (BTM) built from RAFM steels. The definition of additional rules, includes the results from several deliverables of this task, e.g. work on fracture mechanics concepts and creep-fatigue lifetime rules.

Verification of rules on representative models

The low temperature rules (LT) have been applied to three representative first wall models under thermo-mechanical loading including a disruption load pulling towards the plasma with 1MPa. Material data of F82H have been used. Some results: As an example, in Fig. 1 the decomposition of the stress intensity into primary and secondary membrane and bending as well as peak stress is depicted across a symmetry plane. Figure 2 shows the maximal stress intensity at the highest stressed locations as a function of the neutron wall load. Comparing these stresses to the design allowable value (more than 400 MPa) demonstrates the amount of conservatism for an anticipated neutron flux of 1 MW/m$^2$.
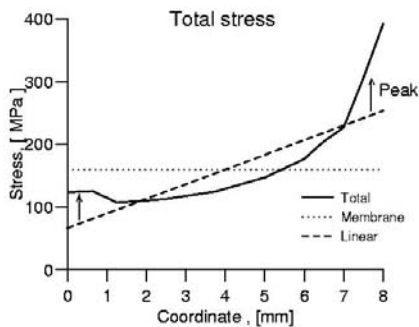


Fig. 1: Example for the application of SDC design rules to BTM first wall (decomposition of stress)

Identification of missing rules

Generally speaking, up to now no high-temperature (HT) rules exist in SDC (ITER Structural Design Code). The rules for monotonic loading could be directly adopted from LT. This does not hold for cyclic loading. Here new rules have to be developed. They have to account for fatigue, thermal creep and irradiation creep and their interaction.

The situation is as follows: Existing rules for creep-fatigue interaction are mainly based on knowledge from austenitic steels. Whether they might be applicable to RAFM steels depends on the mode of failure. For example, linear accumulation laws are not able to describe creep-fatigue interaction for the copper alloys under discussion for ITER. Or they other way round: If applied, the allowable lifetime is insufficient because of a too huge amount of conservatism.
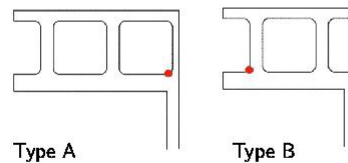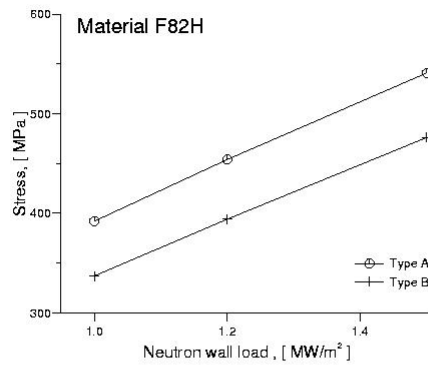


Fig. 2: Maximum stress intensity calculated for two BTM first wall as function of neutron wall loading

What is missing: first, a database from which rules can be deduced and, second, models for extrapolation and verification experiments.

Moreover, to reliably predict lifetime an integrated approach based on the different data-sets is required: (i) creep-fatigue results in terms of stress and strain, (ii) information on the microstructure from TEM and metallography, and (iii) fracture morphology from crack and micro-crack initiation and propagation monitored continuously during mechanical testing. With this in mind a three years integrated programme has been defined and will be started in 2002.

Staff:

E. Diegele
G. Rizzi

## TTMS-005/3
## Local Fracture Criteria for EUROFER in the Ductile-to-Brittle Transition Regime

### Objective

The objective of this subtask is the development and application of methods that enable the generation of design-relevant fracture mechanics material parameters on the basis of micro-mechanical failure models.

A characteristic feature of these models is the utilisation of an integrated (i.e. combined experimental and continuum mechanics) approach, which means extraction of material parameters for brittle or ductile fracture from (fracture) mechanics experiments by accompanying Finite Element stress analyses.

The main advantage of this so-called 'Local Approach' with respect to global failure criteria is the fact that a mechanism-based fracture description is combined with a numerical stress analysis. Geometrical size effects are thus already accounted for within this approach. Limitations of the local approach originate from different fracture mechanisms. Knowledge of fracture mechanisms is therefore essential, so that fractography invariably is an essential part of the evaluation of the experiments.

Local fracture criteria establish a link between metallurgy and mechanical engineering and they are currently being incorporated into design codes such as the R6 code of British Energy, where guidance on Local Approach methodology is included in the latest issue [1].

### Experimental results, fractography

Tensile tests on axisymmetrically pre-cracked specimens were conducted for transferability predictions of F82Hmod cleavage fracture. Pre-cracking was performed under rotation bending as shown in Fig. 1. A quantitative fractographic analysis of the fracture surfaces showed that - contrary to the results from notched tensile tests, where oxide inclusions could be identified at most of the fracture origin sites - oxide inclusions were found at only about 40% of the fracture origin sites and no cleavage fracture facets were observed. The fracture origin sites were located at a distance of about 150-400µm ahead the crack front [5].

For the analysis of EUROFER, tensile characteristics were determined at -150°C, -75°C and ambient temperature. A parametrized Hollomon-type stress-strain law in the form of $\sigma = K^* \varepsilon_{pl}^n$ for the dependence of true stress $\sigma$ from true plastic strain $\varepsilon_p$ leads to a slightly increased yield stress and a somewhat more pronounced hardening indicated by a slightly higher value of the strain hardening exponent n (see Table 1). Compared to F82Hmod, a slightly more pronounced yielding plateau is observed, especially at -150°C. For the subsequent analysis of the notched tensile specimens and the calculation of the Weibull stress, the parametrized law is used only to extrapolate beyond the range of strains that could be reached in the smooth tensile tests, whereas the lower strain range is modelled by linear interpolation of experimental results.
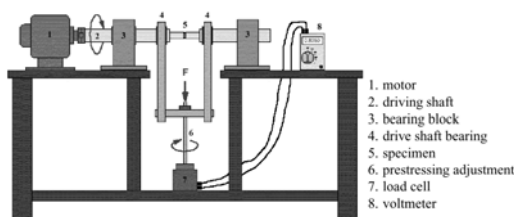


Fig. 1: Pre-cracking rig

Table 1:  Hollomon stress-strain law parameters

| T/°C | EUROFER97 | | F82Hmod | |
|---|---|---|---|---|
| | K/MPa | n | K/ MPa | n |
| RT | 880 | 0,08 | 820 | 0,07 |
| -75 | 1030 | 0,09 | 950 | 0,07 |
| -150 | 1290 | 0,09 | 1200 | 0,07 |

### Statistical inference and modelling

Based on the statistical evaluation of the cleavage fracture parameters from notched tensile tests, prediction of the local risk of rupture was performed for both notched and pre-cracked specimen geometries [2-4]. For the notched specimens that failed by pure cleavage fracture, fracture origin location distributions from experimental observations matched the predictions (Fig. 2). For the pre-cracked specimens, the predicted location of the fracture origins were confined to a small zone ahead of the crack tip (Fig. 3). The reason for the discrepancy between prediction and experiment has yet to be clarified.
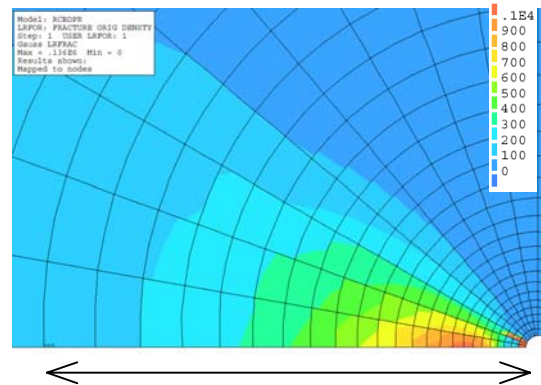


Fig. 3:  Fracture origin location prediction for pre-cracked specimen (length of arrow is 40 µm)

### Perspective

The local approach methodology provides a framework to apply fracture mechanics based design rules for RAFM steels in the spirit of R6 [1] or similar rules as currently developed e.g. in the framework of the European Structural Integrity Society (ESIS). Based on micro-mechanical aspects of fracture and transferability, it is a complementary approach to the master curve approach, whose emphasis is on engineering aspects of fracture characterization. Irradiation effects will be a subject of future investigations after generation of experimental data.

Staff:

E. Diegele
M. Klotz
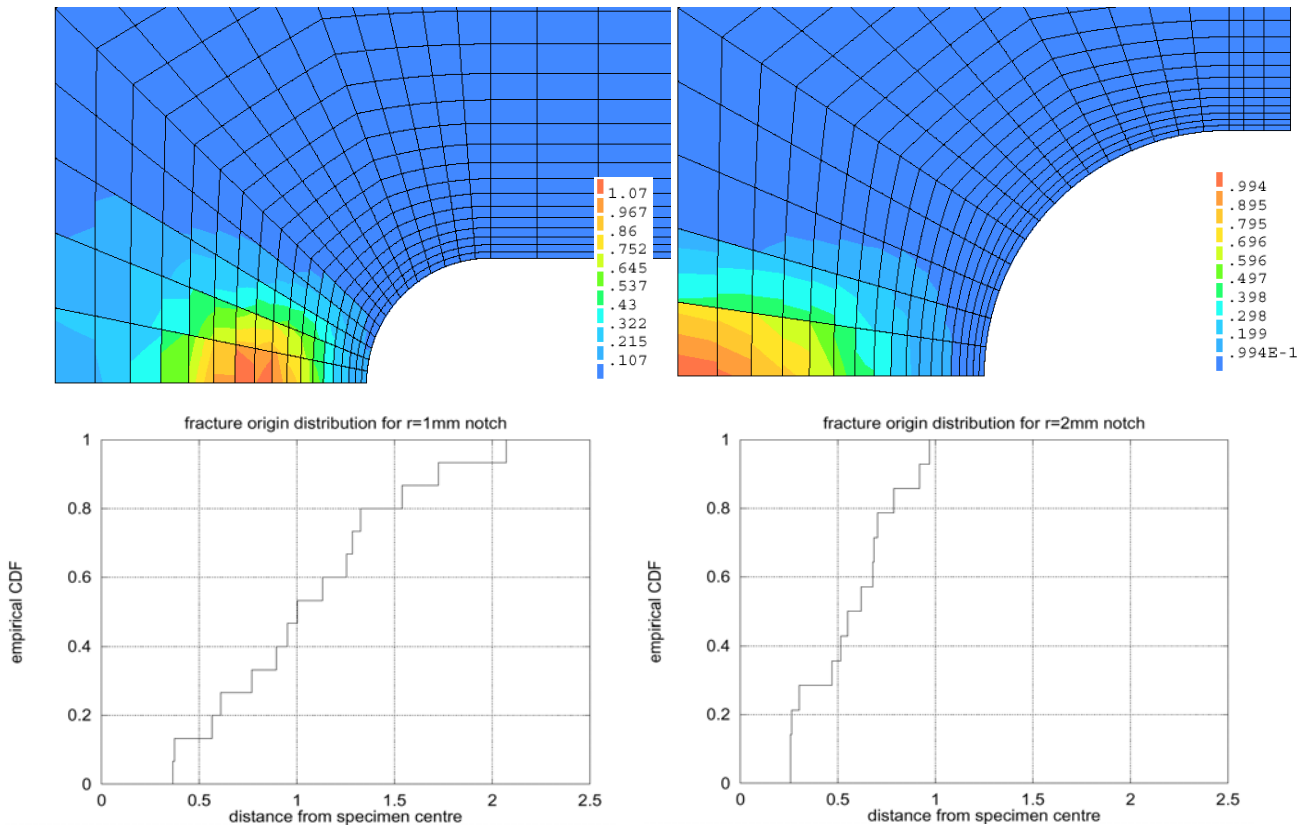C. Petersen
H. Riesch-Oppermann
G. Rizzi
M. Walter

Fig. 2:   Predicted (top) and observed (bottom) fracture origin location distribution

Literature:

[1]  British Energy Generation Ltd, Assessment of the integrity
     of structures containing defects R/H/R6, Rev. 4, 2001.

[2]  H. Riesch-Oppermann, M. Walter, Status report on
     experiments and modelling of the cleavage fracture
     behaviour of F82Hmod using local fracture criteria (Task
     TTMS-005), Report FZKA 6388, Forschungszentrum
     Karlsruhe, 2001.

[3]  H. Riesch-Oppermann, E. Diegele, Local risk-of-rupture
     predictions for notched and pre-cracked round bar
     specimens in the ductile-to-brittle transition regime,
     Charpy Centenary Conference - CCC2001, Poitiers, 2-5
     Oct. 2001.

[4]  H. Riesch-Oppermann, E. Diegele, Towards a micro-
     mechanical description of the fracture behaviour for
     RAFM steels in the ductile-to-brittle transition regime,
     ICFRM-10, Baden-Baden, 14-19 Oct. 2001

[5]  M. Walter, Mechanische und fraktographische Charakte-
     risierung des niedrigaktivierbaren Chromstahls F82H-mod
     im spröd-duktilen Übergangsbereich, Dissertation, Report
     FZKA   6657,   Forschungszentrum   Karlsruhe   (in
     preparation).

**TTMS-005/6**
**Creep-fatigue Lifetime Prediction Rules**

Structural materials of fusion reactors are subjected to complex creep-fatigue loading and high irradiation doses. Correct modelling of their deterioration is a precondition of a sufficiently reliable lifetime prediction procedure. For describing damage of RAFM steels under creep-fatigue conditions the continuum damage model ISRM (Inelastic Strain Rate Modified) presented in the recent literature was selected [1]. The ISRM model has been applied successfully to several high temperatures alloys, among others the austenitic steel AISI 316 L(N) in the pre- and post-irradiated states [2].

The ISRM model has been applied firstly to F82H-mod under isothermal cyclic loading at 450 and 550 °C. Its material and temperature dependent parameters were determined using creep and LCF data. The necessary measurements of damage evolutions under different loading conditions have been performed by identifying the acceleration of cyclic softening in the second half of lifetime as an indirect measure for damage. The measured damage evolutions, and therewith the damage mechanism, show a non-significant dependence on the loading amplitude. Accordingly linear accumulation of damage can be expected for loading with variable amplitude what has to be verified in additional suitable experiments (e.g. in two-step low-to-high and high-to-low cyclic tests).

In order to take into account the complex cyclic softening behaviour of F82H-mod when using the ISRM-model for lifetime prediction, the ISRM-model was coupled with the viscoplastic deformation model by Chaboche which had been modified for describing non-saturating cyclic softening. The parameters of the deformation model were determined for 550 °C and will be currently determined for 450 °C. The application of the models EUROFER 97 is intended within the next year when sufficient data will be available.

Staff:

Dr. J. Aktaa

Literature:

[1] J. Aktaa & B. Schinke, "The influence of the hardening state on time dependent damage and its consideration in a unified damage model," *Fatigue Fract. Engng Mater. Struct.*, vol. 19, pp. 1143-1151, 1996.

[2] J. Aktaa, M. G. Horsten & R. Schmitt, "Effects of hold-time and neutron-irradiation on the low-cycle fatigue behaviour of type 316-CL and their consideration in a damage model," in *Proc. of the 14th Int. Conf. on Structural Mechanics in Reactor Technology*, Lyon, Aug. 1997.

**TTMS-005/7**
**Small Scale Specimens Validity by Analysis**

For irradiation application in high fluence devices the development of small sized specimen is required for several reasons. Either CT-specimens or notched bending bars are foreseen for the determination of fracture mechanical parameters (e.g. fatigue crack growth and fracture toughness). For miniaturized specimens the application of standard procedure (e.g. ASTM 813) for the evaluation of fracture mechanical parameters in the ductile region is doubtful. There is a need to find the limits of reliable transferability of results gained from experiments using small scale fracture mechanics specimens.

In detailed analyses five CT specimen of different size and four bend-bar specimen types (from standard size down to specimens with less than 1% in volume of standard CT) have been investigated. Elastic-plastic analysis fracture mechanic was performed and the J-integral values were compared.

It was recognized, that objectives of the development of miniaturized fracture mechanics specimens have to be critically reviewed and new objectives for the EFDA Technology programme have to be formulated.

Part of this task was dedicated to define the objectives of a meeting held on September 24th at the Karlsruhe Research Center. In particular, it served as input for the discussion during this meeting and guided a proposal for the work to be performed in the forthcoming years, which is an integrated approach of experimental work, metallographic monitoring of failure modes, and, as the main part, modelling including parameter identification and predictions for verification experiments.

Results for the five CT specimens will be discussed in the following. The size is referenced by E for the standard type and H or Q for a reduction in width by a factor of 2 and 4. As a starting point, the elasic-plastic fracture mechanic parameter (J-integral) was determined. In a first step, a standard model of metal plasticity (Ramberg-Osgood law) was used with 4 different hardening coefficients N (3, 5, 10, 20) simulating modest to very strong strain hardening conditions. The results for two models (N=5 and N=10) are shown in Figs. 1 and 2, repectively. The results have been normalized in both in the loading (by geometry factors) and in J (to the a plane-strain condition of a very thick specimen). It is shown that the results are scalable for a material with weak strain hardening (N=5). However, for materials with strong hardening, the transferability is limited for smaller specimens by a different failure mechanism. It this case the ligament completely plastifies and the component is predicted to fail by plastic instability instead of crack growth.
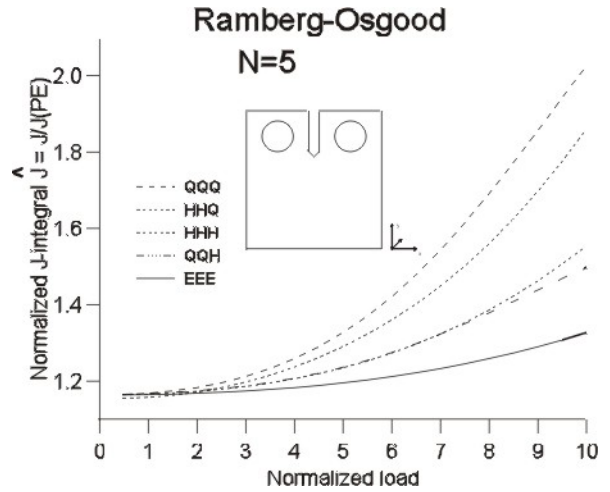


Fig. 1: Normalised J-Integral values for different size of CT specimen for Ramberg-Osgood material law with N=5
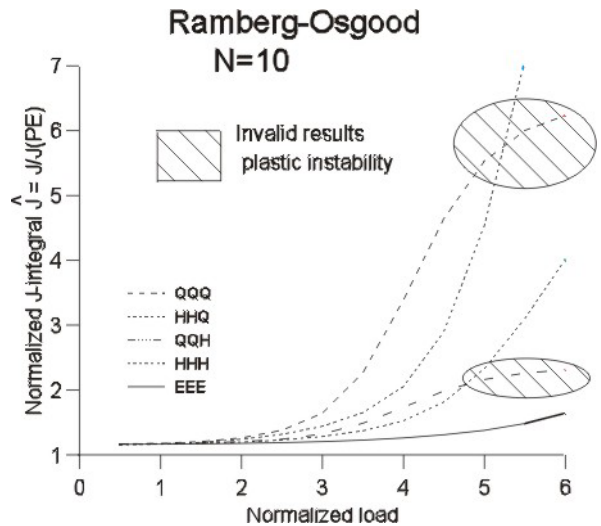


Fig. 2: Normalised J-Integral values for different size of CT specimen for Ramberg-Osgood material law with N=10 indicating regions where results are not ransferable

Staff:

E. Diegele
G. Rizzi

# TTMS-006
## Qualification of High Performance Steels

## TTMS-006/2
## Metallurgical and Mechanical Characterisation of Existing ODS Alloys

The efficiency of future fusion power plants is strongly dependent on the operating temperature. Presently considered conventional RAFM steels for structural applications limit the operating temperature to around 550 °C. Oxide Dispersion Strengthened (ODS) materials would allow to increase the operating temperature by about 100 K. Reduced activation ODS steels are not available commercially at present. As a first step in developing a RAFM-ODS-Steel an existing 9%CrWVTa-RAFM steel, called EUROFER 97 was chosen as base material.

Two variants with different $Y_2O_3$-contents (0.3 and 0.5 wt-%) have been produced by experienced industrial manufacturers. The production process included inert gas atomisation of EUROFER (H. C. Starck) and subsequent mechanical alloying in industrial ball mills by PLANSEE. Special emphasis was laid on low gas contents during all fabrication steps; e.g. the oxygen content, which is of some importance for the properties of the consolidated material, could be kept below 200 appm, Hot Isostatic Pressing (HIP) was chosen as the appropriate consolidation process for the production of bars with 60 mm in diameter and 300 mm in length. The Hipping process is regarded as the most promising production route for nearly end-shaped structures for future fusion reactors.

The microstructural characterisations of the different powders and consolidated materials in different heat treatments using optical microscopy, SEM and TEM and X-ray diffraction treatments have been continued. Apart from few exceptions the material is quite homogenous in its structure, the Yttria particles, which are among others responsible for the strengthening of ODS-EUROFER are statistically distributed. The observed particle size ranges from 4 to 40 nm with a mean size of 12 nm. A crystallographic orientation relation between the smaller particles (~4-6 nm) was found.

Miniaturised specimens with 2mm in diameter and a gauge length of 7.6 mm were fabricated from the as-received bars and subjected to tensile tests in the temperature range between RT and 850 °C. Yield strength and ultimate tensile strength of the ODS-EUROFER (0.5 wt-% $Y_2O_3$) are raised by 50% and more, compared to the non-ODS RAFM steels like EUROFER 97 and F82H mod. (see Fig. 1). This gain in strength is still persisting at elevated temperatures. The uniform elongation of the ODS material is superior to that of common RAFM steels, whereas the total elongation above 400 °C is lower, but remains always above 6%, what is not unusual for this type of alloys.

First creep tests at temperatures of 600, 650 and 700 °C up to test times of 4000 hours confirm the superior creep behaviour of ODS-EUROFER. It exhibits a similar creep and creep strength as RAFM steels but at temperatures 100 °C higher.

The results of first impact tests reveal a similar impact behaviour as comparable ODS alloys, but the Ductile-to-Brittle-Transition-temperature (DBTT) is substantially higher than that of EUROFER 97.

Preliminary results of low cycle fatigue tests on the same type of specimens as used for the tensile tests, show the good LCF-behaviour of ODS-EUROFER. Compared to F82H mod. no cyclic softening, a lower plastic deformation, a substantial higher stress amplitude at a given strain and a higher lifetime can be observed.

The effect of precipitates on work hardening, tensile ductility and impact behaviour of carbon and high nitrogen martensitic 7-12Cr as well as particle strengthened ODS-(9-13)Cr steels have been analysed by models. In accordance to the predictions work hardening and uniform as well as fracture strain generally decrease hyperbolically with increasing yield strength. Pronounced precipitations caused by increasing N and C content or fine $Y_2O_3$-dispersions in ODS-(9-13)Cr steels well-markedly increase work hardening and uniform ductility but decrease fracture strain and upper shelf energy of impact tests. The latter is additionally enhanced by induced localised deformation above 250 °C which reduces ductile fracture stress. The strength-induced increase of ductile-to-brittle transition temperature of ODS-steels observed in Charpy tests, however, is comparable to that observed by irradiation defect strengthening. Work hardening and uniform ductility do not disappear in ODS-steels below yield strengths of about 1500 MPa at RT.

The work on the mechanical behaviour (tensile, creep, impact) will be continued. Further studies are necessary to understand the deviating transformation behaviour compared to conventional RAFM steels with similar composition. This includes the determination of relevant physical properties and the creation of a continuous cooling transformation diagram. Complementary microstructural examinations shall complete the knowledge.
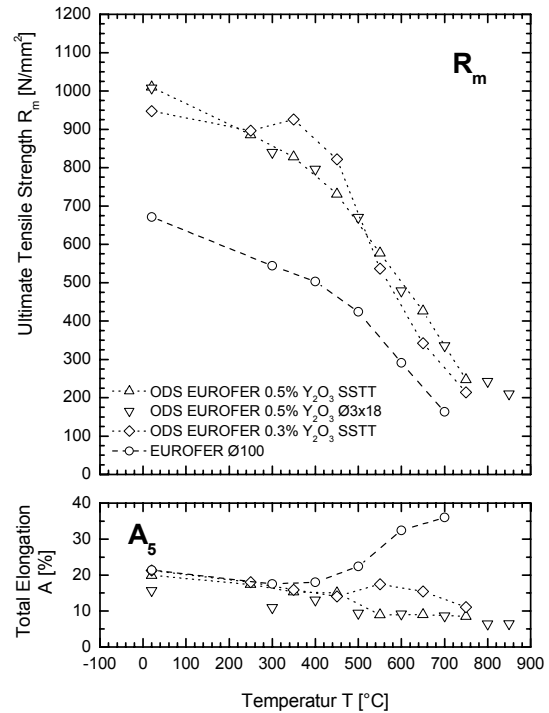


Fig. 1: Ultimate Tensile Strength and Total Elongation of different ODS Alloys compared to EUROFER 97

Staff:

S. Baumgärtner
G. Bürkle
B. Dafferner
P. Graf
M. Klimiankou
R. Lindau
A. Möslang
D. Preininger
M. Schirra
H. Zimmermann

# TTMA-001
## SiCSiC Ceramic Composites

### TTMA-001/11
### Modelling the Damage Behaviour of SiC/SiC

The aim of this activity is to describe the deformation and damage behaviour of SiC/SiC. It includes modelling and experimental investigations on both, the macro and micro scale. The final goal is to have design rules and predictive lifetime models at hand within a time span of decade. This task will be funded in the materials programme under TTMA-001 deliverable 11 starting in 2002.

Within 2001, basic development was performed in the modelling and the experimental part of the task.

**Micro-mechanical modelling**

In a first approach the model should describe the global deformation behaviour using local material data as the elastic constants of fibre and matrix and parameters characterising the interface, e.g. friction coefficients. Starting point is a 2D model with a regular arrangement of fibres. This model was enhanced to describe non-regular arrangements of fibres by including stochastic geometry (Voronoi-tessalation). The work up to now includes simply modelling without determination of model parameters. This will be started as soon as enough material is available from the next European SiC/SiC charge.

**Experimental:**

a) Experimental set-up:

For high-temperature strength and toughness measurements on SiC-ceramics a completely new test device was designed containing a furnace (up to 1200°C) and a vacuum chamber.

b) Development of test samples:

Various failure modes are responsible for failure and finite lifetimes of SiC/SiC materials. *Spontaneous* failure occurs when the applied stress reaches the strength of the material or, in terms of global fracture mechanics, when the stress intensity factor $K_I$ exceeds the fracture toughness $K_{Ic}$ for the most severe local crack in a component. In case of ideally brittle materials, the fracture toughness is independent of the crack extension and, consequently, identical with the stress intensity factor $K_{I0}$ necessary for the onset of stable crack growth. A test method was developed, which enables to determine R-curves from *completely stable* crack propagation tests. The experimental set-up is shown in Fig.1. Pre-notched bending bars are monotonously loaded. From a load vs. time record, the moment of first crack extension can be detected as a pop-in of the load. After a further increase of load, the test is suspended. After unloading, the actual crack length can be measured at the side surfaces using an optical microscope. From the applied load $P$ at the moment of unloading, the crack depth $a$ and the geometric function $Y$, the stress intensity factor $K_{IR}$ present at the moment of unloading, can be computed. A series of tests suspended at different loads then provides the R-curve $K_{IR} = f(\Delta a)$. First measurements were performed so far on conventional ceramics.
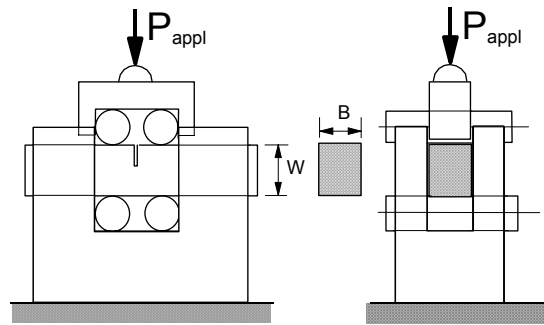


Fig. 1: Device for a 4-roller crack extension test

Staff:

E. Diegele
T. Fett
G. Rizzi

# Neutron Source

**TTMI-001**
**IFMIF-Accelerator Facilities**

## I. Ion Source

### I.1. Plasma investigation and optimisation of volume source for IFMIF

The IFMIF scenario requires a $D^+$-source, delivering a 140 mA deuterium beam in cw-mode with a $D^+$ fraction of above 90 % and a normalized rms-emittance of $0.1\pi$ mm mrad at the end of the LEBT. Within the IFMIF study the *Institut für Angewandte Physik* at the University of Frankfurt has developed a high current proton/deuteron ion source. The Frankfurt 200mA proton source belongs to the HIEFS volume type family and fulfills the requirements for the IFMIF project [1]. The ion source delivers 200mA $H^+$ (corresponding to 141mA $D^+$) @55keV with an $H^+$ fraction of 93% in continuous wave [2].

This report summarizes the results of basic plasma investigations performed on this source. Using an energy analyzer the energy distributions of the ions and electrons as a function of different discharge parameters were measured. Based on these investigations fundamental plasma parameters like the plasma wall potential, the electron and ion temperature are derived. Furthermore, the influence of a transverse filter field on the plasma characteristics is shown.
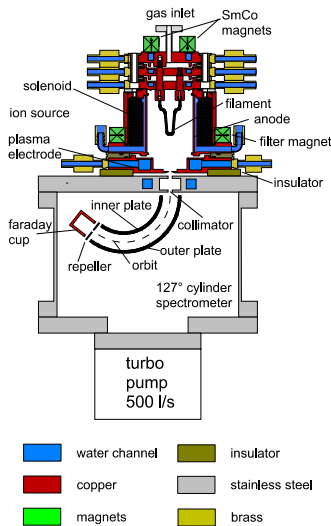


Fig. 1: Experimental setup: ion source and energy analyzer, not in scale

Fig.1 shows a schematic cross-sectional view of the experimental setup. As energy analyzer served an electrostatic 127 cylinder spectrometer with a relative energy resolution of 0.5%. The diameter of the entrance hole is 1mm, the radii of the inner and outer plate are 50mm and 75mm, respectively. At the exit of the spectrometer a slit aperture of 1mm height is installed, followed by a screened faraday cup. A detailed description of the spectrometer and the ion source is given in.

**Ion Energy Distribution**

First, the ion temperature was estimated by means of the measured ion energy distributions. Fig. 2 presents a typical ion energy distribution for an input power of 10kW, a gas pressure of 30Pa and a filter field strength of 15mT. These are optimal source parameters for the extraction of an 200mA proton beam. Moreover, in this operation mode the $H_2^+$- respectively the $H_3^+$

fraction of the ion beam is below 4%. In order to estimate the ion temperature, a suitable Maxwellian fit for the measured ion energy distribution was calculated.

Fig. 2 illustrates the measured ion energy distribution and the calculated Maxwellian fit for an ion temperature of $kT_i$=0.5eV. The height of the Maxwellian distribution was scaled to the height of the measured distribution. A comparison of the half high widths and the high energy tails of both measured and calculated curves, shows that the ion temperature is about $kT_i$=0.5eV. Taking into account the two factors which are responsible for an increase of the energy spread of the measured curve (resolution of the analyzer, gradient of the plasma potential) the ion temperature can be estimated to $kT_i$<0.5eV, a very low value for ion sources.
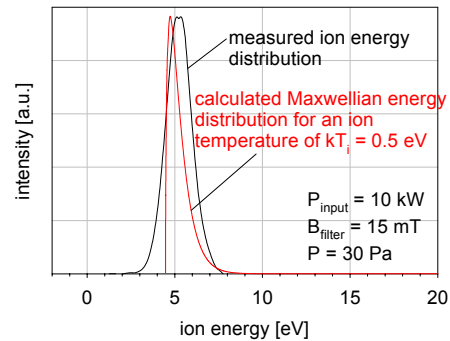


Fig. 2: Comparison of the measured and calculated ion energy distribution in order to estimate the ion temperature

Please note, that the measured mean ion energy of 5.2eV in Fig. 2 is not the mean energy of the ions in the plasma. While leaving the plasma, the ions have to cross the plasma wall potential, leading to an energy of $eU_{PW}$. Within the plasma the ions have only a thermal energy distribution.

**Electron Energy Distribution**

In Fig. 3 the influence of the gas pressure on the ion energy distribution was demonstrated. Therefore, it was a point of interest to investigate the influence of the neutral gas pressure on the electron energy distributions also. As the gas pressure was changed from 0Pa to 30Pa, it was not possible to keep the input power constant. Consequently, with increasing gas pressure the arc current rises too. The spectra were taken in operation without the magnetic filter, in order to detect electrons which were emitted from the filament. The arc voltage was kept at 75V. Fig. 3 presents the result of these investigations.
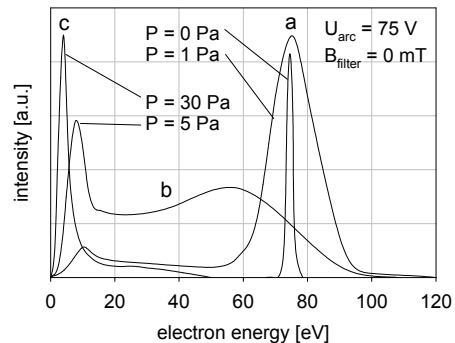


Fig. 3: Electron energy distribution as function of different gas pressures (arc current) at low input powers

According to their mean energy, the electrons energy distributions can be divided into three groups of electrons: high (a), middle (b), and low (c) energy electrons. Without any neutral

gas (the arc is off) there are only high energy electrons with a mean energy corresponding to the applied arc voltage of 75V. These electrons are generated at the filament and accelerated to the plasma chamber or plasma electrode without any interactions. In this operation mode, the mean free path is in the range of the plasma chamber dimension.

For a glow discharge ($P$=1Pa, $P_{input}$=~10W) the energy spread of the high energy electron peak rises because of inelastic and superelastic collisions. Moreover middle (b) and so-called bulk electrons (a) are registered. These are electrons from the filament, which are decelerated due to inelastic interactions with other plasma particles respectively electrons which are generated in the plasma.

The higher the gas pressure, i.e. the arc current, the more middle energy and bulk electrons are observed. At a gas pressure of 30Pa and an input power of about 2kW, more than 80% of the electron population consists of bulk electrons. Only a small fraction of middle energy electrons are detected, high energy electrons are thermalized in the plasma respectively filament electrons do not achieve high energies due to frequent inelastic collisions with other plasma particles.

That means, the mean free path respectively the mean energy of the electrons is affected by the neutral gas pressure and the plasma density. It is remarkable, that a gas pressure of 30Pa (at the gas inlet!) reduces the electron energies to such low values even in operation without filter magnet. Consequently, for an operation with typical arc powers (10kW) and typical source pressures (30Pa), only a small filter field flux density is necessary to prevent the high energy tail of the energy distribution
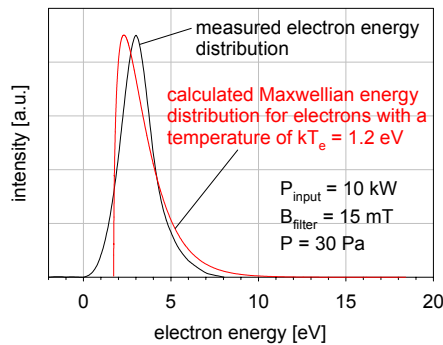


Fig. 4: Comparison of a measured and calculated electron energy distribution in order to estimate the electron temperature

In a further step the electron temperature was estimated with a Maxwellian fit as performed in case of the ion energy distributions. Fig. 4 presents a typical measured electron energy distribution and a suitable Maxwellian fit for an assumed electron temperature of $kT_e$=1.2eV.

The low electron temperature even in operation with full arc power is the basis for a low ion temperature in the plasma. Otherwise the ions in the plasma are heated by means of "Coulomb heating" with hot electrons. This is a big advantage of arc discharge sources compared to ion sources with an rf coupling for plasma generation. In such ion sources the electron temperature is considerably higher as well as the beam emittance.

**Magnetic Filter**

The magnetic filter is a key element for production of a nearly pure proton (deuteron) beam. Therefore, it is important to investigate its influence on the ion and electron energy distribution.

Fig. 5 displays the electron energy distribution for three different filter field strengths. An analysis shows that the magnetic filter has two main influences. First, it reduces the electron temperature and second, in operation with optimal filter field strength only low energy electrons (bulk electrons) are detected.
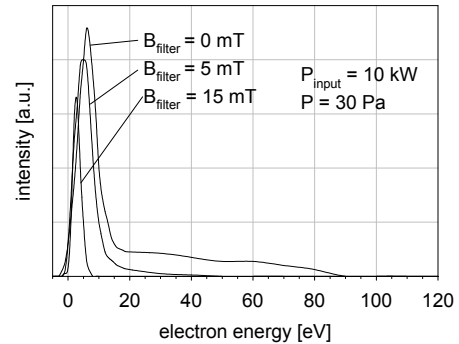


Fig. 5: Electron energy distribution for different magnetic filter field strengths

The reduction of the electron temperature can be qualitatively seen on the decrease of the energy spread with increasing filter field strength. At a filter field strength of 15mT the energy spread of the bulk electron peak is 2eV only, compared to an energy spread of 10eV in operation without the magnetic filter. The influence of the filter field strength on the electron temperature was also observed, studying the positive ion energy distributions (not presented in this paper). In operation with the optimal filter field strength the plasma wall potential is about 0.7V lower than in operation without the magnetic filter.

The influence of the filter field on the high energy tail of the distribution is obvious in Fig. 5. Without any filter field, high energy electrons are detected with energies up to 88eV (arc voltage = 85V). With increasing filter field strength the area of the high energy tail decreases. That means, energetic electrons from the filament or the region around the filament are thermalized. At a filter field of 15mT no high energy electrons are measured.

The effect of the magnetic filter can be understood in the following way. By means of the transverse magnetic field electrons are forced on bend paths. Consequently, the covered distance between two points in the plasma is increased and so the probability for inelastic collisions with other plasma particles. Due to the higher number of inelastic collisions the mean electron energy as well as the electron temperature are reduced. The influence of the filter is stronger the more energetic the electrons are. If the electron energy drops down below the lowest excitation energy, the filter has only a weak influence.

By means of this investigation it could be demonstrated that a filter field flux density of 15 mT is strong enough to keep the mean electron energy below 10 eV, an optimal energy for a high proton (deuteron) yield in the plasma. A higher field strength is not necessary because it would lead to a beam deflection in the extraction system only.

**Summary**

For IFMIF, the Institut für Angewandte Physik developed a high brilliant 200mA proton (deuteron) source (corresponding to 141mA D$^+$) with a H$^+$-fraction of 93%. Operating the source in cw-mode a current density of 400mA/cm$^2$ was achieved.

In order to get an optimal beam performance basic plasma investigations on this source have been performed. From the measured ion energy distributions an ion temperature of smaller than 0.5 eV has been derived. Such a low ion temperature is an excellent basis for a low ion temperature in the beam, which is favorable for a low beam emittance. An analysis of the ion and electron energy distributions for different source pressures shows that a pressure of 30Pa is sufficient to prevent a distinctive high energy tail of the ion energy distribution.

The electron temperature in the plasma could be estimated to values of 1.2eV for full source power. Consequently, there is hardly a heating of the ions by means of the electrons. This is also an important precondition for a low beam emittance. Furthermore, for arc powers between 5 and 10kW, the mean electron energy in the plasma is almost constant. This guaranties an optimal mean electron energy (5 – 10eV) for a plasma generation with a high proton (deuteron) yield.

To find the optimal filter field flux density the influence of the magnetic filter on the electron energy distribution has been studied. It has been found that a filter field flux density of 15mT is necessary to prevent a distinctive high energy tail of the electron energy distribution, a substantial condition for a high proton (deuteron)yield in the plasma and a small beam deflection.

Literature:

[1] A.Möslang, IFMIF-International Fusion Materials Irradiation Facility-Conceptual Design Evaluation Report, A Supplement to CDA by the IFMIF Team, Karlruhe, 1999

[2] R.Hollinger, P. Beller, K.Volk, M.Weber, H.Klein, *The Frankfurt 200 mA Proton Source*, Rev. Sci. Instrum., 71, Volume II, 836-838, 2000

## II Multi-Particle Calculations from Source to RFQ

### II.1. Introduction

The **I**nternational **F**usion **M**aterial **I**rradiation **F**acility (IFMIF) requires a 250 mA continuous current of deuterons at a nominal energy of 40 MeV, with provision for operation at 30 MeV and 35 MeV. The basic layout provides two linacs modules, each delivering 125 mA to a common target.

The accelerators starts with a deuteron ion source and a low energy beam transport to a radio frequency quadrupole (RFQ), buncher and preaccelerator up to ~5 MeV. The **L**ow **E**nergy **B**eam **T**ransport (LEBT) line from the ion source to the RFQ must perform beam steering and focussing, complicated by the presence of strong space charge forces within the beam.

The beam behaviour in LEBT sections is dominated by space charge forces. Therefore space charge fluctuations (e.g. source noise, typically 1-5% below 10MHz) can drastically influence the beam transport. Beam losses and emittance growth are the most seriuos problems.

For space charge compensated transport no major influence on beam transport is expected from fluctuations below a cut-off frequency given by the production rate of the compensation particles. Above this frequency the fluctuations can not be compensated totally, but particle production and redistribution of the compensating particles reduce the influence of the fluctuations.

Transport simulation for the IFMFIF injector including space charge fluctuations (+- 2% at frequencies from 20kHz up to 0.5 GHz) were done for magnetic and electrostatic transport systems [1]. For electrostatic systems the largest growth of the time integrated emittance has been found (77% at appr. 50% degree of lense filling). The investigations had shown, that electrostatic focussing is not sufficient for IFMIF. Space charge compensated transport showed better results (44% for solenoids below a current fluctuation frequency of 20KHz at 50% degree of lense filling) [1].

Therefore at the **I**nstitute of **A**pplied **P**hysics (IAP) magnetic LEBT line are investigated. Thus strong inner beam forces can be handled by the use of the advantages of space charge compensated beam transport.

The IFMIF scenario provides a 140mA $D^+$-source with a normalized rms-emittance of 0.2 $\pi$ mm mrad at the end of the **L**ow **E**nergy **B**eam **T**ransport (LEBT) line. An 140 mA $D^+$ ion beam @ 50 keV/N has a generalized perveance of 0.0041. Production and transport of ion beams of such high perveance (high current, low energy and high beam quality) are very important for future accelerator systems, in particular for the IFMIF project.

In 1998/99 a new high current ion source has been developed and tested. This ion source is of volume type and delivers 200 mA $H^+$ (corresponds to 140 mA $D^+$, according to the Child Langmuir law) in continuous wave operation with a $H^+$ fraction of about 93 %. A triode extraction system was used with an aperture of 8 mm in diameter and was designed for voltages up to 55 kV. For the following accelerator system (RFQ) it is necessary to postaccelerate the 55 keV proton beam to an energy of 100 keV. Therefore a new so-called tetrode system has been designed and investigated.

For the design of a transport system, which reaches the requirements of the RFQ, substantial simulations of beam dynamics in the LEBT system are required.

Simulation of ion beam extraction from the source have been performed using the IGUN code. Simulations of the transport from the ion source to the RFQ-system were done using the **Lin**ear **Tra**nsport simulation code LINTRA [2] for different scenarios of space charge compensation.

This report summarize the results of the beam transport investigations performed with LINTRA. This investigations helps to get a better understanding of the beam dynamic of a compensated transported ion beam and shows the requirements of the LEBT which fulfils the IFMIF requirements.

### II.2. Low energy beam transport calculations

The tetrode system consists of a plasma-, puller-, screening-, and ground - electrode. The used extraction system has an aperture of 8mm in diameter. By use of a puller electrode between plasma- and screening electrode, the postaccelerating system yields beam energy up to 100keV.

Calculations of the emittance of a 140mA @ 100keV $D^+$ - beam, extracted from the ion source (figure 1) were done using the IGUN code. The ion extraction was calculated for the matched case. At the entrance the beam has a radius of 2.9mm, a divergence angle of 35mrad and an emittance of 0.0497 $\pi$ mm×mrad. This is much smaller than the IFMIF requirements of 0.2 $\pi$ mm×mrad.

The emittance of a 140mA @ 100keV $D^+$ - beam calculated by IGUN has been taken as entrance emittance for further simulations of beam transport from the ion source to a following acceleration section (RFQ) using LINTRA.

## II.3. Magnetic (space charge compensated) transport

The LINTRA code was improved to take space charge effects into account. Using LINTRA calculations of beam dynamics of 140mA, 100kV $D^+$ ion beam have been done. Simulations of beam transport from the ion source to the RFQ accelerator using a magnetic LEBT section were performed for three different scenarios to take space charge effects into account:

A: A global space charge compensation of 90% through the whole LEBT.

B: A global space charge compensation of 90% except a decompensated drift section of 30mm at the end of the LEBT system to simulate the entrance into the RFQ - field.

C: A space charge compensation of 90% in the drift sections and a decompensated drift section at the end of the LEBT system was assumed. In contrary to case B no global distribution of the compensation electrons was assumed in the solenoids, instead a concentration of the electrons on the beam axis within a cylinder of 10mm radius was used for the simulations (in agreement with measurements).

All results of the simulation are compared with the RFQ acceptance, drawn in as ellipse in the following plots. Figure 1 shows the envelope of an 140mA @ 100kV $D^+$ - beam transported through a magnetic LEBT section under conditions of scenario A using the illustrated entrance emittance calculated by IGUN. The plotted ellipse shows the input emittance taken for the beam dynamics calculation in the RFQ.

The results show a growth of the normalized 100% RMS - emittance of 34% in the transport line. At the LEBT exit the focused ion beam has a radius of 1mm.
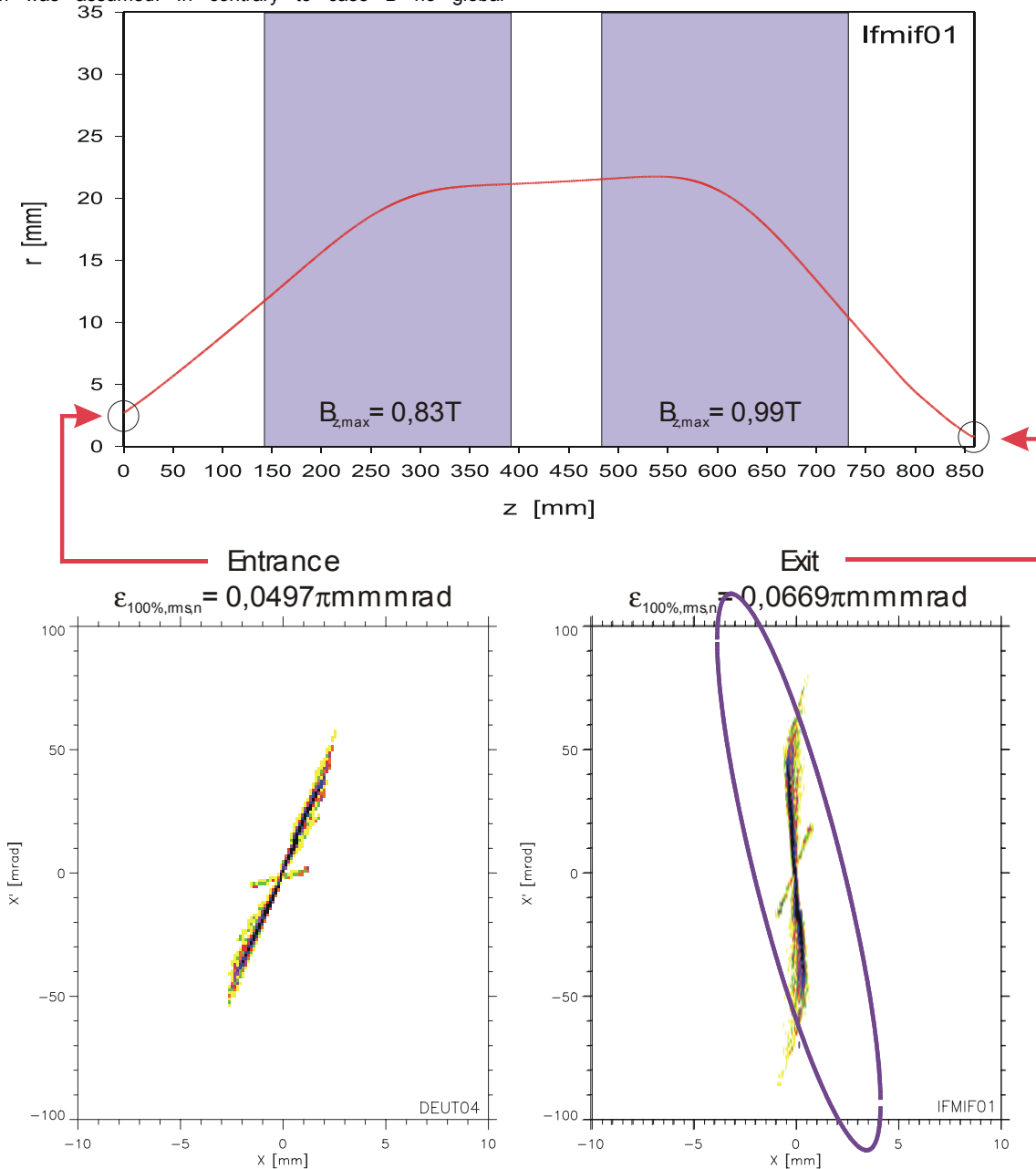
Entrance
$\varepsilon_{100\%,rms,n} = 0,0497\pi mmmrad$

Exit
$\varepsilon_{100\%,rms,n} = 0,0669\pi mmmrad$

Figure 1: LINTRA simulation of the transport of a 140mA@ 100kV $D^+$ - beam for scenario A
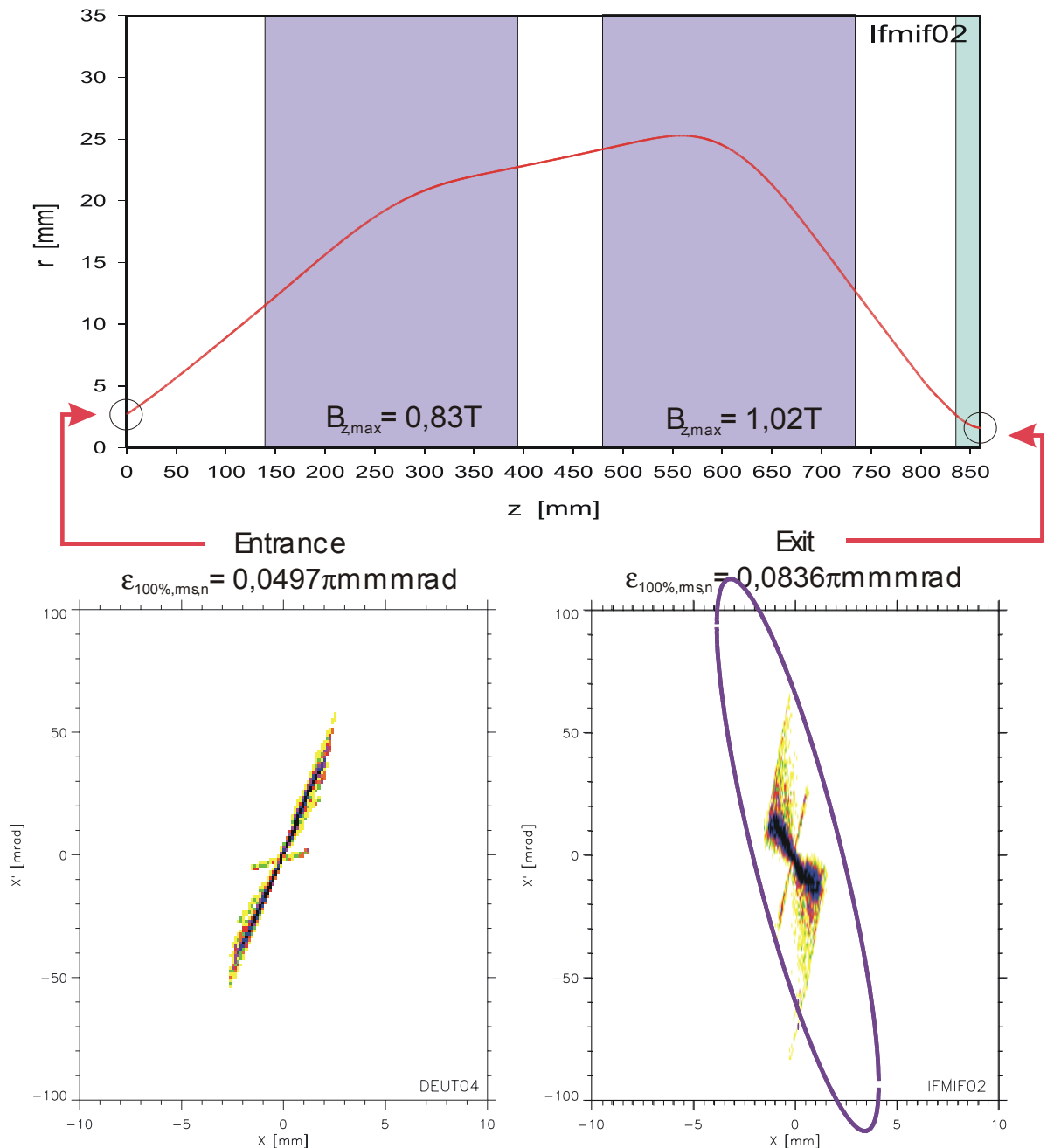
Figure 2: LINTRA simulation of the transport of a 140mA@ 100kV D$^+$ - beam for scenario B

Figure 2 shows results of simulations gained from the LINTRA code under assumption of a global compensation degree of 90% and a decompensation drift section of 30mm at the end of the LEBT system to simulate the entrance of the RFQ structure (scenario B).

The values given by the calculation have slightly higher beam radius and angle (10-20 % deviation).This might be caused by the higher resolution of the CCD chip compared with the conventional detector. Therefrom and due to the numerical errors typical for differential methods the RMS values are greater too. The values concerning the compensation degree are in good agreement with the measurements. The lower values might be explained by improper separation of space charge and emittance effects and are also explaining the smaller pattern.

The simulation shows an emittance growth of 68% due to the transport. The increase of the emittance growth in comparison to scenario A is effected by the decompensation due to the electrical field of the RFQ accelerator. Particularly a change of the shape of the emittance can be observed.

Further on the radius of the focused ion beam increases up to ~3 mm at the LEBT exit. The longitudinal shift of the focus was corrected by a slight increase of the magnetic field strength of the second solenoid.

Figure 3 shows results of simulations gained from the LINTRA code under assumption of scenario C. A homogeneous electron density distribution in the solenoids with $\rho_E = \rho_I$ for r<10mm and $\rho_E = 0$ for r>10mm was assumed.
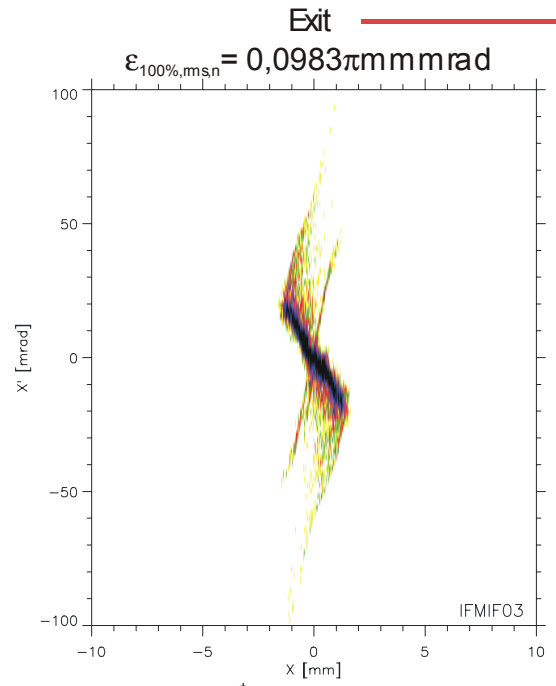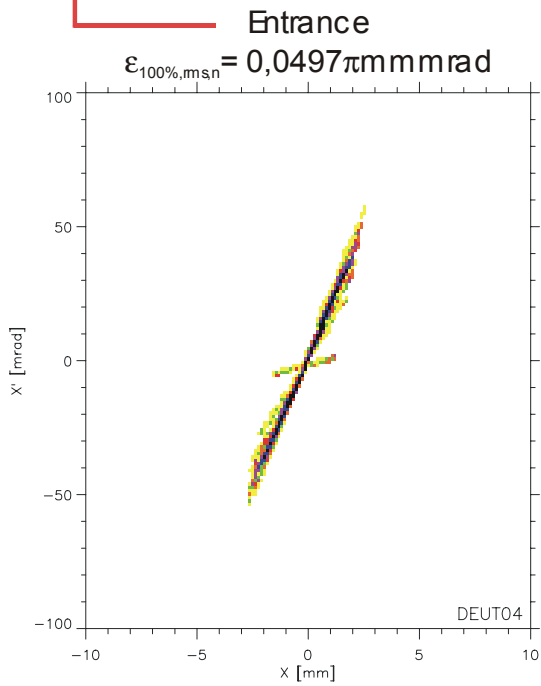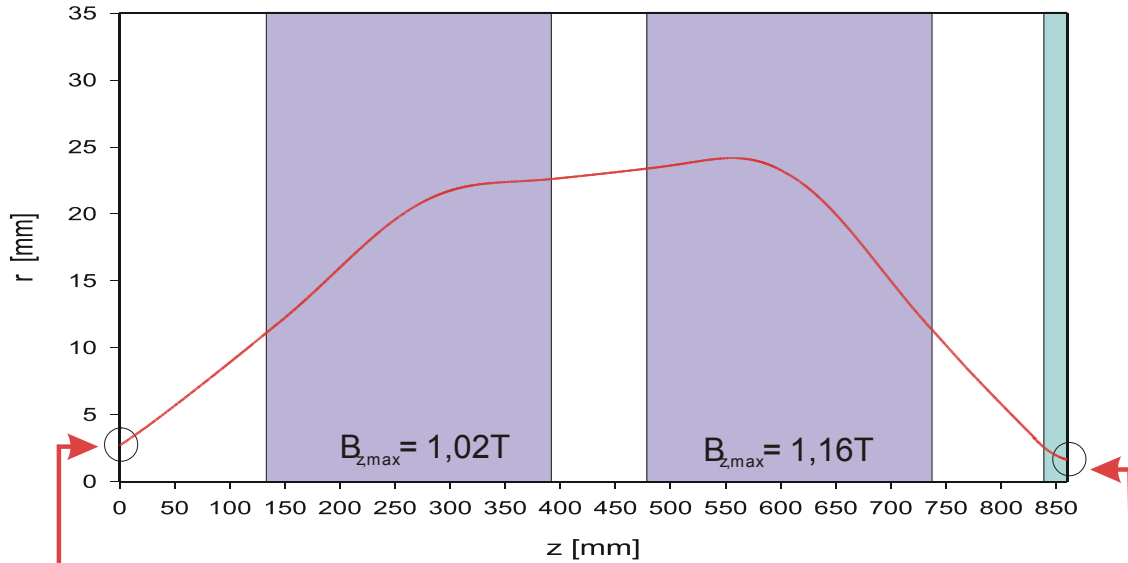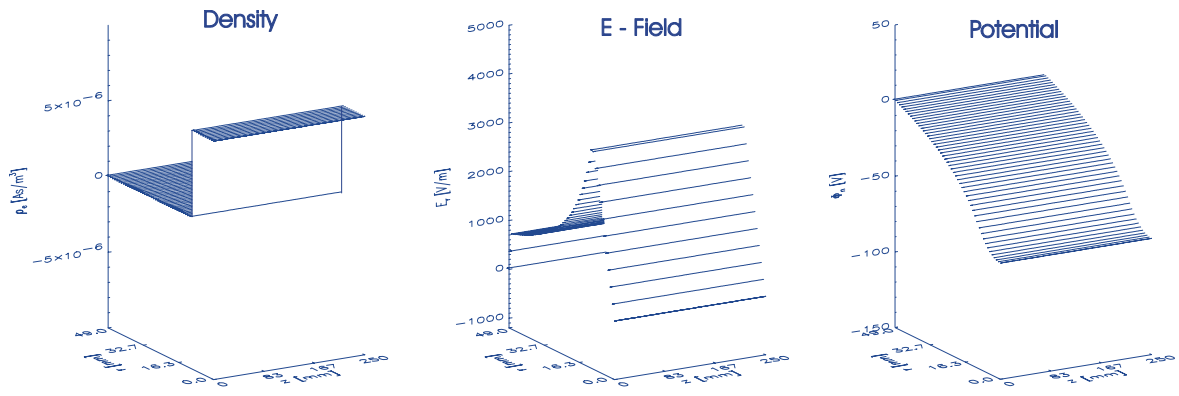
Figure 3: LINTRA simulation of the transport of a 140mA @ 100kV D$^+$ - beam for scenario C

The first three graphs in figure 3 show the assumed electron density, the electrical field and the potential of the electron cloud from beam axis to the wall of the beam transport tube.

The simulation for scenario C shows a growth of the normalized 100% RMS - emittance of 98%, this is a 30% higher growth than calculated for scenario B.

The normalized 90% RMS - emittance at the LEBT exit calculated for scenario B is 0.0571 $\pi$ mm×mrad, the simulation for scenario C yields 0.0590 $\pi$ mm×mrad, this is a difference of 3.3%. In contrary the corresponding 100% RMS – emittance values shows a difference of 17.6%. Thus mainly edge particles contribute to the increasing emittance growth.

The addittional emittance increase is effected by modifications of the compensation conditions in the LEBT section from a global compensation degree in the drift section to a compensation state stemming from the electron cloud in the solenoid. Further on particularly the ions at the edge of the beam see the changing compensation state inside and outside the beam.

### II.4. Conclusion

Calculations for magnetic beam transport were done taken space charge compensation effects into account. Beam dynamic, particularly emittance growth was investigated. For this simulation for three different scenarios (global compensation degree, global compensation degree with a decompensated drift section, global compensation degree with a decompensated drift section and electron distribution in the solenoids) were done. The calculations show the dependence of emittance growth from the state of compensation. Particularly a change of the compensation conditions yields an increasing emittance growth.

For all three scenarios the LEBT section fulfils the IFMIF requirements. The calculated emittance at the injection into the RFQ–accelerator are by 50% smaller than required by the IFMIF reference design. They fit very well into the RFQ accepance in size and shape.

Literature:

[1] J.Pozimski, A.Jakob, O.Meusel, A.Lakatos and H.Klein „Influence of space charge fluctuations on the low energy beam transport of high current ion beams", LINAC 2000, Montery, California, USA, August 2000

[2] J.Pozimski, O.Meusel "LINTRA ein Computer-programm zur Berechnung des Strahltransportes teilkompensierter, hochperveanter Ionenstrahlen" , GrakoNews 1/99 , Graduiertenkolleg Physik und Technik von Beschleunigern, grako@ikp.tu-darmstadt.de

# III Beam Dynamics Calculations for the RFQ and DTL

### III.1. Introduction

Beam dynamics calculations were continued for the RFQ and DTL and a Matching line in between both structures:

   a)   the stability of transmission against errors has been checked for the 1.7 Kilpatrick RFQ design

   b)   the necessity of a matching line between RFQ and DTL has been investigated

   c)   the dependence of structure design and beam behaviour on the available RF input power sources to the Alvarez tanks has been studied

   d)   preliminary layout of an IH DTL for IFMIF has been made

First calculations with a matched input beam from the input of the RFQ to the end of the DTL have been performed to get a first impression on the matching conditions and beam stability with respect to extremely low losses, as required in the IFMIF case.

### III.2. RFQ

In the previous FKZ Annual Fusion Report [1] results of beam dynamics calculations were presented for a 1.7 Kilpatrick design, which showed high transmission (93.3%) and low emittance growth (5% only for the r.m.s. values) for the capture, bunching and acceleration of the 125mA $D^+$ beam for IFMIF. In a next step the sensitivity in transmission against different kind of errors has been studied for this design: the losses must be kept low to avoid activation of the structure. The following parameters have been varied in the calculations: electrode voltage and voltage slope, input beam energy, current and emittances and mismatch at the RFQ entrance. Voltage and voltage slope turned out to be the most critical parameters, as can be seen from Fig. 1+2. By a voltage drop of 5% from the design value or a voltage slope of +5% (this means, if the end-to-end slope of the vane voltage is more than +5%, the voltage is 5% below the average value at the entrance of the RFQ and is linear increased up to 5% above at the exit end) the particle losses are increased to 10%.
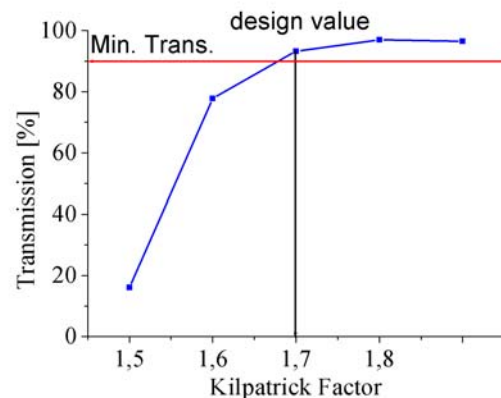


Fig. 1:   Transmission as a function of the electrode voltage of the RFQ

The input beam energy may not be missed by more than 2%, the input emittances may be changed by about 20% and current fluctuations up to 10% are possible for losses less than 10%. These requirements can be fulfilled and are no severe limitations. In the case of imperfect matching the incoming beam can have the wrong size, some off axis positions or a non symmetric form in real space. Deviations up to 20% are maximum permissable. For a special quadrupolar kind of mismatch small oscillations of the beam along the RFQ can be excited, which may cause additional losses.
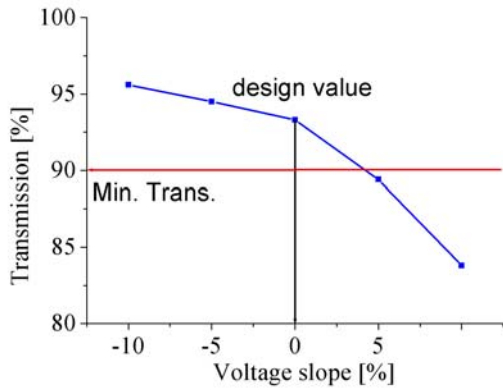
Fig. 2: Transmission as a function of the voltage-slope of the RFQ

Altogether the results show a sufficient stability and reasonable beam behaviour for the 1.7 KP RFQ design, which can be used in first instance for further beam dynamics studies of the IFMIF accelerator [2].

### III.3. MEBT design

In a first attempt the output emittances of the RFQ were injected into one long tank of an Alvarez type DTL for beam dynamics calculations. With a short coupling distance of less than 7 cm the beam has been transmitted without any losses but with considerable emittance growth since the beam is not matched. A loss free transmission could not be achieved for a segmented Alvarez design, as presented in chapter III.4. In addition no rematching possibility exists with a direct coupling of RFQ and DTL. Therefore a short matching line has been designed using the TRACE-3D code. A schematic layout can be seen in Fig.3.
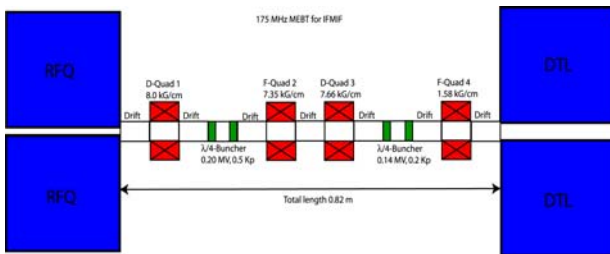


Fig. 3: Schematic layout of the MEBT for matching the beam from RFQ to DTL

The matching line consists of 4 quadrupoles with alternating polarity for the transverse matching and two $\lambda/4$ rebuncher cavities for the longitudinal match. The mismatch factor is reduced to less than 1 compared to 2.5 without MEBT. Beam dynamics studies by tracking the calculated output beam of the RFQ through the MEBT and the DTL with PARMILA gave very good results: The beam is quite nicely matched along the DTL with an r.m.s. emittance growth of less than 15%, no particle losses and output emittances behind the DTL, which are plotted in Fig.4, are well confined [3].
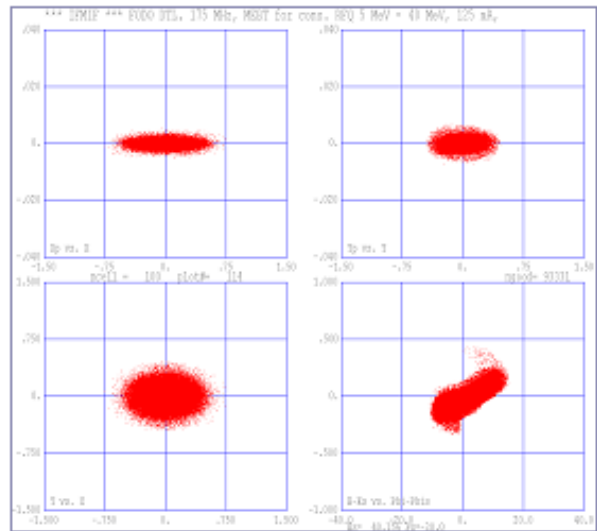


Fig. 4: Output distribution of the DTL with real input of the RFQ and MEBT

In addition to the gain in beam quality the MEBT allows for the installation of e.g. steerers, beam diagnostics elements or valves and bellows, which may help in operating the accelerator facility.

### III.4. Alvarez type DTL design

In a first step the IFMIF DTL has been designed as one long tank for a principal test of beam dynamics with the IFMIF requirements: beam energy 5 to 40MeV $D^+$, beam current 125mA. In praxis the DTL will be built modular with drift spaces in between the tanks. One limiting parameter is the input power from the rf power source, which is necessary to compensate copper losses and beam loading in each single tank. A standard rf power source for the IFMIF reference design frequency of 175MHz is not available, one major issue in the present IFMIF project phase is the development and testing of such an source. As an upper limit an output power of 1.2MW has been assumed, which could be used to feed one tank. When designing the DTL the following constraints have to be taken into account: The used SUPERFISH code may deliver to optimistic values of the shunt impedance by about 15%, about 20% of the input power may be necessary for the regulation system. Another critical issue is the cw operation of the linac, which is limited by the heat load, which determines the structure losses per meter. 5 different scenarios have been investigated [4], Table 1 shows the main parameters for the most restrictive case: maximum usable rf power of 0.8MW and rf power losses of 48kW/m only.

Beam dynamics calculations show again very good results with 100% transmission and 3% emittance growth in every phase space only in the ideal case. Assuming $1 \times \beta\lambda$ drift distance between the tanks it is necessary to introduce one DTL cell with a larger synchronous phase at the beginning and end of each tank to ensure longitudinal matching of 5%. Fig.5 shows the choice of some main parameters along the DTL.

Particle dynamics calculations including errors have been performed in a next step: phase and amplitude errors of the accelerating field as well as quadrupole errors were added. Fig. 6 and 7 shows the transverse beam behaviour in the DTL with combined rf field ($\pm 1\%$, $\pm 1°$) and quadrupole ($\pm 0.1$mm, $\pm 1°$, $\pm 1\%$) errors statistically distributed along the linac.

Table 1: Main structure parameter of the DTL

| Parameter | Alvarez-DTL |
|---|---|
| Frequency [MHz] | 175 |
| Beam Current [mA] | 125 |
| Transmission [%] | 100 |
| Number of tanks | 8 |
| Cell number | 123 |
| Total length [m] | 30.8 |
| Av. effective $E_0$ [MV/m] | 1.15 |
| Aperture radius [cm] | 1.5 |
| B Quad [T] | 1.0 – 0.6 |
| $\varepsilon^{N,RMS}$ (x,y) in [cm×mrad] | 0.04 |
| $\varepsilon^{N,RMS}$ (x,y) out [cm×mrad] | 0.041 |
| $\varepsilon^{N,RMS}$ (z) in [cm×mrad] | 0.08 |
| $\varepsilon^{N,RMS}$ (z) out [cm×mrad] | 0.083 |



Fig. 5: Main structure parameter of the DTL versus the cell number
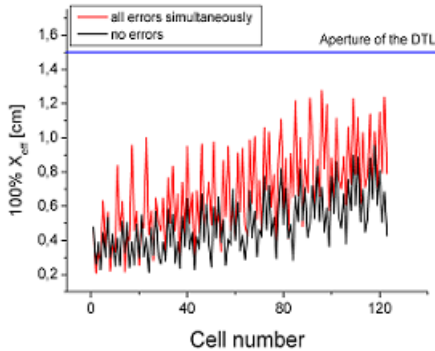


Fig. 6: 100% effective beam size in the X-Ncell-plane of the DTL with and without combined quadrupole + rf field errors

The calculations were done with PARMILA with 50,000 macroparticles. The transverse beam size stays always smaller than 80% of the drift tube aperture of 1.5cm which can be increased to 2.0cm at the high energy end of the DTL without major changes in design (all errors included). For all cases treated beam dynamics results are of the same quality, therefore the available power sources will not limit the beam dynamics performance of the IFMIF DTL [5].
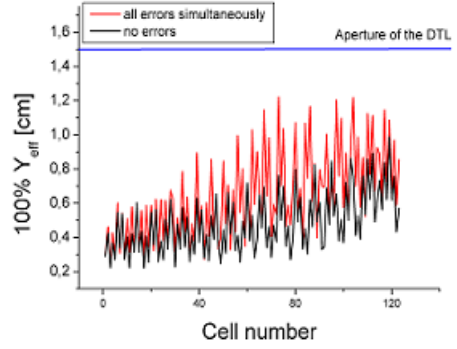


Fig. 7: 100% effective beam size in the Y-Ncell-plane of the DTL with and without combined quadrupole + rf field erors

### III.5. IH type DTL design

Since several years the IH-type DTL linac has been successfully built and operated for the efficient acceleration of light and heavy ions, e.g. at GSI and CERN [6].

This new type of accelerator combines high acceleration rates with a new focusing scheme called KONUS (**Ko**mbinierte **Nu**ll Grad **S**truktur) [6] and leads to compact accelerators. Therefore this type has been investigated for the use in high intensity machines like IFMIF for the first time. Fig. 8 shows the scheme of an Alvarez- and IH –type DTL for IFMIF in comparison.



Fig. 8: Scaled scheme of the an Alvarez DTL and IH-type DTL for IFMIF

Table 2 gives the main parameters of the IH-DTL and Alvarez DTL.

| Parameter | Alvarez DTL | IH DTL |
|---|---|---|
| Frequency [MHz] | 175 | 175 |
| Beam Current [mA] | 125 | 125 |
| Transmission [%] | 100 | 100 |
| Number of tanks | 8 | 9 |
| Cell number | 123 | 152 |
| Total length [m] | 30.8 | 22.3 |
| Av. effective $E_0$ [MV/m] | 1.15 | 1.6 |
| Aperture radius [cm] | 1.5 | 1.5/2.0 |
| B quad [T] | 1.0 – 0.6 | 1.2 – 0.9 |
| $\varepsilon^{N,RMS}$ (x,y) in [cm×mrad] | 0.04 | 0.04 |
| $\varepsilon^{N,RMS}$ (x,y) out [cm×mrad] | 0.041 | 0.070 |
| $\varepsilon^{N,RMS}$ (z) in [cm×mrad] | 0.08 | 0.08 |
| $\varepsilon^{N,RMS}$ (z) out [cm×mrad] | 0.083 | 0.136 |

In the KONUS scheme the particles are accelerated in a number of gaps with 0 degree bunch center phase which are followed by quadrupole triplet focusing and rebunching cells with negative phase. In the first tank of the IH-DTL the quadrupole is still integrated in the tank, in the following sections we have intertank quadrupole focusing, which eases the adjustment and maintenance of the quads. Figs. 9-10 show the beam envelopes at full space charge along the DTL calculated with LORASR for the same size of the input emittances as in the Alvarez case. No particle losses were observed with 1,000 macroparticles for a matched input beam, the r.m.s emittance growth is about 75%. More calculations have to be performed with higher particle number and in addition error studies have to be done to investigate the tolerances in detail.



Fig. 11: Effective shunt impedances of both structures as a function of the beam energy



Fig. 9: 99% transverse effective beam envelopes along the IH-DTL
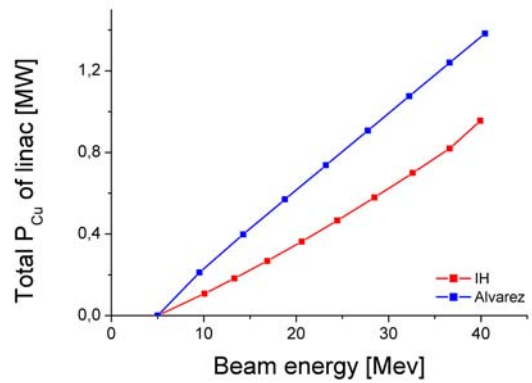


Fig. 12: Sum of the rf copper power losses per tank of both structures as a function of the beam energy

### III.6. Conclusion and outlook

Extended beam dynamics have been performed for the IFMIF linac and showed some major progress [7]:

- A stable RFQ design with lowered electrode voltage is available and can be used for the aimed overall calculations from source to target.

- A short transport line between RFQ and DTL improves the beam matching between both structures with different focusing schemes.

- A modular design of the Alvarez type DTL for a wide range of available rf input power to the tanks has been checked and fulfils the IFMIF requirements in all cases.

- The beam behaviour including errors is sufficient for the present RFQ design and without problems in the DTL.

- First beam dynamics studies for an IH type DTL for IFMIF showed the capability of this approach for the acceleration of high intensity beams with good power efficiency.



Fig. 10: Energy spread along the IH-DTL

A possible advantage of the IH-Type DTL could be the lower total power consumption and shorter length of the linac, which can be seen from Figs. 11-12 where the effective shunt impedances and the sum of copper power losses are plotted along both structures.

Overall calculations through RFQ, MEBT and DTL including combinations of errors in all sections must be still done as well as calculations with a non ideal input beam from the LEBT into the RFQ.

Literature:

[1] Nuclear Fusion Programme Annual Report FZKA 6550-EURO 19707 EN, 12-2000 FZ Karlsruhe.

[2] H.Klein et al., "Beam Dynamics Calculations from Volume Source to RFQ", IFMIF Deliverable 6-2001 IAP, Frankfurt M.

[3] A.Sauer, H.Deitinghoff, H.Klein, "Beam Dynamics Studies for a High Current Ion Injector", LINAC 2000, Monterey, California, August 2000.

[4] A.Sauer, H.Deitinghoff, "Particle Dynamics Studies for the IFMIF D+ 175 MHz Injector", IFMIF Meeting, Karlsruhe, Germany, February 2001.

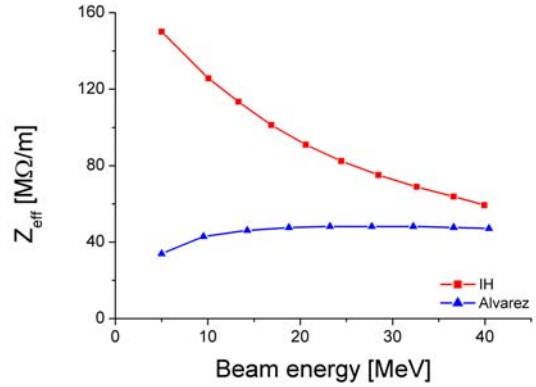[5] A.Sauer, R.Tiede, H.Deitinghoff, H.Klein, U.Ratzinger, "Particle Dynamics Investigations for a High Current D+ DTL", PAC 2001, Chicago, USA, June 2001.

[6] U.Ratzinger, Habilitationsschrift, University of Frankfurt, July 1998, Germany.

[7] A.Sauer, Ph.D. thesis, University of Frankfurt, in preparation, Germany.

## IV 4-Rod RFQ Beam Dynamics Design

### IV.1. Introduction

The RFQ-injector is an 175MHz RFQ accelerator which has to accept a 100keV deuterium beam of $I_{in}$ = 140mA and transport, bunch and accelerate it to an energy of 5MeV with minimum losses and emittance growth.

An important design criteria is a low Kilpatrick value, which especially for a continues (cw) mode operation plays an important role for operational stability and accelerator down time. Our method of electrode design takes into account the special features of the 4-Rod RFQ structure which has advantages at frequencies up to 200MHz. For the low frequency of 175MHz this structure promises a simpler construction and eases problems of rf-stability, cooling and tuning.

All attempts for an IFMIF beam dynamics design using either the standard shaper-buncher-accelerator section for RFQs or versions of the modified method keeping e.g. the phase advances constant lead to RFQs which are much longer than standard accelerators. The reason is the need for a very slow bunching and a rather low accelerating gradient to maximize radial focusing and minimize losses at reasonable electrode voltages. Some designs use a part of the accelerating section with an increased electrode voltage to reduce the total length of the RFQ.

### IV.2.RFQ-design

Our design is using basic parameters of an electrode voltage of 120kV starting with a focusing parameter of B=6.2 at stable phase 90° resulting in a radial phase advance of σ=40 degrees at the RFQ input. These values are smoothly varied to the final values of B=6.5 and $\varphi_s$=50 resulting in a RFQ with length of 12.7m. The Kilpatrick value stays below 1.9Kp. Fig. 1 shows the parameters along the RFQ. Results of Parmteq simulations with an input emittance of ε = 125πmm×mrad and a waterbag distribution are shown in fig. 2.



Fig. 1:    RFQ parameters.
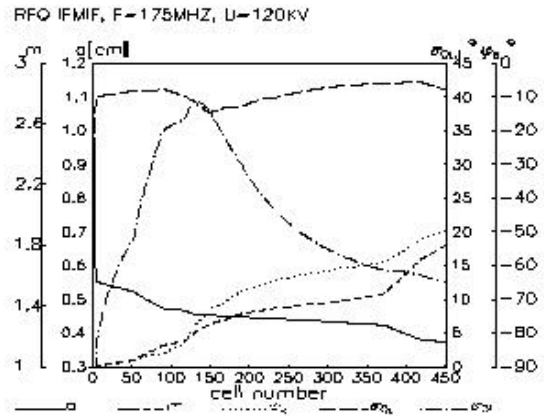


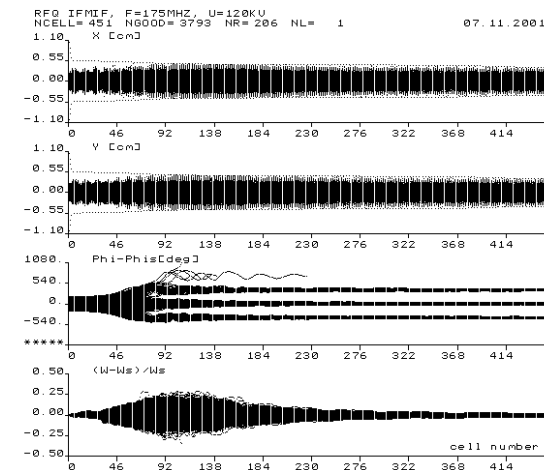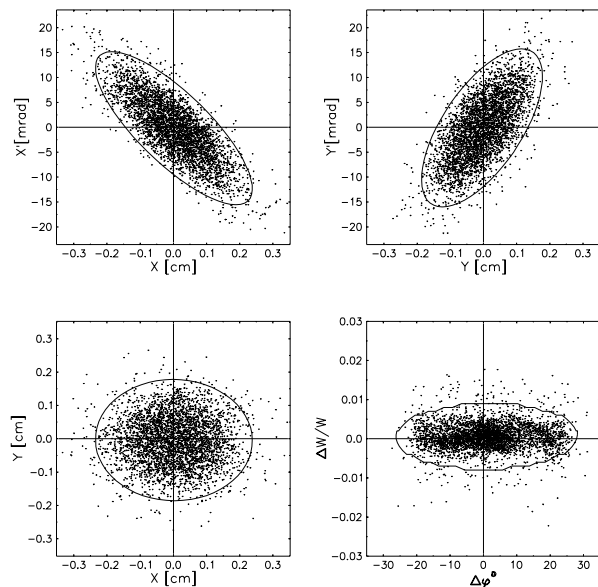Fig.2:    PARMTEQ simulation



Fig. 3:    Output emittance (140mA)

The transmission at 140mA input deuterium beam current is T = 94% with an emittance growth of Δε = 43.5%. Fig. 3 shows the output emittances.

A feature of our design is the constant voltage along the RFQ which results in a rather long RFQ, because the accelerator section can be shortened by an higher electrode voltage very efficiently without touching the Kilpatrick limit and by that make up for an extensively long bunching section. The disadvantages are extreme power losses in this part of the RFQ, which will be hard to realize because even the average value of appr. 120kW/m for our design will be very hard to build and may be a limiting factor. The particle losses along the RFQ indicate that the major losses occur radial at the part where bunching and accelerating are becoming quicker at energy of appr. 200keV (fig.4). At this stage of acceleration many particles are changing to adjacent buckets as one can see in fig.2.

With this design, which is well adopted to the 4-Rod structure with high Kp-value and spacings, useful emittances are between 50 and 250 $\pi$ mm mrad. Further optimization of input matching (e.g. $\alpha,\beta$) additional improvements should be possible.

Depending on the general optimization priorities this design might be modified for lower average power of the RFQ, that means lower electrode voltage, or even higher transmission or improvements in emittance.
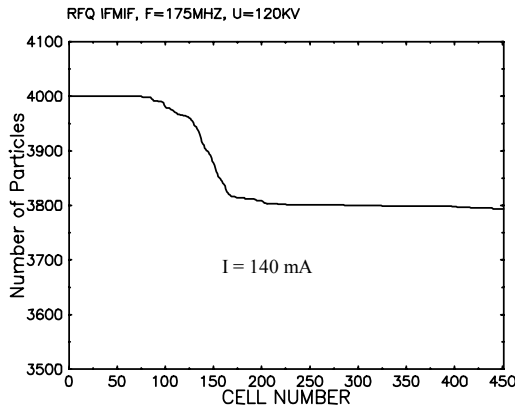


Fig. 4:    Losses along the RFQ

# V Non Destructive Beam Diagnostics for IFMIF

### V.1. Introduction

The determination of the beam emittance using conventional destructive methods suffers from two main disadvantages. The interaction between the ion beam and the measurement device produces a high amount of secondary particles which can influence the beam transport. Additionally the power deposited on the emittance measurement device (for IFMIF up to 1kW/mm$^2$) can lead to extensive heat on the detector itself and can destruct the device. CCD camera measurements of the incident light emitted from interaction of beam ions with residual gas are commonly used for determination of the beam emittance [1,2,3].

### V.2. Experimental Set up

A compact low energy beam transport (**LEBT**) section was used to compare measurement using a conventional destructive Allison type emittance scanner with the results gained from CCD camera measurements. The experimental set up is shown in figure 1. A volume source was used to deliver 4.4mA of He$^+$ at 11keV. The solenoid (0.002T/A; 360A max.) was able to transport 3.7mA of He$^+$ into the diagnostics chamber (85%

transmission). In the diagnostic chamber a Faraday cup, the Allison type emittance scanner, the CCD camera [4] (512 x 512 pixel LN$_2$ cooled), and an absorber tank for reduction of reflected light where installed perpendicular to each other at the same longitudinal beam position. Due to the length of the emittance scanner the first slit defining the position of the emittance measurement is 38mm in front of the common centerline (see Fig. 1). 200 mm behind the main diagnostics a residual gas ion energy analyser [5] was installed to determine the degree of compensation.
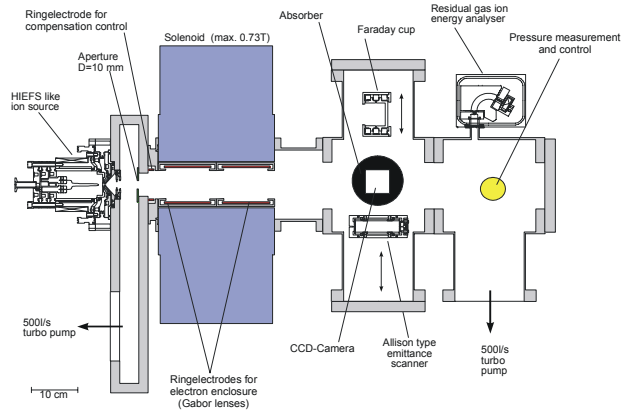


Fig. 1:    Schematic drawing of the experimental set up

### V.3. Experimental Results

Figure 2 shows the result of an emittance measurement using an Allison type measurement device. The solenoidal field was 0.44T (220A), the beam current into the Faraday cup 3.4mA. The potential depression inside the beam was determined to be 9.9V (compensation degree ~80%). The beam is convergent and the envelope radius is appr. 6.5mm, the convergence angle $\pm$30mrad and the normalised beam emittance (rms, 100%) is 0.011 $\pi$mm$\times$mrad.

$$\varepsilon_{rms,n,100\%}=0.011\ \pi mmmrad$$
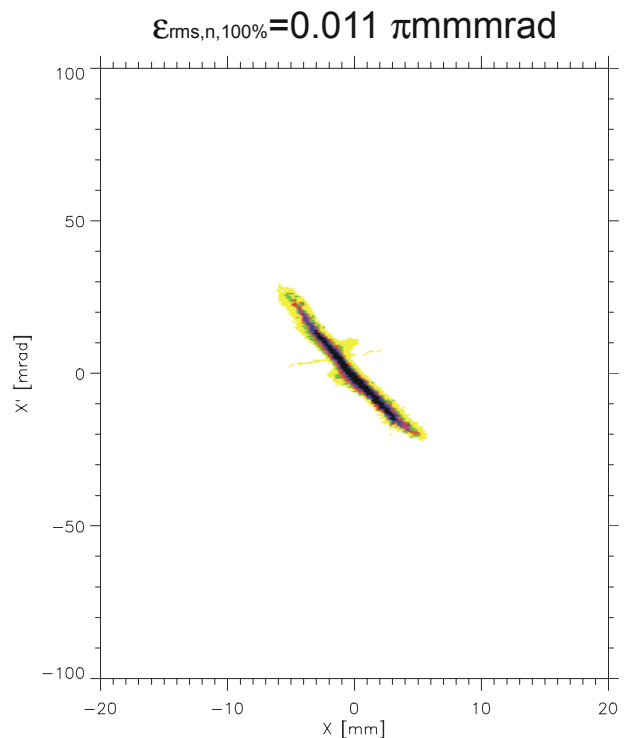
Fig. 2:  Beam emittance measured by the use of an Allison type measurement device (see text for more information)
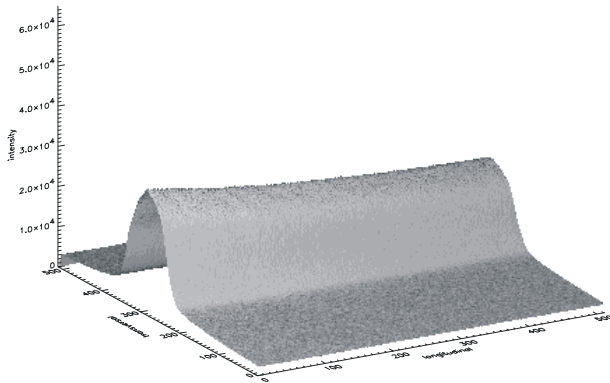


Fig. 3:  Intensity of incident light detected by a CCD camera as a function of transversal and longitudinal position (see text)

The corresponding CCD camera measurement is shown in figure 3 (1 Pixel=0.081 mm). The beam was drifting from left to right, therefore the higher intensity on the left side already indicates a convergent beam. The signal to noise ratio is appr. 8. For comparison figure 4 shows the result of an emittance determination by calculation using the data of the CCD measurement (Fig. 3). The envelope radius is 7mm the convergence angle $\pm$ 35mrad, the normalised beam emittance (rms, 100%) is 0.020 $\pi$mm$\times$mrad. The compensation degree can be estimated from the calculations to be 80%. Comparison of emittances gained from conventional destructive measurements and from CCD camera measurements show an good overall agreement concerning the orientation of the emittance in phase space.

$$\varepsilon_{rms,n,100\%}=0.020\ \pi mmmrad$$
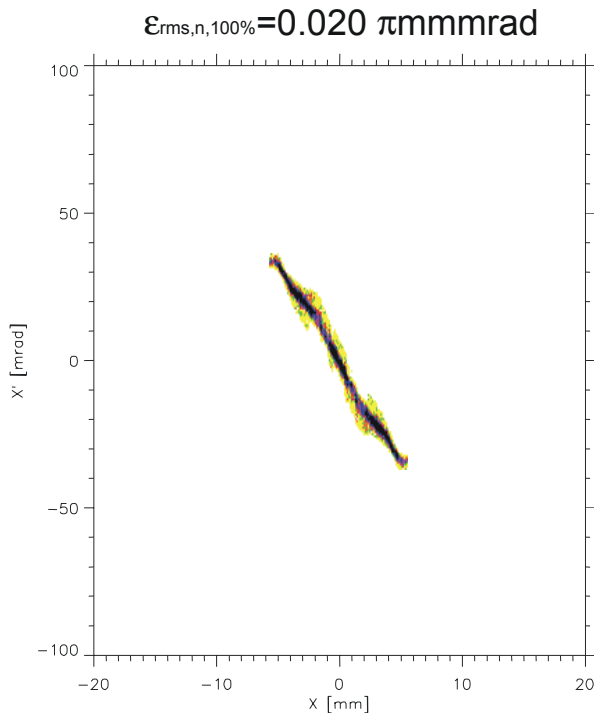


Fig. 4:  Emittance determined by calculation using an CCD camera measurement

The values given by the calculation have slightly higher beam radius and angle (10-20 % deviation).This might be caused by the higher resolution of the CCD chip compared with the conventional detector. Therefrom and due to the numerical errors typical for differential methods the RMS values are greater too. The values concerning the compensation degree are in good agreement with the measurements. The lower values might be explained by improper separation of space charge and emittance effects and are also explaining the smaller pattern.

## V.4. Conclusion

The shown encouraging results proof that the use of a CCD camera for the determination of beam emittance is an alternative to conventional devices at high beam power. Mathematical methods can derive most of the relevant parameters needed for beam transport using a single CCD camera image. Improvements of the used computer codes and the use of tomographic methods are planned for the future.

Literature:

[1]  K.Ebihara et al, Nucl. Instr. And Meth. 202, 403-409 (1982)

[2]  P.Strehl, Beam diagnostics, Proc. Of CAS, CERN accelerator school, CERN 87-10 (1987)

[3]  F.Sittinger, "Untersuchungen zu optischen Profil- und Emittanzmessungen an niederenergetischen intensiven Ionenstrahlen, Dissertation IAP, University of Frankfurt, Germany (1995)

[4]  L.Wicke, "Untersuchungen zu Strahlprofilmessungen intensiver Ionenstrahlen mit optischen Methoden" Diploma Thesis IAP, University of Frankfurt, Germany (1998)

[5]  R.Dölling, "Raumladungskompensation driftender intensiver Strahlen niederenergetischer Ionen und Techniken zu ihrer Vermessung" Dissertation IAP, University of Frankfurt, Germany (1994)

Staff:

H. Deitinghoff
A.Jakob
H. Klein
O. Meusel
J. Pozimski
U.Ratzinger
A.Sauer
A.Schempp
R.Tiede
K.Volk

Institut für Angewandte Physik J.W.Goethe-Universität
Robert-Mayer-STr. 2-4
D-60054 Frankfurt am Main

**TTMI-003**
**IFMIF, Test Facilities**


**TTMI-003-1**
**He Cooled High Flux Test Module**


The re-evaluation of the reference design of the High Flux Test Module in the KEP period [6] comprised on the one hand detailed nuclear analyses and on the other hand considerations on a thermal-hydraulic optimisation.

The nuclear analyses were mainly devoted to the investigation of the effect of a reflector surrounding the HFTM. Recent nuclear cross section data evaluations including γ-production data from the lithium were applied in the related nuclear calculations. The comparison of the dpa-rates with and without a reflector showed a strong neutron back-scattering effect on the HFTM. This applies also for the Medium Flux Test Module (MFTM) region behind the HFTM. Geometry and material composition of the MFTM thus affect the neutronic performance of the HFTM to a large extend. The design of the HFTM and the MFTM must therefore be conducted in an iterative process.

The HFTM design goal "maximum space and flexibility for the specimens" means on the other hand "minimum space for heater, coolant channels and structural material". Therefore, methods for the prediction and demonstration of heat transitions in the transfer chain from the specimen to the helium in narrow geometries or contact areas are investigated. A first integral experiment provided valuable design criteria. A new test section is designed for flow field and heat transfer measurements in narrow gabs with undeveloped flow and temperature profiles. The experimental results will be used for direct numeric code validation.

**Nuclear calculations**

The nuclear calculations assume a simplified HFTM configuration as shown in Fig. 1. Dimensions, materials and material densities are adapted from the reference design. The same assumptions are made for the MFTM. Several materials have been investigated as candidate for a reflector. They are used with 90 % mass density in order to provide some space for cooling.
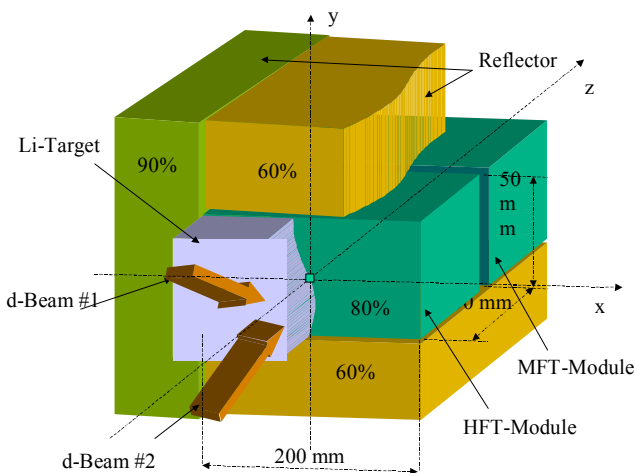


Fig. 1: Geometry and material distribution assumed for the neutronic calculations (x-axis: horizontal; y-axis: vertical; z-axis: beam downstream direction)

The neutronic calculations were performed with the McDeLi Monte Carlo code which is an extension to MCNP with the capability to represent the IFMIF Li(d,xn) neutron source term in the neutron transport calculation. High-energy cross-section data for neutron transport calculations are taken from the LANL 150 MeV data evaluations and from the FZK/INPE Obninsk intermediate energy evaluation. The data from two libraries reasonably agree with each other except in the energy range above 50 MeV where the neutron yield from Li(d,n) source becomes negligible.

**Reflector effects on the dpa-rate and -gradient**

The calculations confirmed higher dpa-rates when using a reflector around the test module. The effect increases with the material sequence aluminium, carbon, lead, nickel/iron (Eurofer), beryllium and tungsten. The reflector effect saturates at a reflector thickness of about 100 mm. The back scattering from the MFTM region behind the HFTM affects both the dpa accumulation and the gradient. This suggests to consider for the MFTM region a similar material composition as for the HFTM with a thickness of 100 mm.

The power density in the HFTM material is increased due to the surrounding reflector, increasing with beryllium, carbon, lead, aluminium, tungsten and iron/nickel.

In the front centre line the dpa-rate increases by 1 to 2 %. At x = 85 mm the peak of the deuteron beam traces through. Between 90 and 100 mm the rate decreases by 1/3. At the front side top the reflector effect enlarges the dpa-rate by about 3 %. The slope of the dpa from the centre line to the top is within the design requirements of no more than 1 % per mm. At the back side the reflector augments the dpa rate by about 20 %. Thereby the gradient becomes less steep both in axial (beam downstream) and vertical direction. The reflector materials tungsten and beryllium showed a slightly better performance than iron (or reduced activation alloy EUROFER).

**HFTM volume**

The reflector effects reported above were related to the results of the centre lines or areas. More information on the volume with displacements rates beyond 20 dpa/fpy or higher values are shown in Fig. 2 with the contour map of the dpa/fpy iso-surface lines. They reveal that 25-30% of the space (dpa/fpy > 20) is outside the reference HFTM which is a rectangular box of 20x5x5 cm3 size. For an optimal performance, the HFTM box, therefore, must be designed with a contour adapted to the dpa/fpy iso-surfaces as indicated in Fig. 2.

**Heat removal**

The HFTM lay-out aims at a maximum of positions for material specimen. They have to be kept at temperatures defined for the individual rigs at 250 °C, 350 °C, 450 °C, 550 °C, 650 °C or 750 °C. The nuclear calculations described above indicate an overall power of $P_{nucl,av}$ = 7 kW. The power density in the specimens amounts to about 25 W/cm$^3$ at maximum and 14 W/cm$^3$ on average. If we assume a balance of power density or power shape with electric heaters and reserves of additional 20 % for heat release in the structural components and the container, an overall power of $P_{total}$ = 15 kW has to be removed. We further limit the temperature increase for the helium flowing along the rigs to $\vartheta$ = 30 °C so that the resulting axial temperature gradient for the specimens is small. This leads to a helium mass flow rate of m = 96 g/s. For the rig arrangement like that of the reference design, a gap between the rigs of $\delta$ = 1 mm and a helium pressure of 0.2 MPa results in a helium velocity of about $c_{He}$ = 300 m/s. The Reynolds-number

| dpa-rate [1/fpy] (No Reflector) | dpa-rate [1/fpy] (with Reflector) |
|---|---|
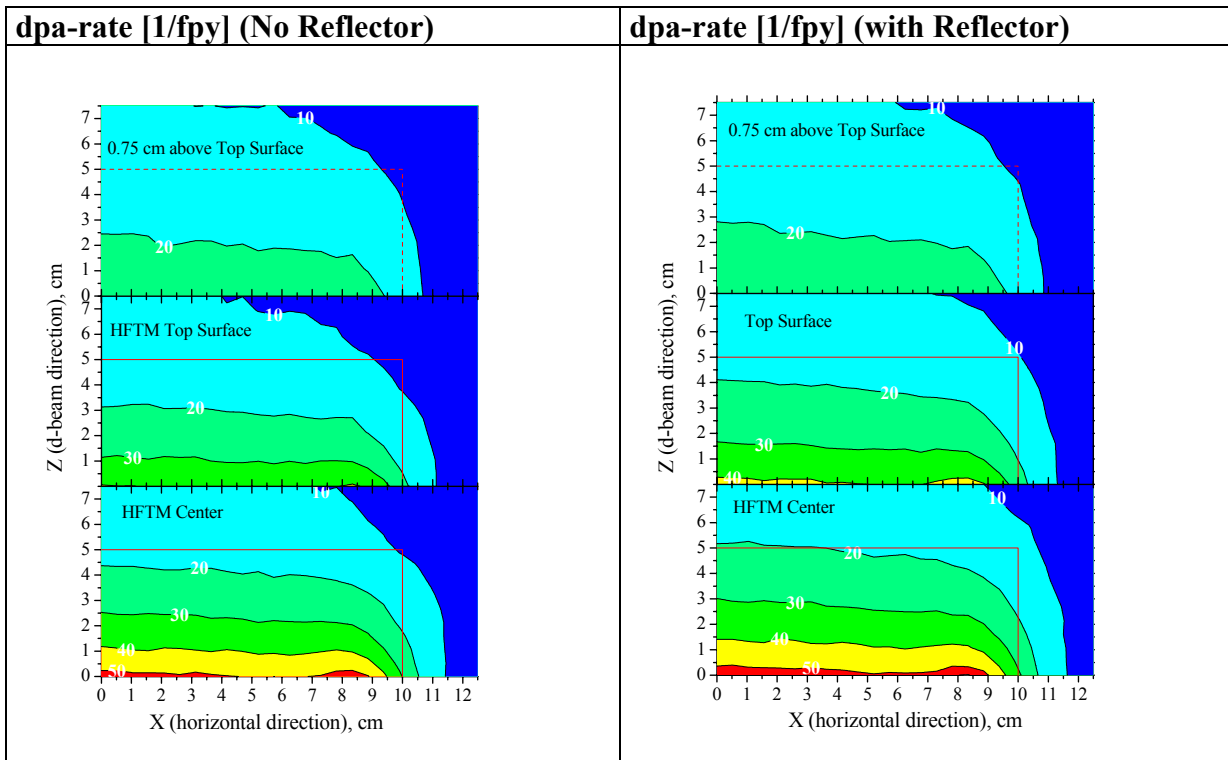


Fig. 2: Contour map with dpa/fpy iso-surface lines at three horizontal levels (*left side: without reflector; right side with reflector (10 cm Eurofer); the beam enters from the bottom*)

is at about Re = 9000. This shows that the over all heat removal with helium is achievable. However local temperature distributions have to be investigated.

**Integral experiments for heat transfer measurements**

An integral experiment was conducted in the helium-loop of the Dual-Beam-Plant at the cyclotron at FZK (Forschungszentrum Karlsruhe) in order to get a first principal demonstration of the rig design. A box representing the rig had a length of 103.2 mm and a cross section of 15.6x20 mm². Electric heaters simulated the nuclear heat and the heater for the temperature control. The box was inserted into a rectangular helium channel with 17.2x21.6 mm². Thus the helium gap had a width of 0.8 mm. In addition simulation calculation of the temperature field in the experimental arrangement were carried on. A suitable FE-Model was developed with the help of pre- and post processors of the CAD-system CATIA V.4. The temperature distributions were then calculated with the FEM-code PERMAS V.7.

**Conclusion from the integral experiment and the simulation calculations**

The analyses of the experimental results and the comparison with FE simulation calculations lead to the following recommendations:

The experiments showed that the specimens can be kept with electric heater up to 600 °C. The heater would allow even higher temperatures. However, the jacket heater wires require a remarkable share of the irradiation volume. This is even more severe if a second heater per rig is required for the power shape balancing.

Manufacturing tolerances have to be as small as possible. A sum up of even small tolerances will change the heat flux to

the outer rig wall. The individual parts have to be positioned reproducible.

The position of temperature sensors have to be unequivocal. Thermocouples should not be installed in areas with low heat conductivity and consequently with high temperature gradient. Otherwise small tolerances in positioning will create large measuring errors. If important data or information for the HFTM lay-out have to be measured, special experiments should be preferred. Integral experiments like the start-up experiments may conceal single effects or limit the necessary accuracy.

Available direct numeric codes provide reliable predictions of the temperature fields in complex three-dimensional geometries if material data, boundary conditions and geometry data are available.

**ITHEX (IFMIF Thermohydraulic Experiment)**

As consequence from the conclusion above a new experiment is under preparation for getting validation bases for direct numeric FE simulation of the flow field, the heat transfer and the pressure loss. First trials to apply the code STRARCD are promising.

Staff:

B. Dolensky
U. Fischer
S. Gordeev
V. Heinzel
K. Schleisiek
S. P. Simakov
E. Stratmanns

Literature:

Neutronic optimisation of the high flux test module of the International Fusion Material Irradiation Facility (IFMIF); U. Fischer, V. Heinzel, S. Simakov, U. v. Möllendorff; Jahrestagung Kerntechnik, 15. – 17. May 2001, Dresden, p. 581

Design optimization of the IFMIF high flux test module; V. Heinzel, B. Dolensky, U. Fischer, S. Gordeev, U. v. Möllendorf, K. Schleisiek, S. P. Simakov, E. Stratmanns; ICFRM 10, 14. – 19. Oct. 2001, Baden-Baden

## TTMI-003-5
## D-Li Reaction Source Term

The d-Li neutron source term is of prime importance for calculating the neutron yield, the neutron spectrum and the nuclear responses in the test cell. The objective of Task TTMI-003, Deliverable 5, of the EFDA technology work programme is to provide the required data in terms of a full data evaluation of the double-differential $^{6,7}$Li(d,xn) reaction cross-sections, using state-of-the-art nuclear models and computational procedures.

Over the reporting period, a complete set of evaluated d + $^{6,7}$Li cross-section data was prepared employing a newly developed method based on diffraction theory, a modified intranuclear cascade model and standard evaluation techniques [1]. The evaluated data include cross-sections for all reaction channels up to 50 MeV deuteron energy as well as energy-angle distributions for the neutrons emitted through the various $^{6,7}$Li(d,xn)-reactions. The data files were prepared in accordance with standard ENDF-6 data format rules to enable further processing with the NJOY-code.

In parallel, an advanced Monte Carlo procedure was developed to simulate in the transport calculation the neutron production on the basis of evaluated the d + $^{6,7}$Li data [2]. The resulting code McDeLicious is a further enhancement of McDeLi, based on a built-in semi-empirical d-Li reaction model [4], with the new ability to sample the generation of d-Li source neutrons from the processed d + $^{6,7}$Li cross-section data files. The McDeLicious approach was tested against available experimental thick Lithium target data. It was shown that the resulting total neutron yield as well as the neutron angle-energy spectra can be predicted with considerably better accuracy than with the semi-empirical McDeLi approach, see e. g. Fig. 1 for the comparison of thick target forward neutron yield data. With the McDeLicious approach the accuracy of the IFMIF neutron source term can be steadily improved by taking into account further advanced and validated d + $^{6,7}$Li data.
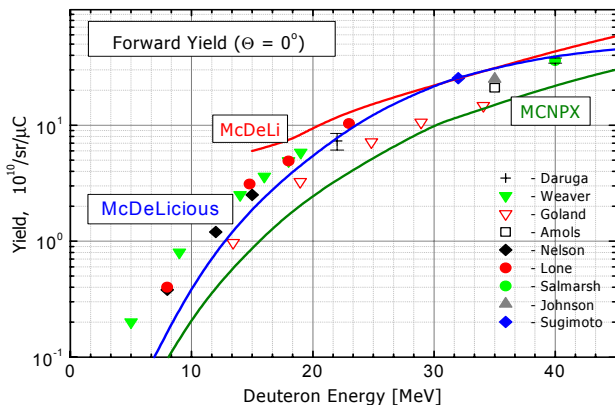


Fig. 1: Thick target d-Li forward neutron yield data.

### Activation Data File

The objective of Task TTMI-003, Deliverable 6, of the EFDA technology work programme is to provide nuclear cross-section data above 20 MeV neutron incidence energy to enable neutron transport and activation calculations for IFMIF. Data evaluations are needed for a variety of nuclides important for neutron transport calculations. A full data set of all potential target nuclides is required for activation calculations.

Over the reporting period, the evaluation effort has focused on the creation of a complete activation data library. The Intermediate Energy Activation File IEAF-2001 [3] includes 679 (stable and unstable) target nuclides from Z=1 (hydrogen) to 84 (polonium) with neutron induced reaction reactions from $10^{-5}$ eV to 150 MeV incident neutron energy. The European Activation File EAF-99 served as basis for the activation cross-section data below 20 MeV neutron energy. Threshold reaction cross-sections were evaluated on the basis of geometry dependent hybrid exciton and evaporation models using a modified version of the ALICE code.

The IEAF-2001 data library has been prepared in standard ENDF-6 data format making use of the MT=5 (neutron, anything) option with the excitation functions stored in MF=3 and the product nuclide vectors in MF=6 (LAW=0). A 256 group library has been generated with NJOY/GROUPR to enable activation calculations for the IFMIF neutron source. Applications tests were successfully performed for the activation analysis of the high flux test module using the recent ALARA activation code [4].

The IEAF-2001 library is ready for distribution via the NEA data bank. It can be used with any activation code capable of handling an arbitrary number of reaction channels. Testing of the IEAF data against integral experiments is considered an important next step to qualify and further improve the IEAF library.

<u>Staff:</u>

U. Fischer
D. Leichtle
<u>U. von Möllendorff</u>
P. Pereslavtsev
I. Schmuck
S. Simakov
P. Wilson

<u>Literature:</u>

[1] A. Yu. Konobeyev, Yu. A. Korovin, P. E. Pereslavtsev, U. Fischer and U. von Möllendorff, Developments of methods for calculation of deuteron-lithium and neutron-lithium cross sections for energies up to 50 MeV, Nuclear Science and Engineering 139 (2001) 1-23

[2] S.P. Simakov, U. Fischer, U. von Möllendorff, I. Schmuck, A.Yu. Konobeev, Yu. A. Korovin, P. Pereslavtsev, Advanced Monte Carlo procedure for the d-Li neutron source term based on evaluated cross sections files. 10th Int. Conf. on Fusion Reactor Materials (ICFRM-10), Baden-Baden, 14-19 Oct. 2001

[3] Yu. Korovin, A. Yu. Konobeev, P.E. Pereslavtsev, U. Fischer, U. v. Möllendorff, Intermediate Energy Activation File IEAF 2001, Int. Conf. Nuclear Data for Science and Technology (ND2001), October 7-12, 2001, Tsukuba, Japan

[4] U. Fischer, P.P.H. Wilson, D. Leichtle, S.P. Simakov, U. von Möllendorff, A. Konobeev, Yu. Korovin, P. Pereslavtsev , I. Schmuck, Application of the IEAF-2001 Activation Data Library to Activation Analyses of the IFMIF High Flux Test Module. 10th Int. Conf. on Fusion Reactor Materials (ICFRM-10), Baden-Baden, 14-19 Oct. 2001

## TTMI-003-10 and -11
## Neutron Moderator/Reflector and Irradiation Conditions

Most of the structural materials will be irradiated in the high flux test module (HFTM) followed by post-irradiation examination in hot cells. More sophisticated in situ experiments are in some cases mandatory for measuring the materials properly. Therefore, in situ push-pull creep fatigue tests and in situ tritium release tests on various breeder materials are foreseen in the medium flux region. In the present study the irradiation conditions and the former reference design of the medium flux test modules (MFTM) are systematically optimized. The main goal is to achieve for ceramic breeder materials and beryllium similar good irradiation conditions in the medium flux test module (MFTM) as already achieved for structural materials in the high flux test module (HFTM).

**Materials screening for a neutron moderator**

The primary goal of the 3D neutron transport calculations is to select a suitable design of IFMIF in order to simulate DEMO fusion reactor irradiation conditions as close as possible. The calculations confirm that a suitable tungsten moderator (spectral shifter) integrated in the MFTM improves further the damage to gas production ratios, and the primary knocked on atom (PKA) spectra that determine the damage morphology and, hence, mechanical properties of irradiated materials. The tritium breeding of lithium ceramics in fusion reactors is dominated by the $^6$Li(n,t)$^4$He reaction because of its very high thermal neutron capture cross section. Systematic MCNP calculations based on several elements and compounds have revealed that an additional carbon block of about 30 cm attached to the HFTM and MFTM significantly increases the population of thermal neutrons and thus greatly improves the irradiation conditions for breeding ceramics.

The materials screening included several materials for the plate moderator. It has been shown clearly, that a tungsten moderator decrease the high energy (> 1 MeV) and increase medium energy part of neutron spectrum. Error analysis shows that the calculated values for the low energy part of the spectrum (< 10 keV) are unreliable and should not be taken into account. The most significant changes of neutron spectrum occur in the Medium Flux Test Module /Universal Testing Machine (MFTM/UTM). Less significant changes occur for MFTM /Ceramic Breeder and for cells in Low and Very Low Flux Test Modules (LFTM/ VLFTM).

Silicon carbide (SiC) and carbon moderators increase more effectively the high energy part of the spectrum, while the magnitude of increase in the medium part of the spectrum is much less than in the case of tungsten for SiC moderator and comparable to that for C moderator. Carbon moderator increases more effectively the neutron flux at lower energies than a tungsten moderator. An interesting feature of carbon as material for the spectral shifter plates in the MFTM is, that it increases the neutron flux mainly at energies lower than 0.1 MeV. Neutrons of such low energy can not affect significantly defect production, but are highly welcome to increase the tritium production via the $^6$Li(n,T) reaction. Tungsten on the other hand is very effective to increase the neutron flux between 0.1 and 0.4 MeV and thus the displacement damage rate. For the set of materials studied only tungsten can increase effectively the neutron flux in this range.

**Materials screening for a coating of test modules**

As already mentioned, the tritium breeding of lithium ceramics in fusion reactors is dominated by the $^6$Li(n,t)$^4$He reaction because of its very high thermal neutron capture cross section. That is,

as soon as breeder ceramics will become tested in the IFMIF MFTM, not only the "high energy part" above 0.1 MeV of a fusion reactor must be reproduced in an adequate manner but also the low energy tail must have sufficient population to account for the tritium production. As outlined in the following, the neutronics calculations have shown that a coating of all test modules by a suitable material will improve the population of epi-thermal neutrons by orders of magnitude.

Several moderator materials that can serve as effective sheathing were analyzed to assess their efficiency on the neutron spectrum. We have compared the neutron spectrum obtained for selected cells with the reference DEMO reactor spectrum. The results for HFTM are represented in Figure 1, and the results for MFTM in Figure 2. The green curve reflects the spectrum without any spectral shifter. Spectral shifter plates in the MFTM made of Tungsten slightly increase the neutron flux for energies less than 1 MeV. The best results were obtained by an additional carbon jacket of 25-30 cm attached to the HFTM, MFTM and VIT. Such a carbon „coating" significantly increases the population of thermal neutrons and thus greatly improves the irradiation conditions for breeding ceramics (blue curve).



Fig. 1: Neutron spectra of IFMIF HFTM without moderator (CDA design 1996), and with W and C moderator/reflector (KEP design 2001) in comparison with the HCPB blanket of a DEMO-reactor

Obviously a major result of the neutronics calculations is, that with two tungsten plates in the MFTM and additional carbon "coatings" of all test modules, the neutron spectrum in the medium flux test volumes follows over several orders of magnitude closely that one of a DEMO-type helium cooled pebble bed breeding blanket. That is, besides the HFTM now also the MFTM provides a test bed that reflects closely DEMO relevant irradiation conditions.

As already mentioned, this carbon jacket is only of major relevance for the irradiation of lithium ceramics. It is not urgently needed for structural materials testing, because in these materials transmutation and displacement damage production is by far governed by neutrons above 0.1 MeV. In near future calculations are performed to determine the geometrical characteristics of the carbon "coating", which can be accepted both from the technical design and the physical requirements.
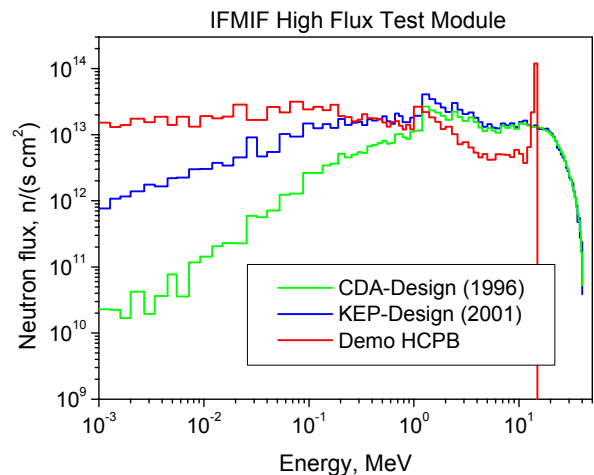
## IFMIF Medium Flux Test Module
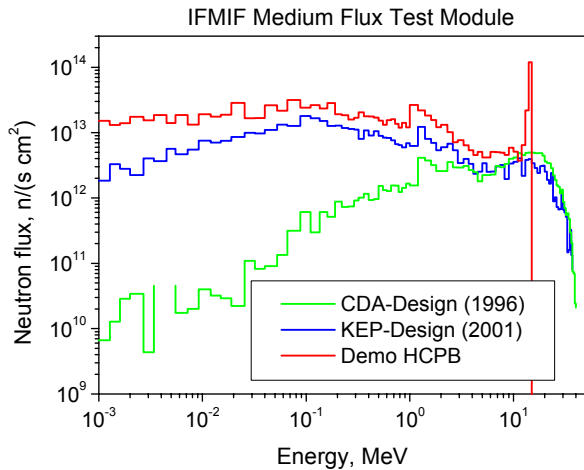
Fig. 2: Neutron spectra of IFMIF MFTM without moderator (CDA design 1996), and with W and C moderator/reflector (KEP design 2001) in comparison with the HCPB blanket of a DEMO-reactor

**Re-evaluation of irradiation parameters**

The positive effect of reflector materials on neutron flux, dpa rate and property gradients in the high flux test module HFTM is shown in task TW0-TTMI-001. In the following results of a sensitivity study are presented that highlights the sensitive relationship between the primary-knock-on atom spectrum (PKA spectrum) and the available damage energy under different irradiation conditions. The so called W(T) function, representing the fraction of displacement damage energy versus the PKA-energy T, is shown in Fig. 3. E.g. in a DEMO blanket (HCPB type) 50% of the total displacement damage is produced by recoil atoms having an energy less than about $2 \times 10^{-1}$ MeV. As shown by the hatched area, IFMIF meets over the entire PKA energy range the DEMO conditions in iron based alloys, as the shape of the W(T) function can be adjusted by using an appropriate combination of W-moderator and C-reflector. On the other hand, the PKA spectrum of the HFR is too soft by about an order of magnitude, while a typical spallation spectrum has a high energy tail as expected but also a quite soft spectrum at intermediate energies.

In the next reporting period it is foreseen to optimize further the irradiation conditions in the MFTM for fusion relevant irradiation of beryllium, and to provide a design outline for a modified MFTM with integrated neutron moderators and reflectors.

Staff:

G. Bürkle
K. Ehrlich
A. Möslang
P. Vladimirov
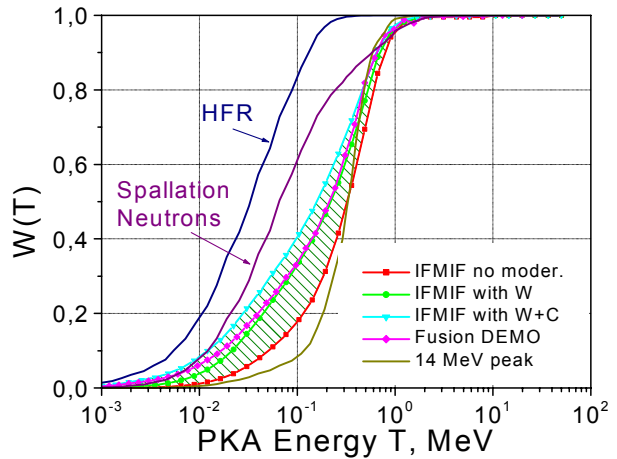


Fig. 3: W(T) function for the HCPB DEMO blanket in comparison with IFMIF (hatched area), the mixed spectrum reactor HFR and a typical spallation source

Literature:

[1] A. Möslang, K, Ehrlich et. al; Suitability and feasibility of the International Fusion Irradiation Facility (IFMIF) for fusion materials studies; Nucl. Fusion, 40; No. 3Y, (2000) p. 319-327.

[2] K. Ehrlich, E.E. Bloom, and T. Kondo, International Fusion Materials Strategy, Journ. Nucl. Mater. 283-287 (2000), 79.

[3] E. Daum, How to improve the irradiation conditions for the international fusion materials irradiation facility, Journ. Nucl. Mater, 282-287 (2000) 1001.

[4] Y. Lizunov, A. Möslang, A. Ryazanov and P. Vladimirov New Evaluation of Displacement and Tritium Production for Breeder Ceramics under IFMIF, Fusion and Fission Neutron Irradiation, ICFRM-10, Oct. 14-19, 2001, Baden-Baden

[5] V. Chernov, R. Ferdinand, R. A. Jameson, H. Klein, J-M. Lagniel, M. Martone, H. Matsui, A. Moeslang, T. Muroga, H. Nakamura, C. Piaszczyk, J. Rathke, B. Riccardi, T.E. Shannon, M. Sugimoto, H. Takeuchi, S.J. Zinkle IFMIF Status and Perspectives, ICFRM-10, Oct. 14-19, 2001, Baden-Baden

# Nuclear Data Base

## TTMN-001
## EFF/EAF Data File Update, Processing and Benchmark Analyses

The European Fusion File / Activation File (EFF/EAF) projects aim at developing a qualified data base for nuclear calculations of fusion reactors. The related Task TTMN-001 of the EFDA technology work programme is devoted to the evaluation, processing, application, and benchmarking of required nuclear cross section and uncertainty data.

The focus of the FZK contribution to Task TTMN-001 is on the qualification of new and updated EFF data evaluations by means of computational benchmark analyses. This includes sensitivity and uncertainty analyses and the processing of the related co-variance data. In addition, advanced computational schemes are being developed for sensitivity calculations based on the Monte Carlo technique.

### Benchmark Analyses of the Cr-52 EFF-3 Data Evaluation

The new Cr-52 EFF-3.01 data are based on EFF-2.4 with a new resonance parameter evaluation up to 1.2 MeV neutron energy. Over the reporting period, extensive testing has been performed for Cr-52 EFF-3.01 data including the processing of the ENDF data file with NJOY/ACER, cross-section comparisons and cross-checks as well as MCNP benchmark calculations for a 14 MeV neutron transmission experiment performed previously on a spherical chromium shell at the Oktavian facility (University of Osaka, Japan) [1]. The benchmark analyses revealed that the energy range above 1 MeV has to be reconsidered to arrive at a better agreement with the measured Oktavian leakage spectrum data (Fig. 1). The 14 MeV neutron emission cross-section, on the other hand, compares favourably with the Vonach et al. evaluation of experimental Cr-nat data (Fig. 2).
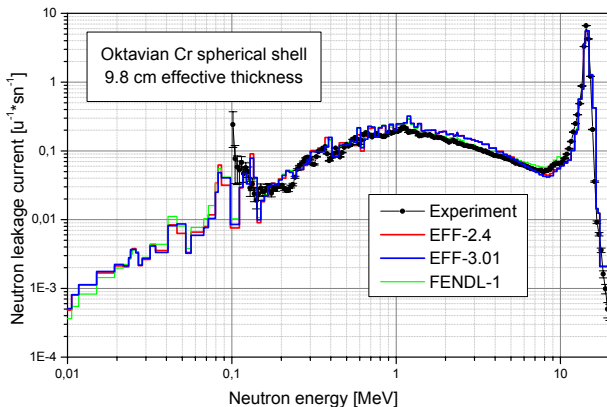


Fig. 1: Neutron leakage spectra of the Oktavian Cr transmission experiment.

### Processing of the Be-9 EFF-3.03 Data Evaluation.

The recent Be-9 EFF-3.03 data evaluation provides a decomposition of the (n,2n) reaction into 16 partial channels. The related cross-sections, energy-angle distributions and co-variance data are stored in the ENDF file in MT sections 875-890. Substantial changes had to be applied to the NJOY modules RECONR and ACER to enable the processing of these data. The resulting ACE data file has been successfully checked for completeness and consistency and is thus ready for application tests [2].

The Be-9 co-variance data could be processed after introducing some modifications to the NJOY module ERROR34 which are specific to the EFF-3.03 data representation [3,4]. Be-9 EFF-3 co-variance matrices were prepared in the VITAMIN-J 175 group structure for use with forthcoming uncertainty analyses taking into account the partial (n,2n) reaction channels stored in MT sections 875-890.
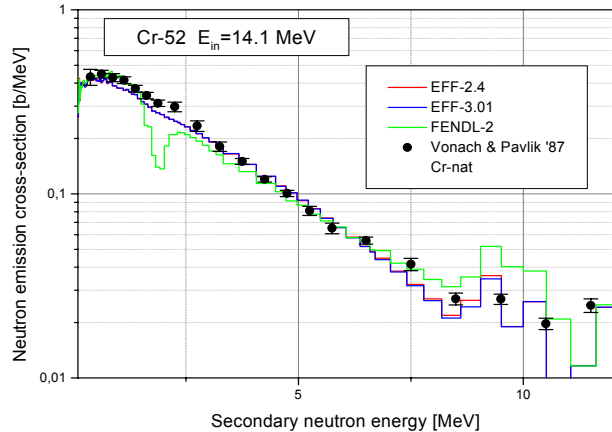


Fig. 2: Cr-52 neutron emission cross-section at 14 MeV incident neutron energy

### Algorithm for Monte Carlo Calculation of Sensitivities to Secondary Angular Distributions

Within the running EFF-programme, development work is being conducted on computational schemes for the calculation of point detector sensitivities to secondary distributions with the objective to implement them into the MCNP code. Suitable algorithms have been previously elaborated for the Monte Carlo calculation of SAD sensitivities based on the differential operator method [5].

Over the reporting period, a sensitivity algorithm based on the use of the Legendre series expansion for the SAD was implemented into MCSEN, a local update to the MCNP Monte Carlo code [6]. MCSEN is thus capable of calculating point detector sensitivities for the SAD Legendre coefficients. The implemented SAD sensitivity algorithm has been verified by means of numerical tests and MCNP comparison calculations with perturbed cross-section data.

### Benchmark for Monte Carlo Sensitivity Calculations

The Monte Carlo technique for calculating point detector sensitivities of excitation functions as implemented in MCSEN has been recently validated through a computational benchmark on probabilistic and deterministic sensitivity and uncertainty calculations [7].

Over the reporting period, the benchmark on the 7.5 cm thick iron spherical shell has been extended to validate the SAD sensitivity approach of MCSEN as described above. Comparison calculations for SAD sensitivities were performed with the deterministic SUSD3D code based on first order perturbation theory [8] by making use of direct and adjoint flux spectra provided by one-dimensional ANISN transport calculations. In addition, direct comparison calculations with perturbed angular cross-section data were performed both with ANISN and MCNP. Good agreement was achieved for the individual sensitivity profiles as well as for the calculated flux changes as compared to direct calculations [9]. As an illustrative

example, Fig. 3 shows the relative flux change caused by decreasing the first Legendre coefficient of the elastic scattering SAD by 5%.  The Monte Carlo technique for calculating point detector sensitivities to secondaries' angular distributions is thus qualified for application to sensitivity analyses of fusion integral experiments.
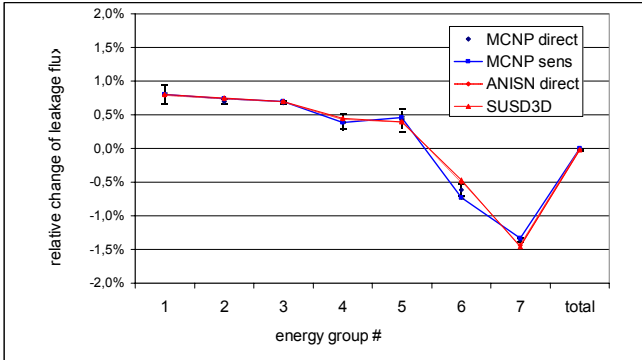


Fig. 3:   Relative flux change due to 5% decrease of first elastic scattering moment

Staff:

U. Fischer
D. Leichtle
I. Kodeli
R. Perel
S. P. Simakov
I. Schmuck

Literature:

[1]  U. Fischer, S. Simakov, I. Schmuck: Benchmark Analyses of the New Cr-52 EFF-3.01 Data Evaluation, EFF-DOC-779, (May 2001)

[2]  D. Leichtle, I. Schmuck, U. Fischer: Status of the 9Be-EFF-3.0/NMOD=3 data processing with ACER, EFF-DOC-782 (May 2001)

[3]  I. Kodeli, Processing of EFF-3 Co-variance matrices with extended options and application tests with SUSD3D uncertainty calculations, EFF-DOC-758 (December  2000)

[4]  I. Kodeli, Processed co-variance matrices for Be-9, Evaluation EFF-3.0, EFF-DOC-745 (December  2000)

[5]  R. L. Perel, Algorithm for Monte Carlo calculation of sensitivities to secondary angular distributions, EFF-Doc-703 (December 1999)

[6]  R. L. Perel, Implementation of an algorithm for Monte Carlo calculation of sensitivities to secondary angular distributions in MCNP, EFF-Doc-749 (December 2000)

[7]  U. Fischer, I. Kodeli, C. Konno, R. Perel, Inter-comparison of Monte Carlo and SN Sensitivity Calculations for a 14 MeV Neutron Benchmark, Proceedings of the Monte Carlo 2000 Conference, Lisbon, October 23-26, 2000, 791-796.

[8]  I. Kodeli, Multidimensional Deterministic Nuclear Data Sensitivity and Uncertainty Code System: Method and Application, Nucl. Sci. Eng., 138, 45-66 (2001)

[9]  U. Fischer, I. Kodeli, R. Perel, Sensitivity to secondaries' angular distributions - Inter-comparison of Monte Carlo and SN Calculations for a 14 MeV Neutron Benchmark, EFF-DOC-780 (May 2001)

## TTMN-002
## Benchmark Experiments to Validate EFF/EAF Data

The European Fusion File / Activation File (EFF/EAF) projects aim at developing a qualified data base for fusion technology applications. The related Task TTMN-002 of the EFDA technology work programme is devoted to benchmark experiments and their computational analysis with the objective to validate the EFF/EAF data for fusion neutronics and activation calculations. The focus of the FZK contribution to Task TTMN-002 is on activation experiments in a white neutron spectrum as well as MCNP based transport and sensitivity/uncertainty analyseis of 14 MeV neutron transport benchmark experiments.

## SiC Neutron Transport Benchmark Experiment

### TTMN-002-3:
### MCNP Transport and Sensitivity/Uncertainty Analysis

In preparation for the computational analysis of the neutron and photon spectrum measurements of TU Dresden (TTMN-002, deliverable 2) first MCNP calculations have been performed to estimate the neutron flux spectra at different detector locations inside the SiC assembly. These calculations were performed on the basis of a preliminary MCNP model using silicon cross-sections from the FENDL-2 data library. A new EFF-3 data evaluation for Si-28 is currently in preparation and will be ready for the final analyses of the SiC benchmark experiment to be conducted by the end of this year.

## Activation Experiments in White Neutron Spectrum

### TTMN-002-6
### Eurofer-97 steel

During the previous reporting period, a sample of Eurofer-97 had been activated in the Karlsruhe d-Be neutron field for 43 hours at about $1.2 \times 10^{11}$ n cm-2s-1. The activated sample was investigated by gamma spectrometry using a high purity germanium detector. Spectra were taken at several different cooling times up to 189 days. By analyzing the gamma spectra, specific activities in Bq per kg of sample were obtained for 17 different product nuclides, that have half lives between 24 hours and 5.3 years. These were compared to specific activities calculated by EASY-99 for the same cooling times. For seven of the nine different radio-nuclides produced from the nominal constituents, Fe, Cr and W, the calculation-over-experiment (C/E) ratios vary from 0.66 to 1.54, with experimental uncertainties of mostly ±15%. The two remaining results are C/E = 3.5 for the sequential charged particle reaction 56Fe(p,n)56Co and C/E = 49 for 54Fe(n,t)52Mn. The conclusion is that the 54Fe(n,t) cross section (and, likely, other (n,t) cross sections as well) in EAF-99 needs a major revision, while the other neutron cross sections involved are good to within a factor of 1.5. More details are found in Refs.[1,2].]

## TTMN-002-9
## Tungsten

Tungsten is important both as an alloy in reduced-activation steels such as F82H or Eurofer and as a refractory material envisaged, e.g., for divertor plates in fusion reactors. Samples of pure tungsten plate (99.95% W) were activated in the white neutron field of the Karlsruhe d-Be neutron source[3]. Gamma spectra were taken at cooling times covering the range from 14 minutes to 190 days. By analyzing the gamma spectra, specific activities in Bq per kg of sample material were obtained for 15 different product nuclides, that have half lives ranging from 7 minutes to 121 days. These were compared with specific activities calculated for the same cooling times by EASY-99. The C/E ratios range from 0.46 to 3.09, with experimental uncertainties of ±15% to ±40%. Interestingly, both of the extreme C/E refer to (n,$\alpha$) reactions: 0.46 for the 182 W(n,$\alpha$)179Hfn and 3.09 for the 183W(n,$\alpha$)180Hfm reaction. In contrast to our former activation experiments on other materials, no products from sequential charged particle reactions were observed in this case, which certainly is a consequence of the high atomic number (electric charge) of the tungsten nuclei. The conclusion is that most of the EAF cross sections for the W isotopes are reasonably good, but that the(n,$\alpha$) reactions should be revised. More details are found in Refs.[2,3].

Staff:

U. Fischer, IRS
H. Giese, IHM
U. von Möllendorff, IRS
H. Tsige-Tamirat, IRS

Literature:

[1] U. von Möllendorff, H. Tsige-Tamirat and H. Giese, Activation of Eurofer-97 steel in the Karlsruhe d-Be neutron field. EFF-DOC-770 (May 2001).

[2] U. von Möllendorff, H. Tsige-Tamirat, H. Giese and F. Maekawa, Integral activation experiments on fusion relevant materials using a white fast-neutron field. To be published as FZKA report

[3] U. von Möllendorff, H. Tsige-Tamirat and H. Giese, Activation of tungsten in the Karlsruhe d-Be neutron field. To be entered in the EFF-DOC series.

**TTMN-002-7**
**Activation Experiment with EUROFER in Fusion Peak Neutron Field**

**1. Introduction**

The radioactivity induced by neutrons in the materials of a fusion device represents a central topic of safety-related investigations. Radionuclides with a broad range of half-life have to be included in the corresponding analyses. The short-term radioactivity (half-life from minutes to weeks) is mainly of interest to heat production and shut-down dose rates, whereas the long-term radioactivity (half-life of the order of 10–100 years or more) determines the waste management.

The spectrum of the neutron flux in a fusion device consists of two parts, a D-T fusion peak at 14 MeV and a continuum ranging down to thermal energies. The radioactivity is mainly produced at 14 MeV neutron energy, where the number of open reaction channels is a maximum, and at thermal energy, where cross section values are large. In the present work, the radioactivity induced by 14-MeV neutrons in the structural material EUROFER was investigated.

In a calculation with the European Activation System (EASY-99), [1]) EUROFER-97 was taken to be irradiated with 14-MeV neutrons of a flux density corresponding to the power of 1 MW/m$^2$, for a period of one year, using the elemental composition of the material as determined by X-ray fluorescence analysis (C. Adelhelm, FZ Karlsruhe). The results obtained for the contact dose rate as a function of the decay time after irradiation are shown in Fig.1.
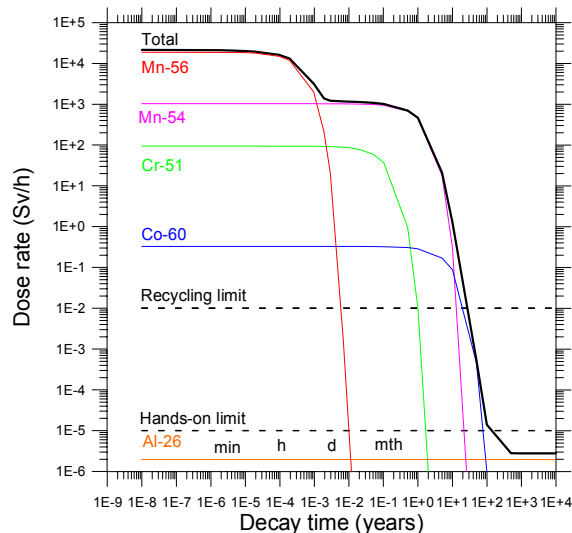


Fig. 1: Contact dose rate of EUROFER-97 after irradiation with 14-MeV neutrons of 1 MWa/m$^2$ as a function of decay time. Besides the total dose rate the contributions of dominant radionuclides are inserted

It is expected that the recycling limit is achieved at ~30 years and the hand-on limit at ~ 200 years.

**Experiment**

A detailed analysis of this calculation suggested carrying out at least two irradiations, a very short one to determine the radioactivity of nuclides with half-life of the order of minutes and a second one to investigate the activity of nuclides in the middle part of the figure.

More details were presented at ICFRM-10 [4].

The irradiations were performed at the high-intensity neutron generator SNEG-13 [2] at Sergiev Posad. The 14-MeV neutrons had, depending on the sample position, a mean energy of $<E_n>$ = 14.93 MeV and a spread of $\Delta E_n = \pm 0.27$ MeV and $E_n$ = (14.37 $\pm$ 0.12) MeV. The applied neutron fluences were determined by the $^{93}$Nb(n,2n)$^{92m}$Nb activity induced in thin niobium foils.

Gamma-ray spectra were taken from the irradiated samples at several decay times with Ge(Li)-spectrometer. The gamma-activities identified by energy and half-life were used to determine nuclide activities with gamma-yield data from EASY.

The results of two experiments are compared in Table 1 with the calculated values of EASY-99.

Table 1: Radionuclides investigated in Experiment 1 (mean neutron energy 14.93 MeV, irradiation time 3.0 min, neutron fluence applied 3.36·10$^{11}$ cm$^{-2}$) and in Experiment 2 (mean neutron enrgy 14.93 MeV, irradiation time 13.93 h, neutron fluence 2.4·10$^{14}$ cm$^{-2}$), their half-life, the producing nuclear reactions with their contribution to the activity, and the ratios of calculated-to-experimental activity (C/E)

| Radionuclide | Half-life | Reaction Contribution (%) | | C / E |
|---|---|---|---|---|
| $^{28}$Al | 2.24 min | $^{28}$Si (n,p) | 99.5 | 1.00 ± 0.32 |
| $^{51}$Ti | 5.8 min | $^{51}$V(n,p) <br> $^{54}$Cr(n,α) | 68.1 <br> 31.8 | 0.91 ± 0.20 |
| $^{52}$V | 3.75 min | $^{52}$Cr(n,p) <br> $^{53}$Cr(n,d) <br> $^{55}$Mn(n,α) | 94.5 <br> 3.5 <br> 2.0 | 0.74 ± 0.06 |
| $^{53}$V | 1.62 min | $^{53}$Cr(n,p) <br> $^{54}$Cr(n,d) | 97.8 <br> 2.2 | 0.82 ± 0.10 |
| $^{56}$Mn | 2.58 h | $^{56}$Fe(n,p) <br> $^{57}$Fe(n,d) | 99.2 <br> 0.8 | 0.94 ± 0.04 |
| $^{57}$Mn | 1.6 min | $^{57}$Fe(n,p) <br> $^{58}$Fe(n,d) | 97.7 <br> 2.3 | 1.11 ± 0.16 |
| $^{53}$Fe | 8.51 min | $^{54}$Fe(n,2n) | 100 | 1.33 ± 0.56 |
| | | | | |
| **$^{24}$Na** | 14.97 h | $^{27}$Al(n,α) <br> $^{27}$Al(n,α)IT | 69.1 <br> 30.9 | 0.80± 0.21 |
| **$^{48}$Sc** | 1.82 d | $^{48}$Ti(n,p) <br> $^{51}$V(n,α) | 5.1 <br> 94.9 | 1.02 ± 0.11 |
| **$^{51}$Cr** | 27.7 d | $^{52}$Cr(n,2n) <br> $^{54}$Fe(n,α) | 88.7 <br> 11.3 | 1.08 ± 0.07 |
| **$^{54}$Mn** | 312 d | $^{55}$Mn(n,2n) <br> $^{54}$Fe(n,p) <br> $^{56}$Fe(n,t) | 22.5 <br> 76.9 <br> 0.6 | 0.80 ± 0.05 |
| **$^{56}$Mn** | 2.58 h | $^{56}$Fe(n,p) <br> $^{57}$Fe(n,d) | 99.2 <br> 0.8 | 0.92 ± 0.10 |

In Experiment 3, the parameters were similar to Experiment 2, but the mean neutron energy was 14.37 MeV.

**Results**

The short-term radioactivity was investigated in Experiment 1. The seven activities measured comprise 97% of the total activity expected. The sum of the activities is underestimated with EASY-99 by less than 20%. In a power plant it is expected that nuclides with C/E values closer to unity will contribute more, meaning that this value may be considered as an upper limit.

The sum of activities of the six nuclides, measured in Experiments 2 and 3, agree within ~ 20% with the EASY-99 result. These nuclides are also dominant for the dose rate in power plant conditions. Together with the C/E obtained in previous measurements [3] for $^{56}$Co, $^{58}$Co and $^{60}$Co, the radioactivity calculated for reactor neutron fluxes can be validated at this level.

The dominant nuclides for the long-term radioactivity in reactor fluxes are $^{26}$Al ($T_{1/2} = 7 \cdot 10^5$ y, 70% of the dose rate at t = $10^3$ y) produced by $^{27}$Al(n,2n) and $^{53}$Mn ($T_{1/2} = 4 \cdot 10^6$ y, 27% of the dose rate at t = $10^3$ y) produced by $^{54}$Fe(n,d). The small Al content of the EUROFER-97 sample was confirmed by the C/E obtained for the $^{24}$Na activities ($^{27}$Al(n,$\alpha$)). The uncertainties of the calculated values for these two channels were estimated by EASY-99 to be at 30% and 60%, respectively.

Summarising it may be stated that the reduced-activation behaviour of EUROFER-97, as predicted by EASY-99 (Fig. 1) is satisfactorily confirmed by the irradiation experiments.

Staff:

H. Freiesleben
D. Richter
K. Seidel
S. Unholzer

Literature

[1] R. A. Forrest and J.-Ch. Sublet, Reports Culham Science Centre, UKAEA FUS 407 and UKAEA FUS 409, December 1998.

[2] V. D. Kovalchuk, A. V. Krasilnikov, V. M. Bagaev, S. I. Bobrovnik, Vit. D. Kovalchuk, V. I. Trotsik, Report IAE-5589/8, Russian Research Centre "Kurchatov Institute", Moscow, 1992.

[3] D. V. Markovskij, R. A. Forrest, H. Freiesleben, V. D. Kovalchuk, D. Richter, K. Seidel, V. I. Tereshkin and S. Unholzer, Fusion Engineering and Design 51 (2000) 695.

[4] K. Seidel, R. A. Forrest, H. Freiesleben, V. D. Kovalvhuk, D. V. Markovskij, D. V. Maximovich and S. Unholzer, 10th International Conference on Fusion Reactor Materials, October 14-19, 2001, Baden-Baden, Germany.

## T 426
## Experimental Validation of Shut-down Dose Rates

The nuclear design of ITER is based on calculations with neutronic codes and nuclear data having inherent uncertainties. Experimental validation is required for design parameters which affect the feasibility of the machine and its safe operation. The shut-down dose rate e. g. must be assessed with high accuracy for guaranteeing occupational safety during hands-on maintenance inside the ITER cryostat.

To this end, a neutronics experiment has been performed at the Frascati Neutron Generator [1] with the objective to validate dose rate calculations for the radiation fields inside the ITER cryostat after reactor shut-down. The associated ITER Task T426 has been conducted in co-operation of ENEA Frascati, TU Dresden (TUD) and FZ Karlsruhe (FZK). This report summarises the experimental results obtained by TUD and their computational analysis by FZK.

### Experimental set up and irradiation

The experimental assembly consisted of a block of stainless steel (SS316) and water equivalent material (Perspex) with a total thickness of 71.4 cm and a lateral size of 100 cm x 100 cm. Detectors were arranged in a cavity of 12.6 cm x 12.0 cm cross section, as shown in Fig.1. A void channel (inner diameter of 2.7 cm) between 14 MeV neutron source and cavity was inserted to simulate a streaming effect.
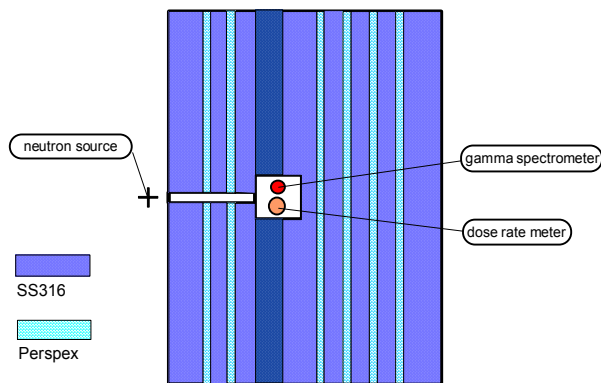


Fig. 1:  Vertical cut of the experimental assembly

The assembly was irradiated by 14 MeV neutrons over a period of two days (August 29-30, 2000) with a total neutron source yield of $1.95 \cdot 10^{15}$.

### Neutron flux spectrum during irradiation

When calculating the neutron induced activity inventory in the material assembly, first of all the neutron flux spectrum distribution must be provided. Therefore, the neutron flux spectrum was measured in the centre of the cavity with a NE 213 spectrometer [2] during irradiation.

The measured spectrum is compared in Fig. 2 with the result of a Monte Carlo calculation (code MCNP-4C, [3]) based on data of the Fusion Evaluated Nuclear Data Library (FENDL/MC-2.0, [4]). The dominant part at the detector position on the streaming channel axis is the 14 MeV neutron peak. The measured fluence of neutrons with E > 13.7 MeV per one source neutron amounts to $(5.91 \pm 0.35) \cdot 10^{-5}$. The corresponding calculated

value is $(5.96 \pm 0.32) \cdot 10^{-5}$, resulting in a ratio of calculated-to-experimental fluence of C/E = 1.01 ± 0.07, which represents a good basis for the next steps of investigation.
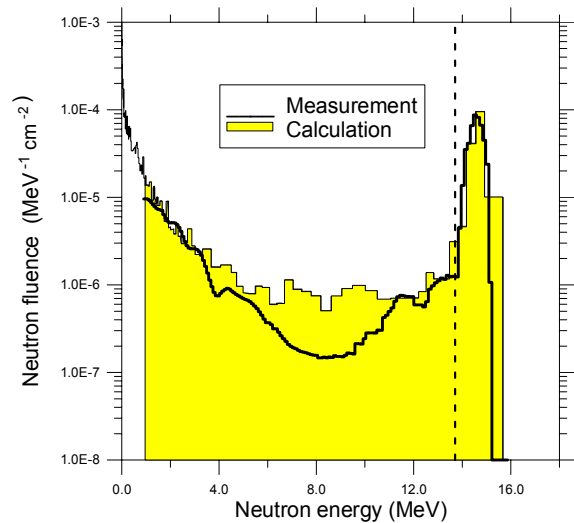


Fig. 2:  Comparison of measured and calculated fast neutron fluence, normalised to one source neutron

### Dose rate as a function of decay time

The gamma dose rate in the cavity was measured with a tissue-equivalent scintillator (4.6 cm in both diameter and height) quasi-continuously over a period from 73 min up to 20 d after the end of the irradiation.

The computational analysis was performed with a rigorous two-step (R2S) method developed in the framework of ITER Task T426 at FZK [5] and a direct one-step method (D1S) developed previously at ITER JCT Garching [6]. The R2S approach makes use of MCNP for the transport calculations of neutrons and decay photons in two sequential steps and FISPACT [7] for the activity inventory calculation. MCNP and FISPACT are linked through a suitable coupling scheme for the automated routing of neutron flux spectra and decay gamma sources. The D1S approach uses an ad hoc modified version of MCNP to handle the neutron and decay gamma transport in one single Monte Carlo run without any activation calculation. Nuclide specific adjustment factors are then applied to account for the proper decay rates at the considered decay times taking into account the actual irradiation history. In either approach, cross-section data from the FENDL-2.0/MC [4] (Monte Carlo transport) and FENDL-2.0/A [8] (activation) were used.

Calculated and measured dose rates are compared in Fig. 3 a and b as a function of the cooling time. There is an overall satisfactory agreement over the considered range of cooling times. The detailed C/E (calculation/ experiment) comparison (Fig. 3b) reveals an underestimation of the measured dose rate at short cooling times (less than ≅ 2 days) by up to 15 % in case of the R2S calculation. The D1S-calculation underestimates the measured dose rate by 20 to 25 %. The dominating dose rate contributions are due to $^{56}$Mn (few hours cooling time) and $^{57}$Ni (1 – 5 days cooling time). At larger cooling times, the dominant $^{58}$Co contribution gives rise to an overestimation of up to 10%.

### Flux spectra of decay gamma-rays

Decay photon spectra were measured with a NE 213 spectrometer (diameter and height of the scintillator: 3.8 cm)

simultaneously to the dose rate at t = 2.08 h, 15.9 h, 25.2 h, 4.0 d, 8.2 d, 12.2 d and 19.3 d after the end of the irradiation.
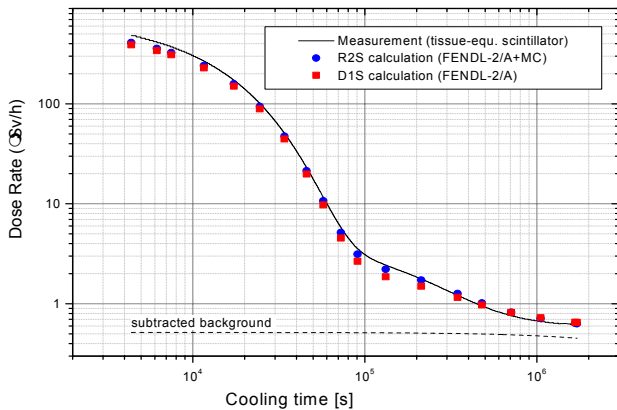


Fig. 3a: Comparison of calculated and measured dose rates
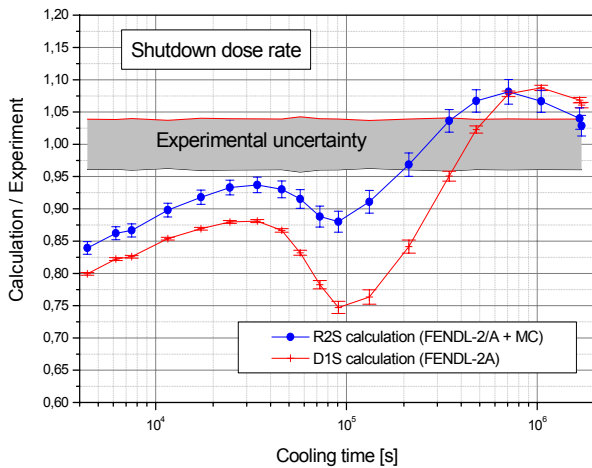


Fig. 3b: C/E (calculation/ experiment) comparison for the dose rate measured with the tissue-equivalent scintillator

The measured decay gamma ray spectra can be well reproduced by the calculations, see e.g. Fig. 4 for the spectra at 15.9 h after irradiation. There is, however, a distinctive difference between the spectra calculated by the D1S and the R2S method due to different representations of the decay gamma ray emission spectra. While the R2S-calculation handles the decay gamma ray spectra in the 24 group structure of the FISPACT code, the D1S procedure makes use of discrete gamma lines for the decay gamma ray emission spectra of the ad-hoc prepared data library.

Staff:

Y. Chen
U. Fischer
H. Freiesleben
D. Richter
K. Seidel
S. Unholzer
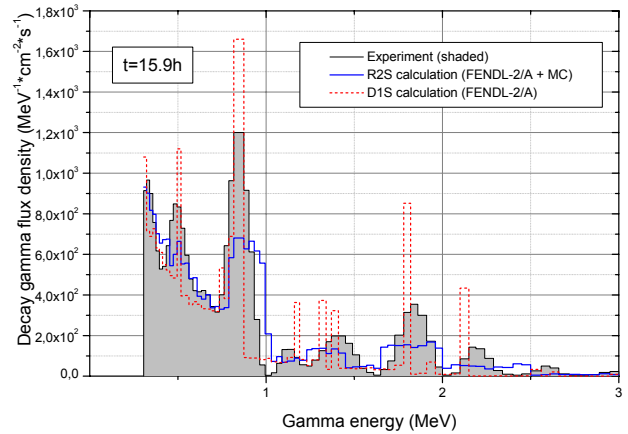


Fig. 4:  Comparison of measured and calculated decay gamma ray spectra at 15.9h after irradiation

Literature:

[1]  M. Martone, M. Angelone and M. Pillon, The 14 MeV Frascati neutron generator, Journal of Nuclear Materials 212 (1994) 1661.

[2]  S. Guldbacke, H. Klein, A. Meister, J. Pulpan, U. Scheler, M. Tichy and S. Unholzer, Response matrices of NE 213 scintillation detectors for neutrons, Reactor Dosimetry ASTM STP 1228, p. 310, Philadelphia, 1995.

[3]  J.F. Briesmeister (ed.), MCNP - A General Monte Carlo N-Particle Transport Code, Version 4C, Los Alamos National Laboratory, Report LA-13709-M, April 2000.

[4]  H. Wienke and M. Herman, FENDL/MG-2.0 and FENDL/MC-2.0 processed cross-section libraries, IAEA-NDS-176, 1998.

[5]  Y. Chen, U. Fischer, H. Tisge-Tamirat, Rigorous MCNP Based Shutdown Dose Rate Calculations, Forschungs-zentrum Karlsruhe, Internal Report, January 2001

[6]  D. Valenza, H. Iida, R. Plenteda, R. T. Santoro, Proposal of Shutdown Dose Estimation Method by Monte Carlo Code, Fus. Eng. Des. 55 (2001), 411-418.

[7]  R. A. Forrest, J-Ch. Sublet, "FISPACT-99: User manual", Report UKAEA FUS 407, December 1998

[8]  A.B. Pashchenko, H. Wienke, J. Kopecky, J.-Ch. Sublet and R.A. Forrest, "FENDL/A-2.0 Neutron Activation Cross Section Library", IAEA-NDS-173, Rev. 1, October 1998

## FU05-CT 2000-00134 (EFDA/00-564)
## ITER-FEAT Shut-down Dose Rate Analysis by Rigorous Method

When operating ITER, a reliable assessment of the shutdown dose rate distribution is needed inside the cryostat to answer the question of the wait time after the machine shutdown until personal access can be allowed for maintenance or repair of components located between the vacuum vessel and the cryostat walls. This requires a suitable computational procedure validated through a nuclear experiment.

In the framework of ITER Task T426, FZK has developed a rigorous 2-step (R2S) computational system for the calculation of the shutdown dose rate distribution in full three-dimensional geometry [1] . The system is based on the use of the MCNP [2] transport and the FISPACT [3] inventory code linked through a suitable coupling scheme for the automated routing of decay gamma sources and neutron flux spectra. The decay gamma source distribution is sampled in a source routine linked to MCNP. This enables to conduct shut-down dose rate analyses for large and complex reactor systems. The R2S approach has been successfully validated in the framework of ITER Task T-426 [4,5]. In the framework of contract FU05-CT 2000-00134 (EFDA/00-564), the R2S method was then applied to the shutdown dose rate analysis of the ITER-FEAT mid-plane maintenance port with the objective to compare the results with those of simplified methods such as the direct 1-step (D1S) approach [6] developed by the ITER JCT.

A 3D torus sector [20°] MCNP model provided by the ITER JCT Garching was used for the shutdown dose rate analysis. Fig. 1 shows a horizontal cut through the mid-plane maintenance port section with MCNP cell numbers indicated. Neutron flux spectra and decay gamma ray sources were calculated for a total of 1663 geometry cells. The assumed irradiation history follows the ITER M-DRG1 irradiation scenario [7] with a total first wall neutron fluence of 0.306 $MW/m^2$ after 20 years.
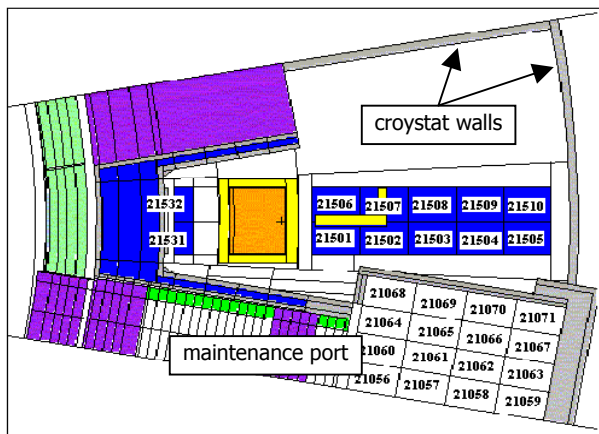


Fig. 1: Mid-plane port section of MCNP model (horizontal cut)

R2S and D1S shut-down dose rate calculations were performed with the same MCNP geometry model for cells #21531, 21532 in between the vacuum vessel and the TF-coil, cells #21501 – 21510 outside and cells #21056 – 21071 inside the mid-plane extension port as shown in Fig. 1. Adjustment factors, required for the D1S calculation of the shut-down dose rate, were derived on the basis of FISPACT/FENDL-2/A inventory calculations.

Fig. 2 displays the dose rates as calculated by the R2S approach for the cells #21531, 21532 and 21501-21510 outside the maintenance port as a function of the cooling time. It is noted that cells #21502-21510 are shielded to some extent by the TF-coils. Hence the dose rate limit of 100 μSv/h is reached very quickly in this region. Cells #21531 and 21532, placed in front of the TF coil, are only shielded by the blanket and the vacuum vessel and, therefore, remain above the 100 μSv/h dose rate limit over the total 30 days time period considered.
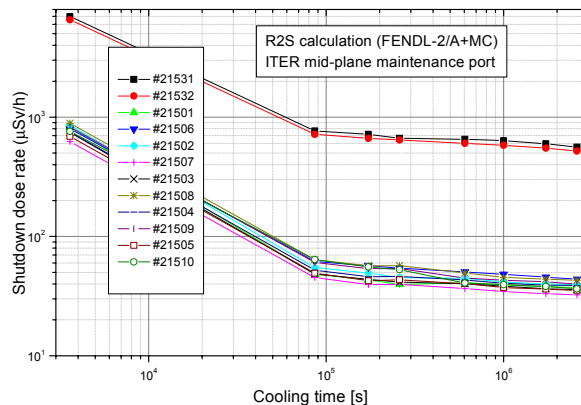


Fig. 2: Shutdown dose rates calculated by the R2S system

The shutdown dose rates calculated by the R2S procedure are in general larger by a factor 2 to 3 than those calculated by the D1S approach. This is in contrast to the T-426 irradiation experiment, where the maximum difference between the R2S and the D1S dose rate results is in the order of 20 %. Detailed investigations revealed that this discrepancy is due to different conditions of the T-426 experiment with a hard neutron spectrum and the ITER mid-plane maintenance port with a degraded neutron spectrum resulting in different radio-nuclide production paths and different neutron flux gradients [8].

Staff

Y. Chen
U. Fischer

Literature:

[1] Y. Chen, U. Fischer, H. Tisge-Tamirat, Rigorous MCNP Based Shutdown Dose Rate Calculations, Forschungs-zentrum Karlsruhe, Internal Report, January 2001

[2] J.F. Briesmeister (ed.), MCNP - A General Monte Carlo N-Particle Transport Code, Version 4C, Los Alamos National Laboratory, Report LA-13709-M, April 2000.

[3] R. A. Forrest, J-Ch. Sublet, "FISPACT-99: User manual", Report UKAEA FUS 407, December 1998

[4] H. Freiesleben et al., Experimental Validation of Shut-down Dose Rates: Measurement of dose rates, decay gamma rays and neutron flux, Report TUD-IKTP/01-01, March 2001

[5] P. Batistoni et al, Experimental Validation of Shut-down Dose Rates, Report ENEA FUS TN GE-VD-Q-001, June 2001

[6] D. Valenza, H. Iida, R. Plenteda, R. T. Santoro, Proposal of Shutdown Dose Estimation Method by Monte Carlo Code, Fus. Eng. Des. 55 (2001), 411-418.

[7] K. Moshonas, Operational safety assessment specifications, Revision 1, Memo, SEHG, ITER Garching JWS, June 7, 2000

[8] Y. Chen, U. Fischer, ITER-FEAT Shutdown Dose Rate Analysis by Rigorous Method, Forschungszentrum Karlsruhe, Internal Report, September 2001

# Safety Analysis and
# Environmental Impact

## SEA 3 (N 11 TD 72)
## Reference Accident Sequences – Magnet Systems (2)

**Subtask 2: Magnet System Safety**

Within the subtask 3.2 FZK-IRS investigates the accident sequence 'unmitigated quench' for ITER FEAT superconducting coils.

In terms of model development the convergence behavior of the MAGS module COINLOSS (COil INsulation LOSS) has been improved. Further COINLOSS has been modified to handle now also PF coils which have a different arrangement of structural material and insulation than the TF (Toroidal Field) coils. To determine the volume of molten material an additional tool in MAGS has been prepared. To simulate arcs during an unmitigated quench a simplified arc model has been introduced. Improved material properties for Glass Epoxy (GE), measured at IRS, became available and have been introduced into MAGS.

The updated version of COINLOSS has been applied again to the sequence of an unmitigated quench in a TF coil. The previous results could be confirmed: The cable insulation keeps the current and the heat within the cable space until insulation failure. This keeps the surrounding radial plate relative cold. At insulation failure the heat source and the electrical current leave the cable space and move into the radial plate. For a short period of time practically the complete copper volume of a cable is molten but due to the improved heat transfer between cable space and plate the copper is solidified after about 220 s after begin of melting. Variation of material properties changes the amount of stored energy between 5 GJ and 6 GJ. Inclusion of an arc model has no big consequences. This is reasonable because most of the voltage is caused by the ohmic resistance of the intact portions of the cable. A variation of this voltage by arcs, typically some percent of the total plate voltage, is unimportant.

Consideration of Helium flow has lead to extreme pressures inside of cables. The relevance of this finding is not yet clear because the model assumes the friction factor of an intact cable bundle even though the strands are molten. In the vicinity of the cable ends the situation is also less clear. Here Helium at copper melting temperature and high velocities is leaving the cables.

The analysis of the PF3 (Poloidal Field) coil, having the largest stored energy out of the PF coils, shows that copper melt temperature is surpassed for about 50 m of the innermost turn. The steel structure around, carrying here also current, is not much colder but does not reach the steel melting temperature. Because there is insulation around each cable, the heat to solidify the melt again has to flow through two layers of insulation. This takes more time than in the case of the TF coils. However, as the energy dumped into these structures is lower, solidification in total takes only 100 s more than in the TF case.

Staff:

R. Meyder

Literature:

[1] R.Meyder : Second report on unmitigated quench. ITER Task G 81 TD 12 FE, Nov. 2000

[2] R.Meyder : Survey analysis of an arc shorting a TF coil during dump. ITER Task G 81 TD 12 FE, Oct. 2000

[3] R. Meyder : Analysis of an arc shorting a TF coil during dump in the vicinity of the Cryostat. ITER Task G 81 TD 12 FE, Nov. 2000.

[4] R. Meyder : Unmitigated coil quench. Final report. ITER Task G 81 TD 12 FE. May 2001

# SEA 3.5
# In-Vessel Hydrogen Deflagration/Detonation Analysis

## Three-Dimensional ITER First-Wall Coolant Leak Simulation with GASFLOW

### 1. Introduction

To better define and justify in-vessel hydrogen limits for the ITER-FEAT safety assessment and licensing process, three-dimensional hydrogen distribution, deflagration and/or detonation calculations are necessary for different accident sequences. The first investigated scenario assumed air ingress, production of 5 kg hydrogen, formation of a stoichiometric hydrogen-air mixture, and ignition of a local detonation [1]. The objective of this work is to investigate the formation of combustible hydrogen-air-steam mixtures in the system for a detailed accident sequence with special emphasis on size, location, composition and hazard potential of the evolving reactive cloud. The results can be used to investigate the feasibility of risk reducing counter measures.

### 2. Accident Scenario

The ex-vessel LOCA scenario leading to an in-vessel release of steam and air was selected for the analysis because it is one of the most challenging accident sequences for the ITER safety systems [2]. It is assumed that a break in the heat transfer system occurs in the TCWS (Tokamac Cooling Water System) vault without plasma shut-down (Fig.1). The cooling of the affected first-wall section (one loop out of three) is drastically reduced, leading to structural failure of the first wall and an in-vessel breach within a few minutes. Steam from the cooling system is transported through the cooling pipe and the leak into the vacuum vessel, where it can contact hot beryllium. Recent MELCOR calculations suggest a production of about 15 kg $H_2$ from the steam-beryllium reaction [3]. After the steam inventory

in the cooling pipe has been injected into the vacuum vessel, air enters through the leak as long as the vessel is at sub-atmospheric pressure. The burst membranes isolating the suppression pool and the drain tank from the vacuum vessel open when the differential pressure exceeds 0.8 bar [4].

### 3. GASFLOW Model

A new extended version of GASFLOW [5] has been developed to model the ITER specific phenomena in adequate detail. It includes three code modifications:

1) An isentropic expansion model to introduce super-heated water vapor and air into the plasma chamber;

2) A hydrogen production - water vapor destruction model to simulate the $Be + H_2O > BeO + H_2$ chemical reaction in fluid cells adjacent to the hot Be surfaces; and

3) A water vapor destruction and energy destruction model to simulate the effects of the water pressure suppression pool.

The ITER vacuum vessel, the connected pressure suppression pool and drain tank were set up in 3d cylindrical grids using in total about 23,000 cell volumes. The steam, hydrogen, and air sources for the accident sequence were taken from best-estimate MELCOR calculations [3].

### 4. Discussion of Results

In the investigated accident sequence, three distinct phases can be observed: The initial hydrogen generation phase (0 – 5,000 s), the pure-steam injection phase (5,000 – 10,500 s), and the air ingress phase (> 10,500 s). Hydrogen initially appears only in the vacuum vessel due to the steam/Be reaction. After failure of the burst membranes, steam and hydrogen flow from the vacuum vessel through the connecting lines to the suppression pool and the drain tank. Since the steam entering
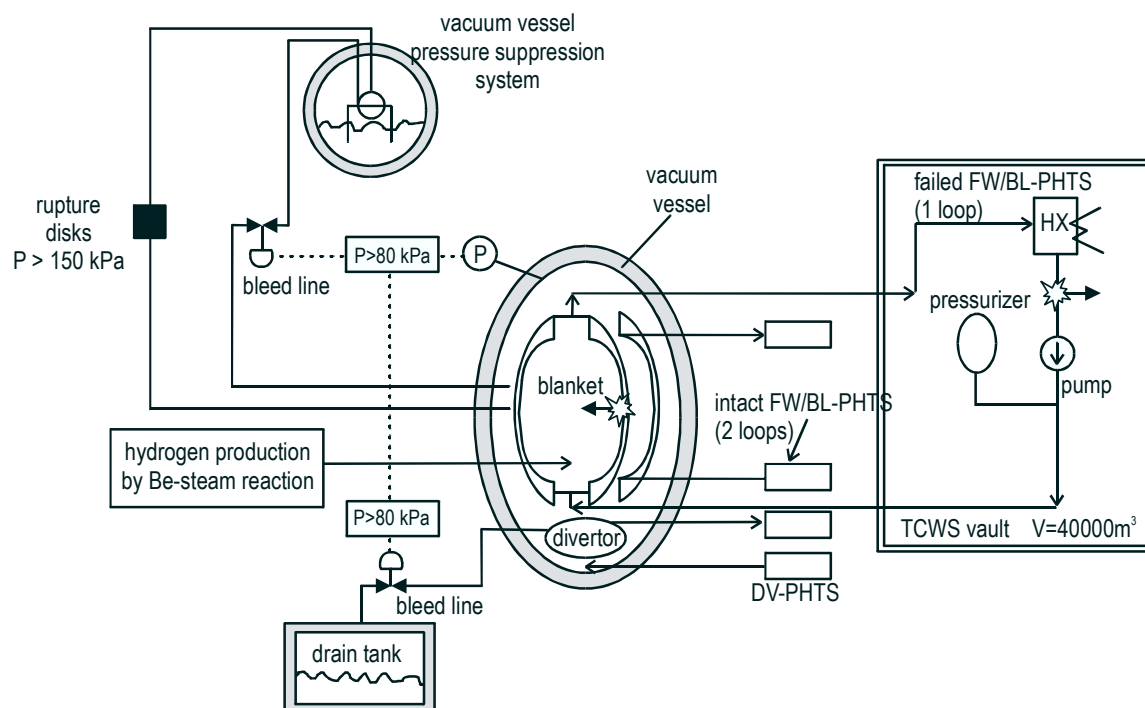


Fig 1:   Ex-vessel LOCA scenario without plasma shutdown, leading to in-vessel break and injection of steam and air into the vacuum vessel. Burst membranes open flow paths to the safety systems when the differential pressure exceeds 0.8 bar

the suppression pool is assumed to condense completely, the noncondensable gases $H_2$ and $N_2$ accumulate continuously in the cover gas phase of the suppression pool (Fig.2). No steam condensation is modeled in the drain tank. At the end of the hydrogen generation phase, almost all $H_2$ and $N_2$ are found in the suppression pool cover gas volume. The vacuum vessel and the drain tank are predominantly filled with steam. Due to the continuous vortex and turbulence generation, the gas in each vessel is quite well mixed.

During the second phase, steam continues to enter the vacuum vessel, but the structural temperatures are too low to produce further hydrogen. The still continuing "pumping" by the steam condensation in the suppression pool further concentrates the noncondensable gases $H_2$ and $N_2$ in the suppression pool gas volume. Steam remains the dominant gas component in the vacuum vessel and the drain tank.

The third phase starts about 3 hours after accident initiation. It is characterized by air ingress into the vacuum vessel. The basic mechanisms remain the same, leading to accumulation of $N_2$ and $O_2$ in the suppression pool cover gas. Burnable and detonable $H_2$-$O_2$-$N_2$ mixtures exist after 13,600 s. At 21,000 s a stoichiometric $H_2/O_2$ ratio has formed, involving 14 kg of hydrogen. Since the gas mixture in the suppression pool evolves from the hydrogen- rich side, flammability and detonability are obtained nearly at the same time, and they persist for many hours. In case of ignition, the transient peak detonation pressure in the suppression pool would reach about 8.8 bar, and the quasi-static pressure after combustion would amount to about 4.4 bar.

## 5. Conclusions

Three-dimensional distribution calculations were performed for the ITER-FEAT vacuum vessel, the suppression pool and the drain tank. An ex-vessel / first wall coolant leak without plasma shutdown was simulated. The steam, hydrogen and air sources for this sequence were taken from best-estimate MELCOR calculations. The time and space dependent gas distribution in the system was calculated using the verified 3d computational fluid dynamics (CFD) code GASFLOW. A new extended version of GASFLOW was developed to model the ITER-FEAT specific phenomena in adequate detail.

The main conclusions of the GASFLOW distribution calculation are as follows:

– combustible mixtures develop only in the cover gas phase of the suppression pool,

– since the mixture in the suppression pool evolves from the hydrogen-rich side, flammability and detonability are obtained nearly at the same time, they persist for many hours,

– in case of ignition the transient peak detonation pressure (Chapman-Jouguet value) would reach about 8.8 bar, the initial quasi-static pressure after combustion would amount to about 4.4 bar.

The substantial hydrogen risk in the analyzed scenario is restricted to the suppression pool only. Different passive mitigation measures could be considered to control this risk by design optimizations.

Staff:

W. Baumann
W. Breitung
B. Kaup
G. Necker
P. Royl
J.R. Travis
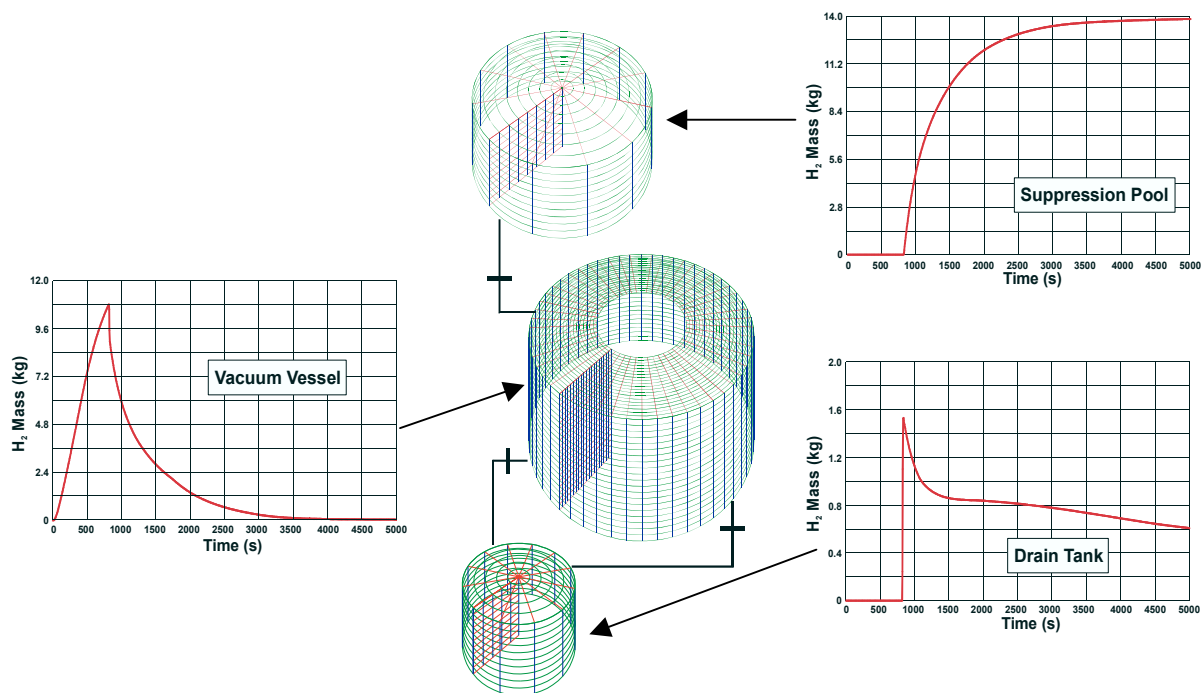


Fig.2: Results of the ITER First-wall coolant leak simulation with GASFLOW: Calculated hydrogen masses in the ITER-FEAT vessels for initial phase of accident (< 5000 s)

Literature:

[1] W. Baumann, W. Breitung, B. Kaup, R. Redlinger, J.R. Travis, "ITER-FEAT Accident Analysis on Hydrogen Detonation Using DET3D and GASFLOW", Report FZKA 6584 (Febr. 2001), Forschungszentrum Karlsruhe.

[2] Michael J. Gaeta and Brad J. Merrill, Hans-Werner Bartels, Carine Rachel Laval, Leonid Topilski, "Short-Term Hydrogen Production Issues for ITER", Fusion Technology, Vol. 32, Aug. 1997.

[3] MELCOR calculations, ITER-Team Japan, e-mail by H.W. Bartels and L.Topilski, ITER-JCT, Garching bei München.

[4] Safety Analysis Data List-3 (SADL-3), Vers. 2.9, ITER-Server, H.W. Bartels, L.Topilski, T. Honda, ITER-CT, Garching.

[5] J.R. Travis, J.W. Spore, P. Royl, K.L. Lam, T.L. Wilson, C. Müller, G.A. Necker, B.D. Nichols, R. Redlinger, "GASFLOW: A Computational Fluid Dynamics Code for Gases, Aerosols, and Combustion", Vol. I, Theory and Computational Model, Reports FZKA-5994, LA-13357-M (1998).

# SEA 5
# Validation of Computer Codes and Models

## Magnet analysis code MAGS

Electrical resistivity experiments:
Insulators surround conductors in magnetic field coil systems. If unmitigated quenches occur, temperatures higher than 1800 K can be reached. In the case of ITER-FEAT the insulator is composed of polyimide film co-wound with pre-impregnated glass. Because the behavior of such an insulation at temperatures higher than 600 K is not well known, experiments were started, to measure the resistivity of such an isolation as a function of temperature. The experiment assembly is shown in figure 1 below.
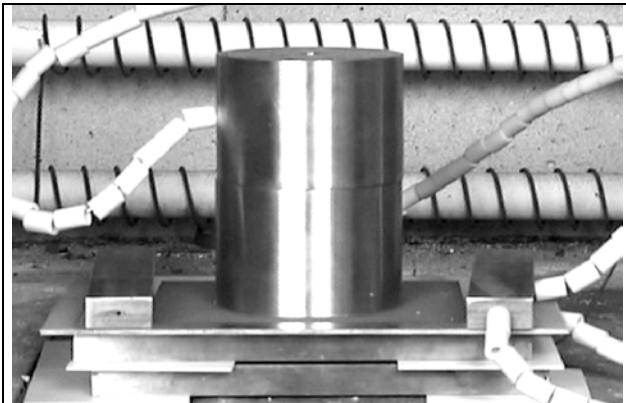


Fig. 1:  Test arrangement to measure electrical resistivity. The test sample is located between the cylindrical slab and the uppermost plate

Three foils with somewhat different specification were measured. The first, called specimen #1, was composed of three layers of 0,125 mm Kapton polyimide film and four layers of 0,270 mm fiberglass cloth filled with Araldite. The measured thickness was 1,40 mm and the ratio of polyimide film to fiberglass cloth was 0.35. The second and the third foil, called specimen #2 and #3, were composed of six layers of 0,050 mm Kapton polyimide film and five layers of 0,270 mm fiberglass cloth filled with Araldite. The measured thickness was 1,80 mm and the ratio of polyimide film to fiberglass cloth was 0.20.

At room temperature the resistivity $\rho$ of foil number 1 was measured to be $9.1*10^9$ $\Omega$m. Up to a temperature of 623 K the resistivity decreases to $1.0*10^5$ $\Omega$m. Within the short range of about 50 K, i.e. between 623 K and 673 K, the resistivity increases then to a value of $1.9*10^7$ $\Omega$m. From there the resistivity decreases to 1 $\Omega$m at a temperature of 1073 K.

In order to make use of the results in computer programs it seems reasonable, to fit them an appropriate mathematical equation. Because foils number 2 and 3 better meet the specification of insulator material, only they were considered. The resulting fit is given by the following equation:

$$\rho\,(T) = \exp\{\ 1{,}247*10^{-07}*T^3 - 2{,}704*10^{-04}*T^2 + 1{,}381*10^{-01}*T + 7{,}734\ \}$$

Thermal conductivity experiments:
The thermal diffusivity, $\alpha$, of an insulation layer was measured by using the laser flash method. During the measurements, three samples were in a vacuum chamber under high-vacuum conditions ($\approx 10^{-6}$ mbar). The laser flash apparatus was a commercial type from Theta Industries, Inc. (New York). A neodymium (Nd) gas laser that operates at a wavelength of 1.06 $\mu$m was used to apply a short heat pulse with duration of 1 ms

on the front surface of the cylindrical sample. The temperature rise on the rear face is measured by an indium antimonide (InSb) infrared detector as a function of time. The thermal diffusivity of the sample can be calculated using standard formalism of one-dimensional heat flow. Since the specimen were translucent for laser light of this special wavelength, it is necessary to cover the front face of the sample with a thin layer of graphite to ensure that the laser energy is absorbed in a thin surface sheet and to avoid direct transmission of the laser light. The rear surface is also coated with graphite to enhance the emissivity and to define the thickness of the sample for the infrared detector. This procedure does not change the measured $\alpha$-value. Knowing the density and the specific heat of the specimen the thermal conductivity, $\lambda$, can then be calculated from the thermal diffusivity value.

Three specimen of one foil were measured. The foil was composed of five layers of 0,125 mm Kapton polyimide film and four layers of 0,27 mm fiberglass cloth filled with Araldite. The measured thickness was 1,7 mm and the ratio of polyimide film to fiberglass cloth was 0.58. A temperature range between 298 K and 773 K could be covered, because at higher temperatures the specimens started to disintegrate themselves. Within this temperature range a fit of the mean value of the measured thermal conductivity can be given by the following equation:

$$\lambda(T) = 9{,}675*10^{-07}*T^2 - 1{,}061*10^{-03}*T + 4{,}376*10^{-01}$$

Recalculation of the EVITA experiments on condensation of steam:
In the frame of the IEA-ESE Task2 "Transient Thermofluid Modeling and Validation Tests" a new multilayer condensation model has been implemented into the module CRYOSTAT of the code system MAGS and validated by several pretest calculations of the EVITA-experiment test matrix. Due to the fact, that cryogenic condensation on very cold surfaces will lead to a relative large layer thickness, it was necessary to treat the total layer thickness not as a single layer, as done before, but subdivide into several layers, each of them with individual, thermal variables of state, depending from the average layer temperature. The condensation, resp. evaporation, process itself takes place only in the first boundary layer to the volume, the so-called "active" condensate layer.

The new condensation model has been validated by pre test calculations for several EVITA experiments considering "normal condensation" on the vacuum vessel (vv) surface at an initial temperature of 298K and "cryogenic condensation" on a cryogenic copper plate, cooled by a liquid nitrogen circuit, at an initial uniform structure temperature of 80 K (vv-structure: 438K). In all cases Initial vv pressure was 500Pa and injected superheated water steam had 0.7MPa/438K. Mass flow rates were in the range of 0.7 to 3.6g/s. The multi layer modeling gives a detailed description of the condensation process and the behavior of frost-, ice- and liquid condensate layers. Due to the fact, that the convective heat transfer has an important influence to the condensation rate, the corresponding equations have been examined and improved. Heat transfer in the structure, including possible heat sinks or sources is calculated in 1d by the MAGS-module HEAT1D.

The experiment with an injection of 2.1g/s, where the total incoming heat is removed by the nitrogen circuit and the structure temperature remains nearly at the initial value of 80K, shows a continuous built-up of ice layers to about 10mm until the ice-point temperature is reached on the condensate surface. Afterwards a liquid layer on a still growing ice layer is formed. On vertical or sloping surfaces it is assumed, that at a thickness of 0.5mm a draining down of the liquid layer starts and this maximum thickness cannot be exceeded. This leads to a thermohydraulic equilibrium status with an ice layer of about 11mm, covered by a 0.5mm liquid layer at least.

In the experiment with a limited heat removal of 40kW/m$^2$ from the cryogenic plate, the condensation leads to an increasing structure temperature. The formed ice layer reaches a thickness of about 2mm at ice-point temperature on the surface when the condensate becomes liquid. Afterwards a growth of the liquid layer up to the maximum thickness appears with a simultaneous melting of the ice layer until it disappears and the equilibrium status with only a 0.5mm liquid layer is reached.

The results were presented at Idaho Falls Task2-meeting (March 19-23, 2001) and discussed with other analysts from different labs which accompany these experiments. Up to now no cryogenic condensation test has been performed, only the data of normal condensation experiments are available. So first post-test calculations of the test with 1.92g/s injected water steam at 0.7MPa and 438K were performed. The EVITA non-cryogenic tests are characterized by a strong coupling of the condensation capable vv-surface (1.83m$^2$) to the vv-volume (0.21m$^3$) of about 8.7:1 (cryogenic tests: 0.48:1). This leads to a very sensitive reaction of the volume variables of state in case of condensation (especially the partial pressure of the condensing phase) and an overestimation of the condensation rate. The multilayer model had to be improved for those extreme situations. The experiment shows a very slow increasing vv-pressure up to 0.015MPa during the injection time of 400s. The calculation result is about 0.075MPa at a vv-volume temperature of 381K. 750g of the injected 840g water mass has been condensed, this corresponds to an average layer thickness of about 0.42mm.

The experimental data of tests with condensation on cryogenic surfaces should be available at end of 2001. Then the post-test calculations will be continued.

Staff:

R. Meyder
G.Bönisch
G.Schmitz

Literature:

[1] G. Schmitz: Final report on electrical insulation experiments. GB8-SEA5A Jan. 2001

[2] G. Bönisch: Report on EVITA Pre-test Calculations with the Multilayer-Condensation Model in the MAGS-Module CRYOSTAT. G81TT03 / T506 April 2001

## SEP 2
## Doses to the Public

Dose assessments for ITER-FEAT were performed with source terms defined at the beginning of 2001 /1/. That comprise deterministic calculations for accidental releases of tritium and activation products as well as for releases under normal operation conditions. For the latter scenarios, recorded meteorological data from the potential ITER candidate site of Cadarache were used. Within the deterministic calculations, the release height, the weather conditions and the dispersion parameter sets were varied. Other input parameters such as breathing rate and ingestion habits were the same as in previous investigations. Five different source terms, two for tritium (HT and HTO) and three for activation products (ACP, AP-tungsten, ACP-normal), were considered.

As there is a discussion whether a high stack could be replaced by a low stack with high speed exhaust, results from these two options were of great interest. In case of normal operation releases, the high speed exhaust scenario shows the lowest doses for all source terms. This differs from the deterministic results. The reason is that always deterministic scenarios exist where building wake effects have a strong influence what reduces the final plume rise. The plume touches the ground near to the site and the dose to the MEI is rather high. Another interesting aspect is the fact, that doses from ground level releases are highest. However, in case of tritium, the scenario without rain and in case of activation products the scenario with rain show the highest doses. This can be explained by the different importance of the dry and wet deposited radionuclides. Wet deposition for activation products is much higher and thus dominates the final dose from ground exposure or ingestion.

Work under an INTAS agreement (Project N 654-99) with RFNC – VNIIEF (Russian Federal Nuclear Center – All-Russian Scientific Research Institute of Experimental Physics) in the project of 'Investigation on Verification of Tritium Behaviour Models' is ongoing. Among others, washout experiments performed in this framework provided experimental data to test tritium models.

The work within the BIOMASS (BIOspheric Modelling and ASSessment) project for testing of tritium models for routine releases into the atmosphere and hydrosphere is completed. Draft documents for all scenarios are close to be finalised. Results will be published by the IAEA and presented in a conference in 2002.

Staff:

W. Raskob
I. Hasemann
J. Ehrhardt

Literature:

[1] Raskob, W. and Hasemann, I., Deterministic calculations for source terms from ITER-FEAT, FINAL REPORT, ITER Task G 81 TD 05 (D452) Subtask 4. Report FZKA-6625, Forschungszentrum Karlsruhe (2001)

# Power Plant Conceptual Study

**TRP 4**
**Economic and Operational Analysis**

**TRP 4-D 2**
**Review of Large Sector Handling Methods for Power Core Replacement**

Within the European Power Plant Conceptual Study (PPCS) started in 2000 large sector handling concepts for the replacement of the power core have been reviewed, addressing the impact on the overall machine design, the methods for locking the sectors to the vacuum vessel, the handling and logistics implications of the selected power core replacement method, and the required replacement time.

For a tokamak fusion power plant, the power core has to be designed for a fast replacement of the components. A promising way to reach this goal is to design the power plant for the replacement of entire sectors through large maintenance ports, arranged between the toroidal field (TF) coils. This arrangement has been evaluated and is shown schematically in the figure below with a view into the open torus. The possibility of the attachment of the sectors to the bottom plate in the vacuum vessel have been assessed and the time required for a replacement has been estimated. This attachment has the potential for reducing the replacement time considerably compared to the method of module replacement typical for experimental machines like ITER. Obviously the capital cost of the machine is increased by the large maintenance ports and the larger TF-coils. It remains to be seen, if these larger cost are compensated for by the increased availability of the power plant.

Staff:

L.V. Boccaccini
S. Gordeev
S. Malang
K. Schleisiek
References

Literature:

S. Malang, L.V. Boccaccini, S. Gordeev, K. Schleisiek: Review of Large Sector Handling Methods for Power Core Replacement, (internal FZK-report), December 2000
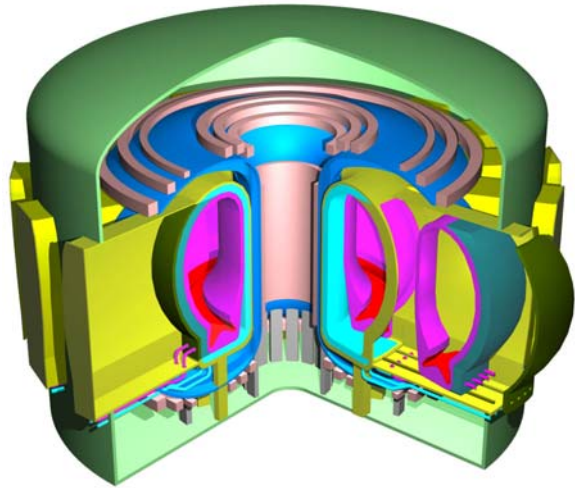


Fig. 1: Full Sector Replacement System (view into open torus, sector partly withdrawn)

**TRP 4-D 3**
**Contribution to Parametric Sensitivity Analyses of Helium-Cooled Divertor Concepts**

Within the European Power Plant Conceptual Study (PPCS) started in 2000 it is considered to integrate a Helium cooled blanket with a divertor using the same coolant. The present work was intended to focus research on concepts that are capable of withstanding the large heat fluxes expected for the divertor.

Five divertor plate concepts – (i) a porous medium concept (PM) with a cross flow pattern; (ii) a multi-channel concept (MC) with a bi-directional longitudinal flow scheme; (iii) a swirl rod concept (SRC) using a helical wire in an annular channel as heat transfer enhancement; (iv) an eccentric swirl promoter concept (ESP), similar to (iii) but with multiple fins and eccentric core; and (v) a slot concept (SLOT). A derivative of (i) but replacing the porous medium by a narrow gap - were assessed on the basis of consistent assumptions and operating parameter ranges. While thermohydraulic performance was judged by maximum wall temperatures and pressure drop, thermal stresses were estimated based on temperature differences across the cooling channel.

The results show that thermal stress is the limiting quantity for all concepts. The temperatures along two lines E and F on the plasma-facing and the back-side of the cooling channel (see Figure 1) exhibit a characteristic pattern for the different concepts under review.
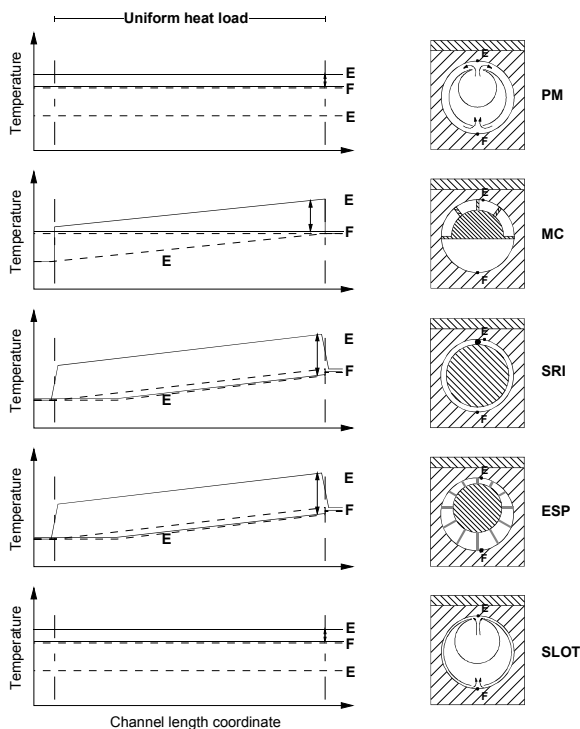


Fig. 2: Characteristic temperature profiles along the coolant flow path ( — wall temperature, - - coolant temp.)

They review confirmed that (i) a large heat transfer coefficient on the fluid side; (ii) the delivery of low temperature coolant to the First Wall, i.e. a flow path transversal to the First Wall; and, (iii) the use of refractory metals are key elements of a Helium cooled divertor. All other differences were judged rather design dependent than generic.

The conclusions drawn from this work are currently being applied in a radical optimisation of the porous medium and slot concepts, with the expectation of surpassing heat flux limits previously assumed for gas-cooled divertors.

Staff:

S. Hermsmeyer
K. Kleefeldt

Literature:

[1] S. Hermsmeyer, K. Kleefeldt: Review and comparative assessment of heliuum-cooled divertor concepts, FZKA 6597, 2001.

**TRP-PPCS 1/2**
**Model A / Model B**


**TRP-PPCS 1/2-D 2**
**Neutronics Modelling and Analysis**


In the framework of the Power Plant Conceptual Study (PPCS) – Phase III, conceptual designs are being developed for power plant variants with a water cooled lithium-lead (WCLL) blanket (PPCS model A, Task 1) and a helium cooled pebble bed (HCPB) blanket (PPCS model B, Task 2). The objective of Deliverable 2, to be provided by FZK for each task, is to provide the neutronic data required for the conceptual design of PCCS models A an B. To this end, suitable 3D reactor models are being developed with the help of the MCNP Monte Carlo code.

According to the PPCS III work programme schedule, the neutronics modelling was started in September 2001 on the basis of the reactor parameters and the neutron source distribution provided by UKAEA Culham for the two PPCS plant variants. In a first step, a first wall contour was adapted to the plasma shape so as to calculate the neutron wall loading distribution as shown in Fig. 1 for the PPCS model B with the HCPB blanket. The integration of the blanket modules into the 20° torus sector model is currently in progress for both of the PPCS power plant models.



Fig. 1: Poloidal wall load distribution calculated with MCNP for PPCS plant model B (HCPB blanket). The total fusion power is 3300 MW


Staff:

Y. Chen
U. Fischer

**TRP-PPCS 2**
**Model B (HCPB)**


**TRP-PPCS 2-D 10**
**Mechanical Analysis, Design Integration**


In the framework of the European Power Reactor Conceptual Study (PPCS) by pre-studies blanket and divertor concepts were examined and that concept was selected, which offers development potential.
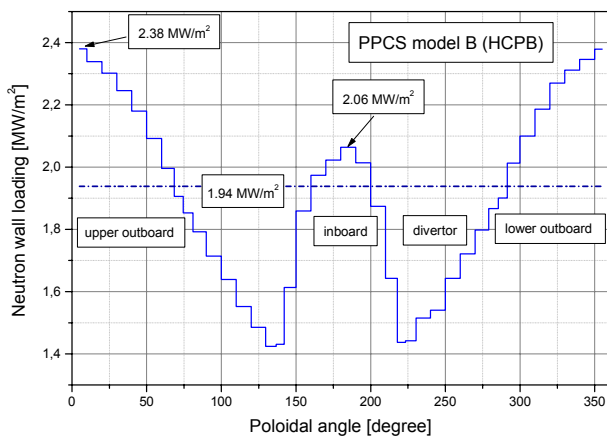
For the thermodynamic circle of Model B a first design calculation was performed. A design calculation for the steam generators and the intermediate super heaters was a precondition for the analysis of the thermodynamic properties of the steam circle. The blanket power is used for the steam generation, while the divertor heat is taken for intermediate super heating. By this design, turbine steam conditions of 460 and 560 °C for steam generation and superheating are attainable, respectively. The principle flow diagram for the turbine circle is given in Fig. 1. The reduction of the operating pressure in the steam circle from 11 to 7 MPa gives more space for the heat transfer from the primary blanket cooling medium to the steam circle, as the pinch point temperature difference increases in the steam generator, which results in smaller heat transfer areas and in lower pressure drops. Also important is the increase of the feed water temperature to improve the overall efficiency up to over 42 %.

The tritium permeation in the steam generators and heat exchangers participates a decisive size for the interpretation. For this reason, the steam generator and heat exchanger design programs were extended by adequate calculation algorithms.

Now it is possible, to determine diffusion and surface limited permeation dependent on heat transfer area, wall thickness, wall temperatures and other parameters.

The thermodynamic cycle efficiency participates an important influence-size for selection a fusion power reactor concept. The temperature level available for disposition decides the value of the attainable efficiency. The temperature level of the concepts considered up to now is mainly placed in the range in between 500 and 700 °C. Since some time concepts are being discussed which allow the range to be extended up to 1000°C and even higher. The thermodynamic processes in question are in the lower temperature area of the Clausius-Rankine-Prozess and in the higher temperature area of the Joule - or Brayton-Prozess. The demarcation between the two processes today is approximately 650 °C. A not sufficient answered question until now was, The possibly attainable efficiencies depending on the temperature level is another issue requiring further attention. An examination, based on design calculation for both processes, was executed. For the Brayton-Prozess, a parametric study was performed and for the Clausius-Rankine-Prozess cycles from earlier designs were recalculated with new design-programs. The calculated results are in a good agreement with the former lay-outs, performed by the industry involved. The most important results are given in Fig.2. The enveloping limit curve corresponds to the highest attainable efficiencies, which participate, for the Clausius - Rankine-Prozeß approximately 50% and for the Brayton-Prozeß 60% and more. As maximum temperature, the respective turbine inlet temperature is selected. The thermodynamic efficiencies don't contain the cycle losses, which still emerge in the primary circle of the fusion power plant including the blanket and diverters cooling circuit.
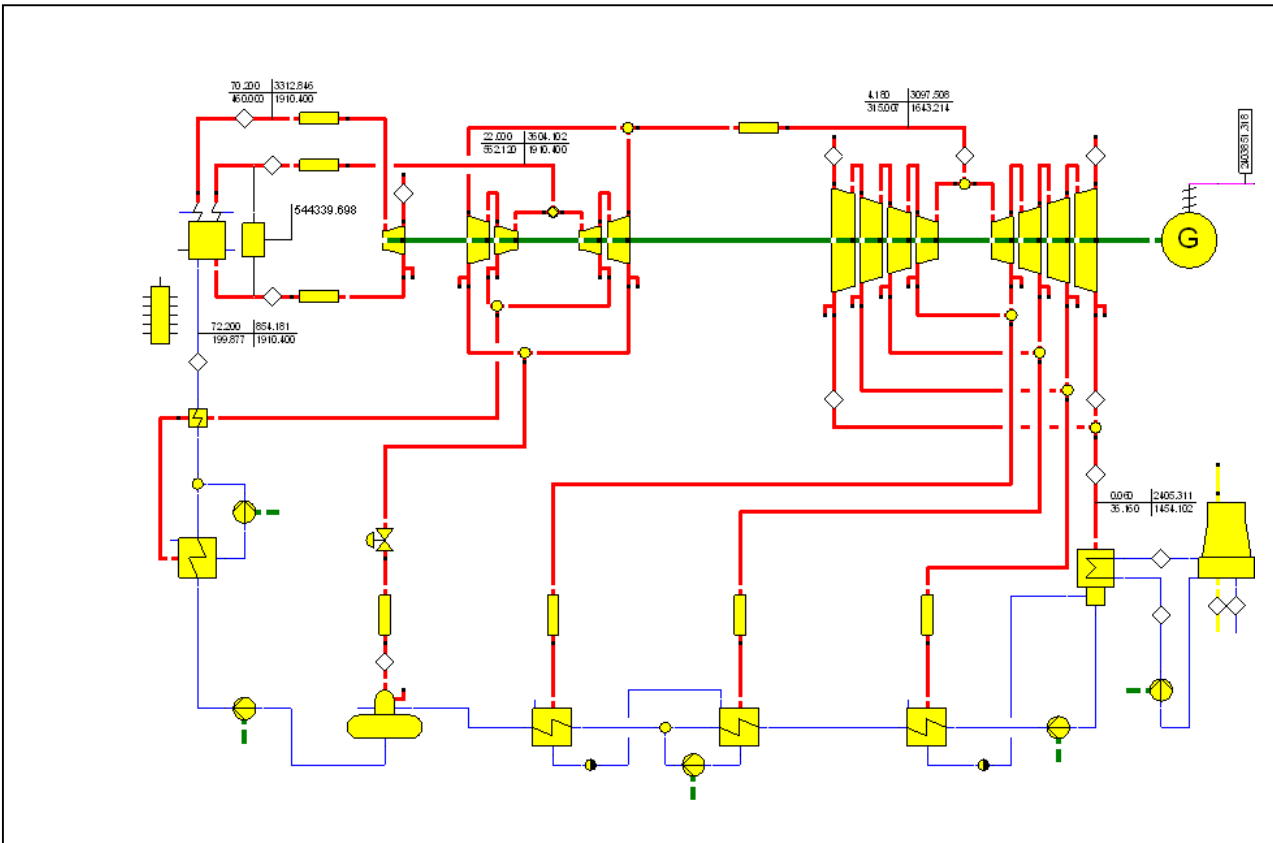


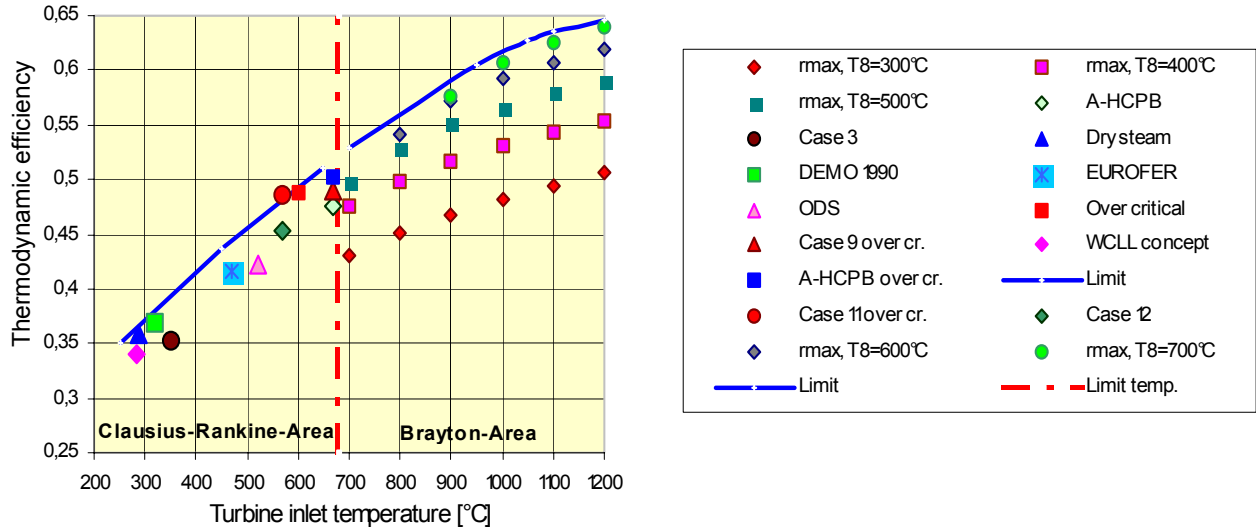Fig. 1: Steam circle for the HCPB-Power Plant Conceptual Study

Fig. 2: Maximal attainable thermodynamic efficiency as function of the thermodynamic process

Staff:

H. Schnauder

**TRP-PPCS 3**
**Selection of Advanced Models**


**TRP-PPCS 3-D 3**
**Assessment of Dual-Coolant Li-Pb/He Blanket Concept**


**Introduction**

The dual coolant (DC) lead-lithium/helium blanket concept (Fig. 1) is based on the use of ferritic steel structure which is cooled by high pressure helium, the self-cooled Pb-17Li breeder, and SiC/SiC flow channel inserts serving as electrical and thermal insulators. This avoids the need for insulating coatings on the steel structure inside the liquid metal flow channels (for MHD reasons) and allows a high exit temperature of the lead-lithium which enables the potential for a high efficiency of the power conversion system. Moreover, the use of ODS ferritic steel as FW material - by choosing EUROFER as base material for the whole structure which contains a thin ODS layer plated onto the plasma facing surface - allows about 100 K higher temperature limit of the first wall in comparison with the base material with Tmax ≤ 550°C.
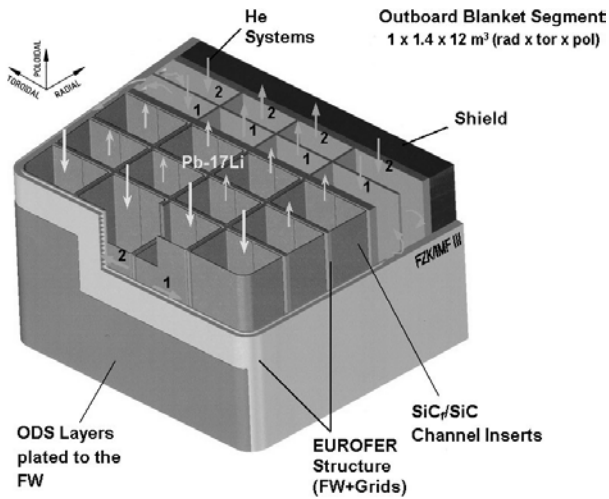


Fig. 1:  Dual-Coolant Pb-Li/He Blanket


As shown in a preparatory power plant conceptual/availability (PPA) study [1] for the DC blanket concept in 1999, a relatively high average neutron wall load of 4 MW/m$^2$ for reference case could be achieved. The thermal efficiency of about 44 % could be reached by using a closed-cycle helium gas turbine in the power conversion system.

In the following stage of the power plant conceptual study (PPCS) the DC blanket performance of the reference case should be normalized and adapted to a typical size of commercial reactors of e.g. 1500 MWe which requires iterative calculations between the blanket layout and the system code analysis. The results of these calculations including radial blanket size, TBR, power densities, thermohydraulics data, energy multiplication factor as well as thermal efficiency will serve as input for the system code analysis to achieve the global reactor geometry for the re-run.

**Preparation of the initial input**

Preliminary ideas and initial input for system code simulations of DC blanket was provided following the basic data of zero set of power plant parameters provided for HCPB model by Culham:

| | |
|---|---|
| Unit size | 1.5 GW$_e$ |
| Recirculating power fraction | 0.2 |
| Heating power | 203 MW |
| Average neutron wall load | 2.1 MW/m$^2$ |
| Divertor peak load | 4.5 MW/m$^2$ |

with an additional assumption

- Entire alpha-power (25 % of the neutron power) is distributed to the first wall of the blankets

Based on these information and assumptions, the following values for DC model have been estimated:

a) Blanket energy multiplication factor

The values of energy multiplication factor for the blanket system and the overall plant which were used in the PPA 99 calculations are listed in Table 1.

Table 1:  Energy multiplication factor (PPA 99)

| Blanket concept | Energy multiplication factor for the blanket system (outboard) | Energy multiplication factor for the overall plant |
|---|---|---|
| Advanced HCPB | 1.22 (1.19) | 1.24 |
| Improved HCPB | 1.38 (1.34) | 1.41 |
| Advanced DC | 1.15 (1.11) | 1.18 |

Under consideration of maximum 1% waste heat due to low temperature cooling the correcting factor for the usable heat of about 0.99, as suggested by Siegfried Malang, should be taken into account. Thus, the value for the DC whole ractor has become 1.18 x 0.99 = 1.168.

b) Thermohydraulic and net power conversion efficiency

After adapting appropriate thermohydraulic parameters to the power balance in this case, first estimation calculations show that the same value of net power conversion efficiency of 44 % as determined in the PPA study [1] could be further assumed.

c) Inboard and outboard blanket and shield thicknesses:

The estimation of radial thickness yields 1.5 m for the outboard and 1.0 m for the inboard, respectively, taking into account an application of the low temperature and high temperature shields.

d) Limit to first wall heat load

As a consequence of the additional assumption (entire alpha-power distributed to the FW), the FW heat fluxes will increase and may limit the power density. The use of a value of 1 MW/m$^2$ as a limit for the maximum surface heat flux to the FW, which is lower than the maximum value given in [1] of 1.5 MW/m$^2$, is considered to be reasonable for this case.

e) Maximum divertor heat load

During the PPA-study, two helium-cooled divertor concepts had been evaluated. For both of them a heat flux limit of 5 MW/m$^2$ was estimated. Due to the fact, that the limit on the power load

of the divertor has an decisive impact on the overall performance of the power plant, this issue was re-evaluated in task TRP4 of PPCS, phase II [2] leading to the main result, that innovative divertor plates based on porous body heat exchangers made of tungsten alloy can allow - under certain conditions - surface heat fluxes up to 10 MW/m$^2$. Therefore this value could be suggested as an upper limit.

The initial input data suggested for system code simulations of the DC blanket are summarized in Table 2.

Table 2:   Summary of recommended values for DC blanket

| | |
|---|---|
| Blanket energy multiplication | 1.168 |
| net conversion efficiency | 44 % |
| blanket and shield thicknesses (distance between FW and VV): - inboard - outboard | 1.0 m 1.5 m |
| limit to first wall heat load | 1 MW/m² |
| maximum divertor heat load | 10 MW/m² |

Staff:

L. Bühler
U. Fischer
S. Malang
P. Norajitra
G. Reimann
H. Schnauder

Literature:

[1]  P. Norajitra, et al., FZKA 6385, 1999.
[2]  S. Hermsmeyer, et al., FZKA 6597, 2001.

# Underlying Technology

# Underlying Technology

## Operation and Upgrade of the Fusion Materials Laboratory

The Fusion Materials Laboratory (Fig. 1) provides the infra-structure for the performance of tasks defined in the EFDA workprogramme related to the characterisation of irradiated and non-irradiated materials. Methods such as optical and electron microscopy, He-pycnometry and Hg porosimetry, crush-, micro-hardness-and charpy tests as well as long time annealing tests are applied.

In the framework of the HFR Phase IA some 30 instrumented charpy test on ferritic/martensitic steels (constituting precursors of EUROFER) irradiated at temperatures ranging from 250 to 450°C have been performed. Crack surfaces have been investi-gated by fractography. The results achieved are described under Task TMS-001. The investigation of specimen irradiated in the HFR Phase IB has been stared and will last by the end of 2002. The calibration and benchmarking of the new fully auto-mated testing device for irradiated specimen has been com-pleted.

The characterisation of ceramic breeding materials was con-tinued aimed to control the quality and to characterise fresh lithium orthosilicate pebbles (diameter 0,25 – 0,63 mm). The aim is to determine properties such as the chemical composition of pebbles, their microstructure, porosity and density as well as their deformation and hardness. Results achieved in the re-porting period are described in Task TTBB-005.

The characterisation of fresh beryllium pebbles has concen-trated on investigations on the influence of impurities such as Al, Mg, Fe and Si on the their mechanical properties (see Fig. 2). The results achieved are presented in Tasks TTBB-007-1. The release rate of helium and tritium from irradiated beryllium peb-bles is of specific importance in connection with requirements to minimize the tritium inventory of blankets. The formation of gas bubbles has been investigated by TEM examination of irradiated beryllium in co-operation with the European Institute dor Trans-uranium. The results are used for the validation of the code ANFIBE which is being developed to model the generation of gas bubbles and temperature dependent release rates.

## Operation and Upgrade of the Tritium Laboratory Karlsruhe (TLK)

The TLK (see Fig. 3) is an installation for research into tritium technology and testing components on a technical scale with considerable amounts of tritium involved. The license allows for the handling of up to 40 g of tritium, about 20 g are actually available. Safe operation of the installation requires numerous safety devices, strict surveillance, and extensive documentation. Therefore, a considerable percentage of the total personnel of almost 30 scientists, engineers and technicians is occupied with infrastructure services. Presently, the TLK has glove boxes for experiments and infrastructure installations with a total volume of 120 $m^3$.

As far as tritium processing issues are concerned emphasis is put on the semi-technical scale demonstration of the ITER exhaust gas handling system by an integral experimental plant called CAPER. Endurance tests with relevant concentrations of tritium and impurities have started, an overall decontamination factor DF > $10^8$ is expected.

Getter beds are being developed for the storage of tritium, aimed at providing storage devices with a rapid delivery of tritium. In addition, these beds should enable in-situ assaying of tritium by calorimetry.

A novel roots pump concept aims at the development of a tritium-compatible mechanical roughing pump. Tightness is achieved by a ferrofluidic liquid kept in place by magnetic forces. A scaled-down roots pump, modified with such a new sealing, will be investigated.
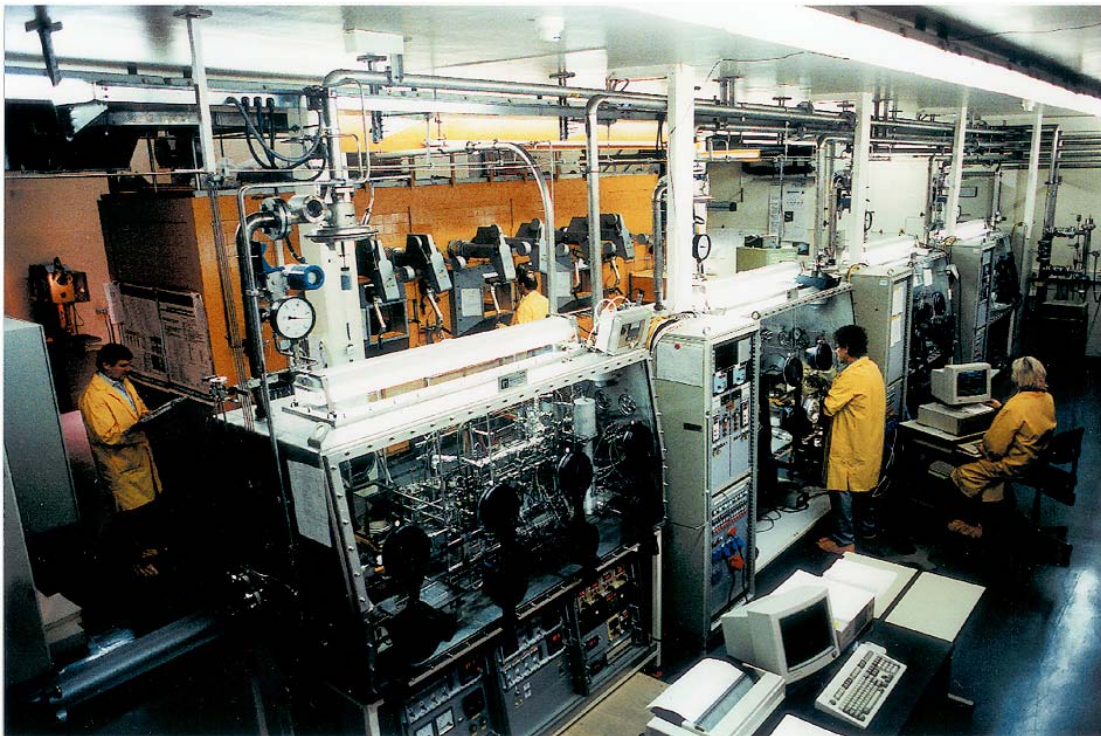


Fig. 1: View to the Fusion Materials Laboratory

Fig. 3: View to the Tritium Laboratory Karlsruhe

A facility called PILATUS is being built to test main components of the subsystems of the Helium Cooled Pebble Bed (HCPB) Test Blanket Modules (TBMs) of ITER. In the tritium extraction subsystem, tritiated water is frozen out in a cold trap and gaseous hydrogen isotopes and impurities are adsorbed on a molecular sieve bed operated at -196$^{\circ}$C.

Graphite and CFC (Carbon Fiber Composites) tiles from JET exposed to high tritium levels during the DTE1 campaign were examined with regard to the tritium distribution in the surface layer and the bulk of the material.

Detritiation techniques are being developed for solid materials and liquids for reuse/recycling of components or for easy repository storage of wastes. These activities are directly related to JET and TLK operation, but will also contribute to requirements for ITER. Out of the multitude of conceivable tritiated materials and components carbon (graphite and CFC) tiles, water, molecular sieve beds, and vacuum oil are actually being investigated for detritiation.

Broad efforts are devoted to the optimization of tritium analyses and enhancements of the infrastructure of the tritium laboratory. All ITER-related R&D projects benefit from these activities and take advantage from progress in this field.

An example of optimization of analytical methods is the successful testing of micro-gascromatographs with sample volumes much smaller than for conventional systems.

The isotope separation system of the TLK has been upgraded by a gas chromatography displacement column, yielding reduced separation times and improved separation factors.

Molecular sieve beds used in tritium retention systems of the TLK have been routinely regenerated and reconditioned in the AMOR facility. A total of about 300 molecular sieve beds containing more than 4 tons have been reactivated over the last 6 years. By this strategy, a considerable reduction in radioactive waste has been achieved, also reducing the TLK operation costs.

Calorimetry based on the measurement of the beta decay energy produced by tritium is being further developed to quantify the tritium content in plasma facing materials, such as graphite tiles. Another promising application is the determination of tritium in solid and liquid wastes for the definition of the waste category and their final disposal.

Fig. 2: High Temperature Creep Measurement on Be-Pebbles

# Physics Integration

# "Advanced ECRH" for ASDEX-U

## Background and aim

Magnetohydrodynamic (MHD) instabilities are one of the main effects limiting the confinement of plasmas. The stability is to a large extent determined by the distribution of plasma currents. To drive localized currents in a plasma is a very efficient tool to optimize the performance of a tokamak. The suppression of plasma pressure limiting MHD instabilities (so called 'Neoclassical Tearing Modes') has been demonstrated successfully by localized electron cyclotron current drive at ASDEX-Upgrade. Further studies are planned in a cooperation of the German fusion Associations in the frame of the Helmholtzgemeinschaft (HGF) with support of the European Fusion Programme

The resonance condition for absorption of the rf-wave is dependent on the magnetic field . By changing the injection angle and/or the rf-frequency, the location of the externally driven current is determined. A multi frequency tunable, 1 MW, long pulse gyrotron is the appropriate tool for advanced ECRH experiments to be carried out in ASDEX-Upgrade at IPP Garching.

## Status of the work

Multi frequency gyrotrons have to be equipped with a matched window in order to avoid reflections. Either a Brewster window or a tunable double disk window would allow a flexible choice of frequencies over a wide range. Such windows will be developed and implemented in a second phase of this project. As a first step, an available CVD diamond single disk window will be used.

For a single disk window the choice of frequencies is determined by the thickness of the disk because low reflection is only given for frequencies corresponding to multiples of the half wavelength. In this particular application , dual frequency operation is intended. The higher frequency of 140 GHz corresponds to the maximum magnetic field in the tokamak plasma. The second frequency is given by the desired location of energy deposition at the plasma edge within a range of 100 to 115 GHz. Using an available CVD diamond window disk, the lower frequency would result in a value of about 105 GHz. Gyrotron cavity modes have to be chosen accordingly. The $TE_{22,8}$ mode at 140 GHz [1] was selected as main cavity mode. The frequency of 105 GHz coincides with the $TE_{17,6}$ mode.

As prototype for the tube to be built by the "Institute for Applied Physics (IAP)" in Nizhny Novgorod, the existing $TE_{22,6}$ gyrotron will be modified to operate in the $TE_{22,8}$ mode. Electron gun, beam tunnel, collector and superconducting magnet system are reused for the new design. The resonator with uptaper and the quasi-optical mode converter system have been calculated and redesigned. The resonator and the uptaper were optimized not only for the two frequencies mentioned but for several other frequencies, also. In case of using a broadband output window (either a Brewster or a double-disk-window) at a later phase, at least 7 frequencies in the range of 105.0 GHz to 140.0 GHz can be excited (Table).

With the $TE_{22,6}$ gyrotron fast frequency step-tunability between two modes has already been demonstrated , as shown in fig.1.
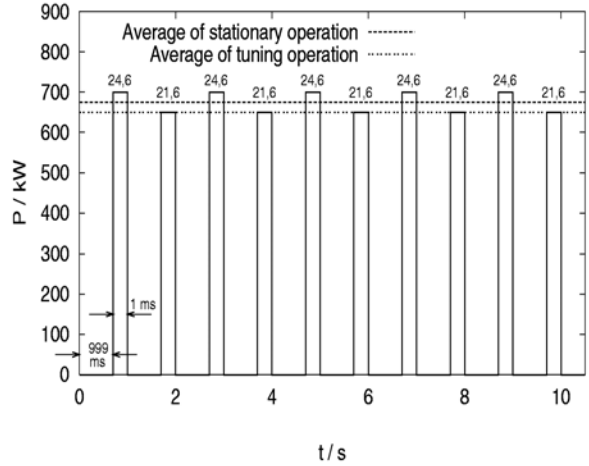


Fig. 1: Fast frequency step tuning (1s) between 136.3 GHz ($TE_{21,6}$) and 147.4 GHz ($TE_{24,6}$)

Table: Operating parameters of different modes

| MODE | F (GHz) | $B_{res}$(T) | $I_{res}$(A) | $I_{gun}$(A) | $R_b$(mm) | $\alpha$ | $E_k$(keV) |
|------|---------|--------------|--------------|--------------|-----------|----------|------------|
| 17,6 | 105.0 | 4.150 | 68.24 | 7.34 | 8.6 | 1.74 | 75.6 |
| 18,6 | 108.4 | 4.281 | 70.37 | 28.01 | 8.5 | 1.47 | 76.2 |
| 19,6 | 111.6 | 4.400 | 72.50 | 28.85 | 8.6 | 1.28 | 76.5 |
| 19,7 | 120.9 | 4.770 | 78.60 | 29.00 | 8.2 | 1.51 | 75.7 |
| 20,7 | 124.2 | 4.909 | 80.74 | 30.20 | 8.3 | 1.32 | 76.2 |
| 21,7 | 127.0 | 5.041 | 82.88 | 31.28 | 8.35 | 1.29 | 76.35 |
| 22,8 | 140.0 | 5.548 | 91.44 | 32.57 | 8.1 | 1.45 | 75.7 |

Calculations of the window design in case of a Brewster window, or for the thickness and distance between disks of a double-disk window have been performed. The new launcher of the quasi-optical mode converter has been designed. Two types of antennas were considered: Vlasov- and Denisov-type. The Denisov-type seems to be advantageous (Fig. 2), but a decision will be made after a few more calculations.
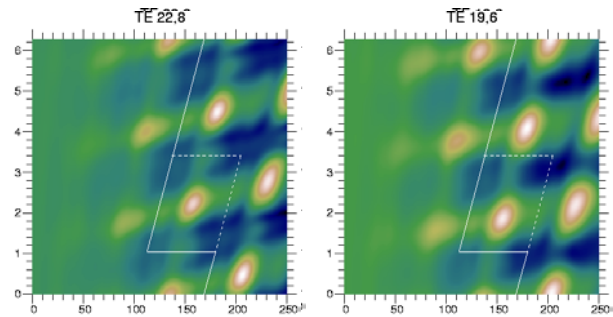


Fig. 2: RF power distribution at the unrolled waveguide wall of a Denisov-type launcher for the $TE_{22,8}$ mode (left) and $TE_{19,6}$ mode (right)

Staff:

A. Arnold (Uni Karlsruhe)
E. Borie
G. Dammertz
O. Drumm (Uni Karlsruhe)
S. Illy
M.V. Kartikeyan
K. Koppenburg
M. Kuntze
B. Piosczyk
M. Thumm
X. Yang

Literature:

[1] E. Borie, K. Koppenburg, S. Illy, O. Drumm, M.V. Kartikeyan, B. Piosczyk, X. Yang, G. Dammertz, M. Thumm, "Possibilities for multifrequency operation of a gyrotron at FZK", Proc. 26th Int. Conf. Infrared Millimeter Waves, Toulouse, 2001, to be published.

[2] G. Dammertz, O. Dumbrajs, K. Koppenburg, B. Piosczyk, M. Thumm, "Frequency-step-tunable high-power gyrotrons for plasma physics applications", J. Communications Technology and Electronics, 45, Suppl. 1, 2000, pp. 60-64.

[3] K. Koppenburg, G. Dammertz, M. Kuntze, B. Piosczyk, M. Thumm, "Fast frequency-step-tunable high-power gyrotron with hybrid-magnet-system", IEEE Trans. on Electron Devices, ED-48, 2001, pp. 101-107.

[4] M. Thumm, A. Arnold, E. Borie, O. Braz, G. Dammertz, O. Dumbrajs, K. Koppenburg, M. Kuntze, G. Michel. B. Piosczyk, "Frequency step-tunable (114-170 GHz) Megawatt gyrotrons for plasma physics applications", Fusion Engineering and Design, 53, 2001, pp. 407-421.

[5] K. Koppenburg, G. Dammertz, M. Kuntze, S. Liu, B. Piosczyk, M. Thumm, "Operation of a fast-frequency step-tunable 1 MW gyrotron with hybrid-magnet-system", Proc. 25th Int. Conf. Infrared Millimeter Waves, Beijing, China, 2000, pp. 17-18.

[6] M. Kuntze, A. Arnold, E. Borie, G. Dammertz, S. Illy, K. Koppenburg, B. Piosczyk, M. Thumm, "Advanced high power gyrotrons for ECRH applications", 27th IEEE Int. Conf. on Plasma Science, New Orleans, USA, 2000, p. 200 (4D08).

[7] B. Piosczyk, A. Arnold, E. Borie, G. Dammertz, O. Drumm, O. Dumbrajs. S. Illy, M. Kuntze, K. Koppenburg, M. Schmid, M. Thumm, "Advanced high power gyrotrons for fusion applications", ITG-Displays and Vacuum

# Microwave Heating for Wendelstein 7-X

## 1. Introduction

The development of ECRH is closely linked to the development of stellarators, and one of the key issues for stellarators is the development and demonstration of high power gyrotrons with CW capability. For the stellarator Wendelstein 7-X now under construction at IPP Greifswald, Germany, a 10 MW ECRH system is foreseen.

The Forschungszentrum Karlsruhe has signed a contract to construct the 10 MW ECRH system at Greifswald, and a European collaboration has been established between Forschungszentrum Karlsruhe, CRPP Lausanne, IPF Stuttgart, CEA Cadarache and TED Vélizy, to develop and build the 10 gyrotrons each with an output power of 1 MW for continuous wave operation (30 min).

## 2. Development of a Prototype Gyrotron

The major problems of high power, high frequency gyrotrons are given by the Ohmic heating of the cavity surface, by the dielectric losses in the output window and by the power capability of the collector. The technical limit of the power density at the resonator surface is assumed to be 2 kW / cm$^2$ for CW operation [1]. For this reason high power gyrotrons are operated in high order volume modes with a large cavity.

A major breakthrough for a CW compatible source is the use of a diamond window fabricated by chemical vapor deposition (CVD) [2-4], which allows the design and the operation of a CW tube at the 1 MW power level [2-4]. The single-stage depressed collector brings the overall efficiency of the gyrotron in the 50% range and at the same time significantly decreases the thermal loading inside the gyrotron.

The pre-prototype gyrotron tube (Maquette) has been first tested in short pulse operation. The measured RF beam patterns agree very well with the designed ones (Fig. 1).



d = 320 mm        d = 500 mm        d = 1000 mm
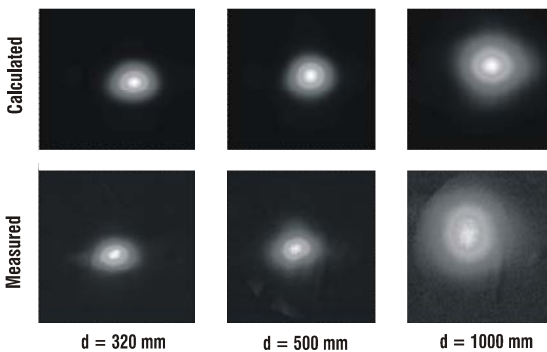
Fig. 1:    Calculated and measured RF-beam pattern at different positions from the window

Near the window, the output power was measured as a function of the accelerating voltage between cathode and cavity (Fig. 2) without and with depression voltage. Without depression voltage, an output power of 1 MW at an accelerating voltage of 82 kV could be achieved. With a depression voltage of 25 kV the same output power was obtained for the corresponding voltages; however, a higher voltage could be applied without losing the oscillation. Accelerating voltages up to 84 kV could be applied and an output power of 1.15 MW was achieved. This corresponds to

an output efficiency of 49%. The depression voltage could be
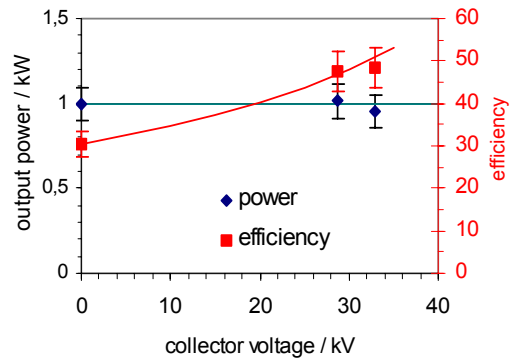


Fig. 2: Output power vs. depression voltage

increased to about 33 kV at the design values without any increase in the body current (lower than about 10 mA) and
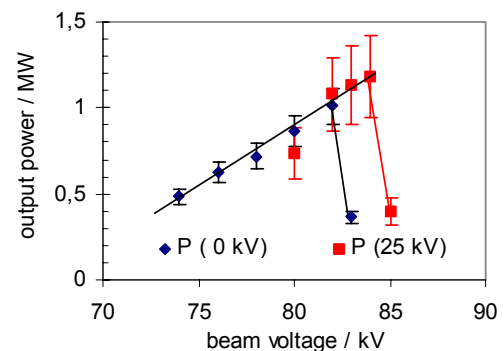


Fig. 3: Output power vs. accelerating voltage: without and with a depression of 25 kV

without any reduction of the output power (Fig. 3).

The output power of the gyrotron was also measured in short pulse operation at different positions of the calorimeter: behind the gyrotron window and in front of the calorimetric long pulse RF-load at a distance of about 2.5 m. The difference in output power between these two positions was less than 3%. Between the gyrotron and long-pulse RF-load, two focussing mirrors have been installed in order to focus the Gaussian RF beam toward the load. The second one of these mirrors was equipped with a directional coupler connected to a diode detector. The diode signal was calibrated in short pulse measurements, and the power in long pulse operation is measured from these signals.
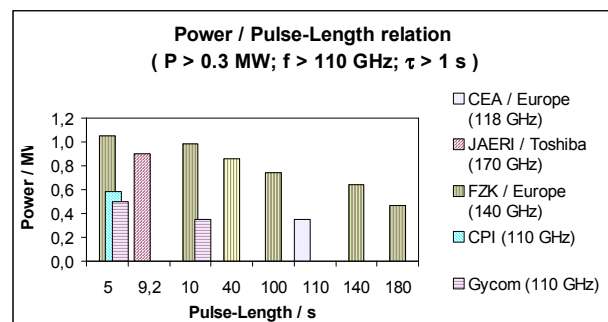


Fig. 4:   Output power vs. pulse length

Table 1: Experimental long pulse results

| pulse length | Power MW | current (average) | accelerating voltage | depression voltage | efficiency (with SDC) | Remarks |
|---|---|---|---|---|---|---|
| 180 s | 0.47 | 39 A | 77 kV | 27.7 kV | (23) % | |
| 140 s | 0.64 | | 80.2 kV | 27-30 kV | | arcing in load |
| Replacement of mirror in load | | | | | | |
| 100 s | 0.74 | 40.7 A | 82 kV | 24.5 kV | (32) % | ion getter pump I = 150 µA |
| 40 s | 0.86 | 41.5 A | 80.0 kV | 25.6 kV | 26 (39) % | |
| 10 s | 0.98 | 39.5 A | 83.5 kV | 30.3 kV | 29 (47)%) | |
| 5 s | 1.05 | 39.3 A | 83.4 kV | 30.3 kV | 32 (50) % | |
| 1.5 ms | 1.15 | 40 A | 84 kV | 25 kV | 34 (49) % | |

The results of long-pulse experiments are given in Table 1 and Fig. 4 (As a comparison the results of other companies and institutions are also given in Fig. 4). At the beginning of the experiment, arcing of the RF-load limited the pulse length to about 5 s at power levels exceeding 850 kW. Therefore, the rotating corrugated mirror of the RF-load was replaced by a fixed, almost conical one. This shifted the arcing beyond the 1 MW level. With the new mirror inside the RF absorber load an output power of about 1 MW could be obtained with a pulse length of 10 s. This gives an efficiency of almost 50%. For an output power of 0.74 MW at a pulse length of 140 s, an energy content as high as 90 MJ per pulse has been produced. This is the highest achieved value in gyrotrons operating at this frequency and power level [5,6]. The pulse lengths given in Table 1 are determined by the preset values of the pulse generator, and due to lack of experimental time no attempt was made to increase the pulse length. Only for the 100 s pulse at an output power of 740 kW a limitation in pulse length could be found: the pressure inside the gyrotron increased to values in the range $10^{-7}$ to $10^{-6}$ hPa (corresponding to 150 µA current of the ion getter pump).

Within the measurement accuracy, a low level of internal stray radiation was obtained.

As part of the long pulse measurements in-beam and post-operation studies were performed with brazed and bare CVD diamond disks put into the RF beam outside the gyrotron.

The video image of the gyrotron window produced direct evidence of light emission from the gyrotron window. Isolated bright spots were observed which were irregularly distributed over the window area, (Fig. 5), their number and intensity increased strongly for higher power levels. Video images clearly showed that the characteristic light emitting spots were not present at the spare window placed in the RF beam outside the gyrotron despite similar bulk losses, brazing history, and RF power. The only light emission event at the spare window followed an arcing event in the initial test phase of short pulses but did not show up at any later stage.

For the dismantled Maquette window, surface loss measurements showed an exceptionally high surface term for the growth face, which was the outer face, whereas the loss properties on the nucleation (vacuum) face did not differ much from the originally brazed condition. The surface loss is remarkably reduced by hydroxide cleaning on the growth face in contrast to the nucleation face. Loss mapping of the dismantled window proved that the average value of bulk loss remained close to the typical values ($\tan\delta = 3.5 \cdot 10^{-5}$) of the

original bare disk. This clearly indicates that most of surface losses were introduced by an on-site surface treatment which was applied to demonstrate that the light emitting centres could not simply be removed chemically from the outer window face. Apparently in this case, there was a protonic loss term introduced by acids which the original on-site hydroxide treatment could not fully suppress (Fig. 6 ) [7].
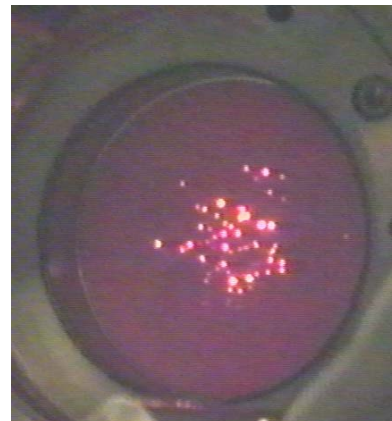


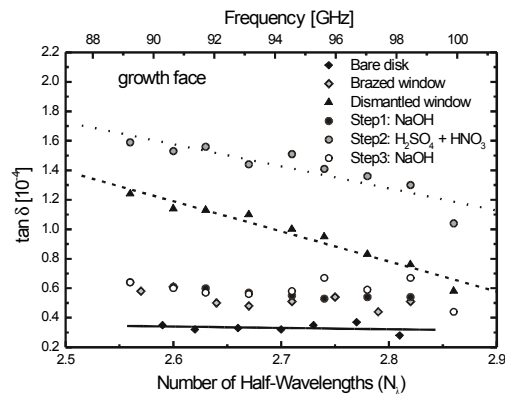Fig. 5: Video image of the Maquette window during a 750 kW / 6 sec pulse



Fig. 6: Apparent dielectric loss values measured at 90-100 GHz at different testing stages of the Maquette window

The positive identification of the origin of these light emitting centers requires much more experimental data. The light emitting spots proved to be a stationary phenomenon in the gyrotron window. It is assumed that they are related to the vacuum conditions of the gyrotron. All present evidence hints at a stable, even curing, performance of the properly integrated CVD diamond output window.

### 3. Development of Quasi-Optical Transmission Line

As the multi-beam waveguide (MBWG) mainly determines the transmission properties of the complete transmission system, a careful optimisation of the shape of the mirrors as well as their orientation was performed.

Calculations give very low mode conversion resulting in a high transmission efficiency of the transmission system. For the design of the water-cooled mirrors, thermo-mechanical calculations have been performed for several materials or combinations thereof, and for a variety of frame structures on the backside of the mirrors.

Two MBWG mirrors with the chosen frame structure were fabricated and will be tested in order to compare the behaviour of the mirrors with the calculations. Now the positions of the MBWG in the beam duct were fixed, and the detailed shape of the surface has been determined. The specification of the mirrors has been performed; the call for tender is on the way.

Two polarizers were fabricated and tested at the IPF Stuttgart in order to check the quality of the milled surface structure. The order for the polarizers has been placed.

The single-beam waveguide mirrors on the gyrotron side of the MBWG were specified, most of the mirrors are in fabrication or the order for them has been placed.

Most mounting devices for the mirrors have been fabricated.

### 4. Development of In-Vessel Components

Development has been started to optimise the surface structures for the back reflectors which will be mounted at the inner wall of the vacuum vessel of W7-X to redirect the non-absorbed part of the beam back into the plasma in a controlled way. This is necessary for heating of high-density plasmas in the 2nd harmonic O-mode, where the absorption is modest.

Experimental material investigations have been performed. Small specimens of graphite tiles with a plasma sprayed tungsten-coating of different thickness have been fabricated in order to investigate the reflection properties of this surfaces.

Furthermore, measurements were performed on the W7-AS torus in order to investigate the stray radiation inside the empty or plasma-filled torus-vessel in order to check the validity of computer-codes.

### 5. Auxilliary Systems

The cooling module for the RF transmission system (mirrors) with an overall cooling capacity of 700 kW and 150 $m^3$/h cooling water flow has been commissioned; the call for tender to install the water pipes inside the beam duct has been placed.

The fabrication of the 4 cooling modules for the TED gyrotrons has been started. These modules consists of 3 individual cooling loops for the different parts of the gyrotron. The collector loop for example has a cooling capacity of 1.6 MW at 108 $m^3$/h flow.

The fabrication of the cooling module for the RF absorber load loads with a cooling capacity of 1 MW at 50 $m^3$/h has been started.

The installation of 24 HV cages (for 12 Gyrotrons with power supplies) has been completed. This includes the required hardware for access control (pneumatic locks, manual earth switches) and personnel safety. 20 pneumatic earth switches have been delivered and are awaiting installation. The HV-feedtroughs (connecting the ground floor with the first basement floor) for the cathode voltage supplies have been installed. The installation of the 230 / 400 V power distribution to all HV-cages has been completed.

Staff:

A. Arnold (Uni Karlsruhe)
E. Borie
G. Dammertz
A. Götz
P. Grundel
R. Heidinger (IMF I)
S. Illy
K. Koppenburg
H.-R. Kunkel
M. Kuntze
W. Leonhardt
R. Lukits
D. Mellein
G. Neffe
S. Nold
B. Piosczyk
M. Schmid
W. Spiess
J. Szczesny
M. Thumm

Literature:

[1] S. Alberti, A. Arnold, E. Borie, G. Dammertz, V. Erckmann, P. Garin, E. Giguet, S. Illy, G. LeCloarec, Y. LeGoff, R. Magne, G. Michel, B. Piosczyk, C. Tran, M. Thumm, D. Wagner, "European High Power CW gyrotron Development for ECRH Systems", Fusion Engineering and Design 53, pp. 387-397, 2001.

[2] M. Thumm, "MPACVD-diamond windows for high-power and long-pulse millimeter wave transmission", Diamond and Related Materials, 10, pp. 1692-1699, 2001.

[3] O. Braz, A. Kasugai, K. Sakamoto, K. Takahashi, M. Tsuneoka, T. Imai, M. Thumm, "High power 170 GHz test of CVD diamond for ECRH window", Int. J. Infrared and Millimeter Waves, 18, pp. 1495-1503, 1997.

[4] M. Thumm, A. Arnold, R. Heidinger, M. Rohde, R. Spoerl, "Status report on CVD-diamond window development for high power ECRH", Fusion Engineering and Design 53, pp. 517-524, 2001.

[5] G. Dammertz, A. Arnold, E. Borie, S. Illy, W. Leonhardt, B. Piosczyk, M. Schmid, M. Thumm, V. Erckmann; H. Laqua, G. Michel, W. Förster, G. Gantenbein, W. Kasparek, G. Müller, P. Garin, R. Magne, E. Giguet, G. LeCloarec, Y. LeGoff, S. Alberti, M.Q. Tran, "1 MW, 140 GHz, CW gyrotron for Wendelstein 7-X", Proc. 9th Int. Conf. Displays and Vacuum Electronics, Garmisch-Partenkirchen, 2001, pp. 143-147.

[6] G. Dammertz, V. Erckmann, G. Gantenbein, W. Kasparek, H.P. Laqua, G. Müller, M: Thumm, "Electron Cyclotron Resonance Heating for the Stellarator W7-X", Proc. Jahrestagung Kerntechnik, Dresden, 2001, pp. 575-579.

[7] R. Heidinger, G. Dammertz, A. Meier, M. Thumm, „CVD diamond window studies for high power mm-wave transmission", Proc. of the 26nd Int.Conf. on Infrared and Millimeter Waves, Toulouse, 2001, to be published.

## Appendix I: FZK Departments Contributing to the Fusion Programmet

| FZK Department | FZK Institut/Abteilung | Director | Ext. |
|---|---|---|---|
| Institute for Materials Research | Institut für Material- und Festkörperforschung (IMF) | I.  Prof. Dr. K.-H. Zum Gahr<br>II.  Prof. Dr. D. Munz<br>III.  Prof. Dr. H. Haußelt | 3897<br>4815<br>2518 |
| Institute for Pulsed Power and Microwave Technology | Institut für Hochleistungs-Impuls- und Mikrowellentechnik (IHM) | Prof. Dr. M. Thumm | 2440 |
| Institute for Nuclear and Energy Technology | Institut für Kern- und Energietechnik (IKET) | Prof. Dr. U. Müller | 3450 |
| Institute for Reactor Safety | Institut für Reaktorsicherheit (IRS) | Prof. Dr. D. Cacuci | 2550 |
| Institute for Technical Physics | Institut für Technische Physik (ITP) | Prof. Dr. P. Komarek | 3500 |
| Institute for Micro Process Engineering | Institut für Mikroverfahrenstechnik (IMVT) | Dr. K. Schubert | 3114 |
| - Hot Cells | - Heiße Zellen (IMVT-HZ) | Dr. W. Nägele | 3650 |
| - Tritium Laboratory Karlsruhe | - Tritiumlabor Karlsruhe (TLK) | Dr. M. Glugla | 3226 |
| Institute for Data Processing and Electronics | Institut für Prozeßdatenverarbeitung und Elektronik (IPE) | Prof. Dr. H. Gemmeke | 5635 |

Contributing:

| | | | |
|---|---|---|---|
| Institute for Nuclear and Particle Physics, Technical University Dresden | Institut für Kern- und Teilchenphysik Technischen Universität Dresden | Prof. Dr. H. Freiesleben | +49 351/4635461 |
| Max-Planck-Institute for Plasma Physics Berlin | Max-Planck-Institut für Plasmaphysik Berlin | Prof. Dr. G. Fussmann | +49 30/20366130 |
| Max-Planck-Institute for Plasma Physics Berlin | Max-Planck-Institut für Plasmaphysik Berlin | Prof. Dr. B. Jüttner | +49 30/20246 760 |
| Institute for Applied Physics University Frankfurt | Institut für Angewandte Physik J.W. Goethe-Universität Frankfurt | Prof. Dr. H. Klein | +49 69/7982 3489 |
| Institute for Measurement Systems and Sensor Technology Technical University Munich | Lehrstuhl für Messsystem- und Sensortechnik Technische Universität München | Prof. Dr. A.W. Koch | +49 89/28928692 |

## Appendix II: Fusion Programme Management Staff

**Head of the Research Unit**          Dr. J.E. Vetter                    ext. 5460
                                                                         e-mail: joerg.vetter@fusion.fzk.de


      Secretariate:                  Mrs. I. Sickinger                 ext. 5461
                                                                         e-mail: ingeborg.sickinger@fusion.fzk.de

                                       Mrs. I. Pleli                     ext. 5466
                                                                         e-mail: ingrid.pleli@fusion.fzk.de

                                       Mrs. V. Lallemand                 ext. 5466
                                                                         e-mail: vera.lallemand@fusion.fzk.de


**Programme Budgets, Administration,**   BW. G. Kast                     ext. 5462
**Documentation**                                                        e-mail: guenter.kast@fusion.fzk.de


**Studies, ITER / NET Contracts,**       Dr. J.E. Vetter                 ext. 5460
**Superconducting Magnets,**                                             e-mail: joerg.vetter@fusion.fzk.de
**Gyrotron Development**

**Blanket Technology, Reactor**          DI. W. Bahm
**Studies, Neutron Source,**                                             ext. 5465
**Public Relations**                                                     e-mail: werner.bahm@fusion.fzk.de

**Tritium Technology, Structural**       DI. S. Gross                    ext. 5468
**Materials**                                                            e-mail: Sigurd.Gross@fusion.fzk.de


**<u>Address:</u>**          **Forschungszentrum Karlsruhe GmbH**
                     **Nuclear Fusion Programme Management**

                     **Post Office Box 3640, D - 76021 Karlsruhe / Germany**


**<u>Telephone No:</u>**     **07247-82- Extensions .....**


**<u>Telefax No:</u>**       **07247-82-5467**


**<u>world wide web:</u>**   **http://www.fzk.de/fusion**

## Appendix III: Glossary

| | |
|---|---|
| ADS | Atmosphere Detriation System |
| AGHS | Active Gas Handling System |
| BET | Brunauer, Emmet and Teller |
| BIOMASS | BIOspheric Modelling and ASSessment |
| BSMI | Bed-structure Mechanical Interaction |
| CBM | Carbon Based Materials |
| CCD | Charge Coupled Device |
| CDA | Conceptual Design Activity |
| CDE | Conceptual Design Evaluation |
| CECE | Combined Electrolysis and Catalytic Exchange |
| CFC | Carbon Fibre Composite |
| CICC | Cable in Conduit Conductor |
| COINLOSS | Conductor Insulation Loss (software module) |
| COOLSORP | Measurement of Sorption Isotherms at Cryogenic Temperatures |
| CP | Cooling Plate |
| CRPP-EPFL | Centre de Recherches en Physique des Plasmas Ecole Polytechnique Fédérale de Lausanne |
| CS | Central Solenoïd |
| CT | Cold Trap |
| CT | Compact Tension |
| CVD | Chemical Vapor Deposition |
| CW | Continuous Wave |
| D | Deuterium |
| DBTT | Ductile Brittle Transition Temperature |
| DP | Dew Point |
| DTE1 | Deuterium Tritium Experiment 1 at JET |
| DTL | Drift Tube Linear, accelerator structure |
| EAF | European Activation File |
| EASY | European Activation System |
| EB | Electron Beam |
| EC(R)H | Electron Cyclotron (Resonance) Heating |
| ECCD | Electron Cyclotron Current Drive |
| EDM | Electro Discharge Method |
| EDS | Exhaust Detriation System |
| EFF | European Fusion File |
| EISSG | European ITER Site Study Group |

| | |
|---|---|
| EMPA | Electron Microprobe Analysis |
| EOL | End-of-Life |
| EVITA | Experimental Vacuum Ingress Test Apparatus |
| FBI | F = Force, B = Magnetic Field, I = Current |
| FCGR | Fatigue Crack Growth Rate |
| FCI | Flow-channel Inserts |
| FDR | Final Design Report |
| FE | Finite Element |
| FEAT | Fusion Energy Advanced Tokamak |
| FEM | Finite Element Method |
| FM | Ferritic-martensitic |
| FNG | Frascati Neutron Generator |
| FPCC | Fusion Power Coordination Committee |
| FW | First Wall |
| HCPB | Helium Cooled Pebble Bed |
| HCS | Helium Cooling Subsystem |
| HEBLO | Helium Blanket Test Loop |
| HECOP | Heat Conduction of Pebble Bed |
| HETP | High Equivalent to a Theoretical Plate |
| HFI | High Fluence Irradiation |
| HFR | High Flux Reactor at Petten |
| HIP | Hot Isostatic Pressing |
| HP | Heating Plate |
| HVAC | Heating, Ventilation, Air Conditioning |
| ICS | Intercoil Structure |
| IP | Impurity Processing |
| IEAF | Intermediate Energy Activation File |
| IFMIF | International Fusion Materials Irradiation Facility |
| IGA | Inert Gas Atomization |
| IGUN® | Ion GUN, program code |
| IPF | Institut für Plasmaforschung der Universität Stuttgart |
| ISRM | Inelastic Strain Rate Modified |
| ISS | Isotope Separation System |
| ITER | International Thermonuclear Experimental Reactor |
| JAERI | Japan Atomic Energy Research Institute |
| JETT | J Evaluation on Tensile Test |
| LARA | Laser-Raman Analysis System |

| | |
|---|---|
| LCF | Low Cycle Fatigue |
| LCT | Large Coil Task |
| LEBT | Low Energy Beam Transport |
| LM | Liquid-metal |
| LOFA | Loss of Flow Accident |
| LPCE | Liquid Phase Catalytic Exchange |
| LSC | Liquid Scintillation Counting |
| MAG | Metal Arc Gas (Weld) |
| MAGS | Magnet Safety (software module) |
| MCE | Multi-channel Effect |
| MEBT | Medium Energy Beam Transport |
| MEKKA | Magneto-hydrodynamic Experiments in Sodium and Potassium Karlsruhe |
| MHD | Magneto Hydrodynamics |
| MS | Molecular Sieve |
| MTS | Material Testing Systems (Trade mark of MTS company) |
| ODS | Oxide Dispersion Strengthened |
| PD | Point Defect |
| PF | Poloïdal Field |
| PFC | Plasma Facing Components |
| PFD | Process Flow Diagram |
| PFM | Plasma Facing Material |
| PICOLO | Pb-Li Corrosion Loop |
| PID | Pipe and Instrumentation Diagram |
| PIE | Post Irradiation Examination |
| QMS | Quadrupole Mass Spectrometer |
| RA | Reduced Activation |
| RAFM | Reduced Activation Ferritic Martensitic |
| REP | Rotating Electrode Process |
| RF | Radio Frequency |
| RFQ | Radio Frequency Quadrupol, accelerator structure |
| R-MHD | Radiation Magnetohydrodynamics |
| RMS | Root Mean Square |
| SAD | Secondary Angular Distributions |
| SAGBO | Stress Accelerated Grain Boundary Oxidation |
| SDS | Storage and Delivery System |
| SEM | Scanning Electron Microscope |
| SiC | Silicon Carbide |

| | |
|---|---|
| SULTAN | Superconductor Test Facility, Villigen, Switzerland |
| TBM | Test Blanket Module |
| TCF | Thermal Low Cycle Fatigue |
| TCWS | Tokamak Cooling Water System |
| TEM | Transmission Electron Microscope |
| TEP | Tokamak Exhaust Processing |
| TES | Tritium Extraction System |
| TFMC | Toroïdal Field Model Coil |
| TIG | Tungsten Inert Gas |
| TIMO | Test Facility for ITER Model Pump |
| TITAN | Tieftemperaturadsorption |
| TLK | Tritium Laboratory Karlsruhe |
| TMS | Tritium Measurement System |
| TOSKA | Toroïdalfest Spulentest Karlsruhe |
| TPB | Tritium Permeation Barrier |
| TÜV | Technischer Überwachungs Verein |
| UCT | Uniaxial Compression Test |
| VHP | Vacuum Hot Pressing |
| VTA | Vertical Test Assemblies |
| WCLL | Water Cooled Lithium-lead Blanket |
| WDS | Water Detritation System |
| XRD | X-ray Diffraction Analysis |
| ZrCo | Zirconium-Cobalt |